This report details work undertaken to correlate data obtained from inspection systems in the casting plant, scarfing area and rolling mills in order to track product quality throughout the steel mills. The project was a collaboration between Corus UK Teesside Technology Centre (the coordinator), Arcelor and Scuola Superiore Sant'Anna (SSSA).

Two main inspection systems were tested for use in the continuous casting plant. The first was conoscopic holography, which was developed from an industrial prototype into a system where the entire slab top and bottom faces were inspected. The second was a hybrid laser-EMAT (electromagnetic acoustic transducer) system and was tested at pilot plant scale. Significant work was conducted to analyse data automatically so that a real-time, online inspection system could be conducted on plant.

Slabs were inspected in the slab yard using a variety of techniques which were compared. This inspection work was used to measure how well the caster was performing, by data mining plant signals and, for Arcelor, equating these with the conoscopic holography readings. Slabs were successfully tracked through the steel mill by the partners. Comparisons were made from upstream inspection to the downstream Parsytec system and inspection of the final product.

Different scarfing practices were compared and it was found that scarfing was no longer necessary for some steel grades.

Metallographic work was undertaken to assess defects in steel samples to determine the cause of cracking. Upon recommendations from this project, plant practices were changed and the defects no longer arose.

KI-NA-23176-EN-S

Price (excluding VAT) in Luxembourg: EUR 20

Publications Office
Publications.europa.eu

ISBN 978-92-79-07647-3

EC The measurement and prediction of surface quality by new developments in EMATS and scarfing and the effect of scarfing on surface defects through the mills EUR 23176

EUROPEAN COMMISSION

Community research

The measurement and prediction of surface quality by new developments in EMATS and scarfing and the effect of scarfing on surface defects through the mills

PROJECT REPORT

Research Fund for Coal & Steel

Interested in European research?

RTD info is our quarterly magazine keeping you in touch with main developments (results, programmes, events, etc.). It is available in English, French and German. A free sample copy or free subscription can be obtained from:

Directorate-General for Research
Information and Communication Unit
European Commission
B-1049 Brussels
Fax (32-2) 29-58220
E-mail: research@ec.europa.eu
Internet: http://ec.europa.eu/research/rtdinfo/index_en.html

How to obtain EU publications

Our priced publications are available from EU Bookshop (http://bookshop.europa.eu/), where you can place an order with the sales agent of your choice.

The Publications Office has a worldwide network of sales agents. You can obtain their contact details by sending a fax to (352) 29 29-42758.

EUROPEAN COMMISSION
Directorate-General for Research
Research Fund for Coal and Steel Unit

Contact: RFCS publications
Address: European Commission, CDMA 0/124, B-1049 Brussels
Fax (32-2) 29-65987; e-mail: rtd-steel@ec.europa.eu

European Commission

Research Fund for Coal and Steel

The measurement and prediction of surface quality by new developments in EMATS and scarfing and the effect of scarfing on surface defects through the mills

I. Baillie, P. Griffith, A. W. Smith, M. McDonald
Corus UK Limited
Teesside Technology Centre, PO Box 11, Grangetown, Middlesbrough, Cleveland TS6 6US, United Kingdom

L. Sancho, J. Diaz
Arcelor España S.A.
I+D+I, PO Box 90, E-33480 Avilés, Asturias

V. Colla, M. Sgarbi
PERCO
Scuola Superiore Sant'Anna (SSSA), Viale Rinaldo Piaggio 34, I-56025 Pontedera (Pisa)

Contract No RFSR-CT-2003-00047
1 September 2003 to 28 February 2007

Final report

Directorate-General for Research

2008 EUR 23176 EN

Europe Direct is a service to help you find answers to your questions about the European Union

Freephone number (*)**:**

00 800 6 7 8 9 10 11

(*) Certain mobile telephone operators do not allow access to 00 800 numbers or these calls may be billed.

A great deal of additional information on the European Union is available on the Internet. It can be accessed through the Europa server (http://europa.eu).

Cataloguing data can be found at the end of this publication.

Luxembourg: Office for Official Publications of the European Communities, 2008

ISBN 978-92-79-07647-3

ISSN 1018-5593

Printed in Luxembourg

PRINTED ON WHITE CHLORINE-FREE PAPER

INTRODUCTION

This report details work undertaken to correlate data obtained from inspection systems in the casting plant, scarfing area and rolling mills in order to track product quality throughout the steel mills. The project was a collaboration between Corus UK Teesside Technology Centre, Arcelor and Scuola Superiore Sant'Anna (SSSA) which was coordinated by Corus.

Co-ordination meetings were held twice a year with the partners, at each of the partner sites. Although the project started late due to awaiting RFCS approval, the objectives were completed according to the Technical Annex of the contract which can be found in Appendix 5. All the Tasks were completed by the end of the project, with the exception of Task 2, from Work Package 2 and Task 3 from Work Package 3. Reasons for not completing this work are found in the following section and these were highlighted in previous 6-monthly reports and whilst presenting the mid-term report to the TGS9 Committee.

This project did not exceed the overall budget and the project costs from each of the partners were approved after the submission of the mid-term report. Final, audited cost claims are being submitted.

Two main inspection systems were tested for use in the continuous casting plant. The first was Conoscopic Holography, which was developed from an industrial prototype where only a partial width of the slab surface was inspected to a system where the entire slab top and bottom faces were inspected. The second was a hybrid Laser-EMAT (ElectroMagnetic Acoustic Transducer) system. This system was demonstrated to work on hot moving steel. Significant work was conducted to analyse data automatically so that a real-time, on-line inspection system could be conducted on plant.

Work was undertaken to inspect slabs in the slab yard using a variety of techniques which were compared. This inspection work was used to measure how well the caster was performing, by data mining plant signals and, for Arcelor, equating these with the conoscopic holography readings. Slabs were successfully tracked through the steel mill by the partners and comparisons were made from upstream inspection to the downstream Parsytec system and inspection of the final product.

Different scarfing practices were compared. In some instances, for certain steel grades, it was found that scarfing was no longer necessary.

Metallographic work was undertaken to assess defects in steel samples to determine the cause of cracking. Upon recommendations from this project, plant practices were changed and the defects no longer arose.

Work Package 1: Development of Non-contact Methods of Defect Detection via EMAT Technology to Prototype Systems, Use and Further Development of Conoscopic Holography Method, and Comparison of Systems

The original objectives for this task were:

"To progress the development of non-contact methods of defect detection via EMAT technology to prototype systems from laboratory through to pilot plant and industrial scale systems. To use and further develop the conoscopic holography method. To compare the systems."

Task 1.1 Technical Literature Survey and a Comparison of Methods

A literature survey was conducted and published as part of the mid-term report[(1)]. This examined different techniques for inspecting hot, continuously cast products. A comparison between the Arcelor and Corus systems was made and is most easily presented in a table format and this can be seen in Table 1.

Task 1.2 Specify, Design and Develop Devices for the Steel Industry

This task has been merged with Task 1.3, as detailed below.

Task 1.3 Laboratory and Pilot Plant Trials

Significant progress in developing the EMAT and conoscopic holography (CH) systems has been made in this project. This work has involved the installation of EMAT sensors on pilot plant casting and rolling mills at Corus. However, because the pilot plant caster was taken off-line to be upgraded into a vertical caster with bending, work was done on heated, moving billet samples on the pilot plant rolling mill at Corus, which demonstrated the feasibility of the system. Ultrasonic measurements were taken above 800 °C. Preparation work and preliminary tests have been conducted at casting temperatures on the newly installed caster but no hot ultrasonic measurements have been taken using the new caster. Consultancy on EMAT issues and the loan of equipment from The University of Warwick was performed as part of a sub-contract. Training in ultrasonics and the use of laboratory facilities has also been undertaken at Warwick.

Appendix 1 contains experimental descriptions of the various EMAT experiments conducted at Corus and Warwick. In short, Laser-EMATs have been shown to detect, size and locate defects in moving steel. SSSA was responsible for developing software to analyse the ultrasonic data and to automate the detection inspection process. More work needs to be conducted to develop a fully automated system. Recommendations for the final system are included as part of Appendix 1.

Appendix 2 details trial work carried out on plant by Arcelor. Here, Arcelor compared its manual, visual inspection of slabs in the slab yard to the results found using its automated CH system which inspected the slabs on-line. The system was significantly developed as part of this project. Now the entire top and bottom faces of slabs are inspected before scarfing and the process route has changed as a result due to knowing the surface quality of the steel.

Task 1.4 Adapt, Develop and Carry Out Trials

This work has been combined into Task 1.3 and is detailed in Appendices 1 and 2.

Task 1.5 Evaluation of Results and Correlation of Data

Ultrasonic results from experiments were compared and analysed by SSSA to the predicted results from models developed by SSSA. When defects are present in the steel, a noticeable change in the waveforms can be detected. Examples of this can be seen in Appendix 1. Discussion about the models for predicting signals in different sizes of products can also be found in Appendix 1. Essentially, there

is a change in waveform arrival times, signal amplitude and frequency, which can all indicate the presence of a defect. This can then allow defects to be positioned and sized.

At Arcelor the conoscopic system is compared with manual inspection. Now, the conoscopic system is relied upon to determine the downstream production path of slabs after scarfing. Slab quality before scarfing, after scarfing and processing in the strip mill (using Parsytec) are all used. These results are reported in Appendices 2 and 4.

Task 1.6 Validate and Compare to Other Systems

The Arcelor system is fully installed on-line to inspect both the top and bottom faces of slabs. Slabs from each of the casters are fed through this inspection system, which is located at the end of one of the caster strand lines. This system is suitable for finding surface defects. The Corus EMAT system is at the pilot plant stage of development. It demonstrated the capability to find defects on the surface of hot, moving steel. The EMATs system needs to be further refined, as this is one of the few systems with any potential to be installed on-line for finalising BOTH surface and internal defects. Comparisons were made during partner visits, as part of the RFCS six-monthly meetings and this can be found in Table 1.

Task 1.7 Further Refine Techniques

The Arcelor system was fully developed to inspect slab top and bottom faces. The EMATs system is at the prototype stage and is ready for testing on the pilot caster at Teesside Technology Centre.

Task 1.8 Prepare Recommendations for Full System

The Arcelor system works well for finding longitudinal defects. The system could be adapted to find transverse defects. The Corus system requires more development, but has shown promise. It is hoped to obtain more RFCS funding to develop further both of these systems as part of a newly proposed RFCS project, "NDTCASTING", involving all the project partners from SURFQUALDEV.

Work Package 2: Evaluate and Assess Defect Detection via Scarfing System and Compare with Other Systems

The original objectives for this task were:

"To carry out an evaluation and assessment of the system of defect detection via scarfing equipment as a measurement and predictive technique (Corus together with equipment, consultancy from Heckett MultiServ). To compare with other systems on partners plants."

Task 2.1 Technical Review of Existing Systems

A technical review of the Heckett MultiServ scarfing system was undertaken for an optical inspection system for surface defect detection called 'Opticon', which works by detecting the sparks caused by cracks during the scarfing process. At Corus, the development of an automatic detection system far exceeds the available budget within this project. The Heckett system is currently off-line at its main development site in France. During the course of this project the system was mothballed, as it was too slow to find defects, as compared with a human operator. It has been suggested that the Heckett system could be re-visited in the future as new advances in computing power and inspection systems are developed. Therefore it was not possible to send slabs from the partners there for scarfing trials. Meetings at the start of this project took place with MultiServ, and at one Corus plant, where Heckett is contracted to scarf slabs. Therefore man-hours were diverted from WP2 to other scarfing and inspection work packages. This was discussed in the 6-monthly reports and in the mid-term report[(1)]. It was also raised to the Commission at the TGS9 committee meeting, when the mid-term report was presented by Corus.

Task 2.2 Evaluate and Design System

Arcelor reviewed a series of different inspection technologies to inspect slabs after scarfing and these results can be found in Appendix 3. These different inspection systems included laser triangulation, conoscopic holography and thermography used in the scarfing yard to assess product quality after different scarfing passes. A comparison of the different systems can be found in Appendix 3.

Task 2.3 Compare Scarfing Defect Detection to the EMAT and Conoscopic Holography Systems

Essentially, the EMAT system can be used on-line for both surface and internal defect detection, whilst the conoscopic holography system can be used on-line for surface defect detection only. The additional 'inclusion detection' system used by Arcelor physically removes a strip of metal from the surface so that optical cameras can inspect the clean steel. The optical scarfing recognition system is 'off-line' and is only used during the scarfing process after casting. A full review of available inspection systems was included as part of the mid-term report and is too long to include here[(1)].

Task 2.4 Investigate the Possibility of Development of the Opticon Scarfing Defect Detection System

As stated under Task 2.1, the development of this system under the SURFQUALDEV project is too expensive to progress.

Task 2.5 Complete Assessment and Develop a Proposal for Exploitation of this Method

As stated in Tasks 2.2 and 2.4, the Opticon system is not available for testing. Therefore manpower was diverted to the other scarfing Work Packages. This was discussed at the mid-term TGS9 presentation and in the six-monthly reports.

Work Package 3: Investigate the Effect of Scarfing on the Persistence, Initiation and Propagation of Surface and Sub-surface Defects

The original objectives for this task were to:

"Investigate the effect of scarfing on the persistence, initiation and propagation of surface and sub-surface defects."

Task 3.1 Review of Experience and Knowledge

Meetings have been held by both Arcelor and Corus research staff with the steelworks. Arcelor has assessed its Northern Spain steel plant operations. Corus has held meetings with Plants A, B and C to discuss their scarfing operations, as these sites are where some of Corus' continuous casters are located. Discussions at Plate Mills A and B (end-users of Corus semis) have also taken place. These meetings have helped to establish what methods of scarfing are currently employed throughout Corus and Arcelor.

Trials were conducted in the steel mills to assess the performance of scarfed slabs. For certain steel grades, it was found that scarfed slabs had only marginally better end product quality than those slabs that were not scarfed. Slabs from steel grades that had previously been scarfed as routine practise were then sent through the rolling mill stage unscarfed and no detrimental decline in product quality was reported. Slabs were successfully tracked through both the Arcelor and Corus steel plants.

Task 3.2 Map Defects through the Process Route by Visual Techniques and Other Techniques Before and After Scarfing

As detailed in Appendix 4, some work was carried out on slabs from Corus Plant A which were delivered to Plate Mill B. Magnetic Particle Inspection (MPI) and dye penetrative techniques were used to inspect the semis after different scarfing parameters were applied. This showed that some slabs, passed as clear with only visual operator inspection were passed downstream and yet contained defects. These later caused problems for the customer.

At Arcelor, both unscarfed and scarfed slabs were inspected manually and results were compared with automatic inspection systems that were installed in both the caster and slab yard (Appendix 4). Good correlation existed and Arcelor re-designed its process route to ensure that all slabs are inspected with its on-line system. Arcelor also tested and assessed different inspection systems in the scarfing yard for automatic inspection of scarfer quality (Appendix 3).

Task 3.3 Compare Scarfing and Grinding

This task was not undertaken as grinding is not performed at any of the partners steel mills. Only small amounts of hand scarfing are conducted. This was raised in the fourth, 6-monthly technical report.

Task 3.4 Assess the Effects of Scarfing Parameters (Such as the Temperature and Time of Scarfing)

Appendix 4 details work conducted by the partners to ascertain the effect of different scarfing parameters, such as number of scarfing passes.

Task 3.5 Track Artificial Defects through the Mill

Corus and Arcelor can both track defective slabs through the process route and find them in the final product. This is useful as defects in the final product can be tracked back to the slab and therefore the casting parameters (e.g. speed, oscillation settings, spray cooling etc) can be checked to determine what caused the defects (Appendix 4). Corus determined that one particular type of crack could be attributed to a hard secondary cooling practice and the plant adjusted its parameters to a soft cooling regime and subsequent metallurgical analysis could find no trace of these defects.

Task 3.6 Evaluation of Results via Statistical Analysis and Artificial Intelligence

Significant amounts of data were mined as part of this project. Large statistical data sets were used to analyse product quality, when different factors were changed. This work is presented in Appendix 4. The partners found it possible to track casting parameters and the quality of the resulting slabs with final product inspection of products such as coils and plates. Establishing links to the Parsytec system was particularly useful for doing this work.

Work Package 4: Characterise Scarfed Slabs to Investigate the Occurrence and Source of Defects

The original objectives of this task were:

"To characterise scarfed slab surface and investigate the occurrence and source of defects following rolling of scarfed slab such as laminations, shell and sliver."

Task 4.1 Review Existing Knowledge and Data from Production Systems and Correlation of Defects with Caster, Process, Slab Yard Reheating and Rolling Data

Meetings were held by Corus and Arcelor with relevant research and production personnel where existing knowledge and data sources were identified for each process stage. Steel grades and problems the production plants faced were assessed. Particular emphasis was placed on linking the product

quality data obtained from the plants with the actual product quality. For example, Corus ascertained that scarfing did not always yield significantly better surface quality in the final product (Appendix 4).

Task 4.2 Critical Monitoring of Casting, Slab Rectification, Transport, Reheating Stages of the Process Route with Feedback on Quality After Rolling Processes

Appendix 4 details how monitoring was carried out on plate and strip grades. Slabs were tracked between caster, scarfer and downstream. Samples were taken for metallurgical examination. Recommendations for altering steel plant procedures were made which solved surface quality issues.

Task 4.3 Metallographic and Chemical Analysis of Defects

This work was conducted as part of Task 4.2.

Task 4.4 Simulate Defects and Track Through Process

Artificial pinhole defects were successfully tracked from cast slab through scarfing and rolling (Appendix 4).

Task 4.5 Analyse and Correlate Data

Data were collected and analysed by the partners. At Arcelor, the robustness for the correct identification of defects was proven by comparing the data from automatic inspection with the manual inspection process. Appendix 4 details work conducted to compare the Parsytec system with the CH system. At Corus, data were also collected from manual processes and from various computer databases.

Task 4.6 Software Simulation to Test Strategies

This work was conducted as part of the Clementine work undertaken by Corus. Clementine is the computer infrastructure used to link all the inspection and quality databases at Corus. The feasibility of this work was proven. This involved adjusting the process route for some slabs and tracking the final product quality using the Information Technology infrastructure. This meant that a system was in place where trials relating to potentially adjusting casting and steel plant applications could be conducted "from the office" because the data gathering system was so comprehensive. Arcelor conducted similar trials using its in-house data infrastructure, Mityca. Appendix 4 details this work performed by the partners.

Task 4.7 Collate Data and Specify Improvements

Significant volumes of data were collected during this project. These trial data were generated from both physical samples taken from the plants, data mining databases and from automated inspection systems. This helped formulate recommendations to the steel plants such that improvements to operating procedures could be made so as to reduce costs, increase throughput, decrease stock etc. Improvement ideas were raised with the steel plants, which were acted upon. This allowed for cost savings at the respective partners' plants to be made.

Work Package 5: Optimise Existing Scarfing Practices and Investigate Improved Means of Defect Rectification

The original objectives for this task were to:

"Optimise existing scarfing practices. To investigate improved means of defect rectification."

Task 5.1 Review and Compare Practices at Different Plants

Appendix 4 compares the scarfing practices at the project partners' mills.

Task 5.2 Collect and Analyse Data and Propose New Practices

This was conducted as part of Task 4.

Task 5.3 Apply Proposed Practices and Assess Benefits

This was conducted as part of Task 4.

Task 5.4 Review and Assess Other Rectification Methods

Appendices 2 and 4, concerning the use of the conoscopic system showed that not all slabs of a particular grade needed to be scarfed. Data mining also showed that in some instances slabs that were scarfed exhibited only marginally better surface quality characteristics than those not scarfed. When defects in slabs were highlighted, the information was fed back to the casting plants. Parameters were changed and through assessing the same steel grades again it was found that the problem was rectified. This is not to say that scarfing is not needed. However, if casting plants can produce semis "right first time" then the additional costs incurred during scarfing can be avoided.

Task 5.5 Prepare Proposal for Implementation of Findings

It was decided to feed back information to the steel plants as the work was progressed, so that plants could adjust their operating parameters and manufacture defect free semis. These recommendations are included in Appendix 4.

CONCLUSIONS

Two main inspection systems were tested for use in the continuous casting plant. Conoscopic Holography was taken from an industrial prototype where only a partial width of the slab surface was inspected, to a system where the entire slab top and bottom faces can be inspected. The entire casting operating performance of the Arcelor steel plant was changed as a result of this project, where all the slabs are fed through the CH system before being sent downstream. This means that only slabs with surface defects are therefore scarfed saving energy and manpower costs. Arcelor can also collate and data mine information from the casters, CH system, scarfing bay, Parsytec system and from final product inspection. This makes it possible to determine at which manufacturing stage defects arise and means that there is sufficient information available to identify and correct defects.

The second was a hybrid Laser-EMAT (ElectroMagnetic Acoustic Transducer) system that involved taking a university prototype and developing it for use on hot, moving steel. The system was demonstrated to work successfully on hot moving steel in the pilot plant rolling mill at 800 °C. The EMAT system could be used for finding internal defects, in addition to surface defects. However, to date, no hot ultrasonic trials have been conducted on a continuous caster, but recommendations have been made in Appendix 1 as to how a system could be realised. Significant work was conducted to analyse the data automatically so that a real-time, on-line inspection system could be installed on plant.

Work was undertaken to inspect slabs in the slab yard. This was done using conventional dye penetrative techniques, Magnetic Particle Inspection and a variety of new techniques including conoscopic, thermographic and laser triangulation such that the inspection process could be automated. This inspection work was used to measure how well the caster was performing, by data mining plant signals and, for Arcelor, equating these with the conoscopic holography. Slabs were successfully tracked through the steel mills by the partners and comparisons were made from upstream inspection to that of the Parsytec system and customer inspections of the final product. Similar work was undertaken at Corus where dye penetration was used to inspect slabs in the slab yard and metallographic work was

undertaken to assess crack structures on steel samples to determine the cause of cracking. Upon recommendations from this project, plant secondary water-cooling practices were changed and the defects no longer arose.

Significant work was undertaken to analyse and compare different scarfing practices. By data mining at both Corus and Arcelor, in some instances, for certain steel grades, the difference to final product quality when a slab was scarfed or not scarfed was minimal. Therefore trials were conducted that showed scarfing was at times unnecessary. As a result, the plants do not scarf these identified grades saving energy and manpower costs. In the case of some steel grades, results were less conclusive and further evaluation based on larger data sets is recommended.

It is hoped to continue this work on automated inspection techniques in a new RFCS project, proposed by the partners, with the addition of BFI, who would co-ordinate the project.

LIST OF TABLES

LIST OF FIGURES

A3.4 Evolution of burr detection along two different days. Slab jump above 10 pixels indicates the existence of burr not properly removed
A3.5(a) Photograph of the plane tool operating on a hot slab at Arcelor
A3.5(b) Drawing of the ancillary mechanical device for sampling of the planed steel strip
A3.6 Partial images of the inspected strip meshed together
A3.7 Scheme of the new automated line scan optical system for inspection of slab surface after scarfing
A3.8 Feasibility tests of the new line scan optical system: (a) in the lab with moving samples and (b) in the plant with scarfed slabs
A3.9 Example of the acquisition of a surface profile using the lab prototype
A3.10 The new line scan optical system inspecting scarfed slabs in the Arcelor plant
A3.11 Blurred image of the slab number obtained with the webcam
A3.12 Examples of acquired surface maps with the new line scan optical system: (a) two scarfed slabs with good surface quality (Nov 2006) and (b) two slabs with poorer quality (Oct 06)
A3.13 Results of the thermographic inspection of the inclusions, before cleaning the surface (left) and after cleaning the surface (right); the real inclusions appear in both images
A3.14 Dimensions and photograph of the slab sample used to test different inspection devices
A3.15 Part of the slab sample used to test different devices for inclusion detection. Pore 1 had a diameter and a depth of 3 mm*0.7 mm. Pore 2 measured 5 mm*2.3 mm, Pore 3 measured 4 mm*0.7 mm and Pore 4 measured 1.5 mm*0.4 mm.
A3.16 Results from the laser triangulation technique at 90 fps, when the slab sample was moving at 5 mm/s
A3.17 Image of sample taken using the CH system at 30 fps when the slab sample was moving at 5 mm/s. All four pores are detected
A3.18 Image of sample taken using the IEEE CH system. 5 mm/s speed, 30 fps second
A3.19 Tests of inclusion detection on a steel sample using the novel IVP-Ranger sensor
A3.20 Inclusion/pinhole detection using machine vision and infrared lighting
A3.21 Wavelength distribution obtained with spectral camera on the indicated line on the sample
A3.22 Tests of inclusion detection on a steel sample using spectral camera
A4.1 Scarfer similar in design to that used at Plant A
A4.2 Androfer™ scarfer in operation
A4.3 Magnetic particle inspection for cast 79532
A4.4 Magnetic particle inspection for cast 79556
A4.5 Proportion of plates rejected against casting speed of associated slab (Courtesy Corus Plant A)
A4.6 Proportion of plates rejected against position in sequence of associated slab (Courtesy Corus Plant A)
A4.7 Proportion of plate rejected against quality code of steel (Courtesy Corus Plant A)
A4.8 Sulphur print sampling diagram
A4.9 Sampling diagram for de-scaling with acid bath and microstructural work
A4.10 Photograph of cracks found on broad face of cast 60933, slab 5C
A4.11 Photograph of cracks found on broad face of cast 60933, slab 5E
A4.12 Section of cast 60933, slab 5B showing surface defects on folded out edge and broad face
A4.13 Section of the cast 60933, slab 6B showing surface defects on folded out edge and broad face
A4.14 Section of cast 60942, slab 5B showing surface defects on folded out edge and broad face
A4.15 Photograph of crack networks from Fig. A4.12, cast 60933, slab 5B, sample 1 after deep etching to remove scale
A4.16 Cross-section and microstructure of crack networks, cast 60933, slab 5B, sample 1, after etching, x50
A4.17 Cross-section of small crack, cast 60933, slab 5B, sample 2, after etching, x50
A4.18 Photograph of cracking from Fig. A4.13, cast 60933, slab 6B, samples 3 and 4, after deep etching to remove scale
A4.19 Cross-section of crack, cast 60933, slab 6B, samples 3 and 4
A4.20 Microstructures of cracks, cast 60933, slab 6B, sample 4

A4.21 Photograph of cracking from Fig. A4.14, cast 60942, slab 5B, sample 5 after deep etching to remove scale
A4.22 Cross-section and microstructure of crack, cast 60942, slab 5B, after etching, x100
A4.23 Schematic summarising the sampling technique
A4.24 Photograph of the sliver found in the scarfed sample
A4.25 Data collection infrastructure for the slab tracking and inspection project
A4.26 The use of Clementine for data analysis
A4.27 Lamination results for steel grades G1 and G2
A4.28 The effect of scarfing on big laminations
A4.29 The effect of scarfing on medium laminations
A4.30 The effect of scarfing on small laminations
A4.31 User interface for the slab surface CH inspection system (Surfin)
A4.32 User interface for hot coil surface inspection system (Parsytec)
A4.33 User interface for product traceability system (Mityca)
A4.34 Examples of surface defects detected from CH with on-line surface inspection of slabs
A4.35 Examples of surface defects detected with CH on-line surface inspection of slabs
A4.36 Examples of surface defects detected with CH on-line surface inspection of slabs
A4.37 Example of a new type of defect detected in the bottom face of some slabs
A4.38 Results for consecutive slabs with longitudinal cracks. From right to left: temperature asymmetry in mould wall, grey scale image of the slab, Conoscopic Holography distance maps and Parsytec defect detection results on hot rolled coil

LIST OF REFERENCES

1. Patrick B, Baillie I, Sancho L, Diaz J, Colla V, Sgarbi M: Mid-term RFCS Report "SURFQUALDEV", Technical Report No. 3, Feb 2005.
A1.1 Scruby, C B, Drain, L E: 'Laser Ultrasonics Techniques and Applications', pub. Adam Hilger ISBN 0-7503-0050-7, 1990
A1.2 Kaye, C W C, Labey, T H: 'Tables of Physical and Chemical Constants', 16th Edition, Pub. Longman, 1995, ISBN 0-582-22629-5
A1.3 Bentley J P: 'Principles of Measurement Systems', 3rd Edition, pub. Addison Wesley Longman Ltd, 1997, ISBN 0-582-23779-3, p156
A1.4 Edwards R S, Dixon S and Jian X 'Depth Gauging of Defects using Low Frequency Wideband Rayleigh Waves', Ultrasonics, Vol. 44, pp93-98, 2006
A2.1 Obeso F, Sancho L F, Alvarez I, Díez A, Sirat G, Falesi R: 'Novel on-line surface quality control for hot slabs in continuous casting', La Revue de Métallurgie, March 2002, pp267-275
A2.2 Sirat G Y, Psaltis D: 'Conoscopic holography', Optics Letters, 10, 4, 1985
A2.3 Diaz J, Sancho L F, Alvarez I: 'Application of conoscopic holography to control melt stirring', La Revue de Métallurgie, March 2006.
A2.4 Alvarez I, Enguita J M, Fernández Y, Marina J, Fraga C, Sirat G: 'On-line defect detection with the long-standoff conoline profilometer', 2nd International Conference on Metrology, Eilat (Israel), Nov 2003
A3.1 Boogen, J: 'Informacion sobre equipos de oxicorte y escarpado' (Catalogo) Jose Boogen Maquinaria y Materiales para industrias, 1987
A3.2 Plotnikov, Y A, Winfree, W P: 'Visualization of subsurface defects in composites using a focal plane array infrared camera', Proceedings of SPIE, Vol. 3700, 1999, pp26-31

Table 1: Comparison between Laser-EMAT and Conoscopic Holograph Systems

	Laser-EMAT System	Conoscopic Holography System
Is the system Installed on-line in a steel plant?	Only tested on rolling mill at the pilot plant stage. Work is progressing to install on caster at Teesside.	Yes. Fitted; the final system is being installed over two production lines in the casting area.
What is the stand-off above the steel?	3 mm for EMATs.	1200 mm top, 800 mm bottom
What's the maximum operating temperature?	Tested to 800 °C on the pilot scale mill.	Normal casting plant conditions. Tested with slabs at 900 ºC. The final system has only two fans.
Speed of semi at the inspection point?	Typical casting speeds (0.5 m/min -> 2 m/min)	20 m/min
What type of surface defects are detectable?	* Transverse cracks >1 mm in size * Longitudinal cracks >1 mm in size * Porosity * Inclusions	Mainly longitudinal. Resolutions are: * transverse = 0.5 mm, depth 0.2 mm * longitudinal = 6 mm (at 20 m/min). The longitudinal resolution is inversely proportional to slab speed (at 1 m/min - 0.3 mm approx)
Can internal defects be found?	Yes; segregation, cracks, porosity, inclusions	No
Is the system affected by scale?	Not yet determined. Should not be a problem.	No need to remove scale. Scale is eliminated via visual software.
Affected by oscillation marks?	No. Only severe oscillation marks (but this is a defect anyway)	No
Top face coverage?	Yes. Technology could span entire width of slab from one laser.	Yes. Can cover up to 1800 mm wide slabs.
Bottom face coverage?	Could have an array of sensors under a slab. However, top sensors will be able to find bottom defects.	Currently installed on plant. Full bottom width coverage is also 1800 mm.
Side face coverage?	Is feasible.	Feasible. One additional sensor per side face.
Cost?	Approx 1 MEuros per strand?	Approx 1 MEuros per caster.
Real time defect detection?	Could be implemented with dual-core processors and Real-Time Operating System.	The whole set of inspection results is currently obtained in 15 sec. Subsequent process routes for the slab are decided by the software.
Ability to label semis to indicate presence of defect?	No, but could be linked to a system that could.	The position of defects is recorded by a PC and can be recovered when required.
Needs to connect to air supply?	Potentially. More trial work is needed to ascertain durability.	Yes. Air keeps dust off bottom sensors.
Needs to connect to mains water supply?	Yes. To water-cool EMATs.	No.
Health & Safety considerations?	Class 4 laser system in use. Need to ensure beam is fully enclosed at all times.	Class 3b laser.
Size of data file every second?	1.6 Mb per EMAT. May need 15 EMATs to cover the width of the slab, therefore 24 Mb/sec?	For maximum slab coverage, 0.32 Mb/sec.

APPENDIX 1

INTERNAL AND SURFACE DEFECT DETECTION USING NON-CONTACT ULTRASONICS (WORK PACKAGE 1)

A1.1 LASER-EMAT THEORY

A pulsed laser beam incident on the sample surface can generate ultrasonic waves in steel. On thick samples (wavelength << thickness), both surface waves and bulk waves can be generated by this broadband ultrasonic source. The surface waves generated are surface skimming (p-waves) and Rayleigh (r-waves). The bulk waves generated that reflect off the back surface of the sample are shear bulk waves (SS) and longitudinal bulk waves (LL). Mode converted waves can also be detected, such as SL (shear to longitudinal waves) and LS (longitudinal to shear waves) which have mode converted on reflection from the back surface. The arrival times of these waves can all be calculated provided the geometry of the EMATs, laser and sample are all known. SSSA has produced a series of models based on methods developed at Warwick to predict these arrival times as any change from the expected arrival times can be attributed to the presence of a defect.

Corus has used two pulsed laser systems for these experiments, both capable of generating ultrasound. Their specifications are given in Table A1.1. A photograph of the laser enclosure area is shown in Fig. A1.1.

An EMAT is essentially a static magnetic field with a plane of a coil of wire where the wires of the coil remain perpendicular to a static magnetic field. The optimal number of turns for a linearly wound coil, was determined experimentally. The EMATs used initially were designed to operate at room temperature. Later trials involved the design and construction of water-cooled EMATs that were then successfully tested in the Pilot Plant and Laboratory, as ultrasonic measurements were successfully taken at elevated temperatures.

A1.2 INITIAL LABORATORY EXPERIMENTS

A1.2.1 Laser-EMAT Experiments to Locate a Surface Defect

A1.2.1.1 Introduction

When a high energy density pulsed laser beam (800 mJ at 1064 nm or 150 mJ at 532 nm) is incident on a sample surface, a plasma is formed from ablation of the surface. Approximately 4% of this energy is absorbed by a clean steel surface and some of this energy is converted to ultrasound[(A1.1)]. The shape of the impact point is approximately circular, as this represents the natural shape of the laser beam. The beam diameter is determined by which laser system is used, but this is typically between 4 mm to 8 mm. This is effectively a point source and the energy from the beam can be concentrated on the steel by using a standard BK7 glass plano-convex lens. After focusing, the beam is less than 2 mm in diameter. This in turn increases the amplitude of the ultrasonic waves received by the EMAT.

When viewed from above, a point source will generate surface wavefronts that are approximately circular on the surface of the sample and these can be seen in Fig. A1.2a. A point source will generate wavefronts on the surface of the sample that are surface waves 2-D in nature. This can be seen in Fig. A1.2b. The attenuation of bulk and surface waves is different, due to the way their energies are spread. The energy of a surface wave is localised on the surface around a circumference, whereas bulk wave energy is localised on the surface of a hemisphere and are therefore geometrically attenuated more strongly than the surface waves.

A linear EMAT coil is particularly sensitive to crack orientation, but the relative position of the EMAT, laser and defect are all-important. It is necessary to align the system geometry, which is dependent on the product size. The system is particularly sensitive when the linear coil is approximately parallel to

the defect. If the defect is perpendicular to the coil, then it can often be detected via reflected waves. A point source is best for EMAT detection. This is because the point source can be focused on one particular spot and an array of EMATs with coils in different orientations can be used to detect defects in different positions.

A1.2.1.2 Experimental Arrangement for Finding Defects Using a Laser Point Source

Figure A1.3 shows a schematic of the apparatus that was used in the initial experiments. Here, the laser beam was fired through a glass beam splitter. Around 2% of the light is then reflected off this plate and onto a reverse biased photodiode circuit. When the photodiode receives the light from the pulsed laser beam, it produces a sharp positive voltage signal, which can be used as a trigger for the oscilloscope data logger. The remaining laser beam energy passes through the beam splitter and is then focused through a lens onto the surface of the steel, thereby generating the ultrasound. An EMAT was placed on top of the steel surface. When a line source was needed, the convex lens was replaced with concave expansion and cylindrical lenses. An amplifier and a filter were used to increase the signal to noise ratio by filtering out the background noise of significantly different frequencies from the ultrasonic waves.

Figure A1.4 shows a plan view of the steel sample that was tested. This sample was from an as-cast semi steel bloom which contained oscillation marks on the surface. The sample surface measured 196 x 154 mm and was 85 mm thick. A simulated surface defect (a flat bottomed, milled slot) was machined into the surface and measured 4 mm wide and 3 mm deep. The Laser-EMAT system was used to monitor the effect of the defect on the received ultrasonic signal. This involved leaving the laser beam in a fixed position and moving the EMAT. The EMAT was moved into two different locations and ultrasonic measurements were taken:

Location 1; Here, the EMAT is located before the defect, as shown in Fig. A1.4. The ultrasonic results from this trial, detailing the important ultrasonic waves for detection can be seen in Fig. A1.5. Here, it is possible to measure the direct arrival time of the Rayleigh (r) wave and to detect the Rayleigh wave that is reflected back from the defect (r_1). Similarly, the surface skimming (p) wave is detectable. The direct Rayleigh wave has a large signal amplitude, as there is no defect blocking the path between the laser and EMAT. Thus the Rayleigh wave does not lose signal amplitude due to the presence of a defect. The Rayleigh wave is broadband and as such lower frequency components of the Rayleigh wave with wavelengths less than the defect depth will propagate under the defect. However, the wave was in this case sufficiently attenuated such that the r-wave reflected off the left side of the bloom edge was not detectable.

Location 2; Here, the defect is located between the generation and detection point, as shown in Fig. A1.4. The direct Rayleigh wave should be attenuated as the defect is blocking the path between the laser and EMAT. The p-wave is not detectable immediately after the crack. If the EMAT was located further away from the defect, the p-wave would be detectable. This is because the p-wave is a bulk wave and energy can leak out towards the surface. If enough energy has passed around the defect, then the EMAT should detect a reflected wave (r_2) from the billet edge.

A1.2.1.3 Results

A graph of results, comparing the use of a line source when the EMAT is located in the two different positions can be seen in Fig. A1.5. For Location 1, the direct p-wave and r-wave are clearly visible. The reflected wave, r_1 is also detected. For Location 2, the p-wave is no longer detected as the defect is too close to the EMAT. The direct r-wave is significantly attenuated due to the presence of the defect and because the EMAT is further away from the laser generation source.

A1.2.1.4 Discussion and Summary

Some basic calculations were conducted to ensure that the experimentally measured data correlated with measurements that could be predicted. For example, the direct r-wave arrival time can be predicted by using the equation $t = d/v$, where t is time, d is distance travelled and v is velocity. The

distance '*d*' used to calculate the direct r-wave (i.e. the Laser-EMAT separation) was measured by a ruler. The arrival time of the Rayleigh wave can then be calculated as the velocity of ultrasound in mild steel at room temperature is 2996 ms^{-1}[A1.2] and the distance between the generator and receiver is known. The arrival times for the other waves can be predicted in the same manner. The practically measured data, where the arrival times are taken from Fig. A1.5, as compared with the physical results can be seen in Table A1.2. Good correlation exists between the two measurements.

A1.3 AN EMAT-EMAT SYSTEM TO FIND INTERNAL DEFECTS IN STEEL

A1.3.1 Introduction

Rather than using a laser system to generate ultrasound in the steel sample, an EMAT was used at room temperature. Although not as efficient in generating the ultrasound as compared to a laser, using EMATs to generate and receive ultrasound would significantly reduce costs and avoid safety issues associated with the use of a high energy laser. Trial work was conducted on a cold sample to determine whether EMATs could be optimised for finding internal defects. This work was conducted by The University of Warwick.

A1.3.2 Experiment to Optimise EMAT-EMAT Separation

Figure A1.6 shows a photograph of the EMAT arrangements and Fig. A1.7 shows a labelled schematic of the experiment. The generation EMAT was a spiral “pancake” coil. The receiving EMAT was a linearly wound EMAT.

The EMATs were separated by a distance, x, as shown in Fig. A1.7. Signals were stored on an oscilloscope and analysed at a later stage.

The spiral EMAT generated the following waves:

- E_c = Edge longitudinal waves
- E_s = Edge shear waves
- P_s = Plane shear waves (usually occur when generator and receiver are directly opposite one another)
- H_d = Head waves (combination of longitudinal and shear waves)
- R = Rayleigh waves

The waves themselves are emitted as a cone shape from the EMAT spiral. In order to achieve the optimal generation output, the separation distance between the two EMATs (x) is dependent on the thickness of the steel product being tested. The separation distance can be optimised such that the amplitude of the H_d wave is at its greatest and therefore the received signals are at a maximum.

To calculate "x" experimentally, a steel block containing no defects was used. This block was 90 mm thick. The generating EMAT was kept in a constant location and the receiving EMAT was moved from an x separation of 150 mm, as shown in Fig. A1.8. The distance was gradually reduced from 150 mm to 0 mm. This was done by moving the EMAT in 1 mm increments and 150 measurements were taken overall. Waveforms were captured both ‘single shot’ and averaged. The single shot data were very clear and did not contain much noise. A typical A-Scan (single waveform) can be seen in Fig. A1.9, along with the main waves labelled.

Figure A1.10 shows a B-Scan image of all 150 measurements. This B-Scan comprises data from the 150 A-Scans. Because each A-Scan has the same time axis, the voltages can be extracted from each A-Scan and placed in a matrix. This matrix comprises 150 columns, where each column contains the separate voltage values from each A-Scan. The matrix is 10,000 rows long, which is based on there being 10,000 points that make an A-Scan, which has a digitisation rate of $1x10^{-8}$secs. The B-Scan contains the distance the EMAT is moved along the y-axis, of which 150 measurements were taken. The x-axis is the time, the total signal time being 100 µs. Each x,y point in the B-Scan is represented

by a signal, which is a colour representation of the z-axis, which is the height (voltage) of the received ultrasonic signal at one particular point of time. It can be seen from Fig. A1.10 that the amplitudes of the H_d waves are at the greatest when x is 58 mm. Therefore, from Fig. A1.7, $\theta = \tan\left(\frac{58}{90}\right) = 32^o$. An intensity plot of Fig. A1.10 is shown in Fig. A1.11a which shows the amplitude of the H_d wave is at a maximum when x = 58 mm. Similarly Fig. A1.11b shows that the maximum value of the H_d wave is when $\theta = 32°$. This is the critical angle (θ) and as such, when different thicknesses of product are used, the "x" value must be adjusted by $x = h.\tan\theta$, where "h" is the thickness of the product.

A1.3.3 Theoretical Explanation using Finite Element Modelling (FEM) to Optimise EMAT-EMAT Separation

Figure A1.12 shows a FEM for a steel block of thickness 90 mm. This modelled B-Scan shows excellent correlation with the B-Scan obtained experimentally in Fig. A1.10, again showing that the H_d wave amplitude is largest at x = 58 mm.

A1.3.4 Using an EMAT System to Determine Internal Crack Position/Depth

Figure A1.13 shows the particle velocities for a mild steel block of thickness 90 mm using FEM at a time instance 27.5 μs after EMAT generation. Here, the waveform arrival times are:

$$t_{H_d} = \frac{\left(\frac{x+h}{tan\,\theta}\right)}{\nu_c}$$

$$t_{P_s} = \frac{h}{\nu_s},\ x \le r_o$$

$$t_{E_s} = \frac{\sqrt{x^2+h^2}}{\nu_s}$$

$$t_{E_c} = \frac{\sqrt{x^2+h^2}}{\nu_c}$$

where ν_c is the velocity of a longitudinal wave
ν_s is the velocity of a shear wave
r_o is the radius of the spiral coil

At time instance 27.5 μs, E_s waves will not have yet arrived, due to their slow velocity. Some of the other wave modes travel faster and will already have been detected by the receiver. Looking at time instances for a 'slice' of steel at a particular point allows the technique to be used for calculating the depths of defects, as it is possible to show what a signal should look like at this point in time. If the measured signal is different, then subsequent analysis can be conducted to calculate the defect depth.

To avoid false defect detection, the separation of the EMATs (x) cannot be too far apart. When x is too large, the H_d waves arrive much earlier than E_s waves, as can be seen in Fig. A1.14. When looking at Fig. A1.14, when x = 58 mm, the H_d and E_s waves arrive at similar times meaning that the waves cannot be mistaken for a defect.

A1.3.5 Experiment to Find Piping in a Rolled Bloom Section

Figure A1.15 shows a repeat for the experiments conducted in Section A1.3.2. This time, the steel block contained an internal defect. The EMAT was again moved from x = 150 through to x = 0 and the results are shown in Fig. A1.15. This defective block of steel also measured 90 mm thick and again the optimal x was found to be 58 mm.

Figure A1.16 shows a B-Scan obtained when x was fixed to match the critical angle, θ and the steel block was moved past a fixed EMAT generation and detection inspection point. (In the laboratory, the EMATs were moved with a constant 'x' separation between them and the block was kept stationary.)

The waves are significantly attenuated by the presence of a defect and this can be seen in the B-Scan. Here, the length of the defect was found to be 131 mm using the ultrasonic technique and the defect measured the same when the defect in the sample was measured with a ruler.

A1.3.6 Optimising the Design for the Linear EMAT Coil

The location of the EMAT can alter the resolution of A-Scans and B-Scans.

Figure A1.17 is a repeat of the experiments in Section A1.3.2 and can be compared favourably with Fig. A1.10. For Fig. A1.17, the EMAT coil was 20 mm long and 5 mm wide. In Fig. A1.10, the coil was 10 mm long by 5 mm wide.

Similarly, Fig. A1.18 is a repeat of experiments shown in Section A1.3.3 and can be compared to Fig. A1.15. For Fig. A1.18, the EMAT coil was 20 mm by 5 mm. For Fig. A1.15, it was 10 mm by 5 mm.

From these results, it was found that keeping the coil length short was best in order to achieve the best signal resolution.

A1.3.7 Conclusions

An EMAT-EMAT inspection system has been optimised for the inspection of steel samples. Internal defects can be detected via this system. FEM and experimental results correlate well. Additional work would have to be done to water-cool the generation EMAT. The receiver EMAT would be of the same type used in the hot, moving trials. Additional work would need to be undertaken to establish how an EMAT-EMAT system could be used to find defects in hot, moving steel. This work could be undertaken in a subsequent project.

A1.4 DESIGN EVOLUTION OF EMATs FOR COLD TO HOT TEMPERATURE MEASUREMENTS

A1.4.1 Optimising the Design of EMAT Sensors

The EMAT used for the initial trials had a relatively weak permanent magnetic field. Therefore new magnets were purchased which had a significantly larger magnetic field. Using these larger sized magnets meant that there was a stronger magnetic field further away from the magnet face. This is helpful for operating EMATs at a large stand-off from any hot metal surface.

A new holder had to be designed and manufactured to accommodate the larger size and different shape of the magnet. The holder was made from brass as it is non-magnetic and relatively easy to machine. Initially the magnet was held in place using a grub screw, but later, the magnet was held in place with cyanoacrylate adhesive. At a later date, a cover, to protect the face of the EMAT (i.e. the coil) was used.

In order to achieve the maximum sensitivity possible when using an EMAT, it is necessary to optimise the number of coil windings using the smallest diameter of wire possible. The sensitivity of the

received signals is dependent upon the coil width (and therefore the wire diameter and number of turns). If the wire is too thin, it breaks easily when winding the EMAT coil. If there are too many or to few turns, the overall sensitivity of the EMAT can be affected. There is a compromise between the diameter of the coil wire, width of the coil and the number of turns. Initial tests involved winding the magnet with 20 turns of wire and placing it on a steel block, using the 800 mJ laser system to generate ultrasound. Then, the EMAT was removed and one turn of wire was removed. The EMAT was then placed back onto the same position on the steel sample before acquiring the next ultrasonic signal. The A-Scans with the greatest resolution, dependent on the number of turns, were then used.

A1.4.2 Optimising the Design of EMAT Sensors for High Temperature Applications

The permanent magnet used in this project has a Curie temperature of 120 °C. There are other magnets available that have a Curie temperature of 180 °C, but these magnets do not exhibit such a strong magnetic field. When a permanent magnet exceeds its Curie temperature, it loses its magnetism, thereby making any EMAT sensor ineffective. The magnet can survive brief time intervals where the Curie point is exceeded, but this cannot be prolonged without incurring irreversible damage where the magnet is demagnetised. Therefore trials had to be conducted to ensure that when the EMAT is in close proximity to steel in excess of 800 °C, the magnet could be sufficiently cooled. Experiments were conducted involving only the EMAT and no ultrasonic measurements were taken in these initial temperature trials.

Rather than designing a special water jacket at the start of the project, it was decided to install the EMAT sensor directly on the vertical billet caster in the pilot plant at Teesside Technology Centre. This trial was performed to determine whether the magnet (and EMAT) could survive casting temperatures. The installation point was in the spray chamber and some of the water sprays were angled onto the EMAT problem, as shown in Fig. A1.19. Having the EMAT so forcibly cooled by water sprays saved costs by not having to design and build a special water-cooled EMAT. Initially thermocouples were placed in direct contact with the EMAT face, but this was not a good measurement technique because of the poor contact between the thermocouple tip and magnet face. Later, special diamond tip drills were purchased to drill into the centre of the magnet in order to embed a thermocouple 1 mm from the front magnet face, closest to the hot billet. This is illustrated in Fig. A1.20. The thermocouple was fed through a brass tube, which was used to clamp the EMAT onto the framework of the caster.

The EMAT itself was aligned above a roll. This is because the steel billet made in the caster can move from side to side in the machine. By installing the EMAT above a roll, this served to ensure that the billet could not move past the roll and hit the EMAT. A casting trial was conducted to assess the performance of the EMAT. A graph of temperature against time for this trial can be seen in Fig. A1.21.

After the trial was finished, there was a large build-up of magnetite iron oxide scale on the face of the magnet, as seen in Fig. A1.22. It was not known whether or not this scale was attracted during the casting process or after it had finished. This is because during the vertical casting process, loose scale falls from above and could therefore be attracted to the magnet. Similarly, as the billet moved past the magnet, the EMAT could essentially be de-scaling the billet. Additionally, after vertical casting has stopped, the billet is left stationary in the machine until it cools, before a crane is used to remove it from the machine. During this cooling process, the steel oxidises further, forming even more scale and therefore scale could be pulled off from the billet during this stage, i.e. when the EMAT is directly opposite the stationary, hot steel. It should be noted that this is not true of real-life operating conditions, when the steel would always be moving past the fixed inspection point. On production casters, the ideal installation point would be when the steel is horizontal and not vertical. However, for initial experimentation, the pilot plant caster was used as it is relatively easy to install apparatus and conduct trials.

A small camera was mounted so that video footage could be recorded to determine at which point scale was attracted to the EMAT. This showed that falling scale, from higher up the billet, above the test location fell off and was attracted to the EMAT. Additional scale was attracted to the EMAT only when casting had stopped. This implied that when the system is installed on a non-vertical casting

profile curved caster, scale would not be attracted onto the EMAT provided it was suitably adhered to the billet surface.

In order to overcome the problem of falling scale, a magnetic scale collector was developed. This involved mounting four magnets (the same type used to make the EMAT) in a thin, carbon steel box, which was then mounted above the EMAT probe in the caster. This can be seen in Fig. A1.23. The video camera was again used to monitor the cast. This time, the scale was attracted to the magnetic scale collector, as can be seen in Fig. A1.24. Later trials involved water-cooling the magnets in this box. The EMAT probe was then removed from the caster before the billet began to cool significantly and only fine particles of scale were attracted to the EMAT face. This entire process was captured on video, and a screen capture can be seen in Fig. A1.25.

Summary

When the sprays were angled onto the EMAT, the magnet remained below 120 °C. This showed that EMAT probes have the potential for on-line use. The video camera showed at which points during casting the scale was attracted to the EMAT. By using a scale remover above the EMAT, the problem of scale adhering to the EMAT could be solved. This justified the next stage of the project which was to design a specially made water-jacket housing for the EMAT to maintain the magnet temperature below its Curie point and to ensure that there was no thermal damage to the coil itself.

A1.4.3 Water-Cooled Jacket for the EMAT Probe

Two designs of water-cooled EMATs were built and tested. The first EMAT design involved significant workshop machining as an existing EMAT sensor was modified to be enclosed by a larger diameter brass tube, forming a water jacket.

An alternative design was made by winding a copper tube around a normal EMAT brass holder. A photograph of this sensor can be seen in Fig. A1.26. Here, the copper tube was silver soldered onto the brass. This design was anticipated to be not as efficient as the water-jacket EMAT, because of the point contact being made by the tube as it was wound around the EMAT sensor. However, this design was implemented, as it was far easier to manufacture/retrofit the existing EMATs. The water flow rate for this EMAT design was lower, at 2.2 l/min.

Both EMATs were installed on the caster, as can be seen in Fig. A1.27. In order to expose both EMATs to the same temperature, they were mounted at the same height below the mould, but on different faces. (Each square billet face should be at the same, or similar temperatures provided they are the same distance away from the mould.) Both EMATs were fed from the same water pipe, which was split using a "T-piece", which meant that the cooling water was the same temperature for both EMATs. Again, thermocouples were embedded into the magnets.

A1.4.4 Summary

The water-cooled jacket design maintained the lowest temperature. Therefore, this justified the next stage of the project, which was to take ultrasonic measurements at elevated temperatures on hot steel using the water-jacket design of the water-cooled EMAT. The EMAT was re-designed to be easier to manufacture and to decrease the overall diameter of the probe, which would be useful when packing probes closely to one another when an array of EMATs would need to be built.

A1.5 INSTALLATION OF A PROTOTYPE LASER-EMAT SYSTEM ON THE PILOT PLANT BILLET CASTER AT TEESSIDE TECHNOLOGY CENTRE

Significant design, mechanical and software development work was conducted in order to install a Laser-EMAT system on the vertical billet caster in April 2005 at Teesside Technology Centre so that hot ultrasonic measurements, on moving steel could be taken.

A1.5.1 Design of an EMAT Holder

Designing and installing a system to hold the EMAT in a vertical position, parallel to the vertical billet was necessary. This was to ensure a near constant stand-off when the billet (which moves around in the machine) moves past the face of the EMAT. The solution to this problem was to use a mechanical system, whereby the EMAT was clamped into a holder and then electrically isolated from the caster frame. The EMAT was held in a 'tripod' trolley, as a tripod would ensure that the EMAT was kept parallel to the billet surface, as seen in Fig. A1.28. The wheels of the tripod were made from 'spring loaded' ball bearings, which have been demonstrated to withstand contact with hot, moving steel in Corus mills in the past. Due to this work, it was known that the ball bearings would not seize up at high temperatures, or become clogged with scale. The balls were sufficiently large in diameter to ensure they would not become trapped in any deep oscillation marks on the steel surface. This tripod was mounted in a specially designed holder and clamped to the frame of the caster. The tripod ball bearings were kept in contact with the billet, thereby allowing the EMAT to maintain a constant stand-off of around 2 mm above the steel surface.

Because the vertical caster could only continuously cast 7 m lengths of billet, it was thought that after casting, the mould and tundish could be rotated away and the hot billet could be driven up and down using the dummy bar system. The dummy bar is fed into the mould prior to casting. When steel is poured into the mould, it chills onto the dummy bar. The dummy bar is driven with motors and is gradually pulled out of the mould and through the casting machine. The billet is welded onto the top of the dummy bar and is also pulled downwards, through the machine. Because the dummy bar can drive the billet both up and down, it was decided to conduct a trial where after casting, the mould would be removed, thereby allowing the hot billet to be moved up and down using the dummy bar system. This would mean that many hot measurements could be taken on moving steel, as the billet would be moving backwards and forwards past the inspection point. As a result of this decision, the EMAT holder was modified to include the magnetic scale collectors both above and below the EMAT probe. This would allow any loose scale to be collected when the steel was moving up and down, past the EMAT. The water-cooling circuit was extended, from cooling not only the EMAT, but also to cool the two scale collectors. After the cast was finished, the magnets in the scale collector units had the same magnetic field as previously measured, which meant that the scale collectors were being kept cool successfully.

A1.5.2 Summary

The final stage of actually testing the Laser-EMAT on-line on the heavy pilot plant was not possible. The proposed trials would have involved the use of the Laser-EMAT system being used to inspect hot, moving steel. This was not done due to the caster at Teesside Technology Centre being enhanced and unavailable. In preparation for the enhancement work, the drive motors for the dummy bar were removed shortly after the cold trial was performed. These motors were removed two months ahead of schedule. Numerous delays occurred since the caster enhancement was part of a total pilot plant rebuild which included the arc furnace and new secondary steelmaking parts. It took 18 months before the caster could be used again. Therefore an alternative method for demonstrating the suitability of Laser-EMATs on hot, moving steel became necessary. This involved heating billets in a furnace and using a pilot scale rolling mill to take measurements.

A1.6 CONSTRUCTION OF A RUN-OUT TABLE TO MOVE STEEL IN SMALL INCREMENTS

A sliding plate conveyor was constructed to move the steel sample past the EMAT and laser beam inspection point. Side guides were installed onto a steel base plate and a metal 'conveyor' plate with four spring-loaded ball bearings was held between these parallel guides. A nut was welded to the bottom of the conveyor. Two other nuts were welded onto the table top and a threaded bar was fed through the three nuts. The pitch of the threads on the bar was 1.75 mm. Therefore, for every complete revolution of the bar, the conveyor (and steel sample) was moved 1.75 mm from top to bottom. Photographs of the trolley system can be seen in Fig. A1.29. An EMAT was mounted on a metal bracket above the steel sample and the stand-off between EMAT and sample could be adjusted. This meant that different sample thicknesses could be tested on the conveyor system.

A1.6.1 The Use of a Prism for the Portable Laser System

A1.6.1.1 Changing the Laser Beam Direction

The portable laser system is designed to direct the laser beam in a horizontal direction. However, the laser cavity cannot be orientated to direct the laser beam vertically. This is because the water-cooling pumps, optics and associated electronics were not designed to operate in that orientation. A prism was used to direct the beam and a prism holder was machined such that the prism could only be used to steer the light in one direction. This can be seen in Fig. A1.29. This allowed a holder to be clamped onto the aluminium base of the laser. The holder and trunking were all made of square section. As the prism is made of square and triangular sides, this ensured that the prism could only be seated in one position, allowing it to be used safely. The trunking was designed to be removed easily, but the holder was machined into the base of the laser system, meaning that the trunking only has to be tightened up, as it is designed to always slide into the same location.

By reflecting the laser light through BK7 glass, the transmission losses can be up to 4% (mirrors have losses of around 1%). An anti-reflective coating of the prism hypotenuse (to reduce losses to 2%) could not be used as the high-energy laser pulses burned the coating off. Thus it was necessary to check whether the losses associated with using the prism had any significant effect on the ultrasonic generation.

A1.6.1.2 Trial Comparing Ultrasonic Waveforms With and Without a Prism

A water-cooled EMAT was used to detect the signals with a stand-off above the steel surface of 1.6 mm. The distance between the laser generator and EMAT receiver was 94 mm. The apparatus arrangement when no prism was present can be seen in Fig. A1.30a and Fig. A1.30b shows the arrangement when the prism was introduced. A comparison between using a prism and not using a prism on the A-Scans can be seen in Fig. A1.31. There is no significant change in the waveform amplitude and shape when a prism is used. The waveforms are somewhat different in their appearance because the location of the laser point source on the steel surface was slightly altered when the steel was moved into a different position. The important aspect of this comparison graph is not the arrival times of the waves, but rather to verify and check whether there is a noticeable effect on the waveforms when a prism is used.

A1.6.2 Detection of a Longitudinal Surface Slot in a Steel Billet using the Run-Out Table

A 100 mm square, 1 m length of steel billet was mounted on the run-out table and tested ultrasonically using the Laser-EMAT system as seen in Fig. A1.29. A longitudinal slot (50 mm long, 2 mm wide and 2 mm deep) was machined into the sample surface to simulate a wide crack-like defect. A schematic diagram of the testing arrangement, showing the location of the laser and EMAT with respect to the billet and slot can be seen in Fig. A1.32. Here, the EMAT coil is parallel with the direction of the longitudinal slot. Figure A1.32a shows the case when the path between the laser and EMAT is not blocked by the slot. Figure A1.32b shows when the billet is moved with respect to the fixed Laser-

EMAT inspection point such that the slot is blocking the path between the laser and EMAT. For this experiment, the billet was moved in 1.75 mm increments under the Laser-EMAT system.

A1.6.3 Ultrasonic Waveform Analysis: The A-Scan and B-Scan Technique

When there is no defect blocking the path of a surface wave between the laser and EMAT, the ultrasonic surface waves have a large signal amplitude. When the billet was moved such that the slot then blocked the ultrasonic path between the laser and EMAT, the signal corresponding to the Rayleigh wave was significantly attenuated when compared with no defect being present. A graph comparing the differences between the presence of a slot and it not being there can be seen in Fig. A1.23. The surface p and r waves, along with the bulk waves, can be seen in the A-Scan when no defect is present. In Fig. A1.33, it is still possible to see the surface skimming and Rayleigh waves when the defect is present, but they are very faint. This is due to some of the wideband Rayleigh wave propagating under the defect. This means that not all of the surface waves are fully blocked by the defect, as it has been shown that longer wavelengths are able to pass under defects more readily than shorter wavelengths[(A1.4)].

Figure A1.33 shows two time–amplitude waveforms (A-Scans) that contain 10,000 data points each, captured at a digitisation rate of 100 MHz (10 ns per point). For ultrasonic analysis, it is possible to convert many A-Scans into a B-Scan, and for this particular case, a matrix of 10,000 rows and 252 columns (representing 252 A-Scans) was plotted. The B-Scan for testing the billet (containing a longitudinal slot) can be seen in Fig. A1.34. Here, the B-Scan comprises a y-axis, which is the number of steps along the length of the sample (1.75 mm incremental movement of the trolley per step), the x-axis is the time and the change in colour represents the waveform amplitude (i.e. the A-Scan voltage) for the 'z'-axis.

As can be seen in the B-Scan (Fig. A1.34), there is a discontinuity in both the Rayleigh wave and surface skimming longitudinal wave at a distance between 103 mm and 153 mm (corresponding to points 10 μs and 20 μs on the x-axis). The dark colour representing the maximum wave amplitude is visible at positions greater than 103 mm and less than 153 mm. By subtracting these distances, we can estimate that the slot is around 50 mm long which is very close to the true defect length as measured with a ruler. Close examination of the B-Scan shows that the bulk waves are unaffected by the surface slot as expected because they pass underneath the slot and are reflected from the back surface.

A1.6.4 Conclusion

This trolley system demonstrated that a Laser-EMAT system was capable of detecting a defect in moving steel. However, the experimental trial was very time consuming to conduct and the entire movement process, data acquisition (saving oscilloscope files to floppy disk) and subsequent B-Scan plotting were all performed manually, taking significant time. The trolley system was also not particularly stable and as a result, the steel moved slightly side-to-side, and the steel could only be inspected in 450 mm lengths. This is because the billet needed to be clamped to the trolley, as the trolley movements caused the billet to rock, and when the billet reached the end of travel, the powerful magnet in the EMAT would lift the billet off the conveyor plate. Longer steel samples also needed to be tested in the laboratory to justify the costs involved in setting up trials in a cold/hot rolling mill for moving steel. However, this system did demonstrate the feasibility for finding defects in cold, moving steel.

A1.7 B-SCAN SOFTWARE

A1.7.1 Software Explanation

B-Scan software was written in C^{++} and utilises a Windows-based Graphical User Interface. The main window is used to display B-Scan images. An example of the main window can be seen in Fig. A1.35.

Various routines have been built to help interpret ultrasonic signals, taken after practical trials. These include:

- Having an adjustable z-axis colour scale (Fig. A1.36 shows how the maximum and minimum values can be attributed to different colours of hue).
- The ability to load different file formats, such as ASCII, binary Matlab etc.
- The ability to save the B-Scan image as a picture, meaning that subsequent loading is only for a picture and not for a very large, raw data set of many hundreds of megabytes.
- The B-Scan can be cropped, such that only the 'interesting' regions (i.e. those indicating the presence of a defect) can be saved. This is shown in Figs. A1.37a and A1.37b.
- The B-Scan image can be zoomed into and individual A-Scans can be selected.
- Algorithms to scan automatically B-Scans and highlight regions of interest can be run (i.e. defects can be automatically found from the data).
- A modelled B-Scan image can also be generated providing the original experimental geometries are used. This allows a comparison to be made between the predicted waveform arrival times and the actual arrival times of the waveforms recorded during practical experimentation.

A1.7.2 Generating Modelled B-Scans when a Defect is Present

The appearance of A-Scans can be predicted, as the arrival times of ultrasonic waves can be accurately calculated using the equation time = distance/velocity. The velocity of different ultrasonic waves can be accurately measured for different steel grades (as discussed in Section A1.9). The distances involved can be measured, for instance the separation distance between the laser and EMAT, the distances these are away from the edges of the steel and the dimensions of the steel itself. As such, models have been written based on these input values.

The software has been written so that the user can enter all geometric data such as Laser-EMAT separation, billet dimensions, crack position etc. This can be seen in Fig. A1.38 for the case of a transverse defect.

Models have been written to calculate the arrival times of waves for each of the following instances:

(i) Pitch-catch for transverse defects
Here, the dimensions of the steel semi can be entered and the arrival times for the ultrasonic signals as they travel along the surface, through the bulk of the steel and are reflected from the edges are all given. The software considers whether or not a transverse slot is present. As a result of this slot, it can be shown that the arrival times will differ should a defect not be present as compared to being present. This is dependent on the location of the transverse defect to the Laser-EMAT generation and receiving points. By using this model, it is possible to see the effect of the arrival times when defects are or are not present.

(ii) Pitch-catch for longitudinal defects
This program considers the lack of and presence of longitudinal defects respectively. As in the case of the transverse defect software, the various input parameters can all be adjusted and the outputs displayed.

(iii) Through-transmission for internal defects
This model can be used for finding defects inside the bulk of the steel. Although pitch-catch techniques can also be applied to finding defects inside the bulk, the ultrasound has to travel double the distance of the through-transmission system where generator and receiver are separated by the steel and as a result, the waves are not as attenuated or subjected to mode conversions.

Because it is possible to predict accurately what the expected A-Scan should look like, it is also possible to generate many simulated A-Scans and to produce a simulated B-Scan based on these data.

A simulated B-Scan for the case of a transverse defect can then be overlaid on top of a measured B-Scan for comparisons between what is expected via models and what is actually recorded as can be seen in Fig. A1.39. Figure A1.40 shows practically measured data. Figure A1.41 shows, using models, what the theoretical B-Scan should look like. Figures A1.40 and A1.41 show good correlation. Figure A1.42 shows an example of a modelled B-Scan for a longitudinal defect.

These models can also be used to ensure that the laser-EMAT separation distance is optimised. There should not be any overlap in the arrival times of the Rayleigh waves, with, say a bulk wave, as this would mean that when a surface defect was present, the amplitude may not significantly decrease as the bulk wave will still arrive at the same time and be unaffected. Similarly, if an internal defect is present, the Rayleigh wave would still be evident, but the distinction between the two waves plotted so close to one another on the A-Scan would give rise to ambiguous interpretation.

A1.7.3 Automatic Defect Recognition

A new defect recognition algorithm has been developed for surface transverse and longitudinal crack detection. This system uses a model to restrict the region of interest around the Rayleigh wave arrival time. The software looks at the amplitude of the Rayleigh wave, as it is the Rayleigh wave that is used for finding surface defects. In a B-Scan, it is the area in which the Rayleigh wave is attenuated that shows the presence of a defect.

A local maximum function, f(x), can be defined by the following equation:

$$f(x) = max_{tE[t_1,t_2]} |A(x,t)|$$

Here, x is the position of the sample, A is the Rayleigh wave amplitude, and $[t_1,t_2]$ is the region of interest around the Rayleigh wave. $|A(x,t)|$ is the location of the Rayleigh wave at position x. Optimal results have been found when using $t_1 = 0.8$ and $t_2 = 1.2$. The software also filters out the noise and normalises the data. This function is filtered to remove noise and is normalised between 0 and 1. The f(x) value can be previewed using the "Loc.Max" function in the tools menu, which is called lmf(x). A plot of lmf(x) against B-Scan data is presented in Fig. A1.43.

Figure A1.44 plots f(x) when a transverse crack occurs. In this case, the function falls below threshold θ_1 at the start of the defect and rises back to θ_2 when the laser and EMAT have passed over the defect. The analysis tool can be configured in the software, when the user has to enter values for θ_1 and θ_2, which is dependent on the height of the Rayleigh wave when no defect is present. Currently, the θ values are found through trial and error to get the best results. However, the more data that are analysed, the more reliable the automatic selection of θ would be. The site of the search window is typically 1.5 times the Laser-EMAT separation distance.

Figure A1.45 shows the theoretical shape a defect should look like for f(x), compared with f(x) for real data. Investigations into why the ‘real’ signal does not look like the theoretical shape is being investigated, although f(x) for real data does follow the general shape of the theoretical pattern. Figure A1.46 shows a B-Scan with the defective region (a longitudinal defect) automatically highlighted.

A1.7.4 Using A-Scan Signal Amplitudes to Automatically Find Defects

Running the "absolute" tool in the software starts an algorithm that uses the signal amplitudes to determine automatically the presence of a defect. This relies on there being a drop in signal strength when a defect is present. Figures A1.47a and A1.47b show a B-Scan and the corresponding "amplitude plot" respectively. The dip highlights the location of the defect.

A1.7.5 Edge Enhancement and the Local Maximum Function

This detection algorithm uses the models developed as part of this project to predict the ultrasonic waveform arrival times and investigates regions in the B-Scan when waves do not arrive when they are

predicted to do so. These occurrences are the result of a defect being present, therefore either stopping entirely, or else resulting in a much sooner or later waveform arrival.

Here, an "edge enhancement" algorithm is used to clean up the original B-Scan change, as shown in Fig. A1.48a. Figure A1.48b shows the corresponding Loc.Max. function plot, highlighting the presence of a defect.

A1.8 DEVELOPMENT OF AN AUTOMATED TROLLEY SYSTEM

In order to move long, heavy steel billets in very accurate movements, a trolley/conveyor belt system was used. A trolley was designed to mount the moving conveyor on top of a support frame, which could move steel samples with a mass of up to 250 kg. This frame had wheels, as it is necessary to mount the steel samples using a crane before pushing the trolley system into position under the laser beam. This can be seen in Fig. A1.49. The EMATs were held in position, using a specially designed holder, which kept the EMATs at a near constant stand-off, despite the steel not having consistently the same thickness.

The trolley system uses a servo-motor that can move a carriage within micron accuracies. The accuracy of the linear movement was checked and calibrated using a magnetic-base Vernier arm. No digital encoders are used as the system moves accurately 'open-loop'. The system was designed to move steel samples in increments as small as 0.1 mm. A motor was programmed using LabVIEW software, so that the trolley system could be easily controlled.

A1.8.1 Customised PC for Data Logging

As part of this project, a custom PC was constructed. This was used to control the motor system. Oscilloscope data logging cards were installed, which could acquire up to six channels of EMAT data. High-speed hard disks were acquired to write the data rapidly to disk. This is because each A-Scan is 80 kb in size and the laser generates twenty ultrasonic signals every second (80 x 20 = 1600 kb/sec). Six EMATs, each recording 1.6 Mb/sec = 9.6 Mb/sec, need to be recorded. The same PC would also fire the portable laser system. The system was fully automatic and could be started with the press of one button.

A1.8.2 Software for Controlling the Trolley System

LabVIEW software was written to start the carriage at the zero (datum point) position. The carriage can then be moved in increments between 0.2 mm and 20 mm. This can be seen in Fig. A1.50. At each position, ultrasonic waveforms are saved. These data are stored initially in ASCII format and later in Binary. For each position, the data from one waveform are saved in one column. If signal averaging is to be done, say, over 16 waveforms, then 16 columns of data, with 40,000 rows are saved to a text file. When the carriage is moved to the next position, another 16 columns of data, with 40,000 rows are saved and so on. A default file name is saved in a folder and the location of the carriage is appended to the default file name with an automatic incrementing numbering system. This can be seen in Fig. A1.51. Figure A1.51 also shows the configuration settings for the data logging cards. Figure A1.52 shows the waveforms as they are acquired. This is the screen viewed when testing the moving billets.

A1.9 AN ACCURATE METHOD FOR MEASURING THE VELOCITY OF ULTRASOUND IN STEEL

The velocity of ultrasound in the steel is an important factor in predicting and analysing ultrasonic signals and in addition to being temperature dependent, different steel grades will give different velocities. Similarly, changes in grain structures will also affect ultrasonic velocity because the larger the grain size, the more scattered the ultrasonic signal. It is therefore desirable to test a variety of different steels that have been analysed using a spectrometer so that a set of different steel grades with corresponding velocities can be found.

For these experiments, the automated trolley system can be used to move steel samples over fixed distances very accurately. When the steel is moved through known fixed distances, measurements can be taken to calculate the velocity in steel. Here, the EMAT was attached directly onto the steel sample and the steel (with attached EMAT) was underneath the laser source, which was kept in a fixed position. Therefore the EMAT moves a fixed distance (Δd) with the sample, as the EMAT is magnetically clamped to the steel. The change in the waveform arrival time can then be used to calculate the velocity. This is illustrated in Fig. A1.53.

Here, the steel (and EMAT) was moved in 5 mm increments (Δd) away from the fixed position of the laser. Twenty iterations were taken, so that for the last data point recorded, the steel sample had moved 100 mm (in a 'negative' direction). In each position, the waveforms were averaged 100 times. Each ultrasonic wave was then automatically analysed using LabVIEW software.

In particular, the time for the first "maximum" point on the Rayleigh wave was noted for each of the twenty iterations. This program has been written, such that all twenty A-Scans can be loaded on-screen and automatic peak detection algorithms are used to find the same 'maximum' point on the Rayleigh wave in each case. The velocity is therefore equal to Δd divided by the arrival time of the Rayleigh wave. The time vs distance graph can also be plotted in LabVIEW, where the r^2 value, gradient and errors can all be automatically calculated. Should the automatic peak recognition software incorrectly identify the wrong peak, then the software can be manually changed.

A graph of Rayleigh wave arrival time versus distance was then plotted with data from each of the twenty A-Scans. This is a straight-line graph where the gradient of the slope is the velocity of the Rayleigh wave as shown in Fig. A1.54, with a gradient equivalent to a velocity of 2994 + 2 m/s and an r^2 correlation coefficient value of 0.99998. The r^2 value demonstrates how well the line of 'best fit' is, as r^2 is nearly 1.0. The r-wave velocity in the literature is quoted as 2996 m/s for 'mild steel. This work was expanded upon, such that velocities of the surface skimming wave could be calculated. (Bulk wave velocities could also be calculated in this manner, but the test block was not cut precisely parallel and square and therefore these wave velocities were not calculated.) The velocity of the surface skimming wave was found to be 5887±7 ms, with an r^2 value of 0.999972.

A1.10 ON-LINE SURFACE DEFECT DETECTION ON HOT, MOVING STEEL

A1.10.1 Detection of Transverse Surface Defects on a Steel Billet using the Automated Trolley System

Here, a square billet with a transverse surface defect was tested. A plan view of the experimental arrangement can be seen in Fig. A1.55. The billet is moved from left to right, underneath the fixed laser-EMAT inspection point. When the surface defect does not block the path between the laser and the EMAT, then the received signals are very high. Both the r-wave and p-wave should be detectable. When the defect blocks the path between the laser generation point and the EMAT, several phenomena occur:

- The r-wave will be reflected back from the defect and be detected by the EMAT. Therefore both the direct r-wave and reflected r-wave will be detectable.

- Upon the EMAT being very close to the defect, the reflected wave constructively interferes with the direct r-wave, leading to an increase in r-wave amplitude. When the defect blocks the path between the laser and EMAT, the r-wave may not be detectable if the defect is sufficiently deep. This is because the defect is longer than the wavelength of the r-wave. There may still be some evidence of the r-wave, if the defect is shallow (e.g. 4 mm deep) as the wideband r-wave can propagate underneath the defect, as longer wavelengths are able to pass under defects more readily than shorter wavelengths.

- The frequency content of the r-wave will drop by several kHz.

- The p-wave will be mode converted into a r-wave, thereby creating a distinctive pattern in the B-Scan. The p-wave may also not be detectable immediately after the crack. This is because the p-wave is a bulk wave and energy can leak out towards the surface.

- There will be a delay in the r-wave arrival time.

- The r-wave will also be reflected off the ends of the billet and may be detected.

- Bulk waves that travel from the top of the billet to the bottom and are reflected back to the top again will remain unaffected by the presence of surface defects on the top of the billet. However, if surface defects are on the bottom of the billet the waves will be diffracted, which means that defects on the bottom face of the steel can be detected. If any internal defects exist, then arrival times of the ultrasonic waves may occur too early, too late, or not at all.

The resulting B-Scan can be seen in Fig. A1.56.

Regions [a] and [b] corresponding to Fig. A1.56 represent the defect which attenuates the surface waves and this is shown in closer detail, magnified in Fig. A1.57. Regions [c] and [d] show the Rayleigh wave being reflected from the defect. Region [c] is r_1 (from Case 1) and the reflected wave for Case 3 can be seen in Region [d]. Regions [e] and [f] show a Rayleigh wave being reflected from the billet edge.

Figure A1.57, the magnified view of the defective area (from the B-Scan in Fig. A1.56), contains two waves of interest, [m] and [n]. [m] is a surface-skimming p wave that has mode-converted to a Rayleigh wave at the crack tip and wave [n] is a Rayleigh wave that has mode-converted to surface-skimming p wave. Region [b] shows the drop in signal amplitude when a defect blocks the path between the laser and EMAT. There is also a delay in the arrival time of the Rayleigh wave, which can be attributed to the presence of the defect. Some of the horizontal lines that occur in the B-Scan can be attributed to electromagnetic noise from the motor.

Looking at the results in Figs. A1.56 and A1.57, it is interesting to note that the surface skimming and Rayleigh waves are still evident, even when the slot is blocking the path between the laser and the EMAT. This is due to some of the wideband Rayleigh wave propagating under the 4 mm deep defect. This means that not all of the surface waves are completely blocked by the defect, as it has been shown that longer wavelengths are able to pass under defects more readily than shorter wavelengths[A1.4]. This was confirmed by conducting FFT analysis on the recorded Rayleigh waves.

A program was written to extract automatically only the r-wave from each of the A-Scans used to build the B-Scan shown in Fig. A1.56. This program used a peak detection algorithm to extract the r-wave amplitude and arrival time. The r-wave was then Fast Fourier Transformed (FFT) to enable the magnitude FFT and frequency of the r-wave to be extracted. Each of these four phenomena shows the presence of a defect:

- Figure A1.58 for peak frequency of the r-wave plotted against A-Scan number.
- Figure A1.59 for r-wave arrival time plotted against A-Scan number.
- Figure A1.60 for r-wave amplitude plotted against A-Scan number.
- Figure A1.61 for magnitude FFT plotted against A-Scan number.

A1.10.2 Comparison with Modelled Results

A Finite Element Model (FEM) was constructed by Warwick University to plot a B-Scan based on the dimensions given from these experimental trials. This modelled the in-plane particle velocity in steel, as detected by the EMAT from the Rayleigh wave generated by the pulsed laser beam. The FEM calculates the predicted arrival times for the various wave modes and plots a B-Scan. The simulated B-

Scan can be seen in Fig. A1.62, which can be compared favourably with the B-Scans found experimentally, as in Figs. A1.56 and A1.57.

The features in Fig. A1.62 have been identified. Here, [q] represents the Rayleigh waves as they are reflected from the defect. [s] is a Rayleigh wave mode conversion to a surface-skimming p wave. [t] and [u] are surface-skimming p-waves that mode converted to Rayleigh waves. Again, [m] is a surface-skimming p wave that has mode-converted to a Rayleigh wave at the crack tip and wave [n] is a Rayleigh wave that has mode-converted to surface-skimming p wave.

A1.10.3 Pilot Rolling Mill System to Inspect a Moving, Cold Billet Sample

The billet was also moved on a rolling mill at room temperature. Again, by extracting information from the r-wave it is possible to show the location of the surface defect:

- Figure A1.63 for peak frequency of the r-wave plotted against A-Scan number.
- Figure A1.64 for r-wave arrival time plotted against A-Scan number.
- Figure A1.65 for r-wave amplitude plotted against A-Scan number.
- Figure A1.66 for magnitude FFT plotted against A-Scan number.

The B-Scan for this trial can be seen in Fig. A1.67.

A1.10.4 Laser-EMAT Inspection of Steel Moving at Elevated Temperature

A1.10.4.1 Pilot Rolling Mill System to Inspect a Moving, Hot Billet Sample

The billet tested previously was heated to over 1200 °C in a refractory brick kiln and crane lifted into position before the inspection process began. A robust water-cooled EMAT was used to take the measurements. Materials were selected to protect the EMAT face, which had low thermal conductivities. The final design of EMAT can be seen in Fig. A1.68. These materials were tested on a heated billet surface, as shown in Fig. A1.69. The billet began to cool rapidly and the first set of ultrasonic measurements were taken at 850 °C. A thermal imaging camera was used to measure the billet temperature.

A1.10.4.2 Discussion of Hot Trial Results

B-Scan results taken at 850 °C, on the moving billet can be seen in Fig. A1.70. The signal to noise ratio of the A-Scans was very poor, therefore a signal averaging algorithm was utilised to clear up the data.

Single shot A-Scan data from this trial can be seen in Figs. A1.71. This figure also shows how the A-Scans change when a defect is present.

It can be seen from Figs. A1.70 and A1.71 that a transverse defect can be detected above the Curie point of the steel using Laser-EMAT technology. The ultrasonic bulk waves that were detectable at room temperature were not detectable above the Curie point.

Further work is needed to improve the signal-to-noise ratio of the detected ultrasonic signals, which will in turn improve the B-Scan resolution. The industrial robustness of the system is very good; the same EMAT survived the repeatable hot temperature measurements from the moving tests and suffered no noticeable deterioration in performance. A more powerful, portable laser system is recommended. This would increase the signal-to-noise ratio of the received ultrasonic waves and could also generate bulk waves with larger amplitudes. The water-cooled EMAT and specially designed EMAT holder to ensure a near constant stand-off was proven to be mechanically sound. The data acquisition systems and subsequent data analysis showed that the ultrasonic data could be converted into meaningful B-Scans, utilising a high degree of automatic B-Scan plotting using LabVIEW software which was then used to show the location of a defect.

A1.10.5 Calibration of the FLIR Thermal Imaging Camera with Thermocouples

Because the FLIR thermal imaging camera uses a "constant" value for the emissivity level of the steel, error in the temperature measurements can exist. Therefore it was decided to test the new thermal imaging camera and make a temperature comparison with a series of thermocouples. A 2 m length of billet, with 110 mm^2 cross-section was heated in a kiln to 1200 °C and kept at this temperature for 3 hrs to allow for heat saturation. When the burners were switched off, the surrounding refractory bricks were removed so that measurements could be taken. This calibration trial was useful as the same camera was being used to measure the surface temperature of the strand during casting. Ultrasonic velocity varies with temperature.

The billet had a series of ten thermocouples mounted, five on the top face and five on the side. This was to determine whether the top face and side face would be at the same temperature. A schematic of the billet can be seen in Fig. A1.72. The camera software was used to measure the temperature at the location of each thermocouple on the side of the billet, as the camera could not be easily positioned to measure the top face. For experimental trials, the top of the billet would be the point where the laser and EMAT system would be installed. Thermocouple 5, mounted on the side of the billet, was plotted on the same graph as the FLIR readings for that location. A graph comparing these two measurements over time, as the billet cools, can be seen in Fig. A1.72. This shows good agreement between the thermal camera and thermocouple data. Similarly, top and side thermocouples 1, 2 and 4 showed good correlation. (Side thermocouple number 3 was broken when the refractory bricks were removed).

All measurements can be seen in Table A1.3. Good correlation existed between the thermal imaging results and the thermocouple data, which ensured the temperatures monitored with the FLIR camera were realistic and results could be confidently used in future trials. Type K thermocouples typically exhibit errors of 0.75%[(A1.3)]. The accuracy of the FLIR P60 camera is quoted as being "+ 2% of reading".

A1.10.6 Conclusions

An automated system for testing billets and producing B-Scans, with a high degree of automation and all controlled using LabVIEW software was designed and constructed.

The Laser-EMAT equipment successfully demonstrated the detection of a defect on hot, moving steel on a pilot scale rolling mill. Through detailed inspection of the billet at room temperature and under controlled laboratory conditions, it was possible to test the same billet on a pilot scale mill. This work is believed to be the first of its kind.

A1.11 DETECTING DEFECTS ON THE BOTTOM FACE, WITH THE LASER-EMAT EQUIPMENT MOUNTED ON THE TOP FACE

A trial was conducted using the automated trolley system to move a 2 m long billet in 1 mm increments. This billet had a transverse surface defect on the bottom face. The Laser and EMAT were both mounted on the top face. The billet was moved 600 mm in total and the data was averaged 16 times in each position of movement. The resulting B-Scan can be seen in Fig. A1.73. Here, a break can be seen in the arrival time of the ss bulk wave and reflections from the defect show a distinctive "U" shape bending away from the defect. This demonstrates that the equipment can be used to find defects on the bottom face, even though the sensors are mounted on the top face.

A1.12 CONSTRUCTION OF A LASER-EMAT ARRAY

As discussed in Section A1.1, to optimise an EMAT array to detect cracks, the EMAT coil should be as parallel as possible to the crack. It is well established that surface cracking in semis is predominately either longitudinal or transverse. EMAT coils can be orientated to detect these types of defects. In these different orientations, it is also possible to detect surface defects on the bottom and sides of the steel product, as well as any internal defects. An array of up to six EMATs has been used to inspect a

steel billet. An EMAT holder was constructed and tested using the automated trolley system (Fig. A1.75) based on this principle. For this, additional EMAT signal amplifiers, filters and high speed data acquisition cards to write data quickly to disk (as discussed in Section A1.8.1) had to be purchased. Figure A1.76 shows new LabVIEW software which was used to acquire and stream 5 channels of A-Scan data to disk using the automated trolley system. Figure A1.77 shows B-Scans generated as part of a trial to inspect the moving billet.

A1.13 INSTALLATION ON THE PILOT PLANT CONTINUOUS CASTER

At the end of 2006, work started on installing the Laser-EMAT equipment on the newly enhanced pilot plant caster at Teesside Technology Centre. However, due to delays in the caster being ready, no ultrasonic hot, moving measurements have been made in the caster at this time. Figure A1.78 shows photographs of the proposed installation point for the prototype and of some of the measurements being conducted before installation can take place. Preliminary work started in Summer 2006 and continued into 2007 to take advantage of preliminary casts from the new caster. Significant work has been started to prepare a Laser-EMAT system for on-line inspection. This new prototype will use the EMAT array developed as part of this project (Section A1.11) which will involve mounting the EMATs in a new holder. The EMATs/holder and laser will all be kept positioned, even if the billet moves from side to side during casting. Measurements were taken using an LVDT system to monitor how much the billet moved, which was in the order of ±10 cm. A thermal imaging camera was used to take measurements of the strand as it came out of the straightener and at the proposed installation point for the prototype. This is after the strand exits the last of the rolls from the roller straightener unit and before the torch cut-off point.

Consideration has been made regarding the safe use of laser systems. For practicality, casting plant operators cannot wear laser safety goggles. Therefore the Class IV laser beam will be fully contained in a large box, in order to make the entire system Class 1. This means that from the roller straightener unit to the cut-off point will be fully enclosed with sheet metal to form a long tunnel and the equipment inside will be kept air cooled. The entry and exit points of this tunnel should therefore have protection surrounding the perimeter of the billet such that no reflected laser light can escape.

A1.14 RECOMMENDATIONS FOR THE FINAL LASER-EMAT SYSTEM

Although a prototype system has been developed to detect defects in steel, significant work must still be undertaken to perfect the system and to create a system that could be used in steel plants and marketed for other customers. Some of these recommendations for such as system are as follows:

- The laser system; A higher repetition rate laser, e.g. >120 Hz should be used. This would lead to an increase in overall system resolution as more ultrasonic data per mm of product travel would be recorded. A higher energy, Q-Switched laser, with as large an energy output as possible should be used. A study should be conducted to compare different wavelengths of laser with pulse energy for high temperature applications. For slabs, a method to split the laser beam, or else scan the laser across the slab width would need to be found.
- The EMATs; For slabs, three arrays of up to six EMATs could be mounted on the top of the slab. One array each for the left and right slab edges and one for the middle of the slab. The same laser could be used to generate signals in these three locations meaning that all the defects could be detected. Some cross talk between the EMATs could exist, meaning that a multiplexing system should be used to switch between arrays. Top mounted EMAT arrays should also be capable of detecting surface defects on the slab bottom faces, as any defects would cause a change or else stop ultrasonic arrival time. However, EMATs could also be installed on the bottom face.
- The software; Recent developments in hard disk technology and high speed data acquisition cards have made this project possible. It would not have been feasible to record such high resolution signals in 2001 when the project started. What would be needed for a plant based system would be a computer with a dedicated, real-time

operating system, which would be 100% utilised solely for data collection. The new generation of dual-core processor technologies make it feasible to use one processor for data acquisition and the other for data analysis in real-time. It should therefore be possible to save only the "regions of interest", i.e. only save data when a defect is present. By examining the ultrasonic signals, it should be possible to determine the location and size of the defects.

- The plant system; The final system would have to be very robust. The EMATs would need to be very well protected to keep loose scale from damaging them. The entire system would need to be enclosed for laser safety. Any moving parts would require shielding from grit. The high temperature would require the use of low thermal conductivity materials and/or effective cooling to ensure system longevity.

A1.15 REFERENCES

A1.1 Scruby, C B, Drain, L E: 'Laser Ultrasonics Techniques and Applications', pub. Adam Hilger ISBN 0-7503-0050-7, 1990

A1.2 Kaye, C W C, Labey, T H: 'Tables of Physical and Chemical Constants', 16th Edition, Pub. Longman, 1995, ISBN 0-582-22629-5

A1.3 Bentley J P: 'Principles of Measurement Systems', 3rd Edition, pub. Addison Wesley Longman Ltd, 1997, ISBN 0-582-23779-3, p156

A1.4 Edwards R S, Dixon S and Jian X 'Depth Gauging of Defects using Low Frequency Wideband Rayleigh Waves', Ultrasonics, Vol. 44, pp93-98, 2006

Table A1.1: Corus laser specifications

Output Energy (mJ)	Wavelength (nm)	Pulse Width (ns)	Repetition Rate (Hz)	Portable?
800	1064	14	20	No
150	532	8	20	Yes

Table A1.2: Comparison between practically measured data for the laser point source and EMAT in two different locations

EMAT Position	Labelled Wave Name	Wave Speed (From Literature)	Time (From Graph) (us)	Distance Calculated	Measured Distance
Location 1	r	3060	35.7	109	111
Location 1	r_1	3060	54.6	167	166
Location 2	r	3060	15.2	47	46
Location 2	r_2	3060	34.4	105	101

Table A1.3: Table of all measurement results

TIME	THERMAL CAMERA #1	SIDE THERMO COUPLE# 1	THERMAL CAMERA #2	SIDE THERMO COUPLE# 2	THERMAL CAMERA #3	SIDE THERMO COUPLE# 3 (Broken)	THERMAL CAMERA #4	SIDE THERMO COUPLE# 4	THERMAL CAMERA #5	SIDE THERMO COUPLE# 5
15:08:01	835	880.5	916	913	916	0	924	930	943	944
15:09:09		861.5	901	885.5	898	0	904	900	923	913
15:09:41	792	853	898	874	888	0	893	887	910	900
15:10:01	781	843.5	885	861.5	881	0	889	873	905	886
15:10:40	788	835	876	851	872	0	877	861	889	872
15:11:06		824.5	867	837.5	861	0	870	846	878	856
15:12:14	764	811.5	847	819	841	0	841	824	855	833
15:13:10	756	800.5	834	805	827	0	826	805	836	813
15:13:48	765	795.5	827	797.5	820	0	824	797	827	805
15:14:24	772	791	818	791.5	816	0	815	790	822	797
15:15:09	747	782.5	802	780	805	0	799	778	806	784
15:15:53	736	776.5	795	772.5	796	0	791	770	795	776
15:17:07	728	766	779	761	779	0	781	757	785	763
15:18:29		755	765	749	767	0	768	743	767	749
15:21:08	699	736	749	725	752	0	744	718	740	724
15:23:35		718.5	726	704.5	728	0	718	694	722	701
15:25:52	667	701	708	687	708	0	697	672	698	681
15:29:08	646	676.5	685	663.5	681	0	668	644	669	654
15:30:28	632	669	676	655.5	673	0	657	633	658	644
15:32:25	629	655.5	666	639.5	661	0	643	613	642	626

Fig. A1.1: Extended laser containment area at Corus Teesside Technology Centre (2006)

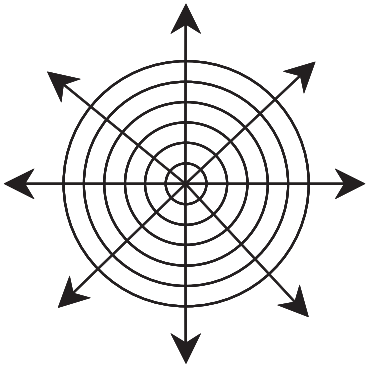

Fig. A1.2a

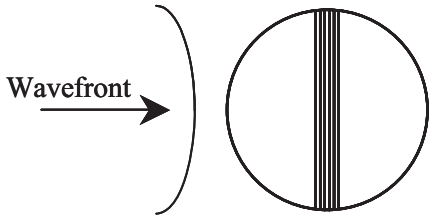

Fig. A1.2b

Fig. A1.2a: Plan view of wavefronts emanating from a point source
Fig. A1.2b: Plan view showing the curved wavefront reaching the linearly wound EMAT coil

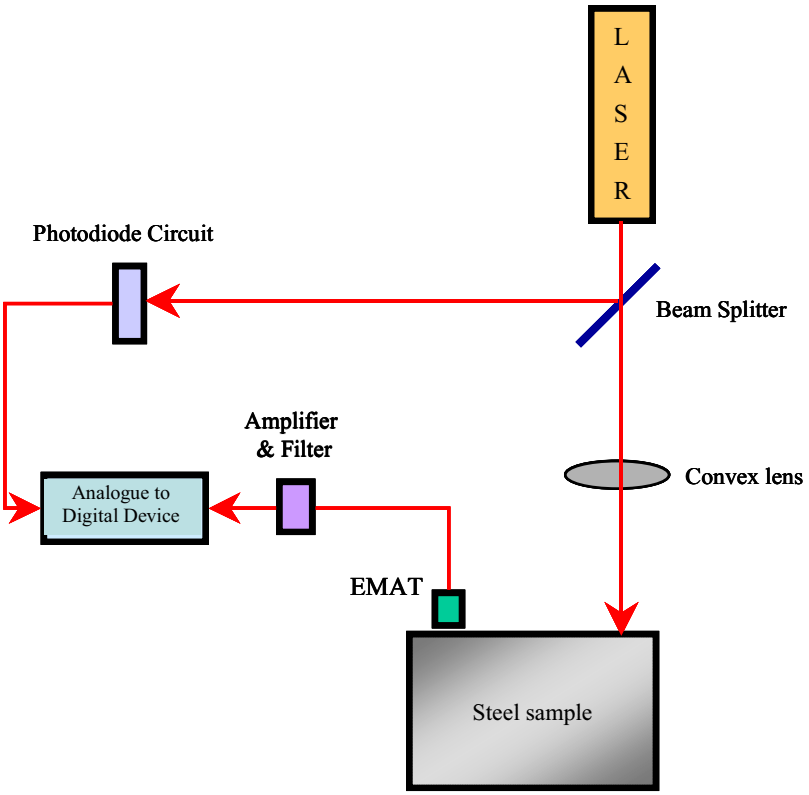

Fig. A1.3: Experimental Laser-EMAT arrangement

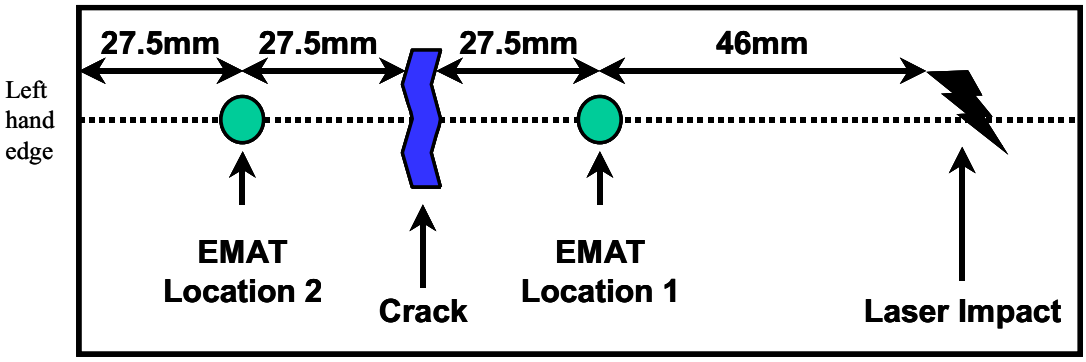

Fig. A1.4: Plan view of the billet being tested

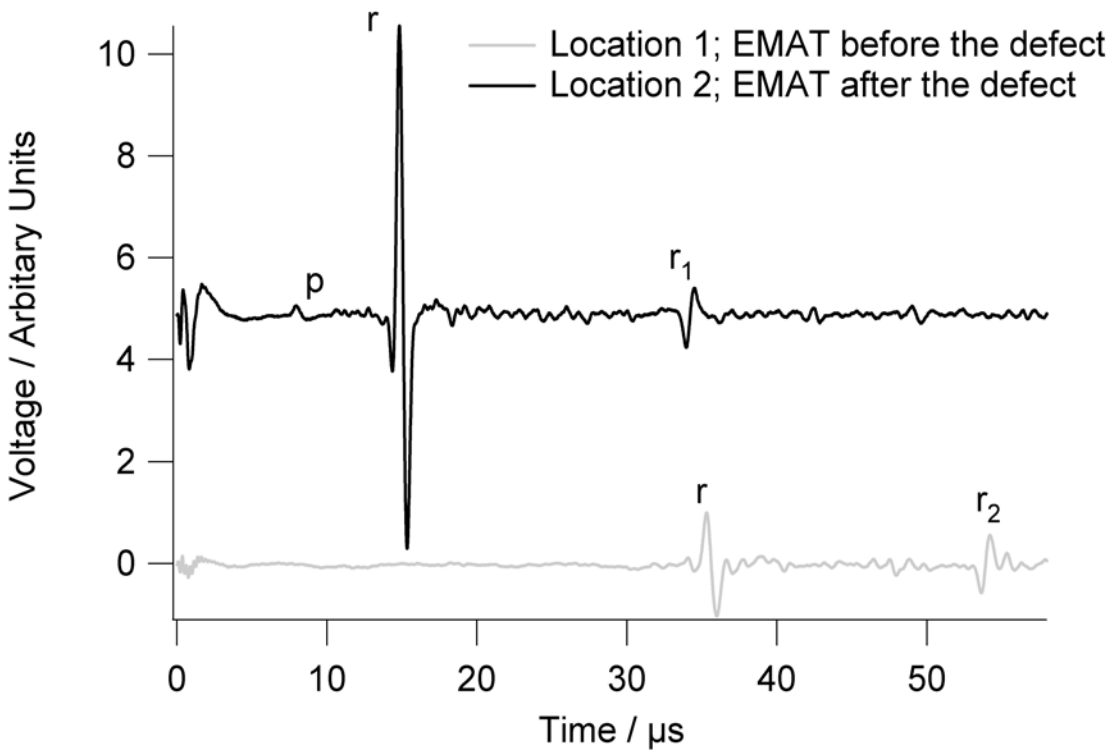

Fig. A1.5: Graph comparing location 1 and location 2, when a laser point source is used

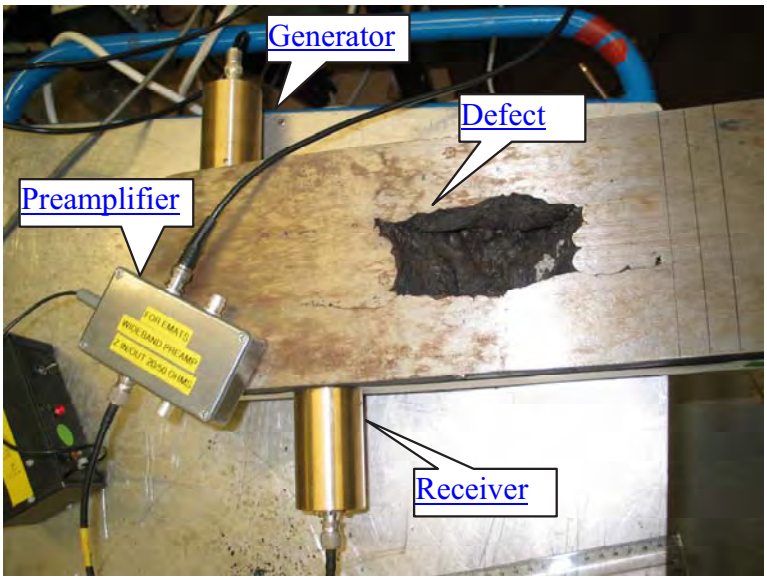

Fig. A1.6: A defect in a billet and the measurement set-up at The University of Warwick

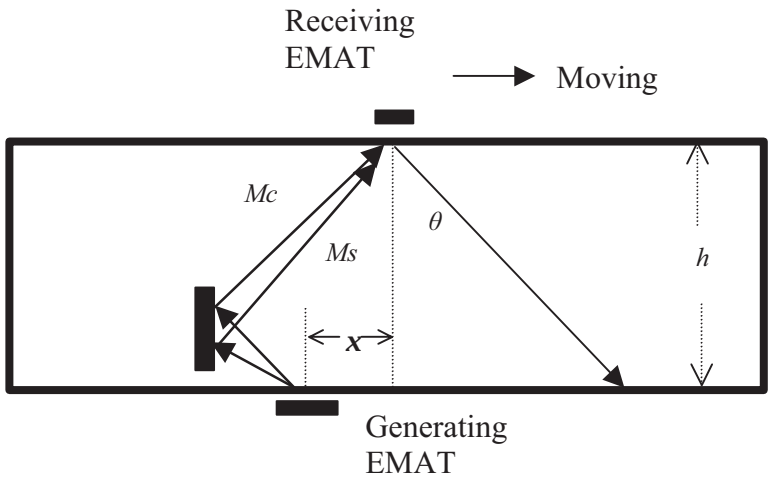

Fig. A1.7 : Schematic EMAT-EMAT through measurement set-up

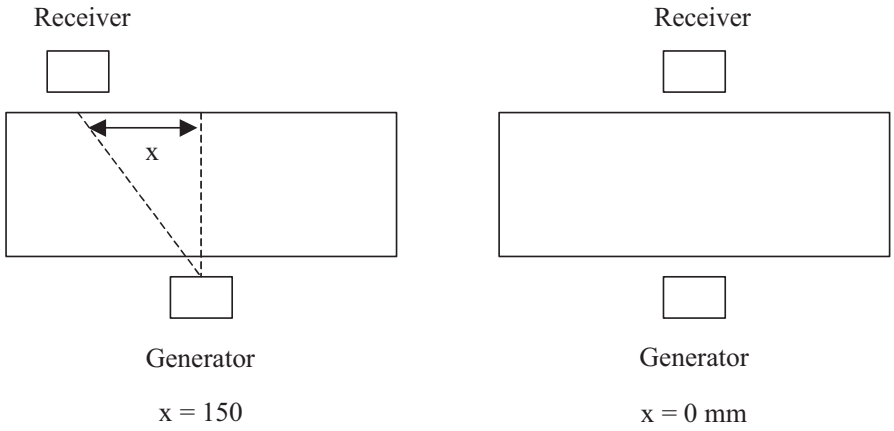

Fig. A1.8: The EMAT receiver being separated by a distance, x

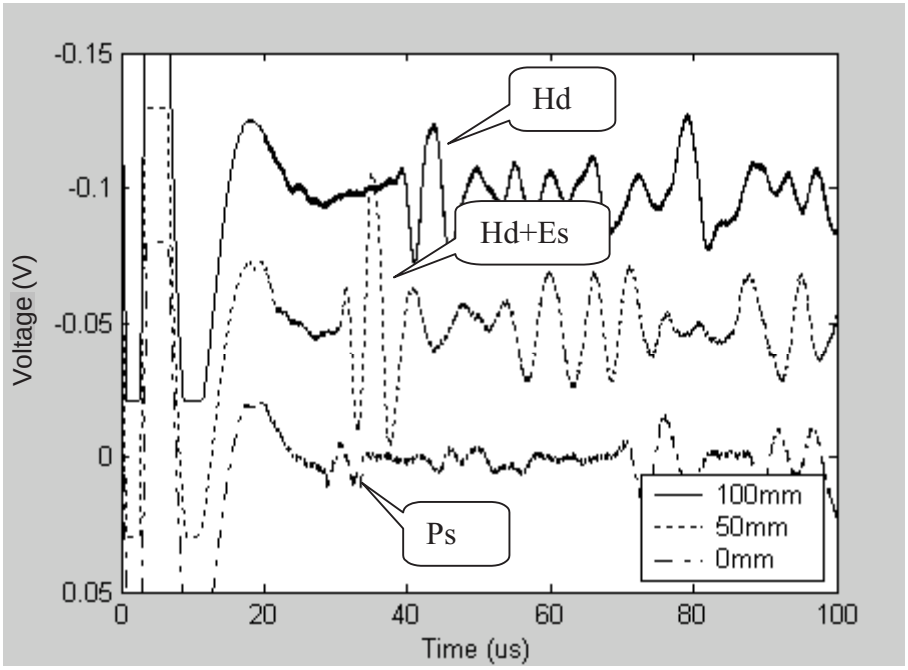

Fig. A1.9: Typical A-Scan waveform using EMAT-EMAT through method

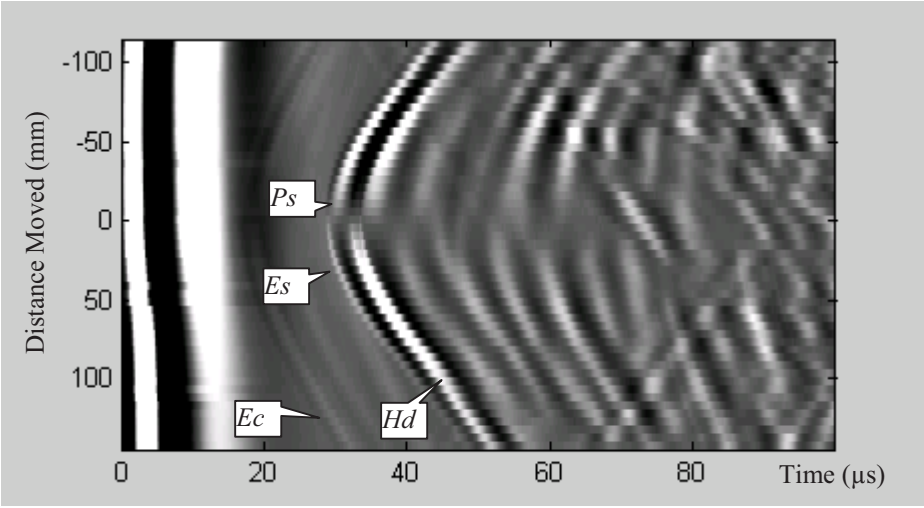

Fig. A1.10: Measured B-Scan image using EMAT-EMAT through method.
The receiving linear EMAT is 10 mm long by 5 mm wide

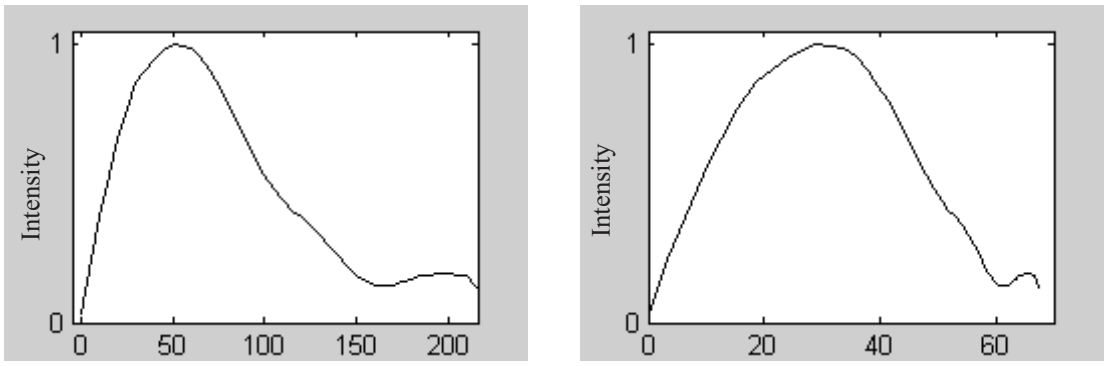

(***x*** mm) (θ degree)

A1.11a A1.11b

Fig. A1.11: Normalised directivity of the spiral generating coil of diameter 15 mm that is measured using the linear receiving coil of 5 mm wide by 10 mm long

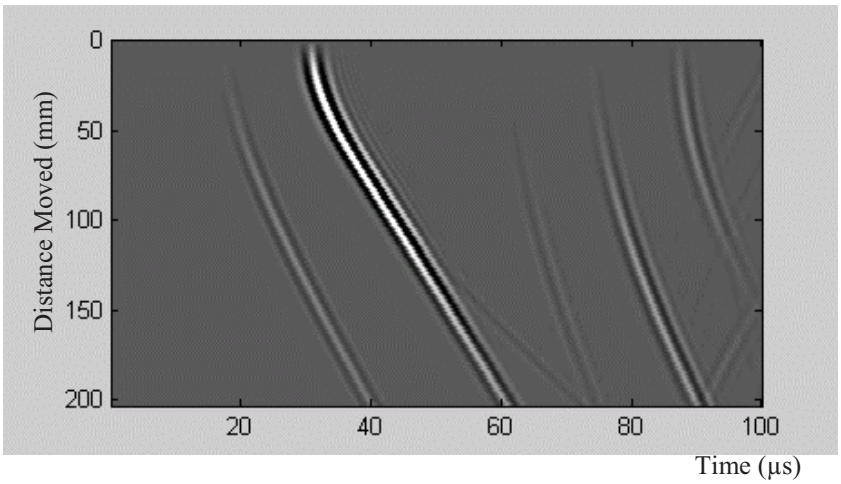

Fig. A1.12: Simulated B-Scan image at depth 90 mm

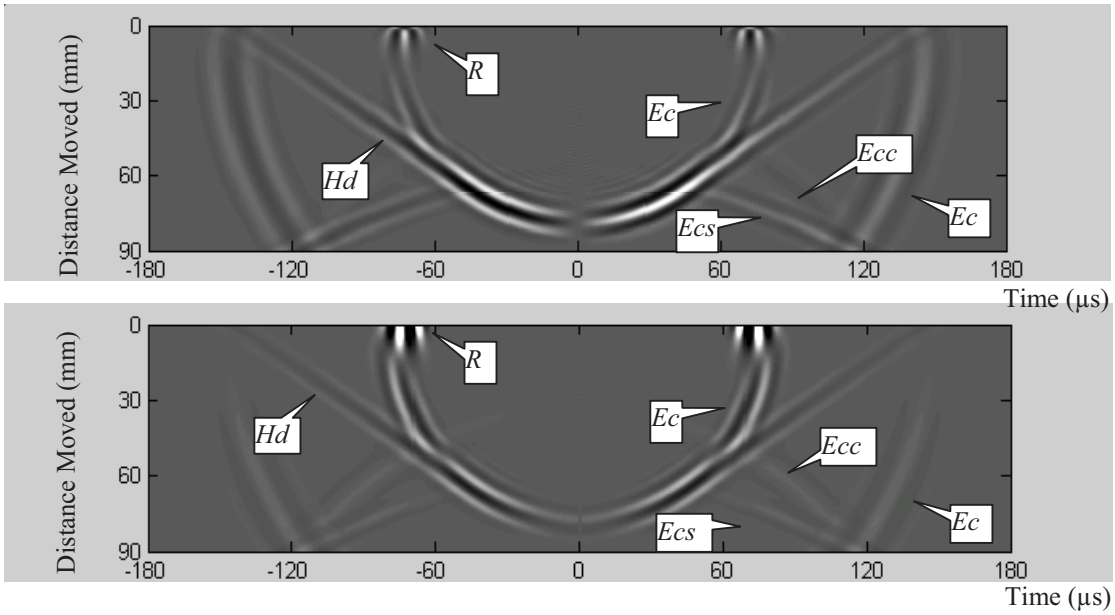

x mm

E_{cc} = Mode converted edge compression waves
E_{cs} = Mode converted edge to shear waves

Fig. A1.13: In-plane (top) and out-of-plane (bottom) particle field at time instance 27.5 μs generated by a spiral coil of diameter 15 mm

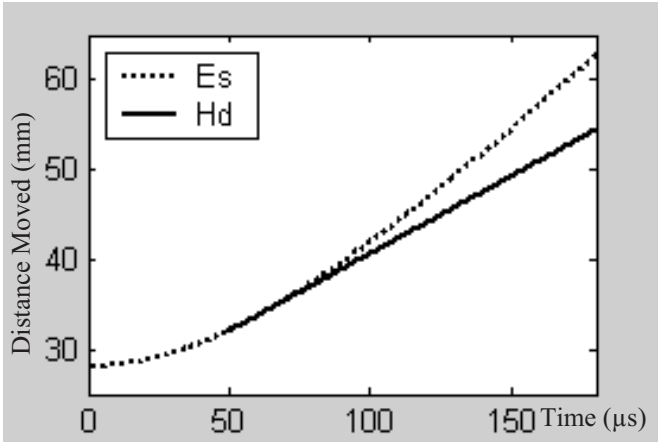

Fig. A1.14: Arrival times of edge shear waves and head waves at depth 90 mm

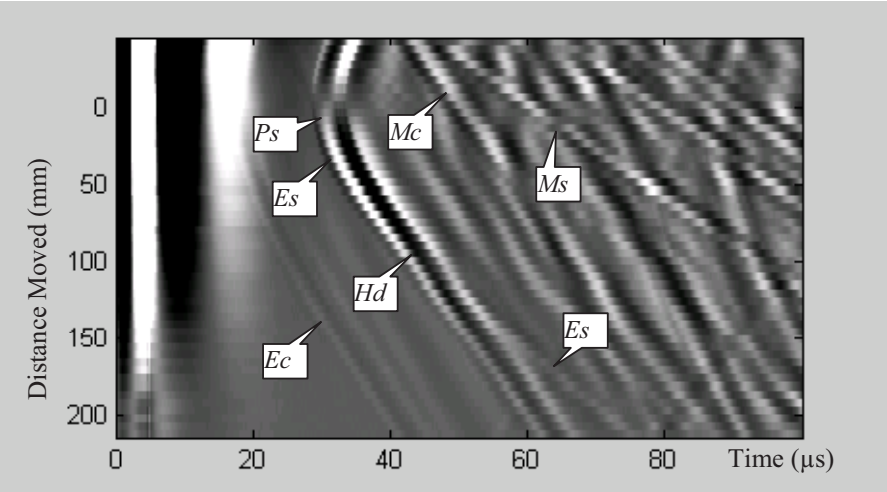

Fig. A1.15: Measured B-Scan image using EMAT-EMAT through method, showing reflection of head waves from a defect
The receiving linear EMAT is 10 mm long by 5 mm wide

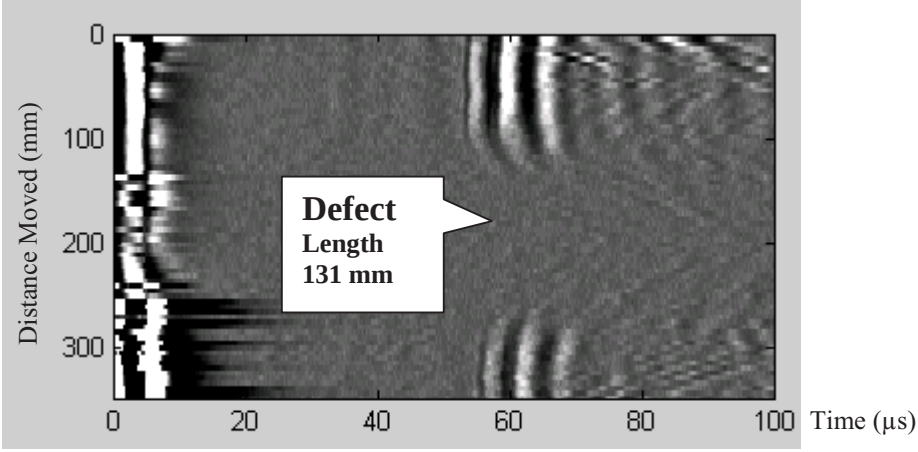

Fig. A1.16: Measured B-Scan image using EMAT-EMAT through method for the defect detection and sizing

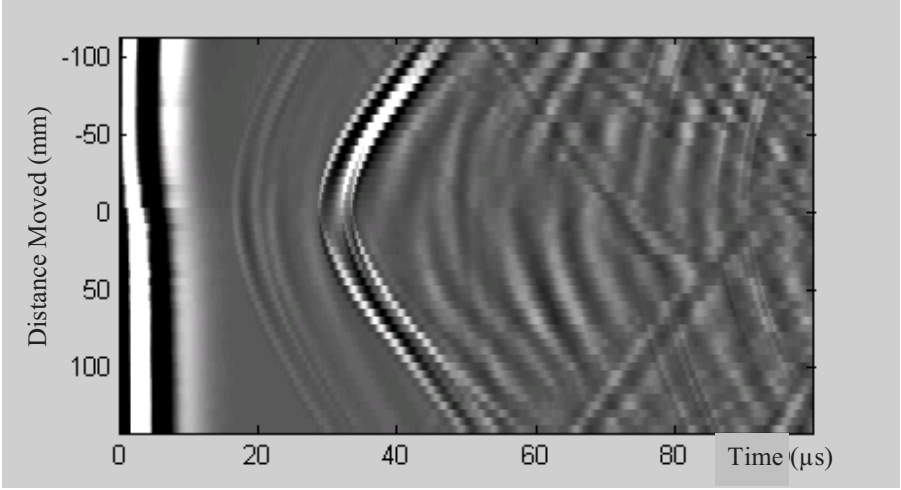

Fig. A1.17: Measured B-Scan image using EMAT-EMAT through method
The receiving linear EMAT is 20 mm long by 5 mm wide showing reduced resolution compared to Fig. A1.5

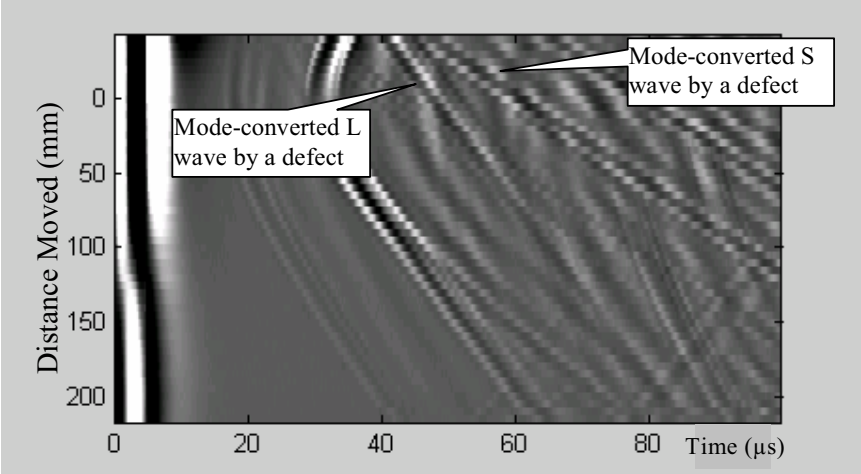

Fig. A1.18: Measured B-Scan image using EMAT-EMAT through method
The receiving linear EMAT is 20 mm long by 5 mm wide showing
reduced resolution compared with Fig. A1.10

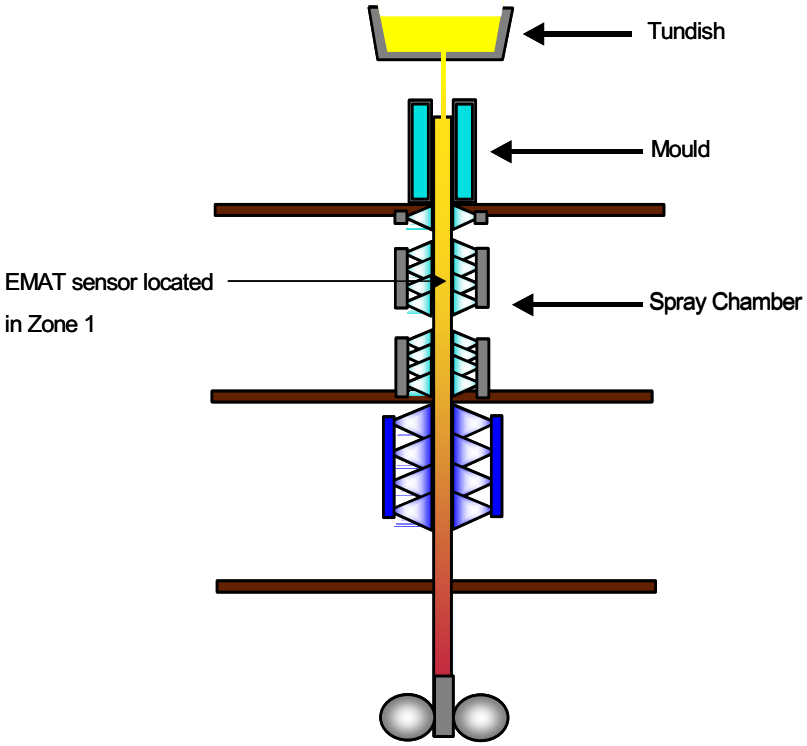

Fig. A1.19: Installation point for the EMAT on the caster

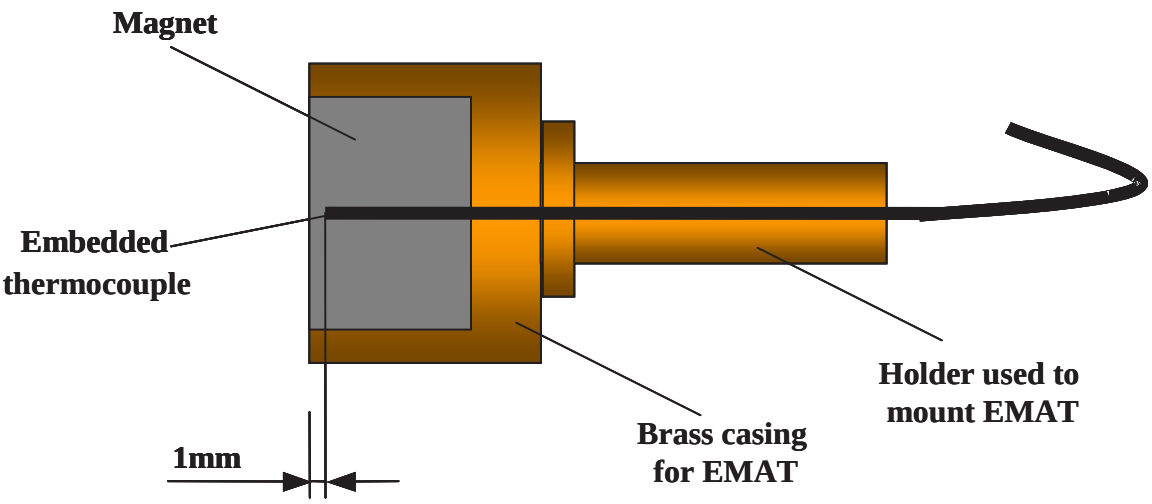

Fig. A1.20: Schematic of the embedded thermocouple

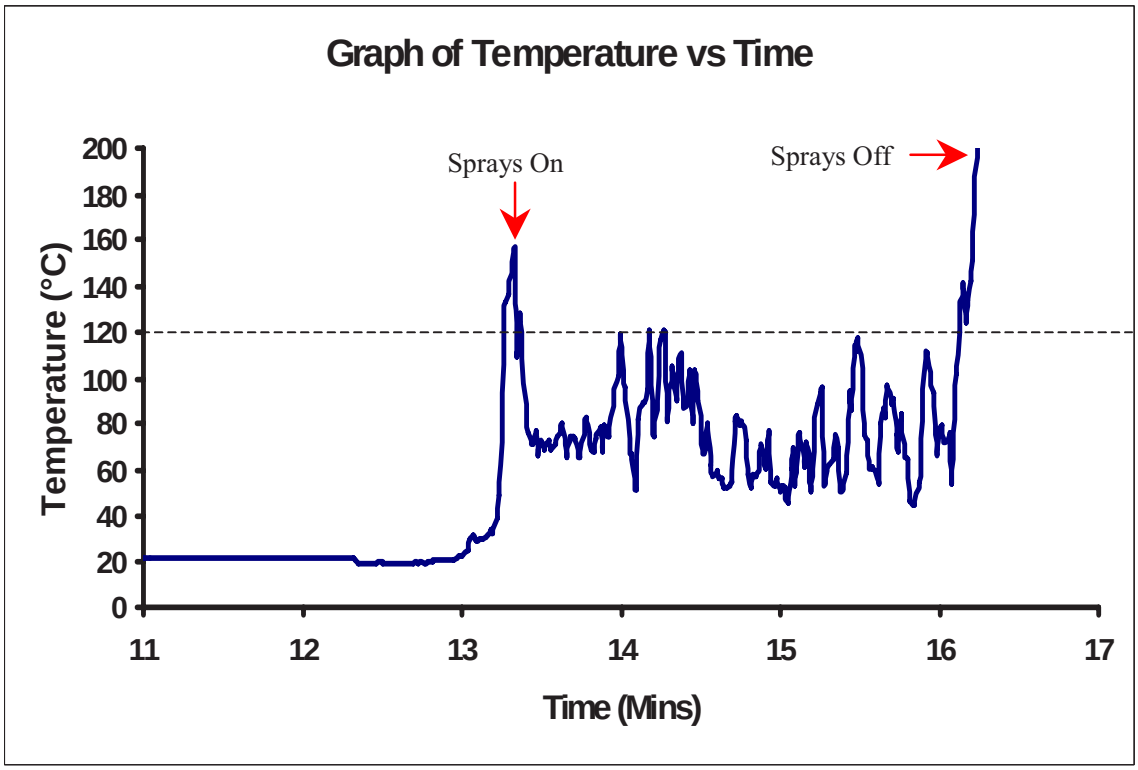

Fig. A1.21: Graph of results, showing the temperature of the EMAT face

Fig. A1.22: The build up of scale on the EMAT face

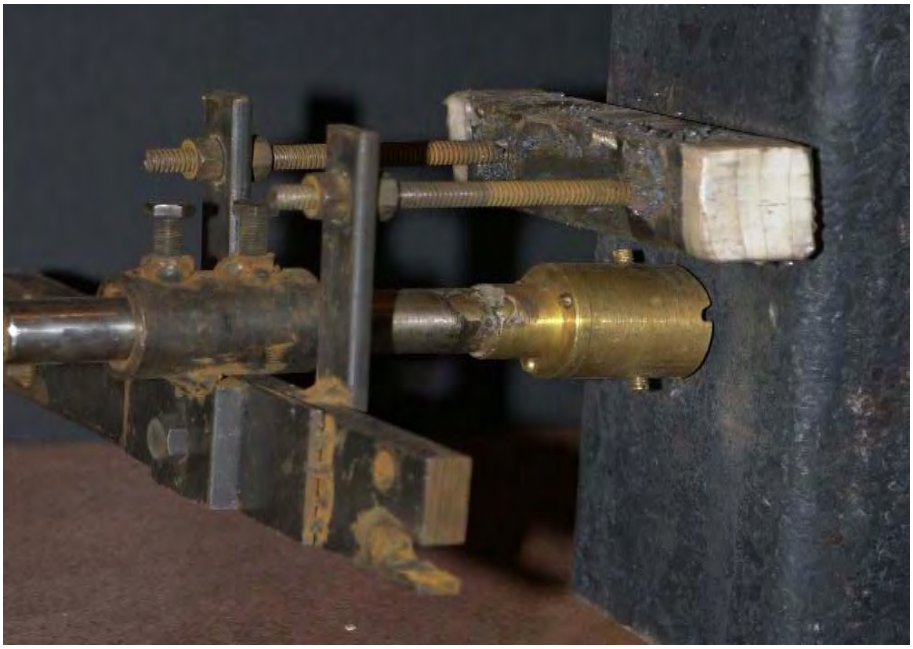

Fig. A1.23: Photograph of the scale collector, mounted above the EMAT

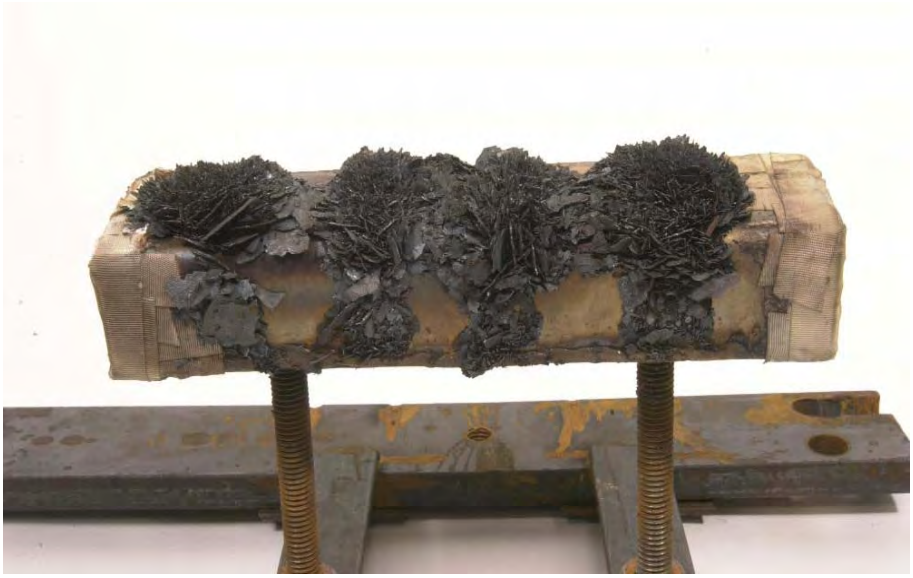

Fig. A1.24: Photograph of the scale collector, with scale piles on top of each of the four magnets housed inside the box

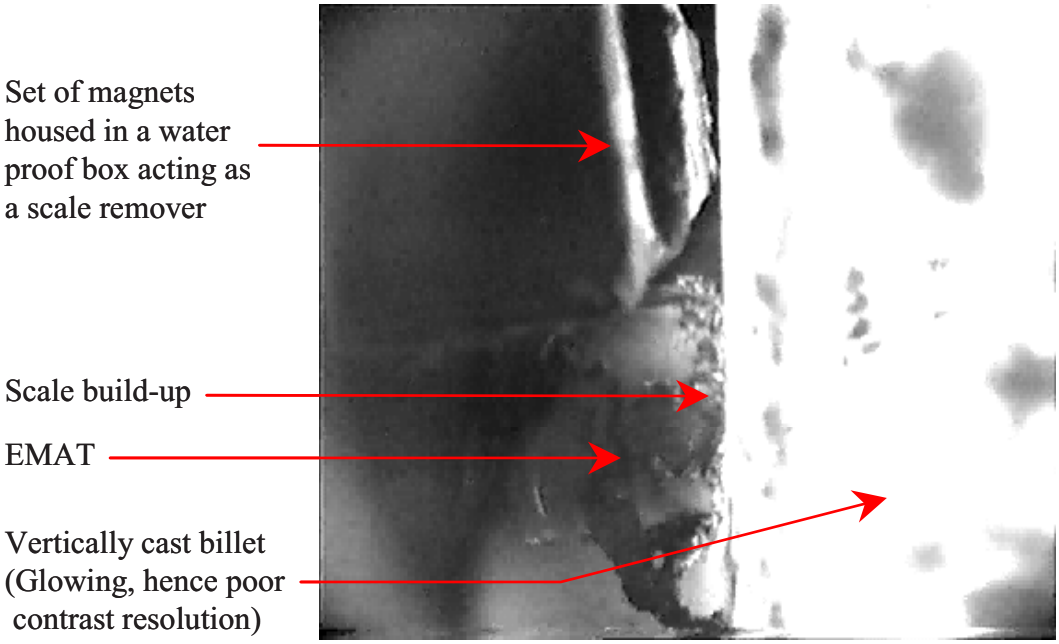

Fig. A1.25: Screenshot from the video camera, used to monitor the attraction of scale to the magnets in the scale collector and EMAT

Fig. A1.26: Photograph of a type 2 EMAT

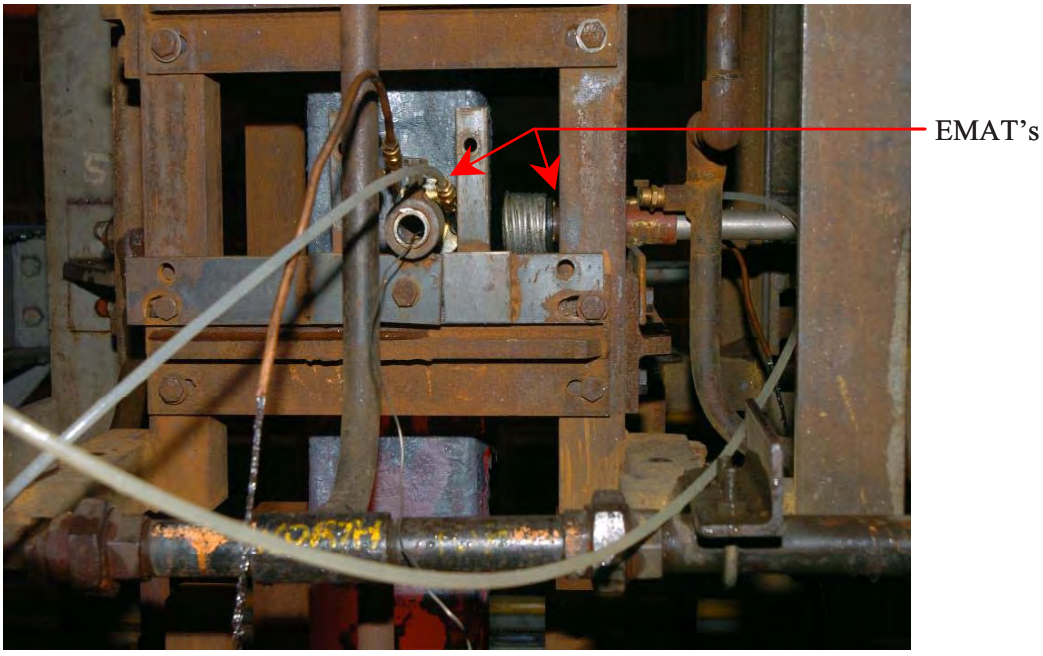

Fig. A1.27: The two EMATs mounted on the caster at Corus Teesside Technology Centre

Fig. A1.28: The water-cooled EMAT mounted in a tripod

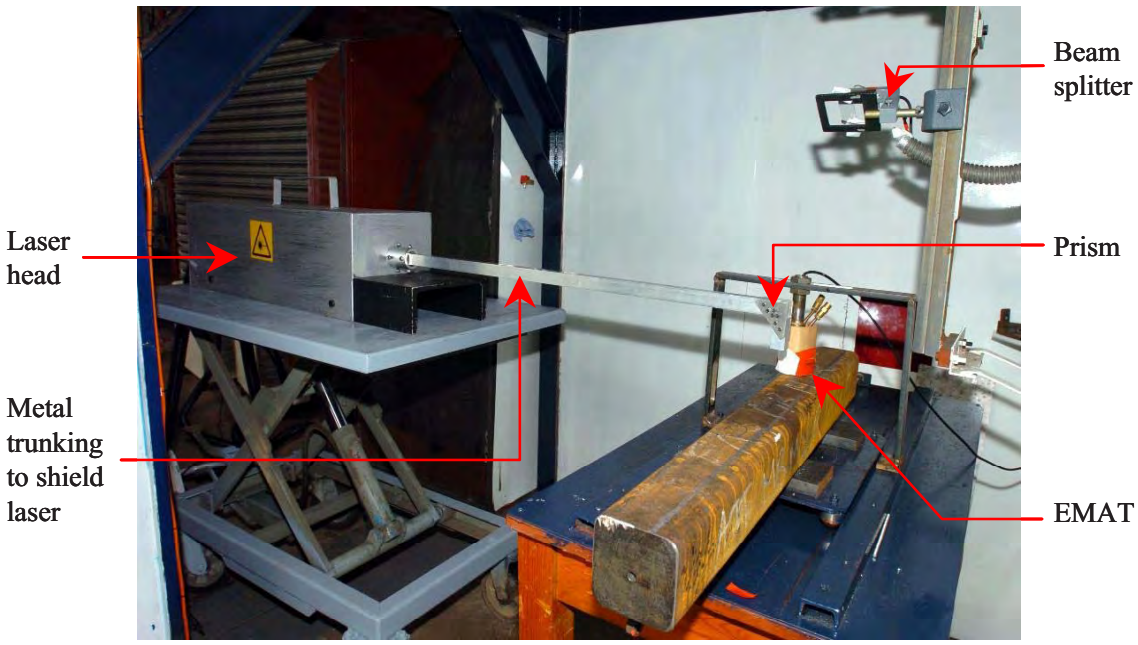

Fig. A1.29: The portable laser system, positioned above the billet being tested at Corus Teesside Technology Centre

Fig. A1.30a: Apparatus arrangement with no prism present

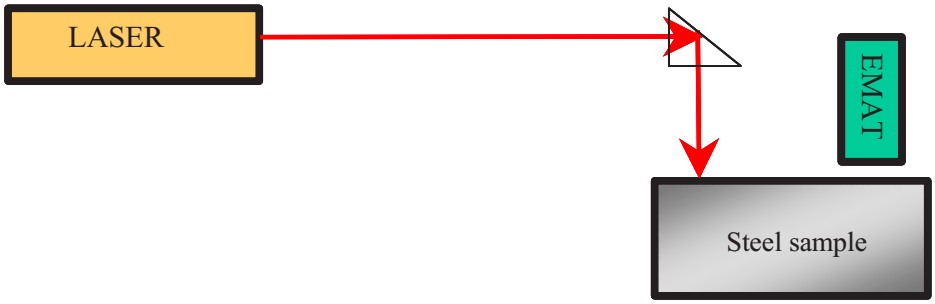

Fig. A1.30b: Apparatus arrangement with the prism present

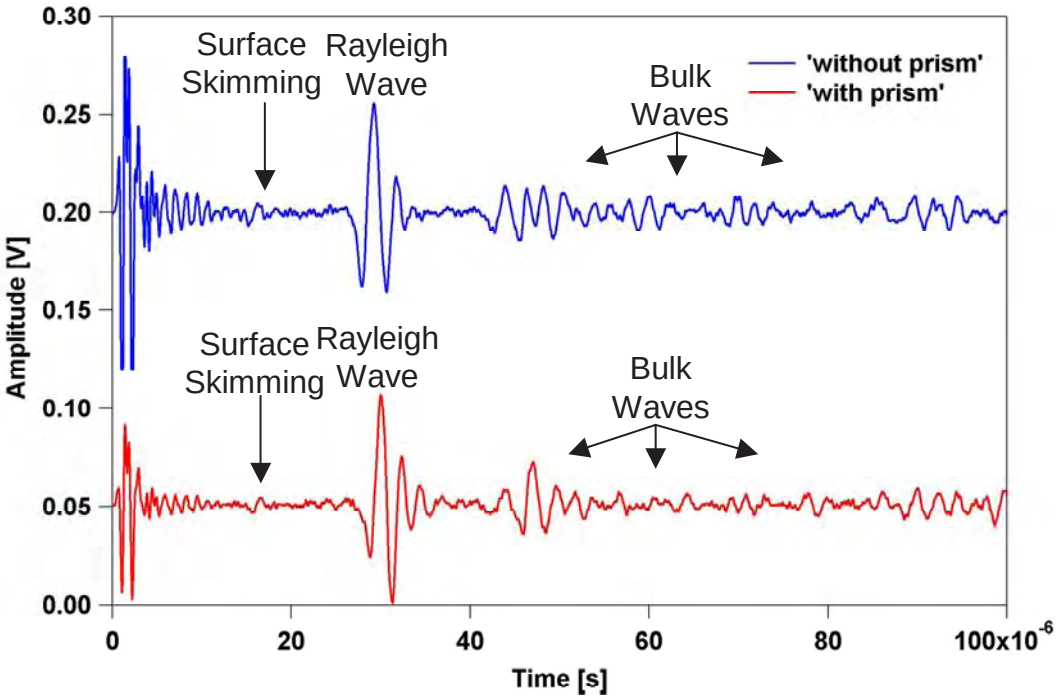

Fig. A1.31: Results showing the difference between using the laser with and without a prism

Fig. A1.32a: Plan view of the billet being tested.
Nothing is blocking the path between the laser and EMAT

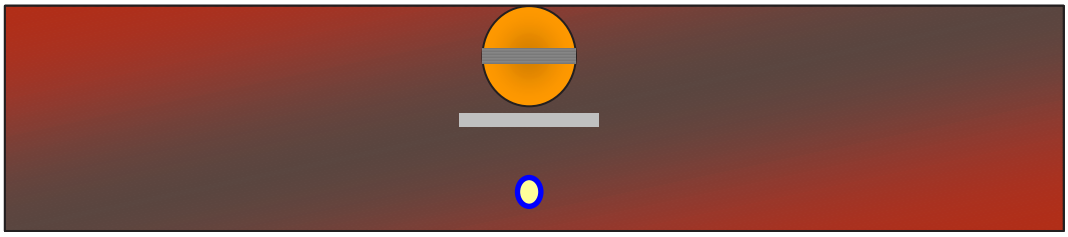

Fig. A1.32b: Plan view of the billet being tested.
The defect is present and blocks the path between the laser and EMAT

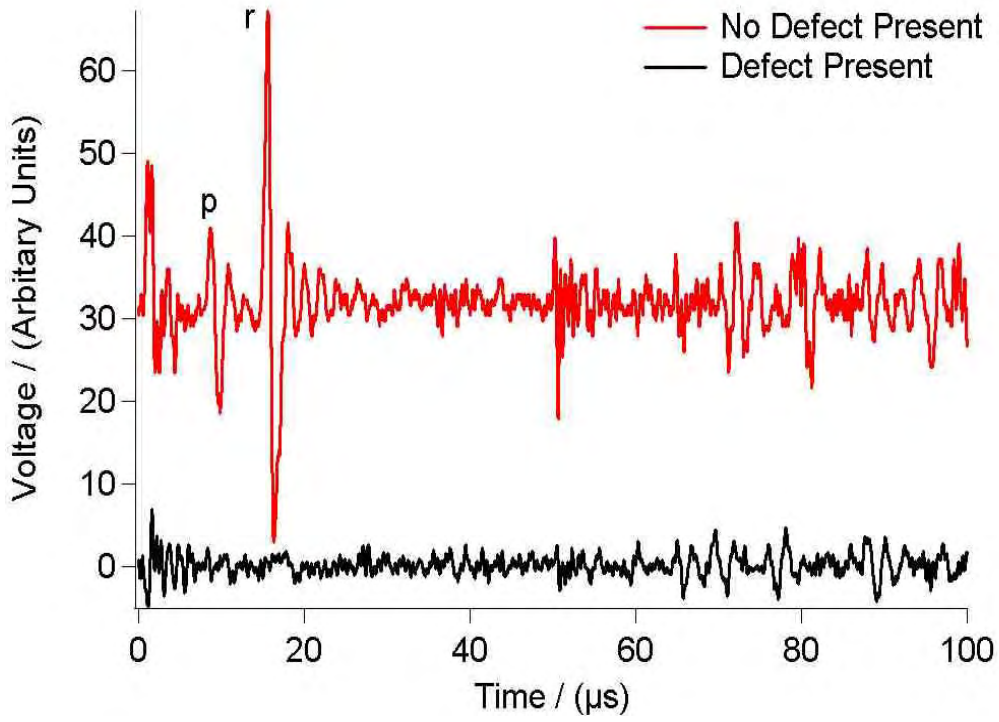

Fig. A1.33: A-Scans showing the change when a defect is present and not

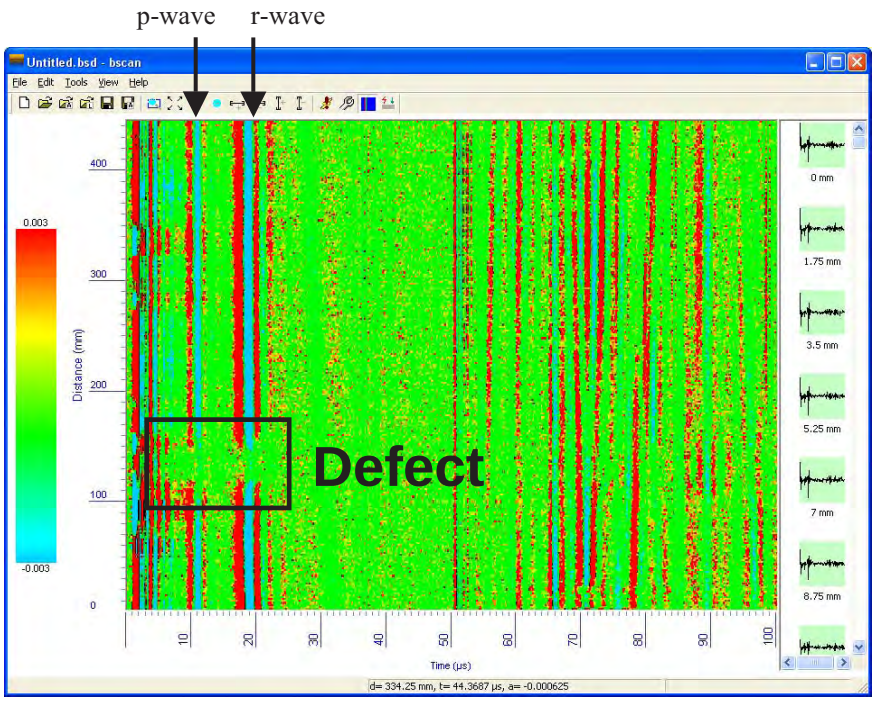

Fig. A1.34: B-Scan showing the location of a longitudinal defect

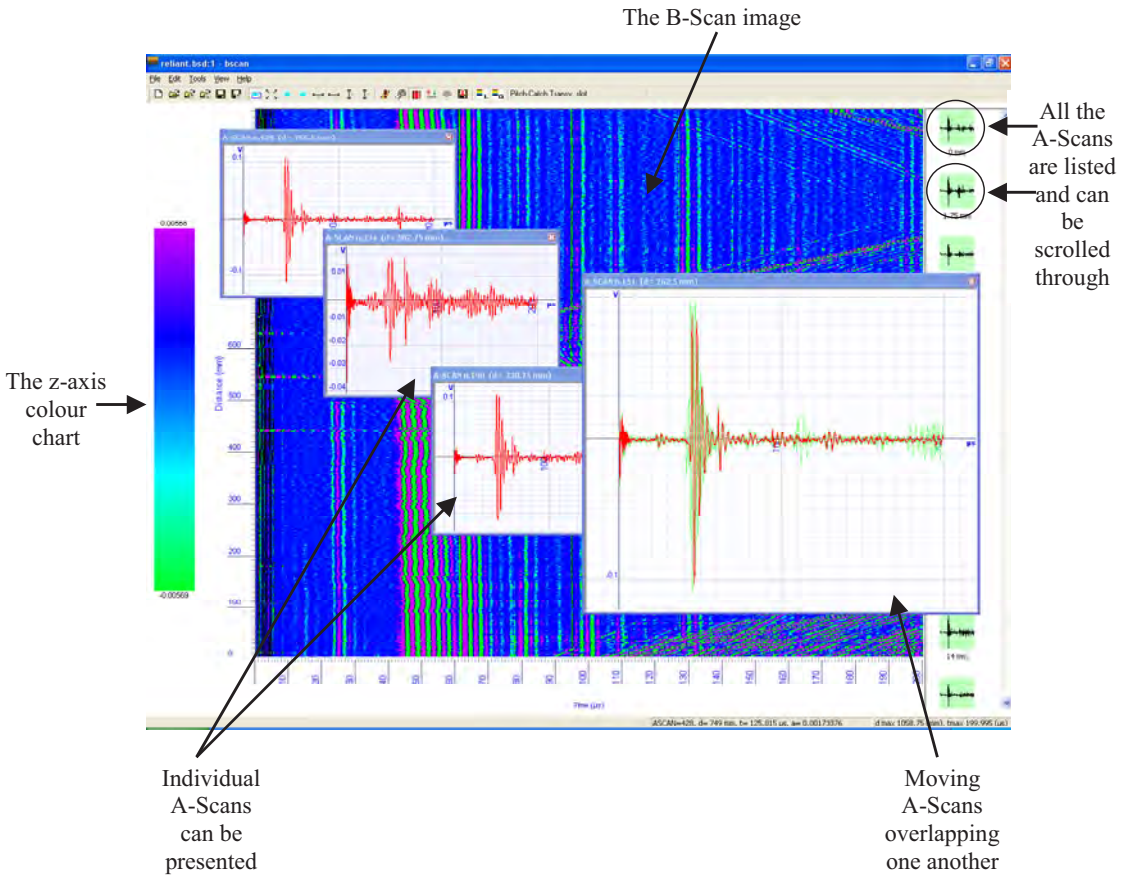

Fig. A1.35: B-Scan software

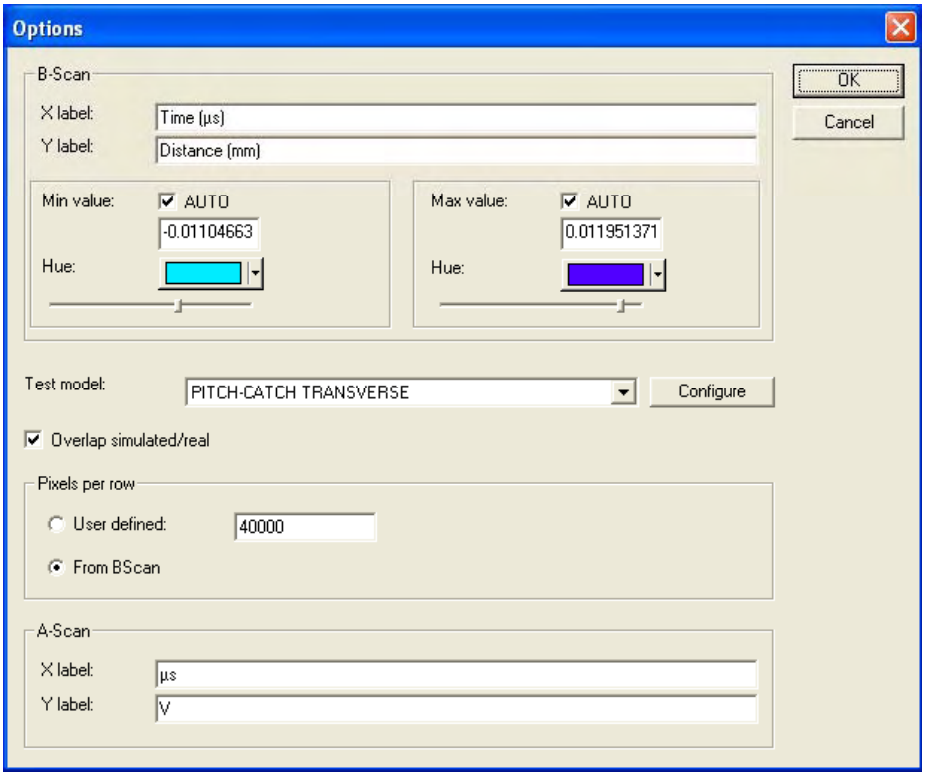

Fig. A1.36: Options to control the x, y & z axis for a B-Scan

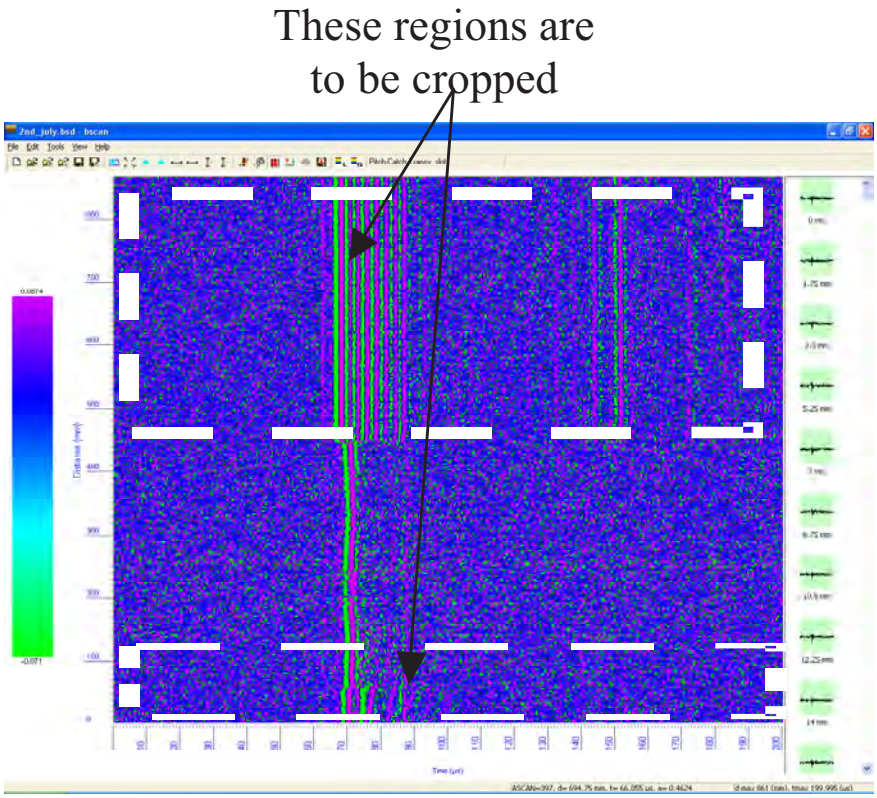

Fig. A1.37a: The original B-Scan

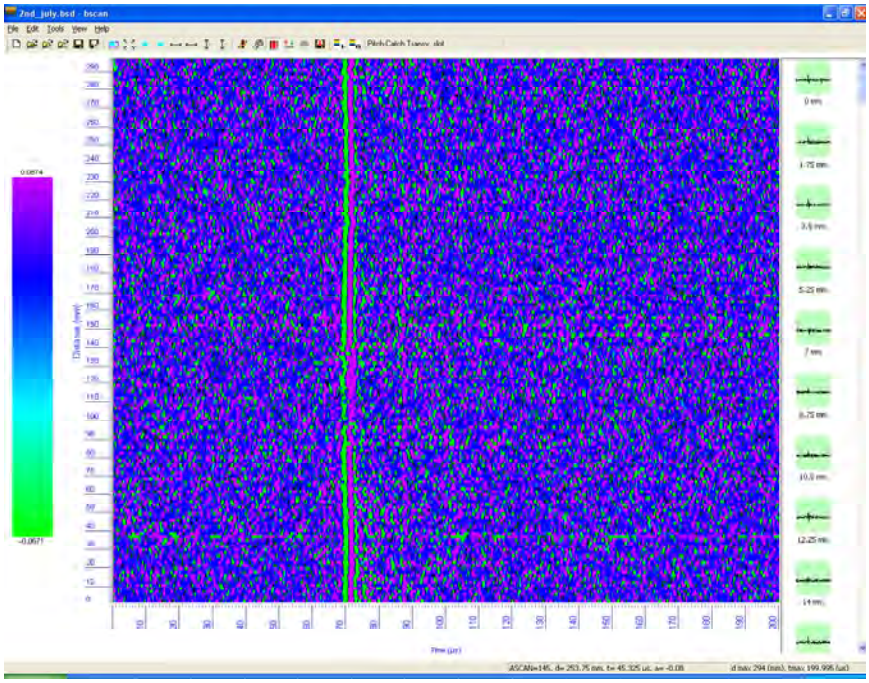

Fig. A1.37b: The now cropped B-Scan

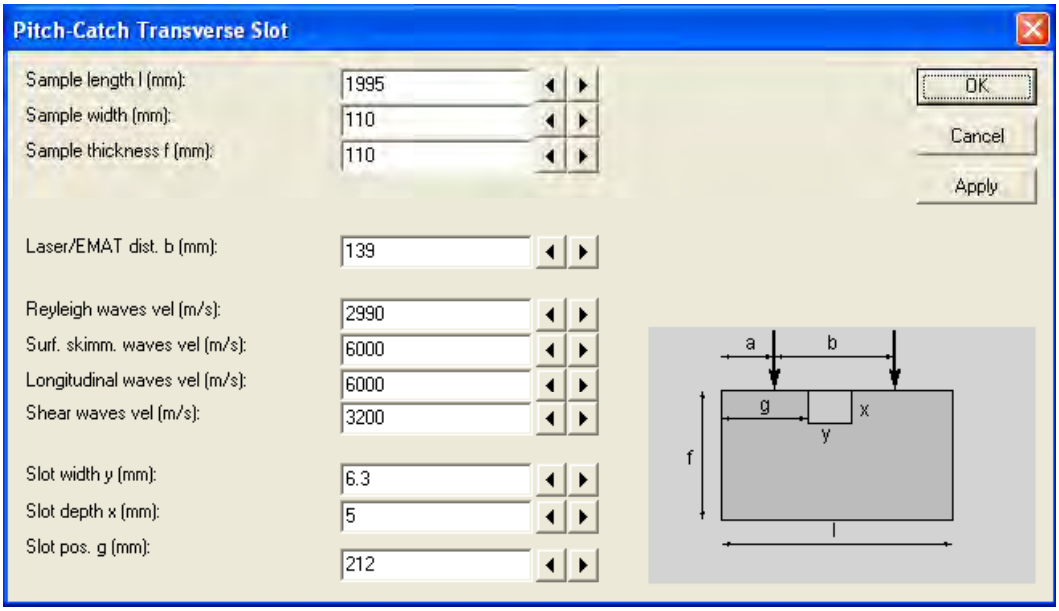

Fig. A1.38: Example of model parameter dialog

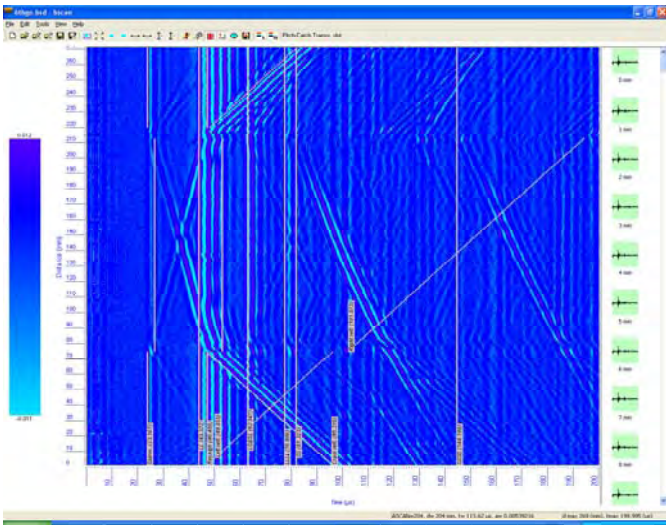

Fig. A1.39: Overlapping measured B-Scan and modelled B-Scan

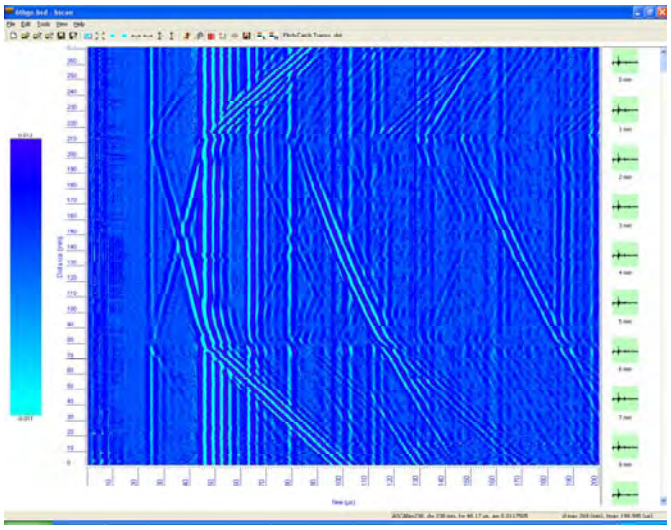

Fig. A1.40: Measured B-Scan

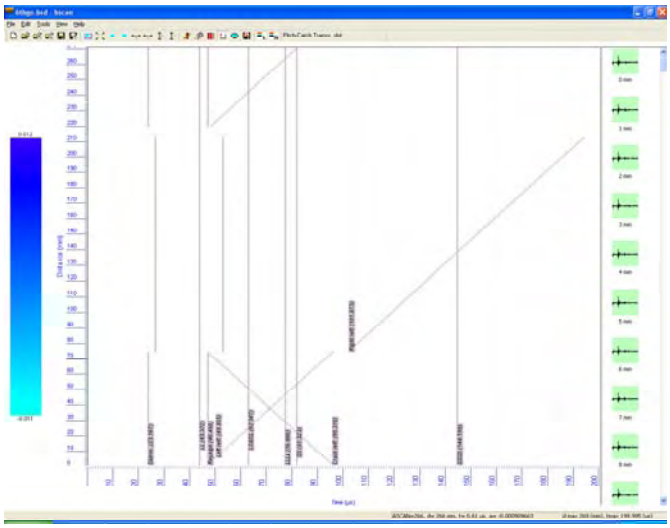

Fig. A1.41: Modelled B-Scan

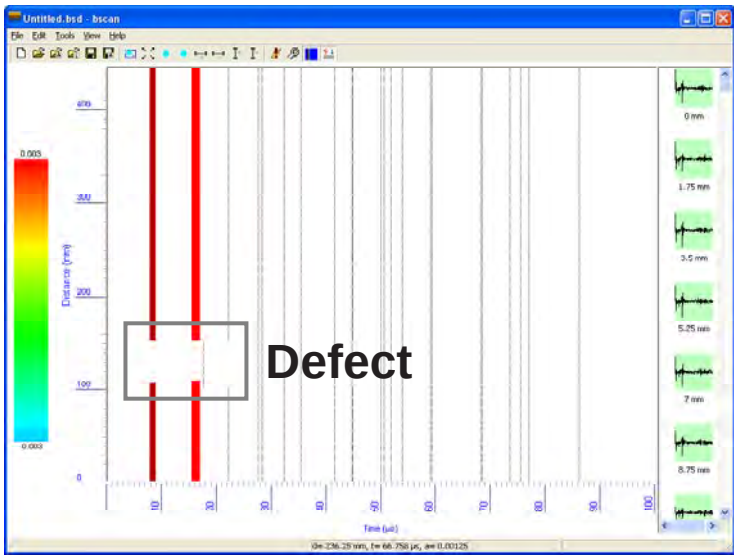

Fig. A1.42: Simulated B-Scan for a longitudinal defect

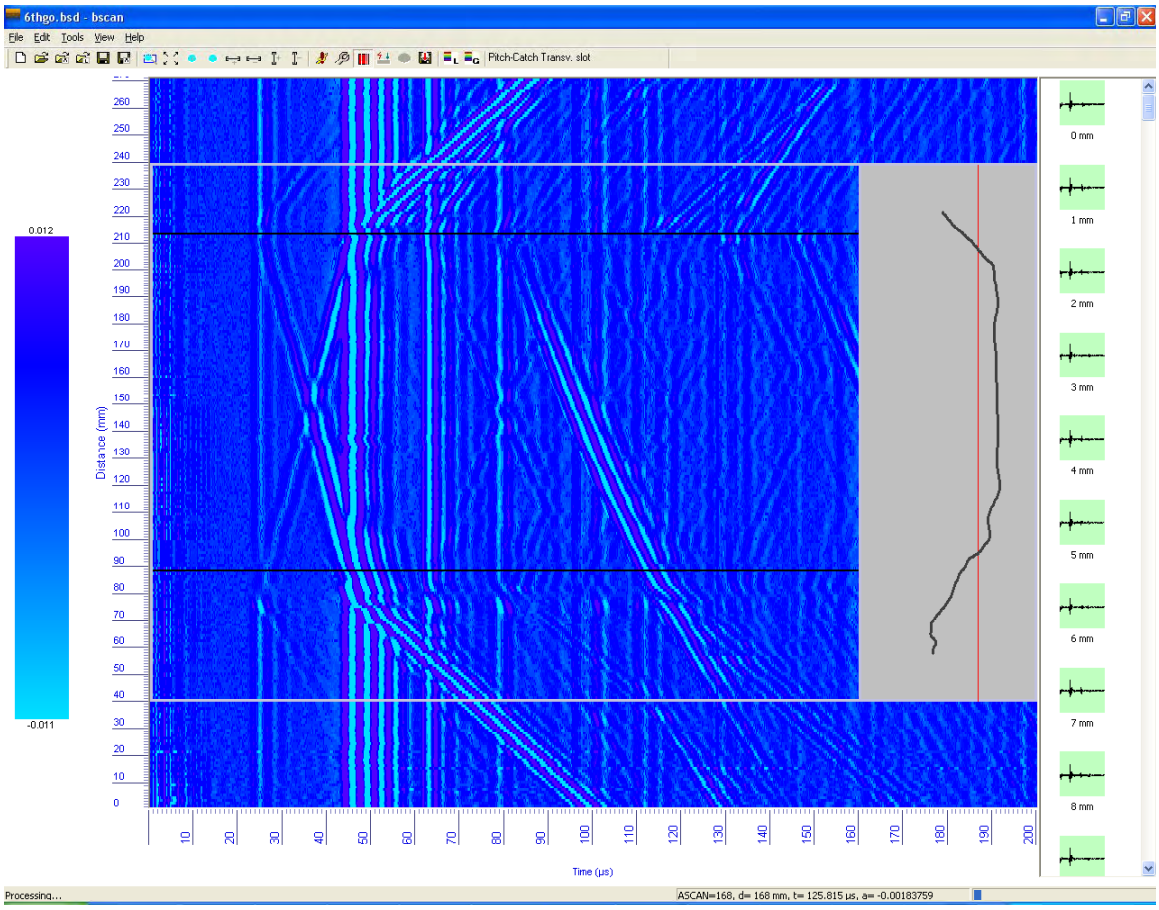

Fig. A1.43: A-Scan view

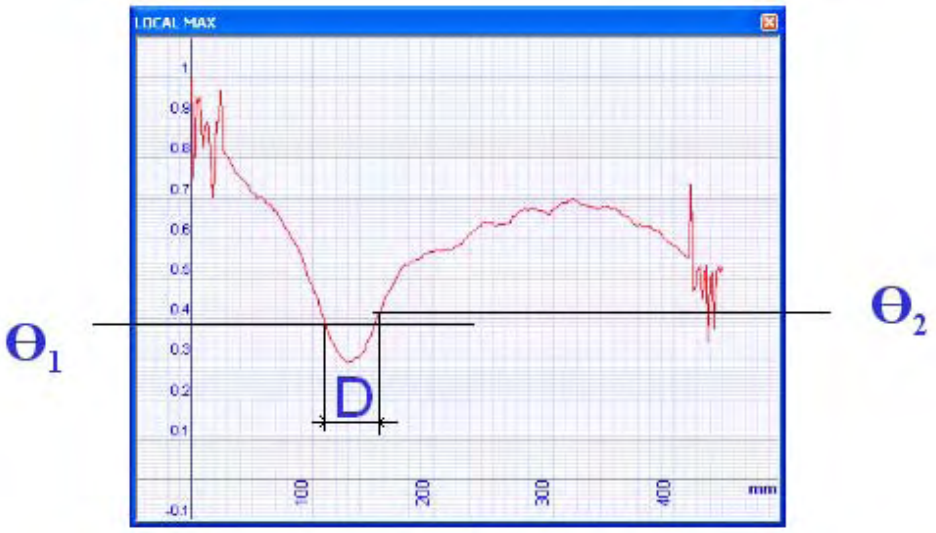

Fig. A1.44: F(x) curve, showing drop in signal, indicating the presence of a defect

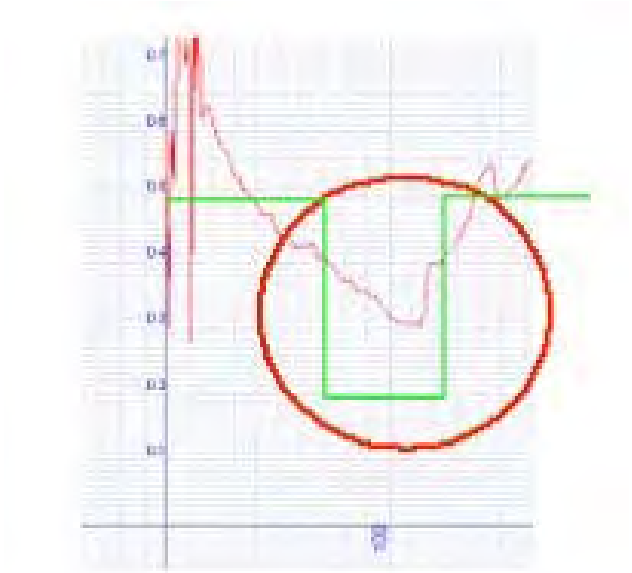

Fig. A1..45: The green line represents the ideal values. The red line shows the plot for "real data". The large dip represents the presence of a defect

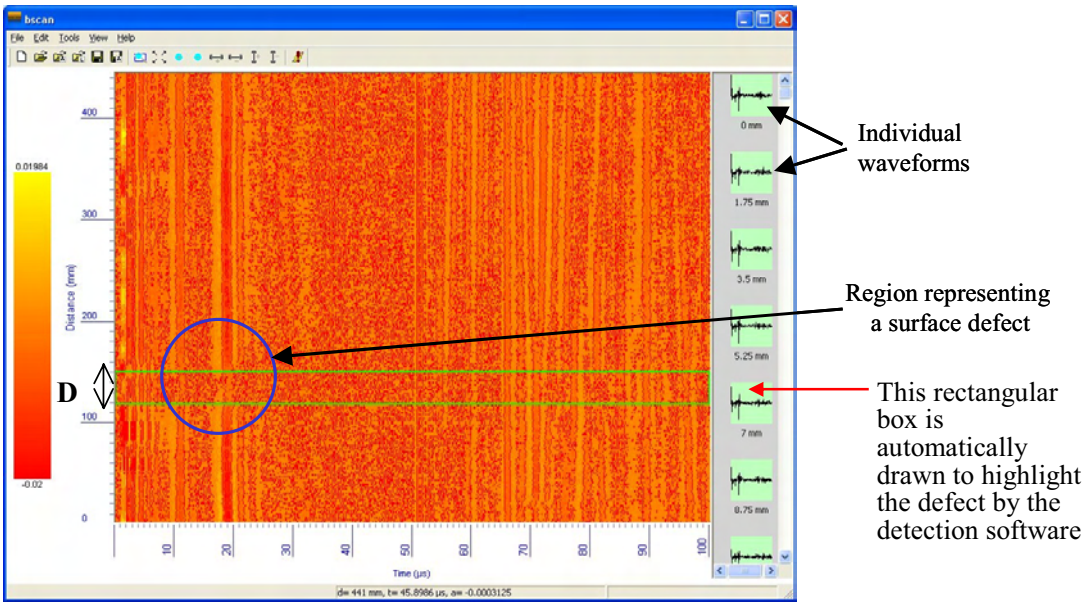

Fig. A1.46: Example of a defect being automatically identified in a B-Scan image

Location of the defect

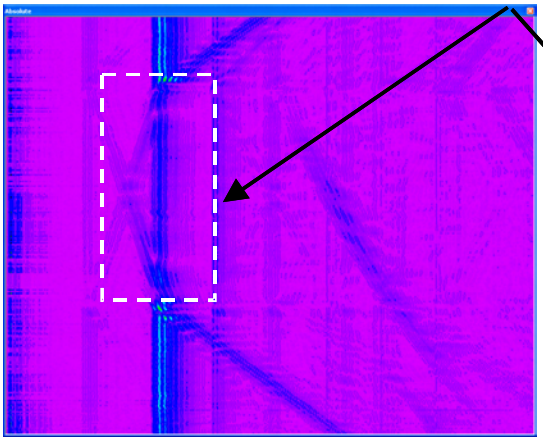

Fig. A1.47a: B-Scan showing the presence of a defect

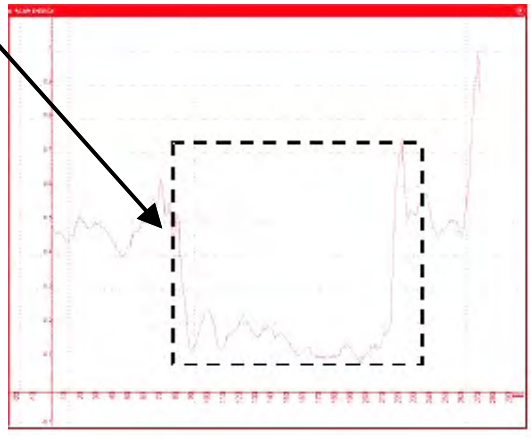

Fig. A1.47b: The corresponding A-Scan amplitude plot

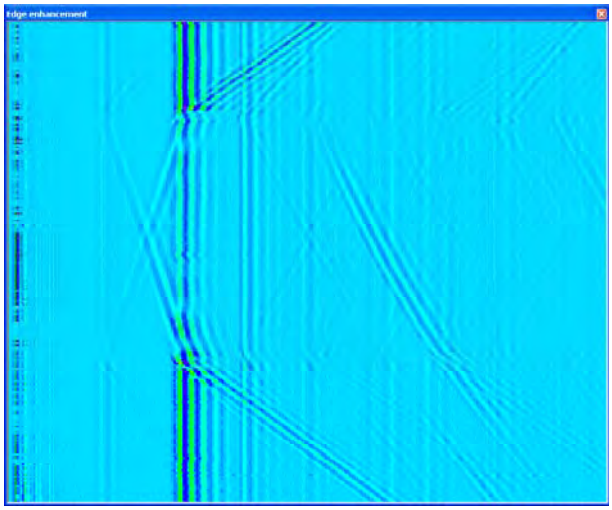

Fig. A1.48a: Edge enhancement to develop the B-Scan

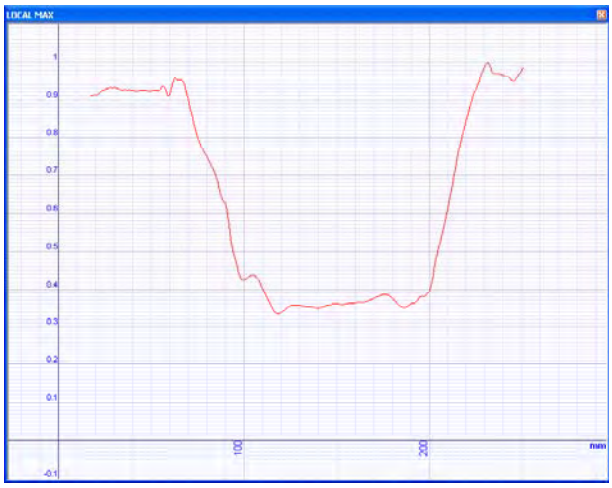

Fig. A1.48b: Using the Loc.Max function

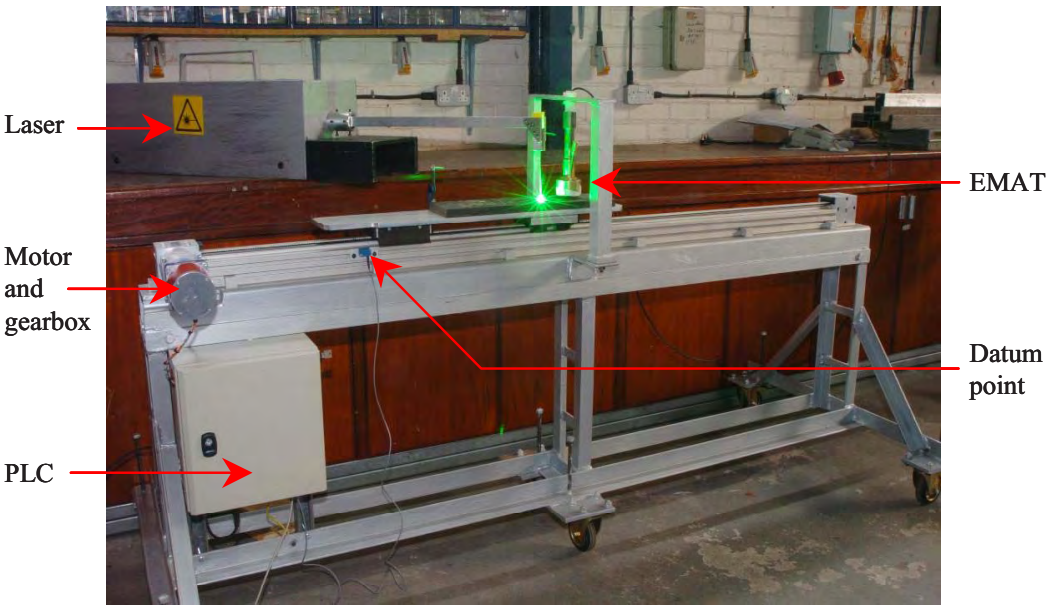

Fig. A1.49: The automated trolley system. Here a LabVIEW program was used to fire the laser, move the steel and acquire the EMAT data

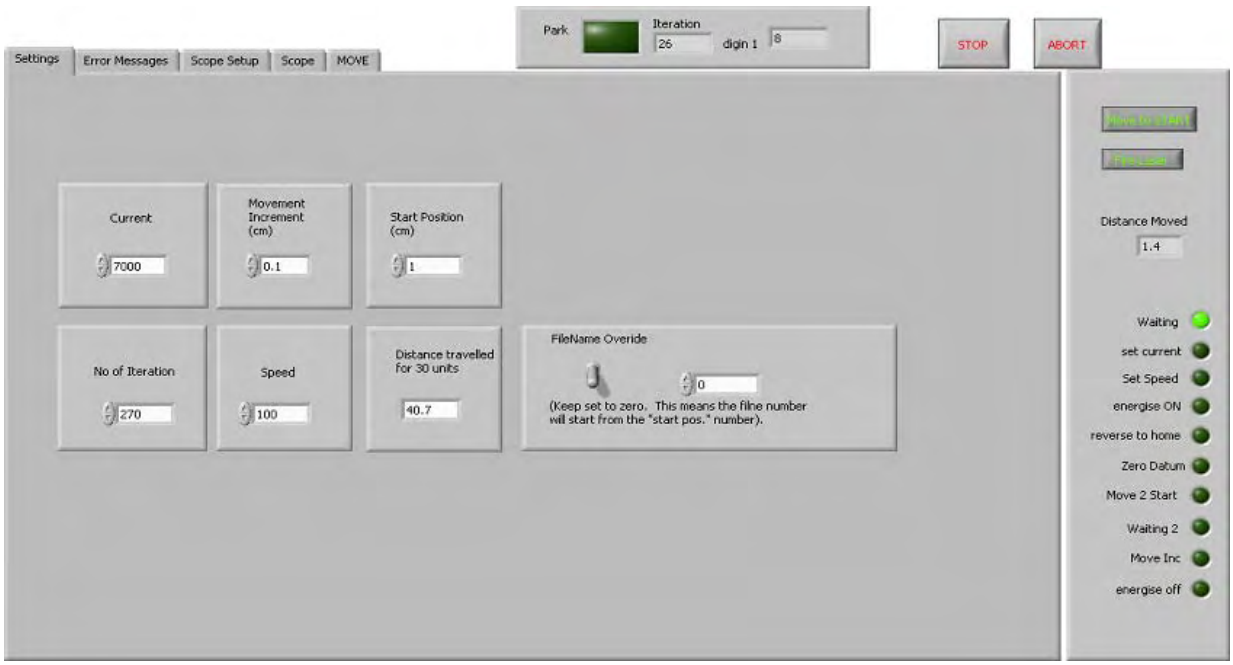

Fig. A1.50: Front software panel showing the required inputs for moving steel samples

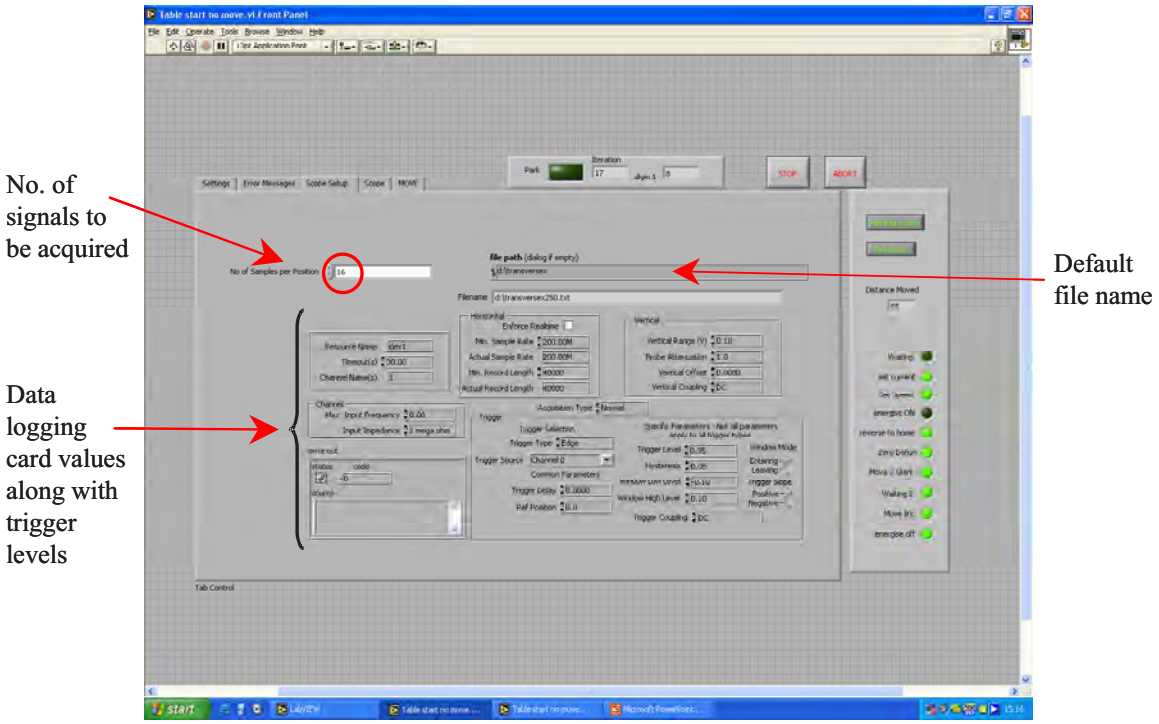

Fig. A1.51: The high speed digitiser set-up panel

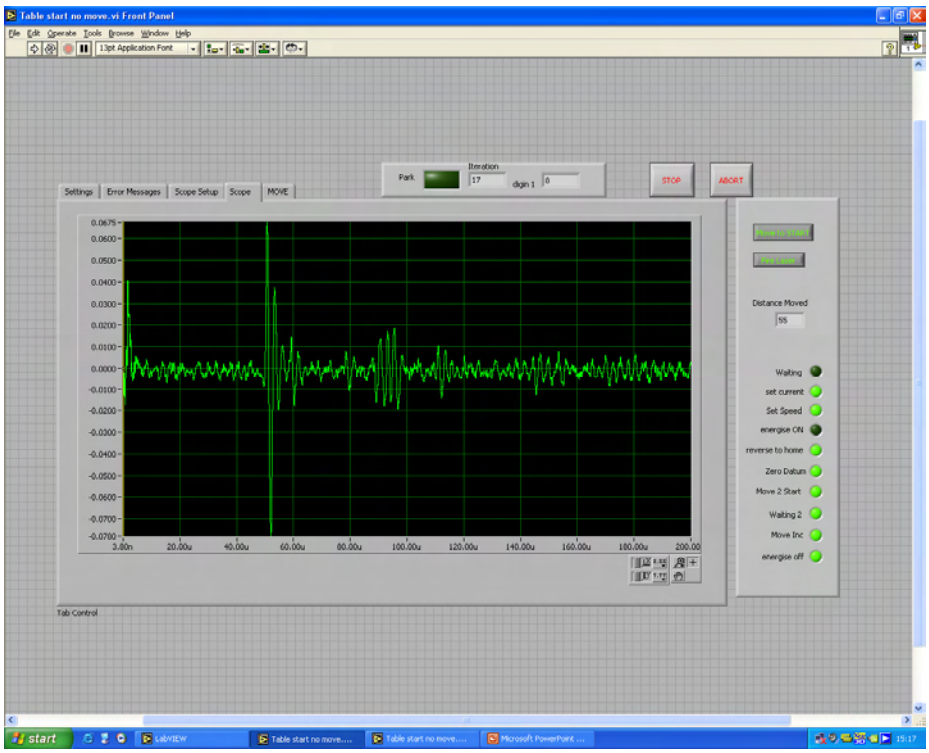

Fig. A1.52: A-Scan output, as given by the digitiser card

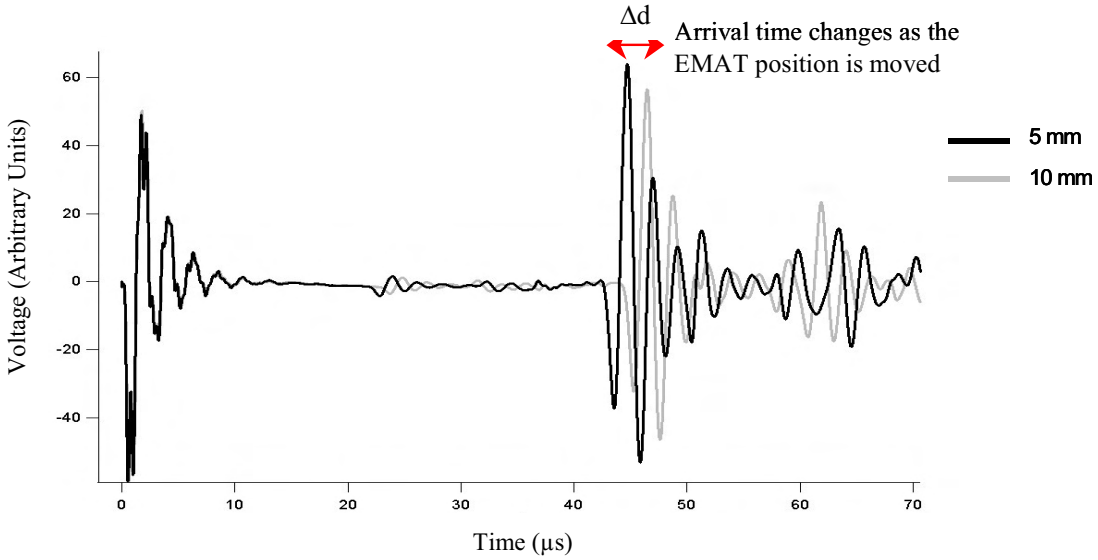

Fig. A1.53: A-Scans, taken when the laser impact position has been moved 5 mm

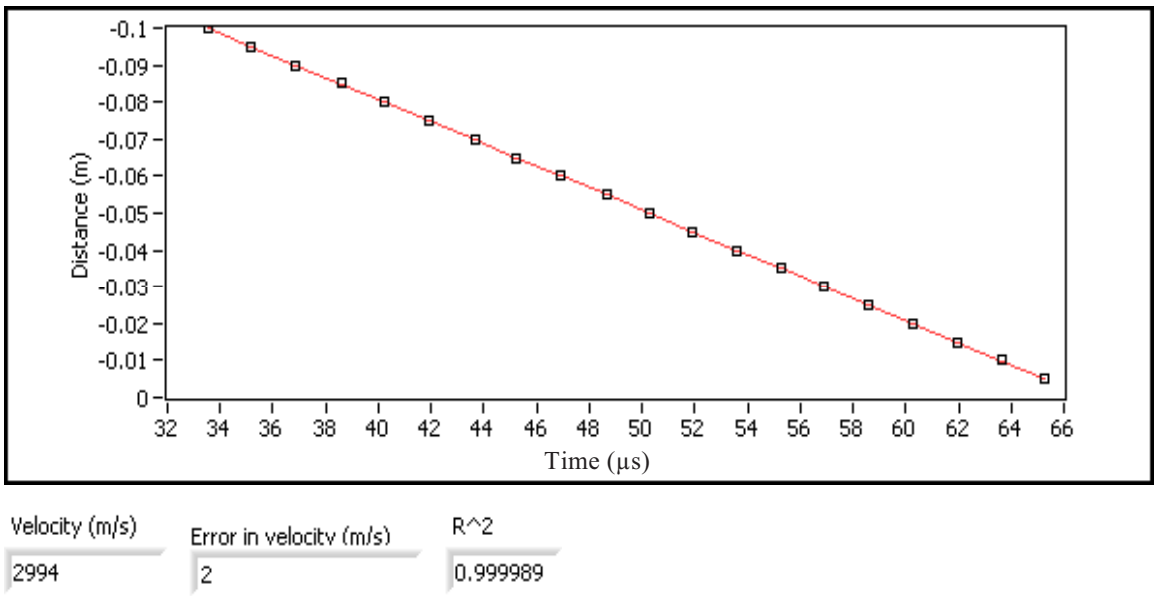

Fig. A1.54: Straight line graph, from LabVIEW, and the associated values from the slope

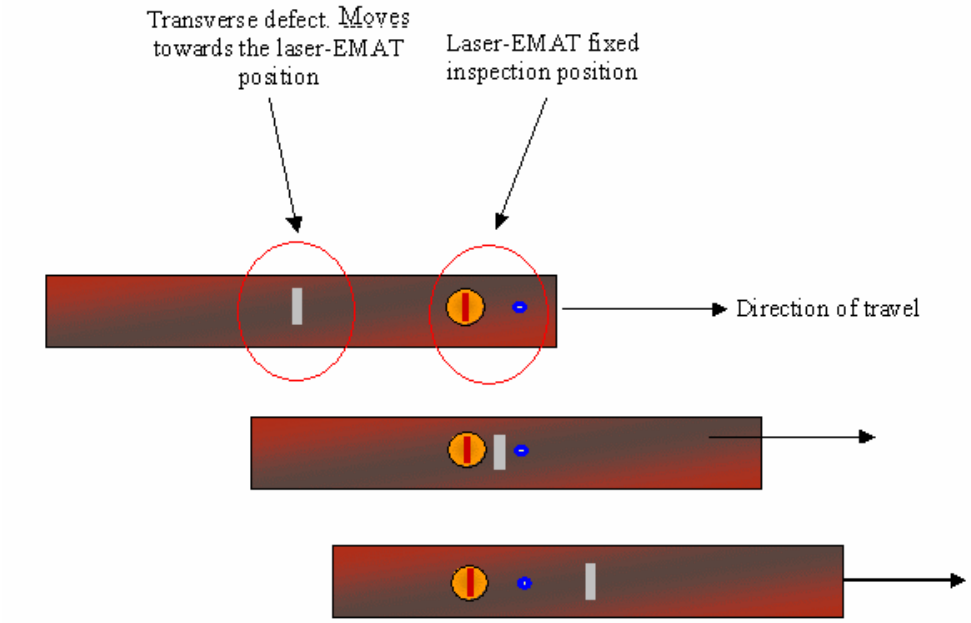

Fig. A1.55: Plan view of the billet, showing relative positions of the fixed laser-EMAT inspection point to the transverse defect as the billet is moved

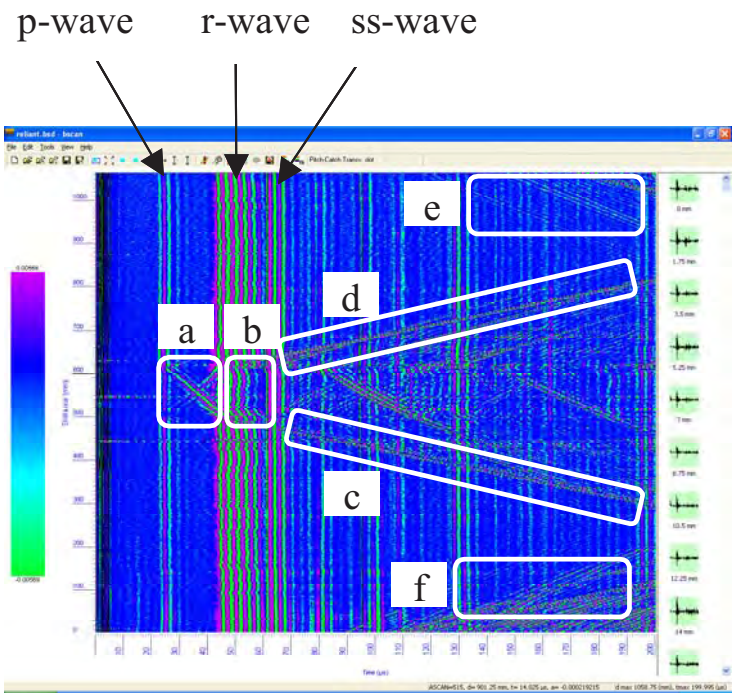

Fig. A1.56: The entire B-Scan

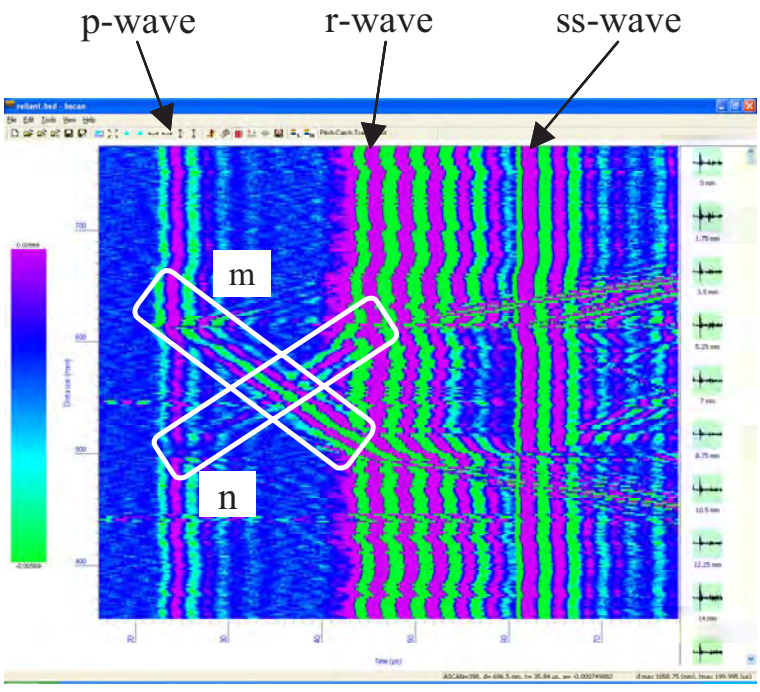

Fig. A1.57: The magnified area of the B-Scan

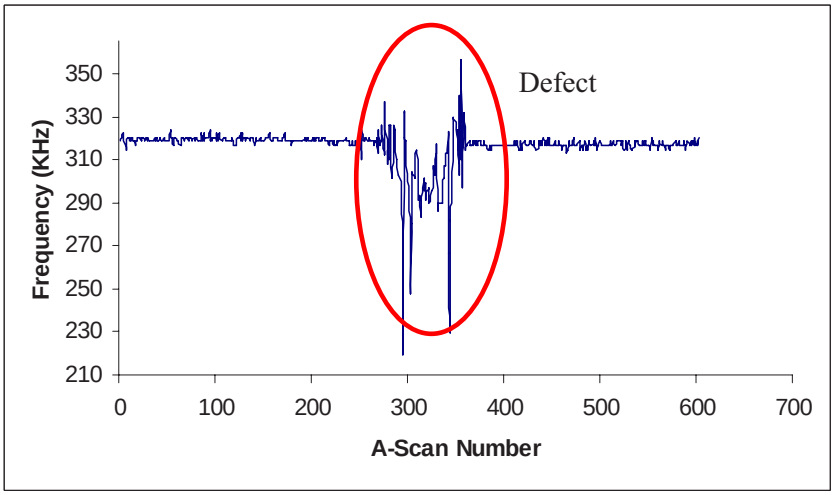

Fig. A1.58: Graph of peak frequency against A-Scan number

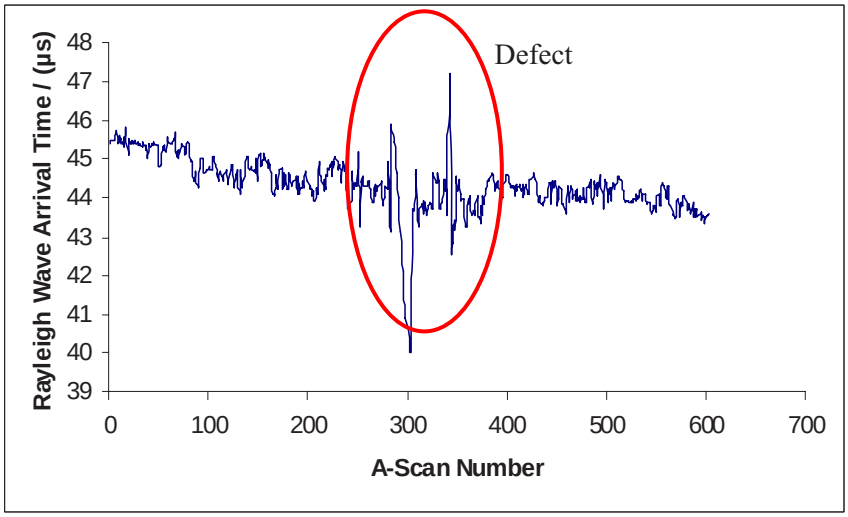

Fig. A1.59: Graph of Rayleigh wave arrival time against A-Scan number

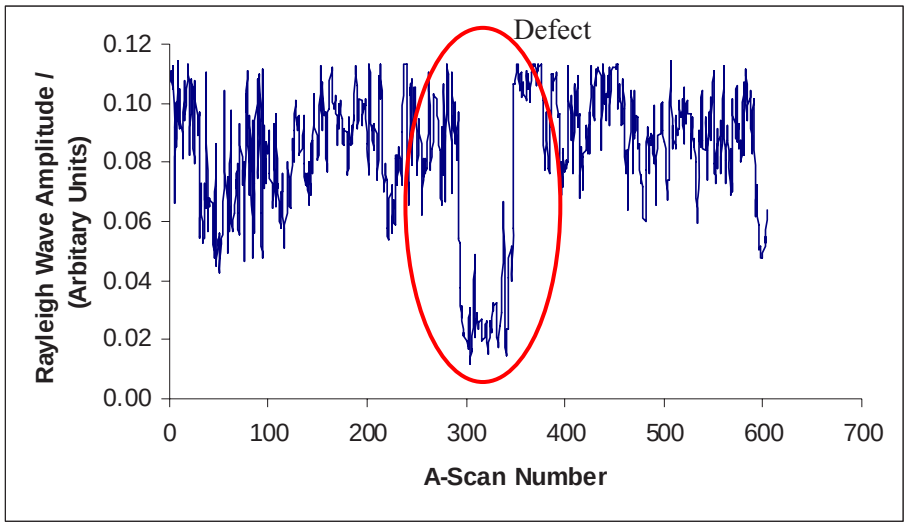

Fig. A1.60: Graph of Rayleigh wave amplitude against A-Scan number

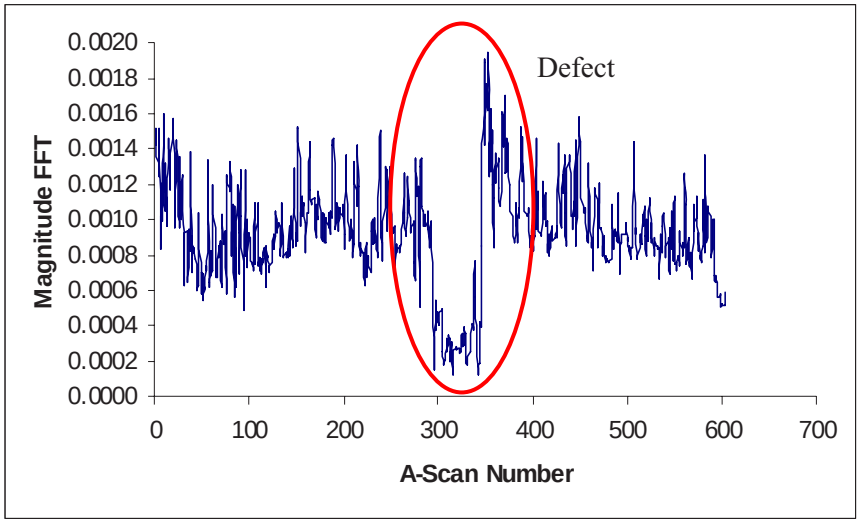

Fig. A1.61: Graph of magnitude FFT against A-Scan number

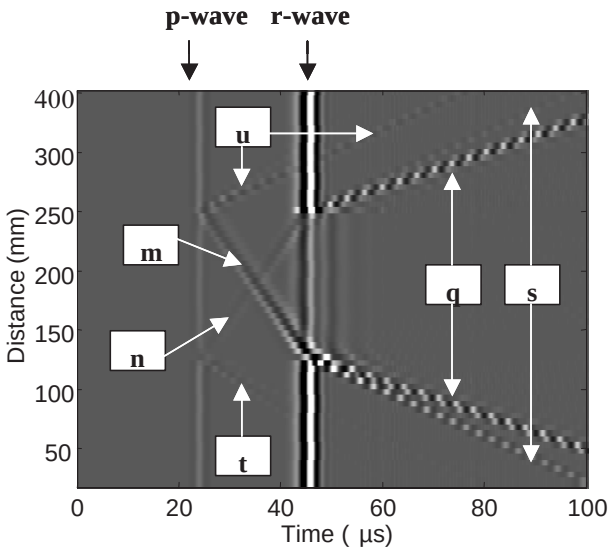

Fig. A1.62: Simulated B-Scan

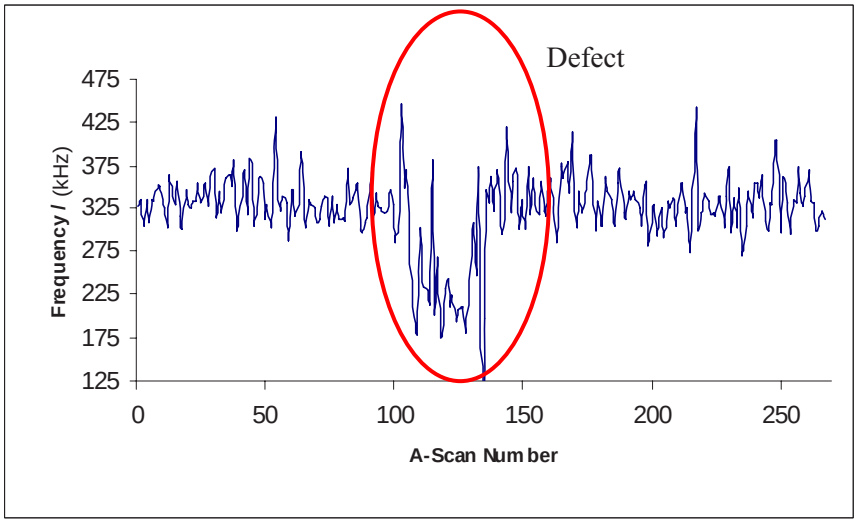

Fig. A1.63: Graph of peak frequency against A-Scan number

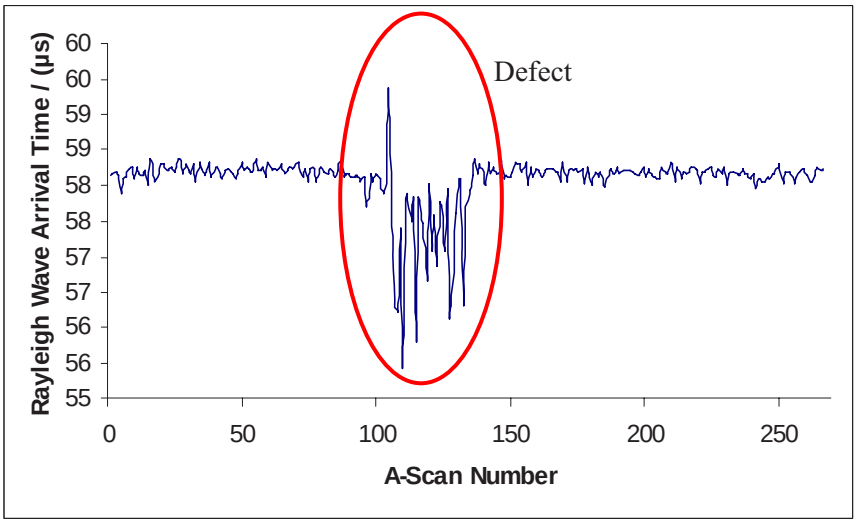

Fig. A1.64: Graph of Rayleigh wave arrival time against A-Scan number

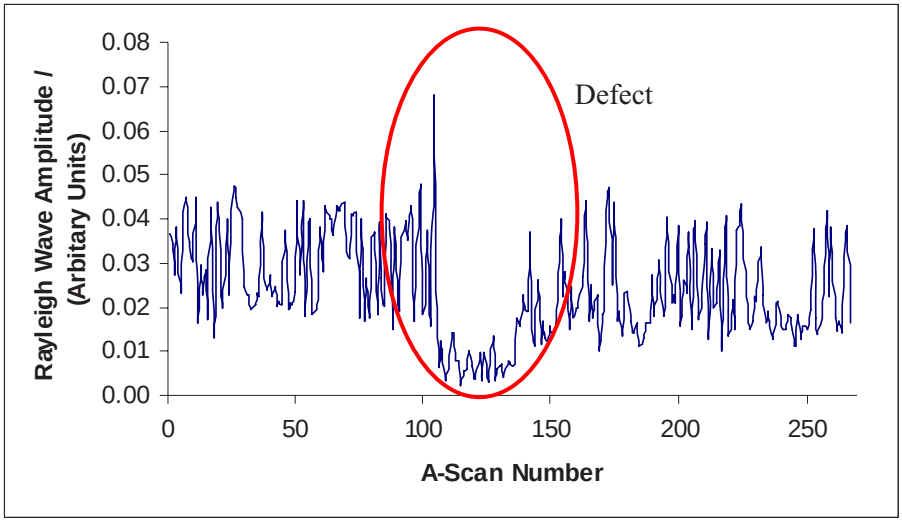

Fig. A1.65: Graph of Rayleigh wave amplitude against A-Scan number

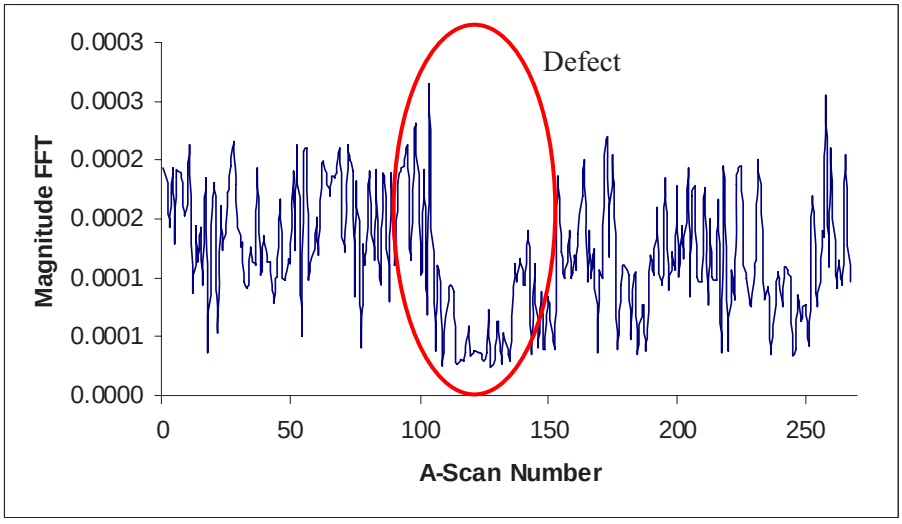

Fig. A1.66: Graph of magnitude FFT against A-Scan number

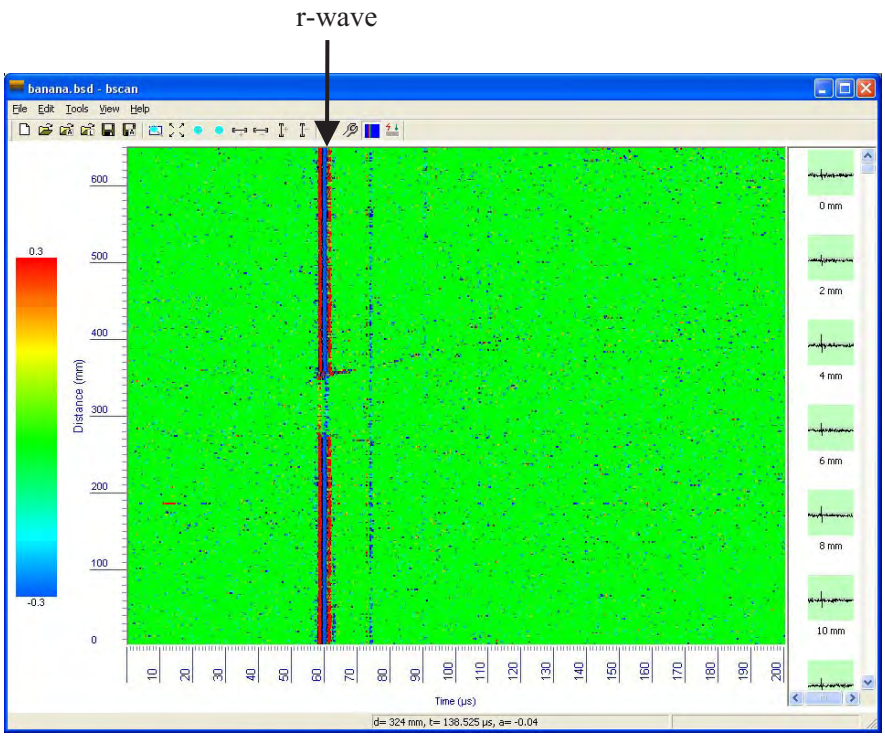

Fig. A1.67: Practically measured B-Scan for a transverse defect

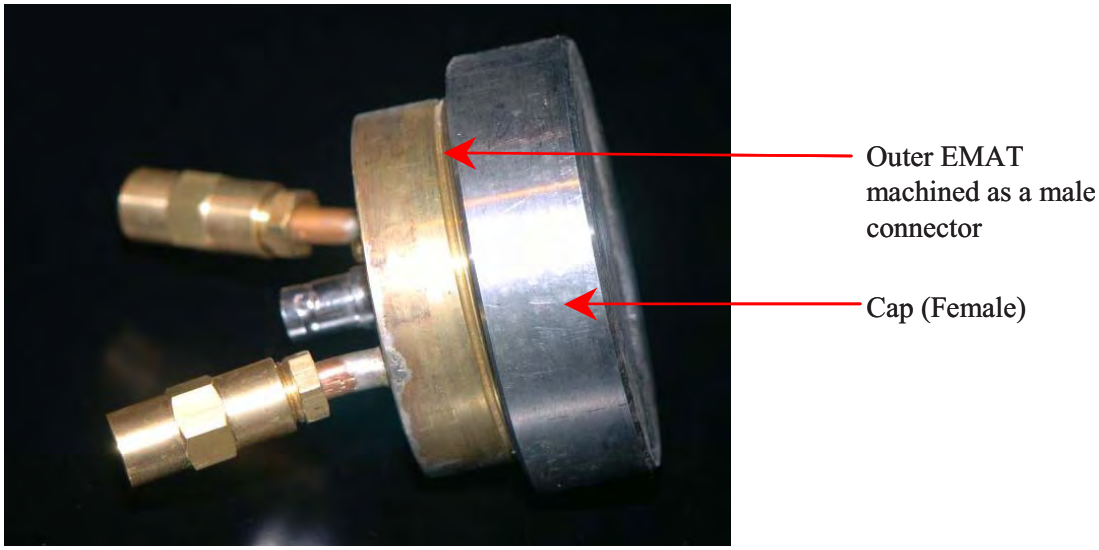

Fig. A1.68: A water-cooled EMAT, with threaded protective cap

Fig. A1.69: A longer billet sample being used to test different ceramic tiles

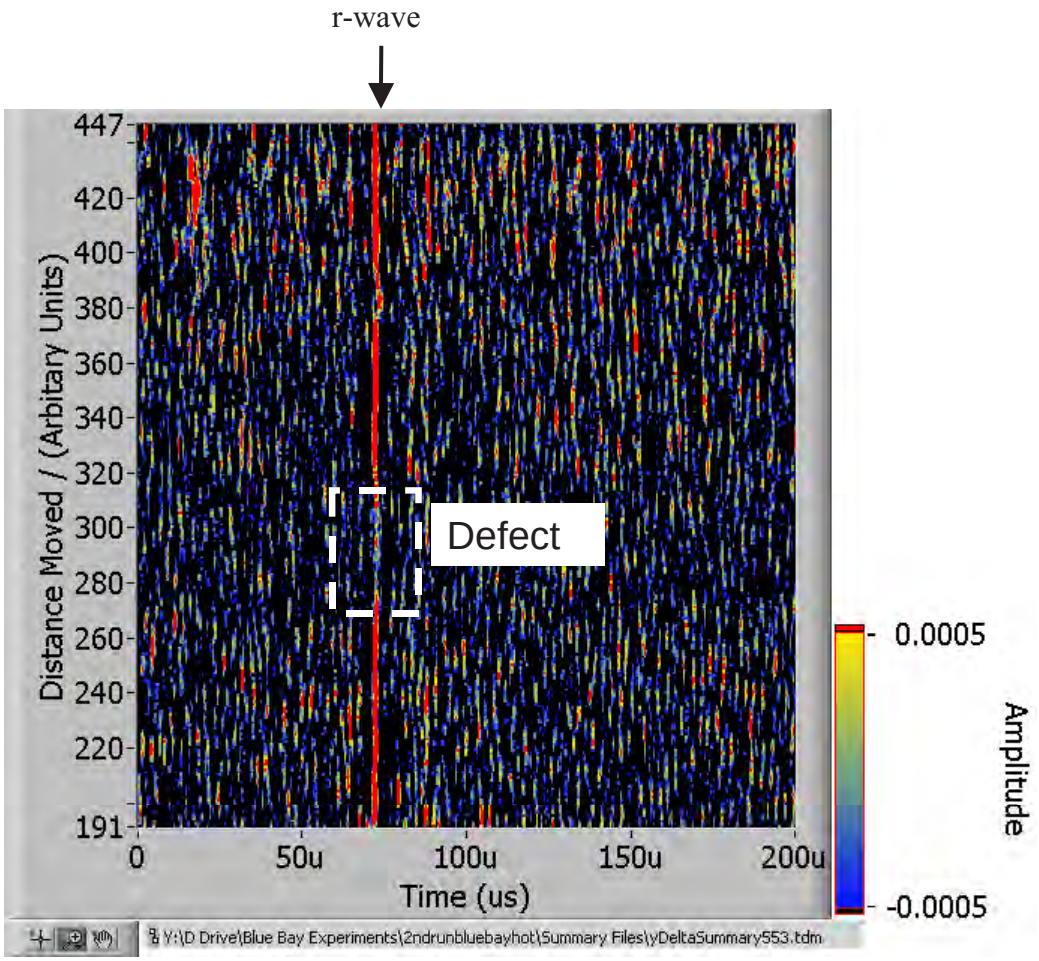

Fig. A1.70: B-Scan taken at 850 °C

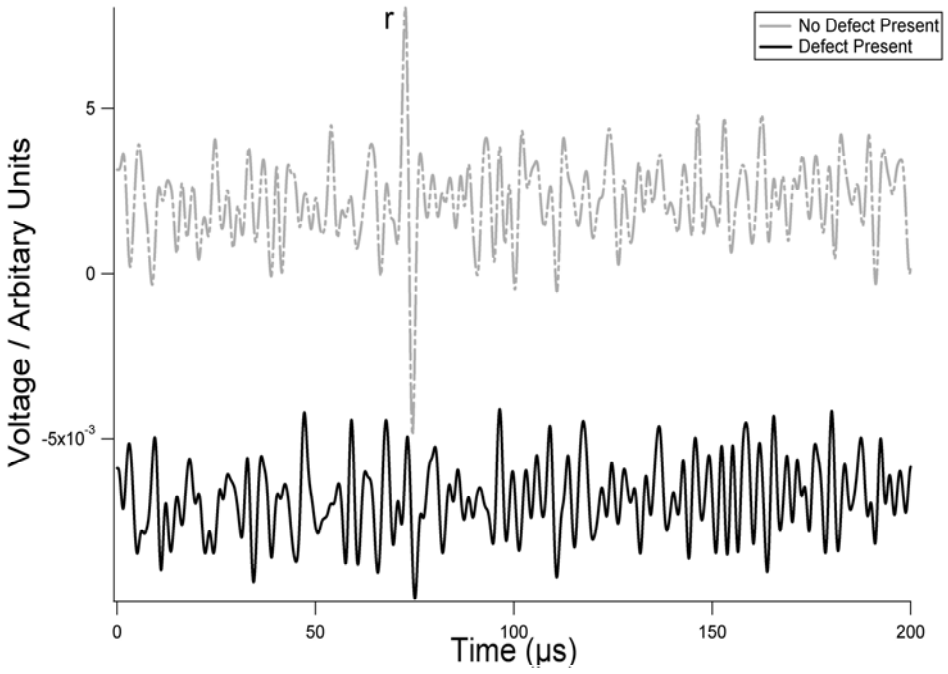

Fig. A1.71: Comparison of two different A-Scans that indicates the amplitude change when a defect is present

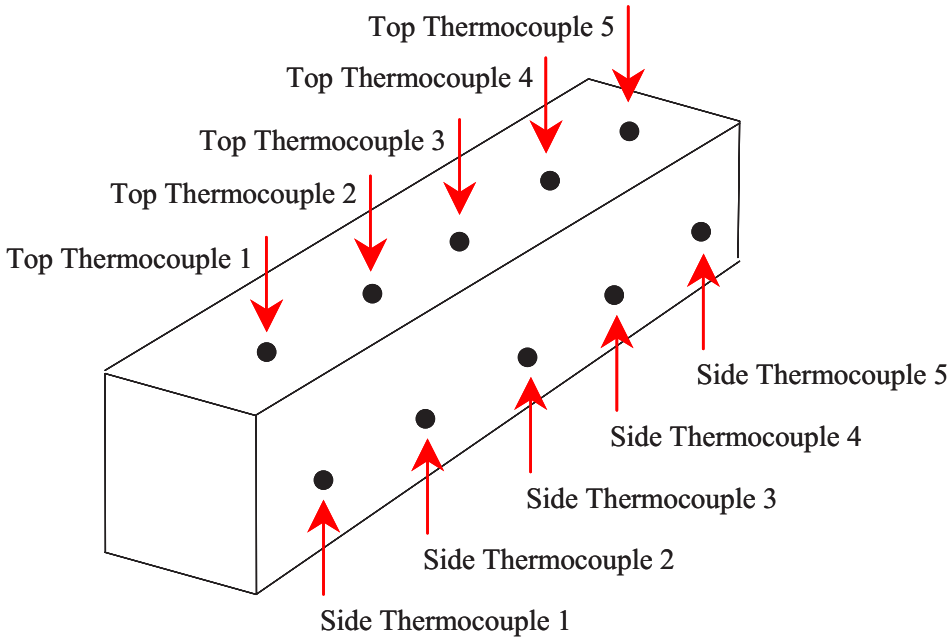

Fig. A1.72: A schematic of the billet, showing the locations of the thermocouples

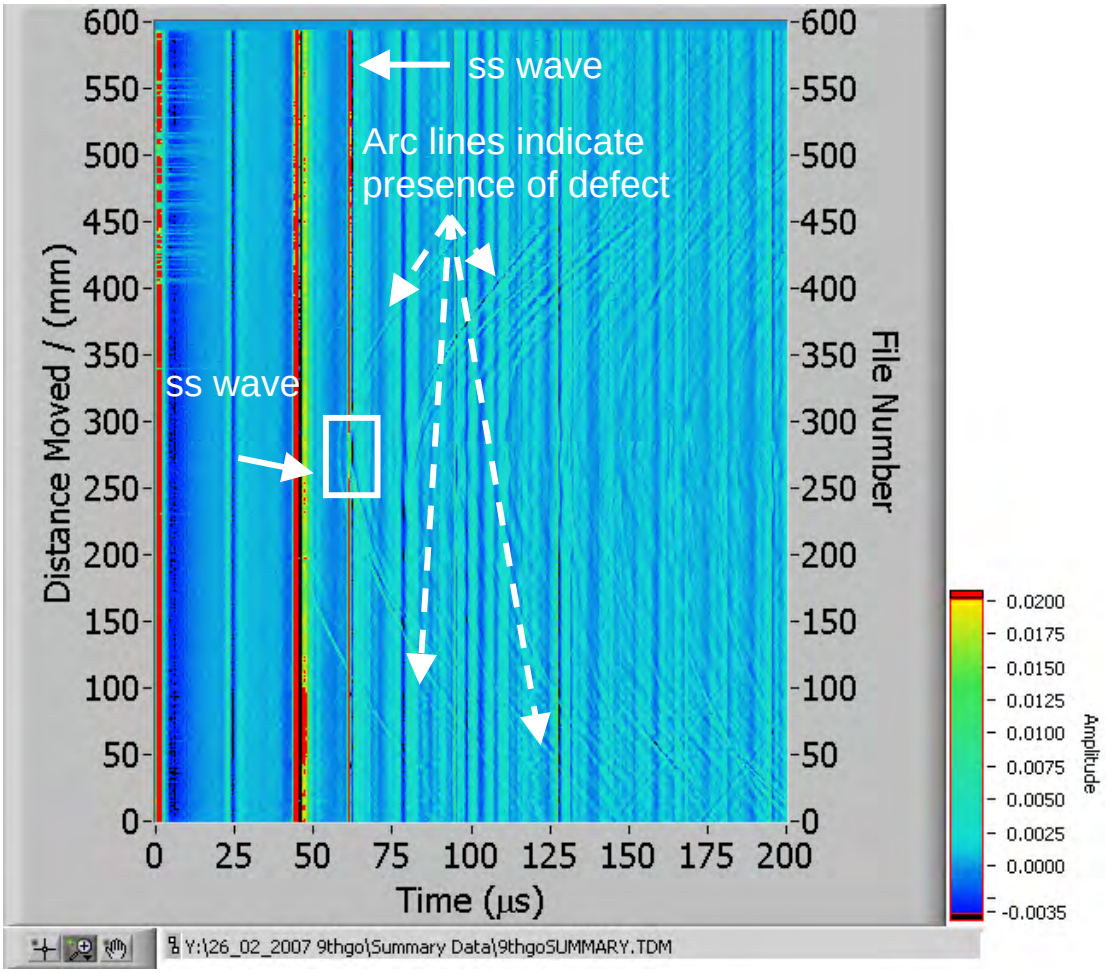

Fig. A1.73: B-Scan showing the energy drop to the ss bulk wave and the reflections from the later bulk waves

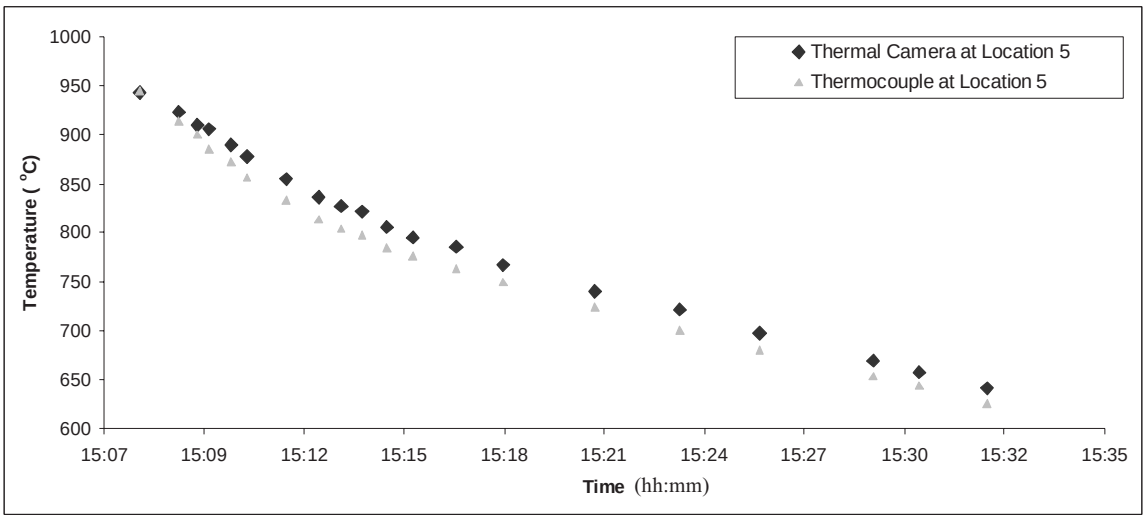

Fig. A1.74: Graph showing a comparison between the thermal imaging and thermocouple temperatures

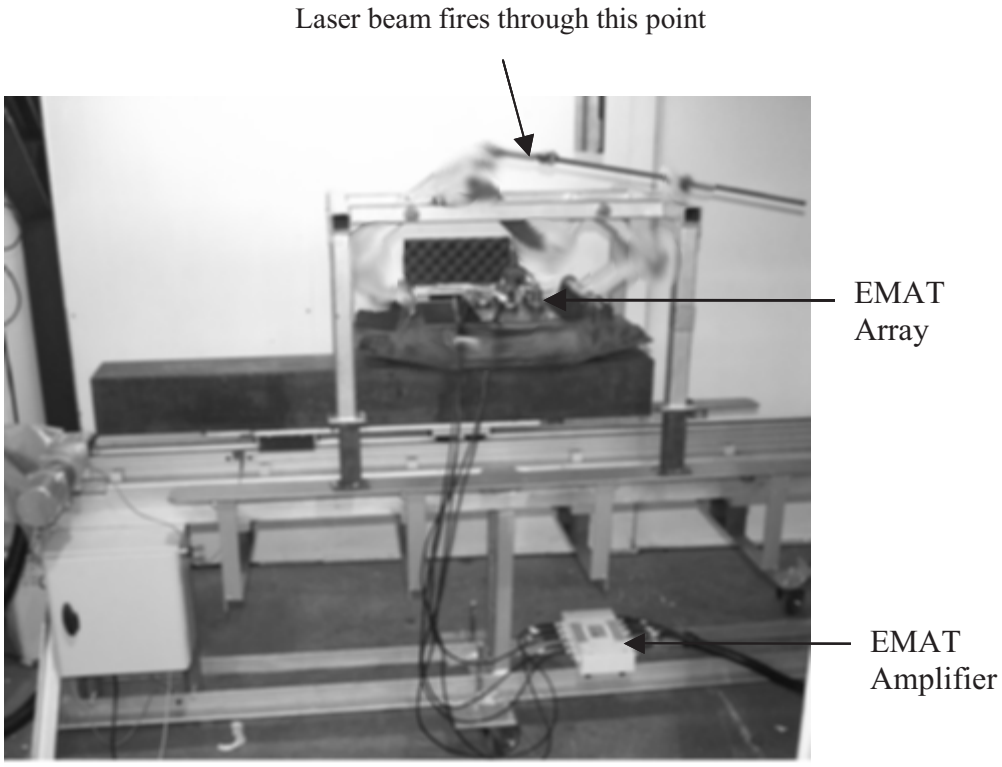

Fig. A1.75: The EMAT array being used to inspect a billet at Teesside Technology Centre

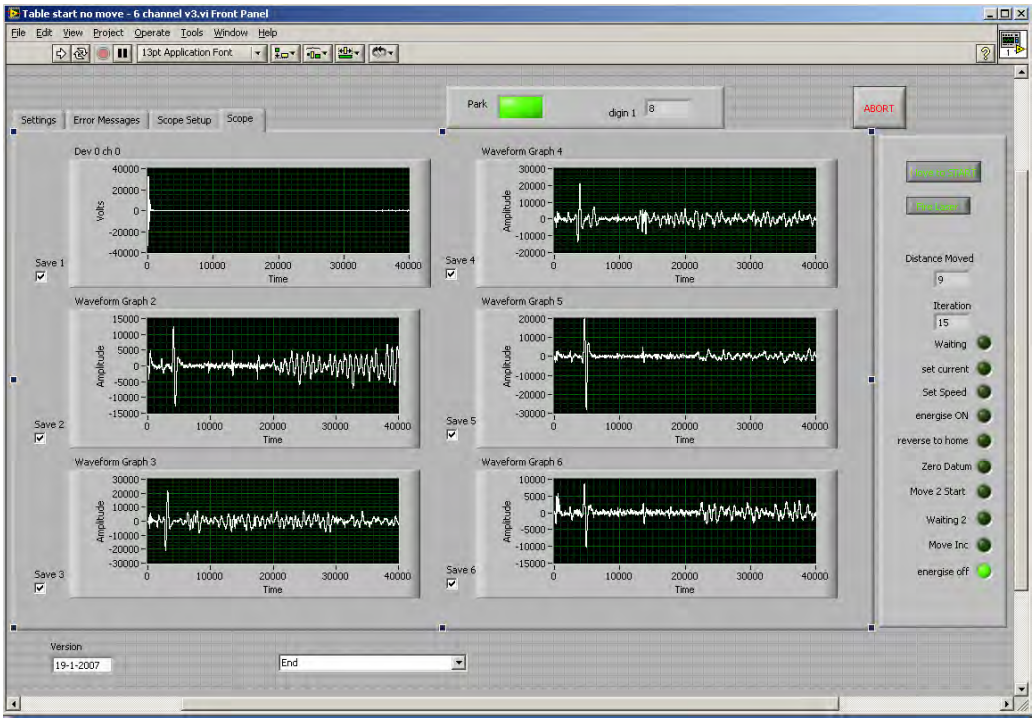

Fig. A1.76: LabVIEW program, used to record data from the photodiode trigger and five EMAT probes

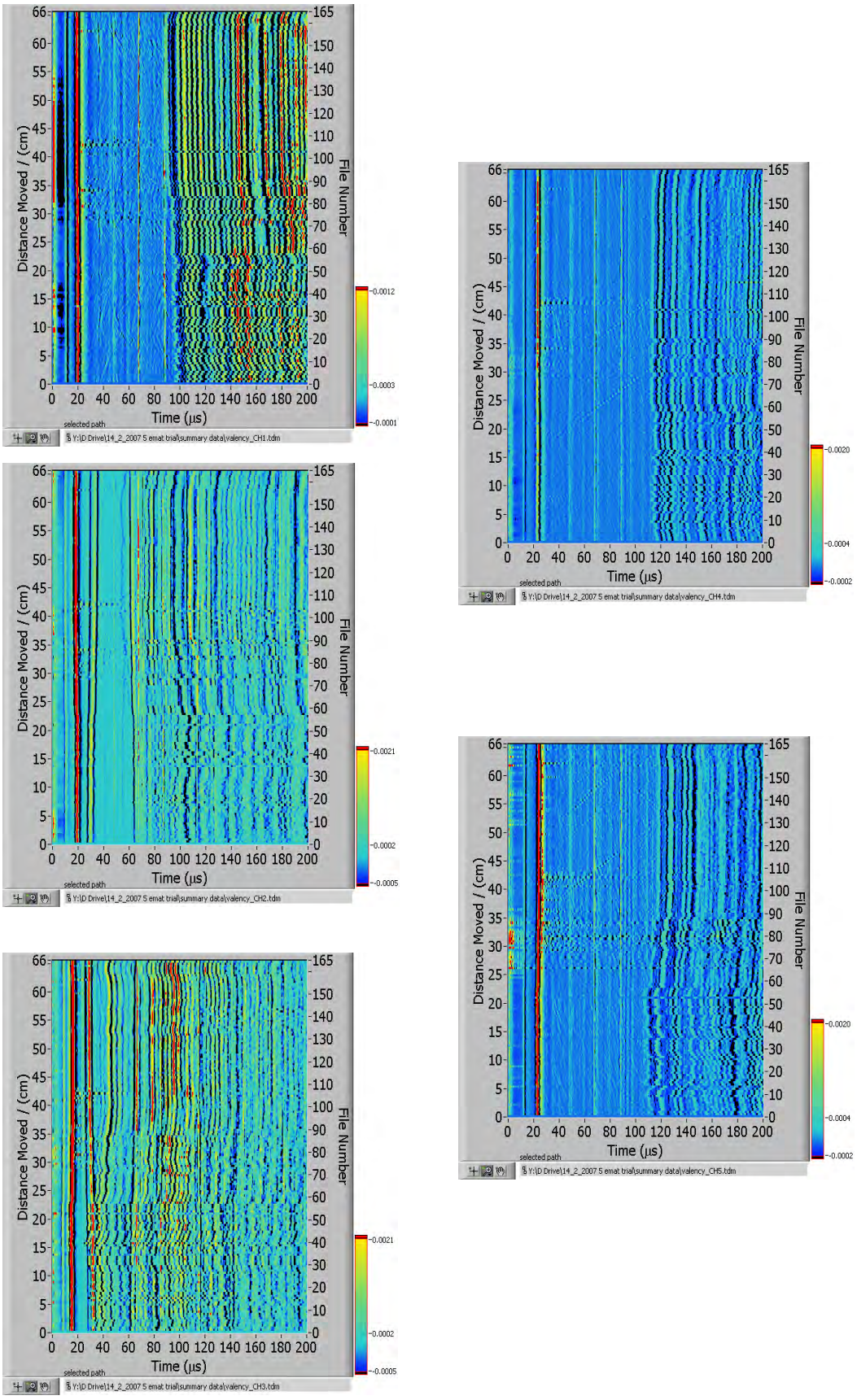

Fig. A1.77: B-Scan output from the EMAT array trial

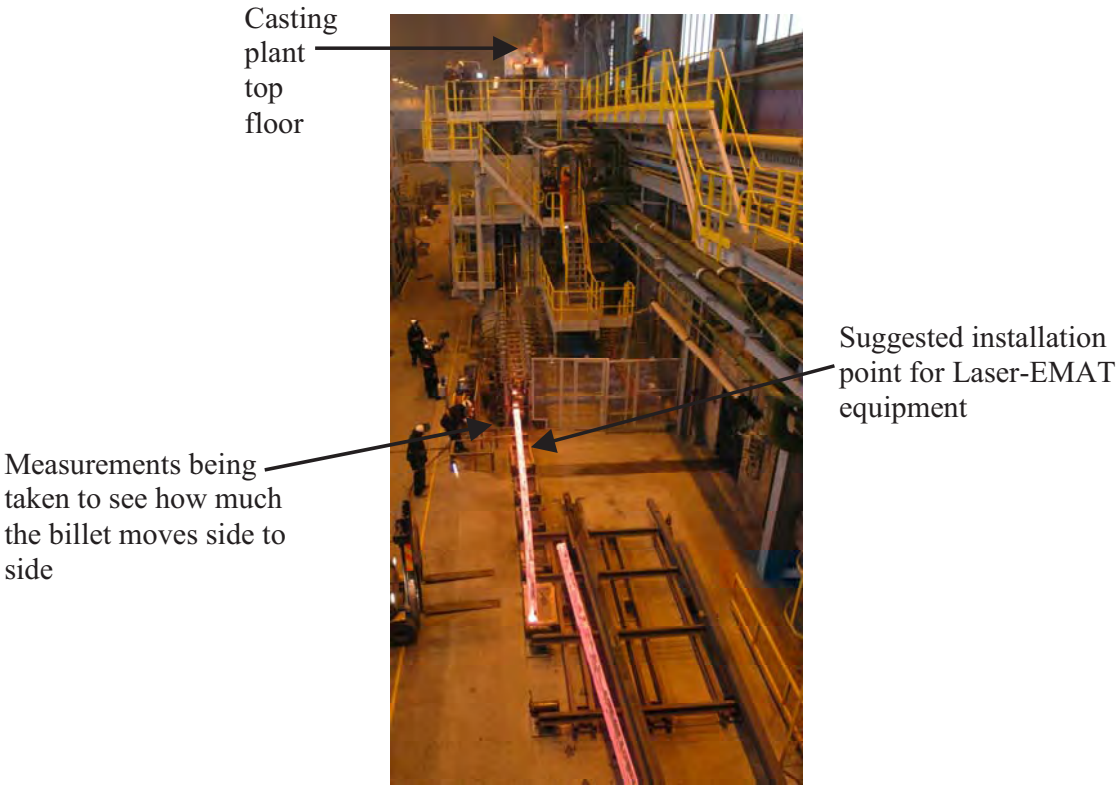

Fig. A1.78a: The newly enhanced pilot plant caster at Teesside Technology Centre

Fig. A1.78b: Side view of the continuous caster at Teesside Technology Centre

APPENDIX 2

SURFACE DEFECT DETECTION WITH CONOSCOPIC HOLOGRAPHY (WORK PACKAGE 1)

A conoscopic holography (CH) system was tested as part of an earlier ECSC project[A2.1]. This system was automated for on-line surface inspection at Arcelor Spain, to detect longitudinal cracks in moving hot slabs, just after casting. Significant improvements have been made to the CH system. Now, large amounts of trial data from casting campaigns have been recorded for analysis. All these developments have made it possible to design and construct a compact system which has replaced the original bulky system. The new system is also capable of inspecting 100% width for both the slab top and bottom faces. All slabs produced in the casting plant are now fed through this inspection system, which is located on Outlet Line No. 3.

A2.1 GENERAL FEATURES OF THE CONOSCOPIC HOLOGRAPHY SYSTEM

The crack detection system uses Conoscopic Holography (CH) which is a long stand-off profilometer sensor. Conoscopic Holography utilises an optical, incoherent interferometric technology that uses the double refraction properties of uniaxial crystals to produce two interfering waves. These waves give a Fresnel figure, where the fringe patterns are related to the distance[A2.2]. In addition to slab surface inspection, Conoscopic Holography has been successfully applied in other areas of process control such as the melt stirring monitoring process for the steelmaking plant[A2.3].

In the casting plant, a map of defects is automatically obtained for each slab that passes the fixed CH inspection point. At Arcelor, the plant is capable of feeding all the slabs, from different casting machines and strands through the CH system. The defects are detected using the distance profiles provided by the CH cameras. A grey-scale image is also provided by a Close Coupled Device (CCD) line scan camera. The long stand-off profilometers[A2.4] are now able to analyse the entire slab width. This enables a surface topography of the slab to be recorded accurately and assessed to detect depressions in the surface that can produce surface cracks (even in the presence of scale).

The system receives information from a process computer regarding the characteristics of the slab which include details such as the dimensions and steel grade. The plant process monitoring computers are linked to the inspection control computer. The slabs passing through the CH system have the following characteristics:

Slab Length:	5.5 m to 12 m
Slab Width:	600 mm to 1600 mm
Slab Thickness:	235 mm or 280 mm
Slab Quality:	All kinds of steel grades
Slab Speed:	20 m/min
Slab Temperature:	600 °C < T < 900 °C
Time between Slabs:	1.5 min
Scale:	Present

The dimensions of the longitudinal crack defects that can be detected are:

Length:	>100 mm
Width:	>1 mm
Depth:	>0.5 mm

A2.2 INNOVATIONS, VALIDATION AND FURTHER DEVELOPMENT OF THE INITIAL PROTOTYPE

The first prototype of the CH system had been developed under a former ECSC Project[(A2.1)]. The system was installed on Outlet Line No. 1, and was able to inspect only the 900 mm central band on the slab top face. The inspected area covered the central two-thirds of the slab, as this is where the majority of longitudinal cracks occur at Arcelor and this is shown in Fig. A2.1. Initially, it was simpler to test the system only on the top face of the slab. However, an accurate quality assessment requires not only automatic inspection of the top face but also of the bottom face of the slab, as statistical analysis has shown that nearly 50% of slabs that have been identified during later processing stages (e.g. scarfing, slab yard, rolling) contained cracks only on the bottom face. Furthermore, it was proven during the ECSC project that the CH system worked to detect other kinds of surface defects such as; roll marks, mould marks and other depressions. These types of defects are often present outside the central two-thirds of the slab that was initially inspected. Therefore it was decided to implement 100% inspection of both the slab bottom and top faces.

Inspecting the entire width of the top face requires the installation of additional cameras and more advanced software to cover the full width. Installing a system for inspecting the bottom face required a different approach to the design and installation of the top mounted CH apparatus, held above the top face. Furthermore, the extraction of data from the inspection system needed to be improved. This was done by enhancing the initial prototype, upgrading computer hardware, enhancing the sensors and developing new software detection algorithms.

A2.2.1 Hardware and Software Developments

The original system was operated by three PCs, but these have now been replaced by industrial computers, as can be seen in Fig. A2.2. This has increased the robustness of the system and provides continuous operation without any hardware or software failures. The data storage capacity has also been increased and several different automatic restart procedures have been implemented. The conoscopic cameras have been updated and tools and procedures for calibration and maintenance have been developed to increase the accuracy of detection.

The cost and maintenance levels have risen due to extending the inspected area to the full surface of the slab, as the number of sensors was increased from three to twelve. Steps have been taken to improve system reliability by using compact PCs with mini-ITX format that utilise solid state hard disks. These disks eliminate any moving parts and moving to a new operating system gave far better stability and control. Because of the change in operating systems, some programs had to be modified. The system now uses newly developed image acquisition software with better drivers which offer an improved ability to interchange cameras or acquisition chips. In addition to this, the sensor housing now contains image acquisition and processing on the same card, which can be integrated in the sensor housing.

The software for the system has been remarkably improved, especially in terms of the automatic detection algorithm development. For example, automatic detection of slab edges has been implemented for both grey-scale images and distance maps. This improvement avoids false error detection at slab borders. Figure A2.3a shows a comparison between the two systems. This introduces an important second benefit in that the width of slabs can be measured on-line, as can be seen for a change in section width, illustrated in Fig. A2.3b. The presence of scale has also been factored into the detection algorithms. These improvements have helped to improve the reliability of the system to distinguish between depressions and cracks. Additionally, they can also give information concerning the casting process and the slab characterisation, such as; width measurements, 'rough surface' assessment, flatness measurements and scale distribution. Detection of closed cracks has also been improved. In some cases a crack appears without the presence of any expected characteristic depression surrounding the area, but this can still be detected using special algorithms for the processing of the grey-scale image. An example of a crack without an associated depression can be seen in Fig. A2.4a. Although the image of the conoscopic camera gives little information about the crack, it can be detected in the grey-scale image.

As can be seen in Fig. A2.4b, a single crack can often appear as a series of small, aligned cracks due to the presence of scale and shape. For this reason, an algorithm has been modified allowing the recognition criteria to be altered when a group of aligned cracks is detected. This allows the system to join individual elements and therefore obtain the real length of the crack.

An important stage in the development work has been to improve the recognition of reference surface contours of the slab. This work was needed as the presence of scale and surface irregularities such as oscillation marks made it impossible to assume that the slab is perfectly flat/uniform. Even across a range of different slabs, a mean 'surface profile' cannot be used due to different manufacturing parameters. Initially, the solution was a polynomial fitted to the surface profile and a general trend was extracted to detail the surface. Two options were considered: (i) one polynomial fit per slab and (ii) polynomial fit based on several slabs. The last solution was the best in most cases, but did not always work in every case. Finally, an iterative algorithm, where the mean surface is obtained and scale removed, was tested and gave better results; these can be seen in Fig. A2.5. This new algorithm improves the detection of a crack when it lies between blocks of scale.

In order to characterise any depression reliably, data from slab inspections were collected and off-line analysis was conducted. Together with manual slab inspection, a significantly large statistical number of slabs have been analysed using both the on-line system and via manual inspection. From these data, detected depressions have been divided into three categories; 'cracks', 'probable cracks' and 'not cracks'. Relevant data for these have been extracted from the topographic images in order to establish an automatic method to determine the relevance of each depression. The length of the crack, average depth and standard deviation of the depth are all used in the main program's parameters in order to give good results for defect classification (Fig. A2.6).

With these parameters, a set of fuzzy rules has been established that gives a relevance value to each depression, ranging from 0 to 100, where thresholds can be defined easily in order to detect only 'very relevant cracks', 'less relevant', or 'all'. This new system was tested and the classification system did not reject any relevant 'real' cracks and the rate of false defect detection was subsequently reduced from 28% to 18%. With the new system, slabs can now be sent directly to the next process, thereby eliminating the need for manual inspection. This saves significant manpower costs, whilst offering the advantages of automated systems.

A2.2.2 Plant Test and Validation Results; Comparing the Automatic CH System to Manual Inspection in the Slab Yard

A large, systematic comparison between the results from the automated CH system and those provided by manual, visual inspection was carried out between September 2004 and September 2006 on 3000 slabs. A total of 70,000 slabs were automatically inspected during the referred period.

After the slabs have cooled for three days, an inspector manually marks on a paper template of a slab any locations of cracks that were found. The resulting defect map was then compared with the results provided by the automated system. If a large discrepancy arose, the slab was held in the slab yard and a detailed visual inspection was carried out in order to measure the characteristics of the cracks and any associated depressions so that the origin of the discrepancy could be assessed. For example, was it from an error that the defect was missed?, or a software recognition problem? This process is illustrated in Fig. A2.7. The results of both inspections are stored in a database together with relevant casting process data and special events for subsequent analysis. This task, although time-consuming, proved to be a useful way for improving the performance of the CH system and tracking defects.

At the end of the validation and improvement process, the automated inspection and crack recognition system was demonstrated to detect 99.5% of cracks successfully, with only a 10% level of over-detection. It should be noted that the system was tuned for over-detection.

A2.2.3 Development of the Inspection of the Bottom Face of the Slab

In order to ascertain the functionality of a bottom face CH system, a prototype was designed, built and tested on-line. Figure A2.8a shows a schematic for the new installation of the bottom face CH system. This work involved building a system that was air-cooled and protected from the radiated heat by using a mineral wool blanket. Because the system is located underneath the slab, it needed to be protected from falling scale by using a window through which the laser light would pass, as shown in Fig. A2.8b. An air supply has been connected to keep the window clean of any contaminants. Figure A2.9 shows the bottom face inspection unit installed in the plant in its final position.

The optimal distance between the lasers and bottom slab surface is 1.2 m. However, the current layout of the steel plant would involve digging a pit underneath the slab to enable the lasers to be positioned directly under this inspection point. As this is impractical, the laser beam is fired horizontally, before it is bent upwards at a 90º angle to make the beam vertical, by using a mirror. This allows an optical path distance equal to that for the top inspection point. Although there were some refraction problems caused by the hot air around the slab, this has been solved through the use of forced air convection by the use of fans. However, there are some other technical aspects that make bottom face inspection easier. One is that the bottom face of the slab tends to be cleaner, as loose scale falls off easily as it passes over rollers. Another is that the slab bottom will always be 1.2 m away and therefore optical displacement technology does not need to be implemented when the slab thickness is changed (unlike the top inspection system, which does require this, when the thickness is changed).

Two factors can affect the results expected from the bottom side:

- Dust, burrs and scale can fall from the slab onto the protecting windows (through which the laser beam is emitted), and this results in problems due to damage and reduction in visibility.
- For practical reasons regarding the amount of available space, a solution with two 45º mirrors was needed, so that the light path was bent through 90º.

The system has been installed for six weeks in order to check the amount of dust and debris falling and obstructing the windows. It has been seen that using the 45º window, with a continuous air flow, reduces the dust lying on the view port. A 4-weekly clean is sufficient and can be conducted as part of standard plant maintenance operations.

The 45º mirrors and external windows were made of materials that were specially selected after checking several factors. The laboratory results have shown little performance losses due to the introduction of these additional optical elements and a comparison between the presence of these materials and the existing optics can be seen in Fig. A2.10. The detectable loss is mainly due to optical transmission losses through different transparent materials, but this effect can be reduced by increasing the output power from the laser system.

Problems with chunky swarf thrown by the nearby deburrer have been a problem, as these are thrown at high speed and have caused damage to the view port window (in these trials, a window was broken in the first week of use). A solution to protect the window was tested in the laboratory using narrow metallic strips. The addition of these strips does not significantly impede performance. In addition to using the metallic strips for structural integrity, a metallic mesh could also be installed.

The development of the inspection of the bottom face of the slab, together with the extension and improvement of the initial prototype (Fig. A2.11) has allowed the design and construction of a final robust system which is used to inspect both wide faces of slabs produced in the four strands. Figure A2.12 shows the system in operation in Outlet Line No. 3. Typical results from the new slab inspection are shown in Fig. A2.13. The installation of the final system was only completed in the last month of this project. In the first week of operation no cracks have been found, but the images provided by the conoscopic sensors have improved their quality compared to those obtained with the initial prototype.

A2.3 REFERENCES

A2.1 Obeso F, Sancho L F, Alvarez I, Díez A, Sirat G, Falesi R: 'Novel on-line surface quality control for hot slabs in continuous casting', La Revue de Métallurgie, March 2002, pp267-275

A2.2 Sirat G Y, Psaltis D: 'Conoscopic holography', Optics Letters, 10, 4, 1985

A2.3 Diaz J, Sancho L F, Alvarez I: 'Application of conoscopic holography to control melt stirring', La Revue de Métallurgie, March 2006.

A2.4 Alvarez I, Enguita J M, Fernández Y, Marina J, Fraga C, Sirat G: 'On-line defect detection with the long-standoff conoline profilometer', 2nd International Conference on Metrology, Eilat (Israel), Nov 2003

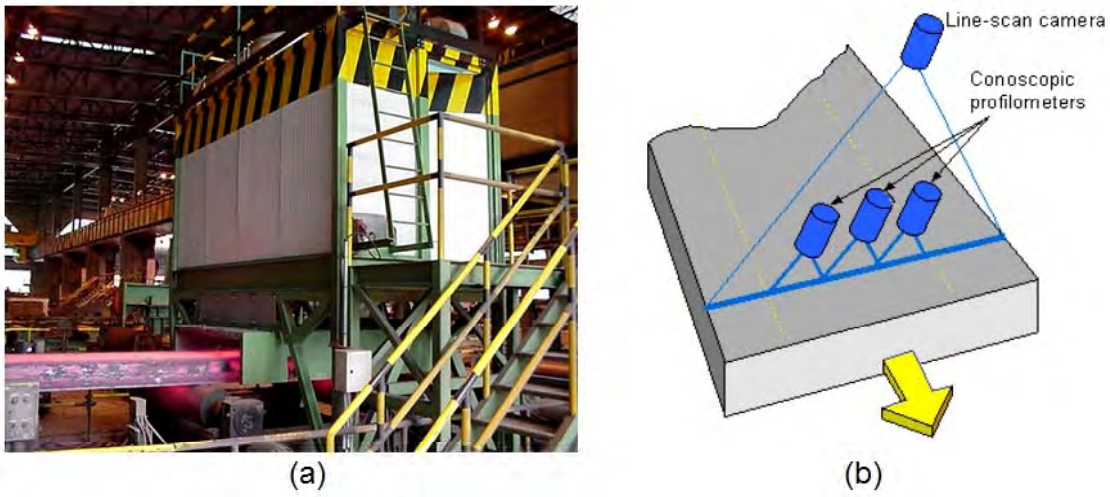

Fig. A2.1: Initial surface inspection system as was installed on plant at Arcelor:
(a) external view of the inspection chamber and (b) arrangement of cameras for slab surface inspection

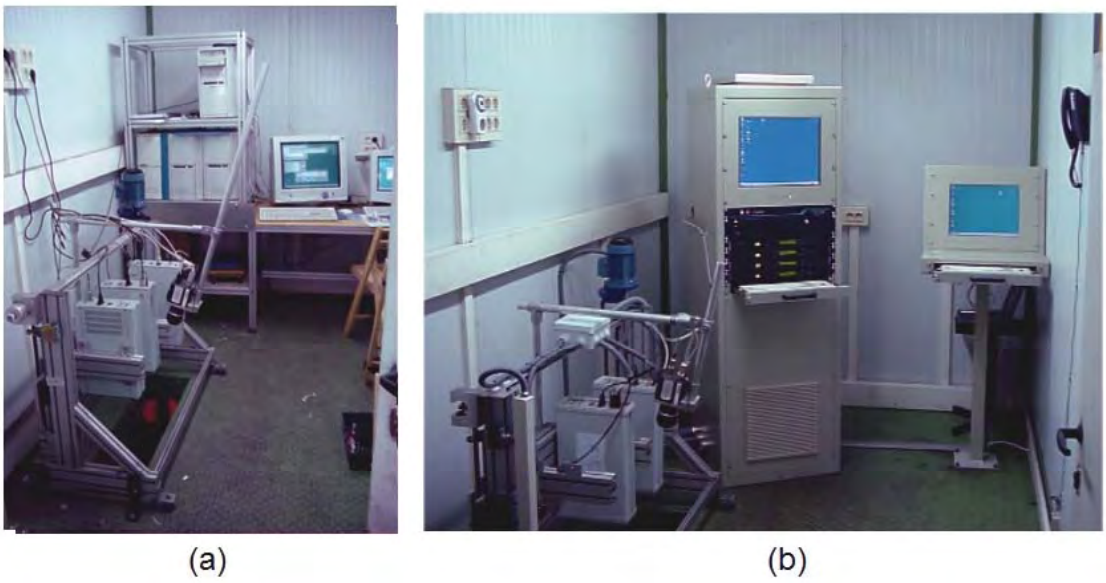

Fig. A2.2: Internal view of the initial surface inspection system at Arcelor:
(a) first version with PCs and (b) second version with industrial computers and monitors

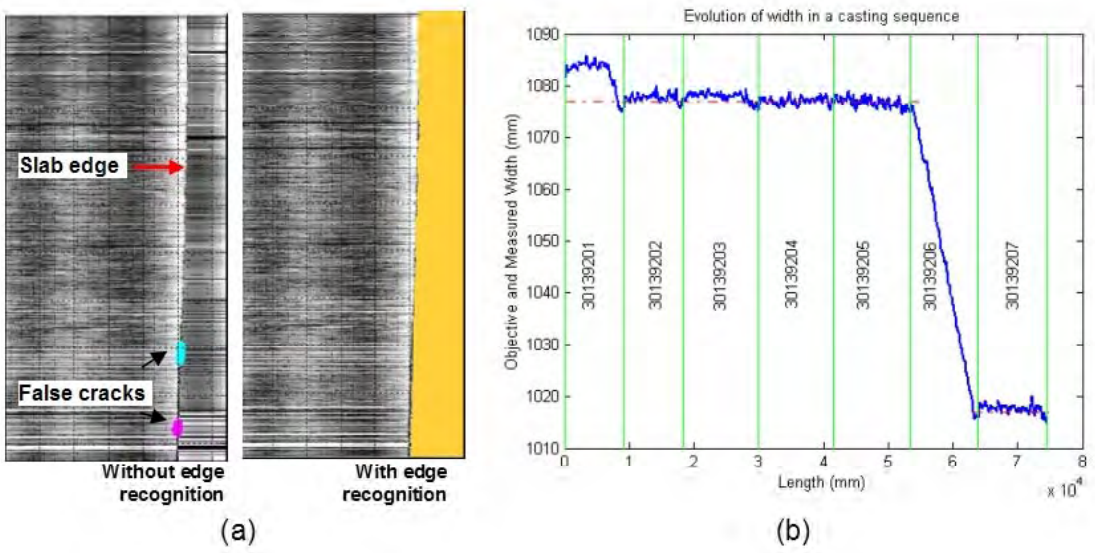

Fig. A2.3: Benefits of automatic edge recognition:
(a) elimination of false detections and (b) on-line width measurement

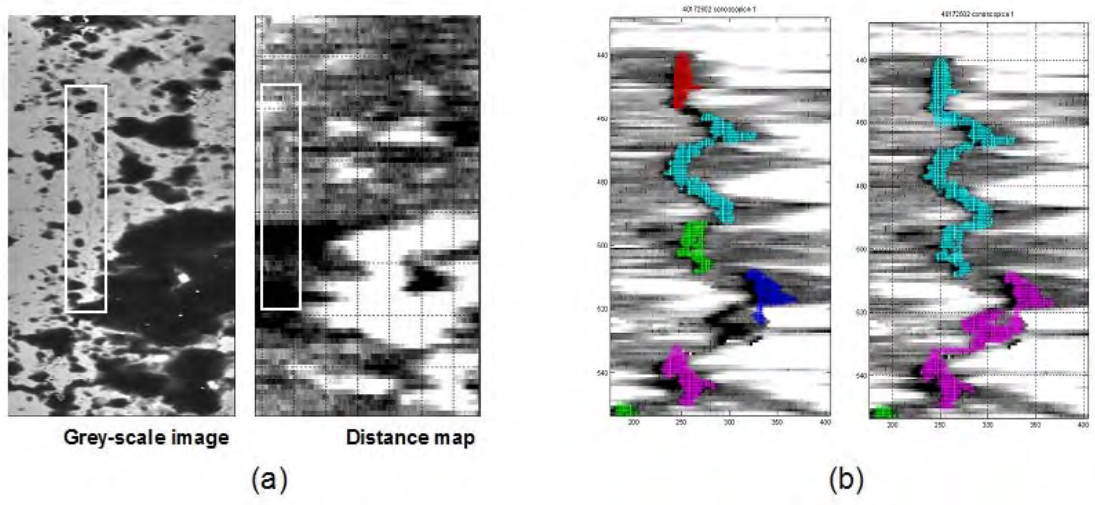

Fig. A2.4: Other improvements to the algorithms:
(a) recognition of a closed crack in the grey-scale image, and
(b) joining of the individual elements of a crack to obtain the real length of the crack

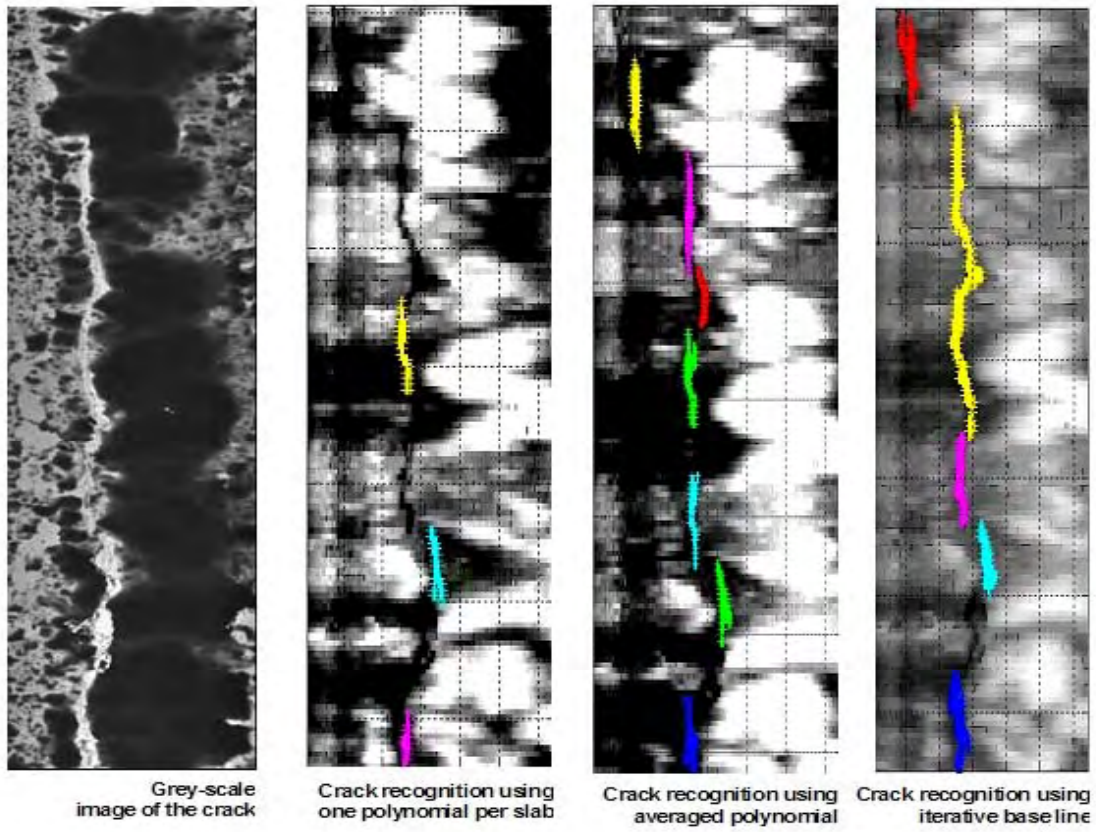

Fig. A2.5: Results of crack detection using different algorithms for the detection of the base surface of the slab

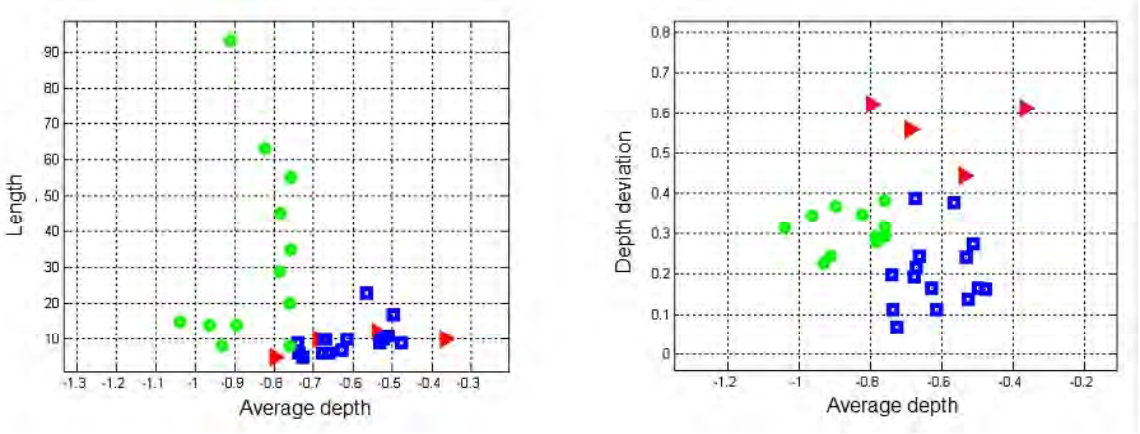

Fig. A2.6: Plots of parameter combinations for relevant depressions (circle), less relevant (square), non-relevant (triangle), as defined by visual inspection of the slabs

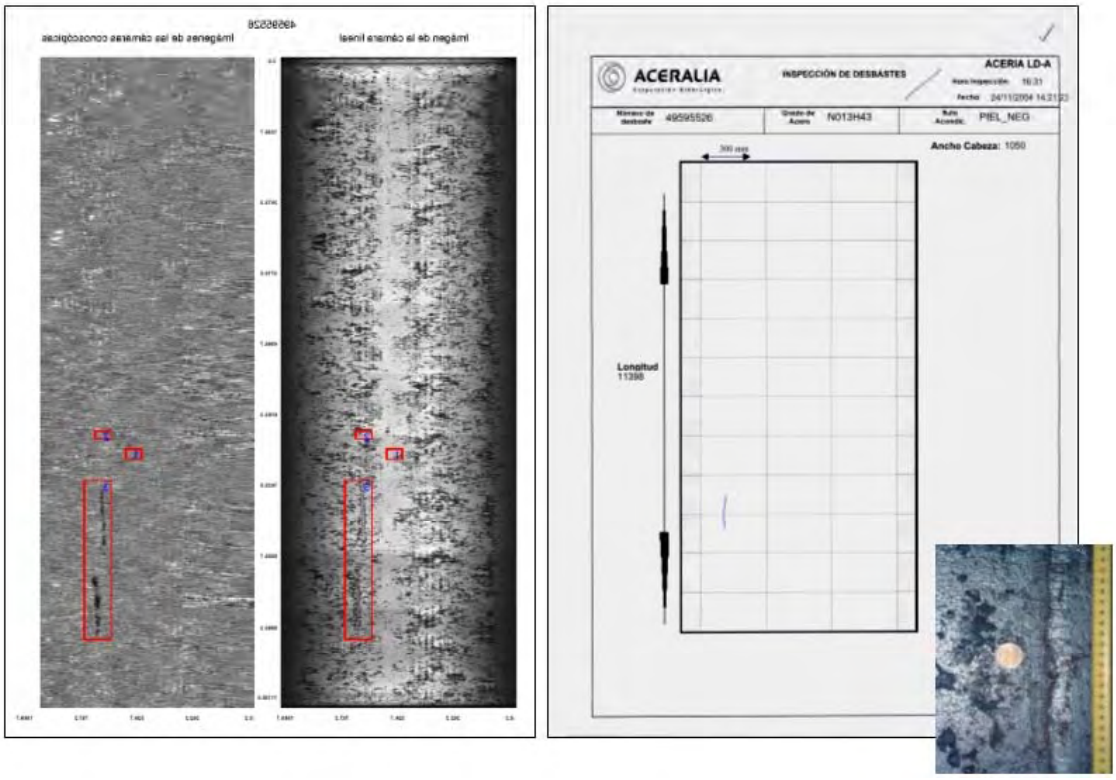

Fig. A2.7: Comparison of the automatic inspection map (left) with the manual template used by the inspector (right); both maps reveal the existence of a longitudinal crack A.
A detail of the real crack is also shown

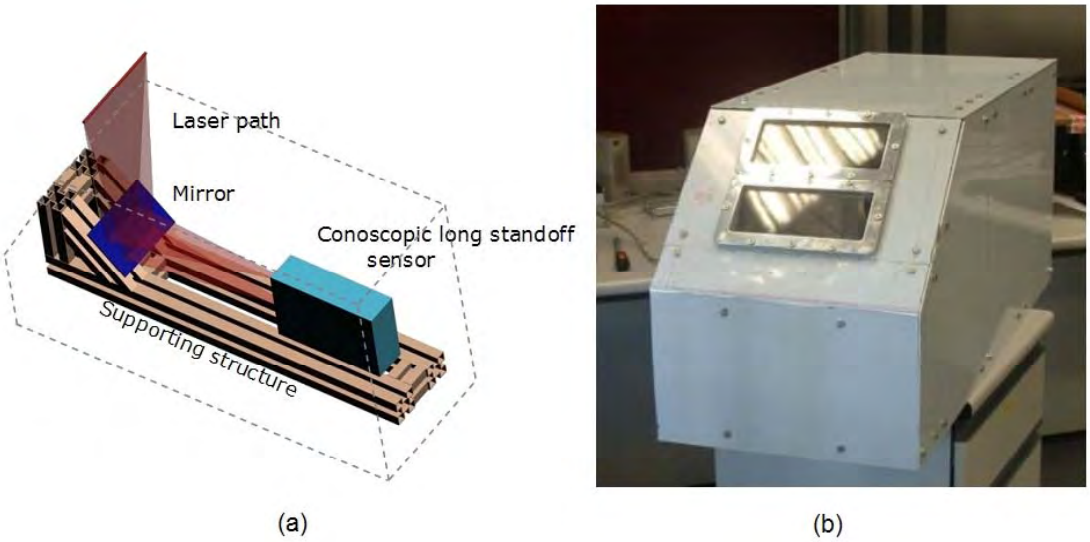

Fig. A2.8: Set-up of the conoscopic sensor for slab bottom face crack inspection:
(a) arrangement of elements and (b) external view showing the glass windows

Fig. A2.9: Plant installation at Arcelor for bottom face crack inspection
The structure with the sensor is placed underneath the strand, with a thermally insulated shield on top of it and a fan to provide fast moving, cool air

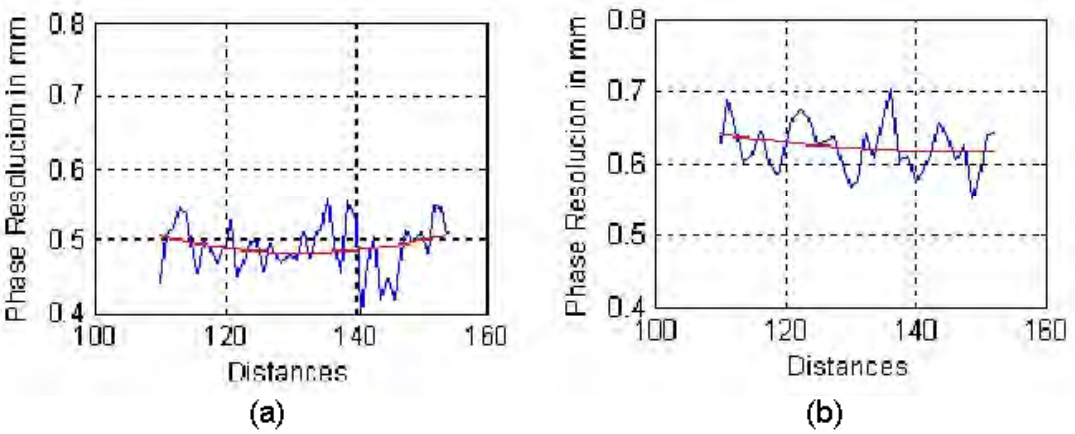

Fig. A2.10: Comparison between the resolution of the sensors:
(a) direct configuration, and (b) mirror and window configuration

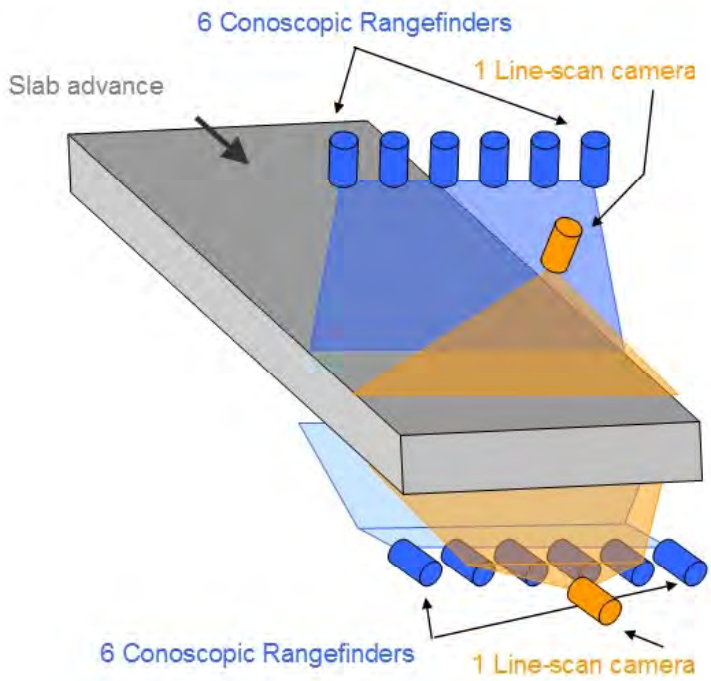

Fig. A2.11: Schematic of the final surface inspection system at Arcelor, showing the arrangement of cameras for slab surface inspection

Fig. A2.12: External view of the final surface inspection system in operation on the steel plant

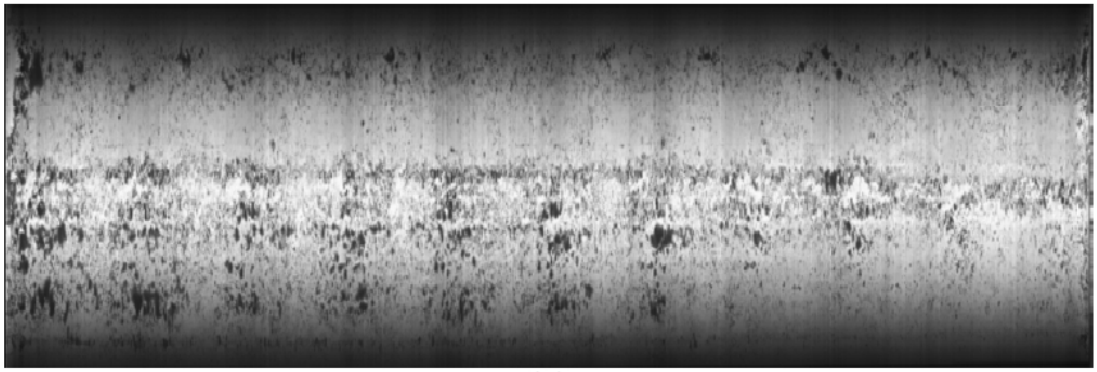

(a)

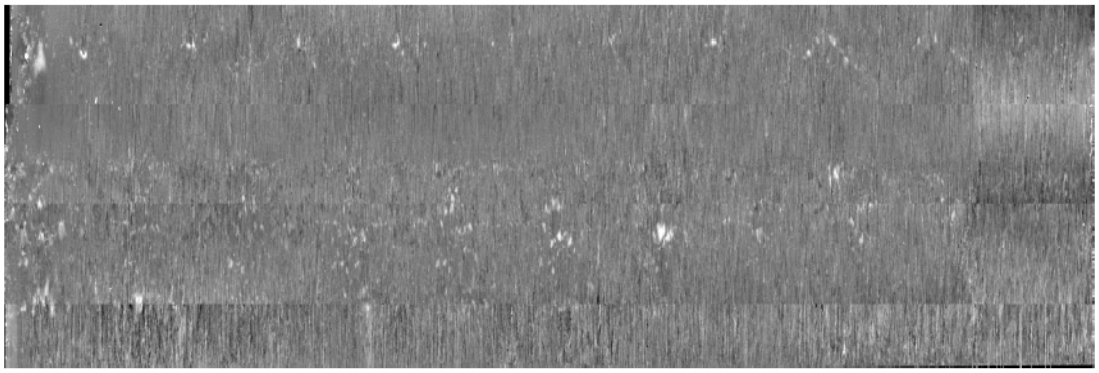

(b)

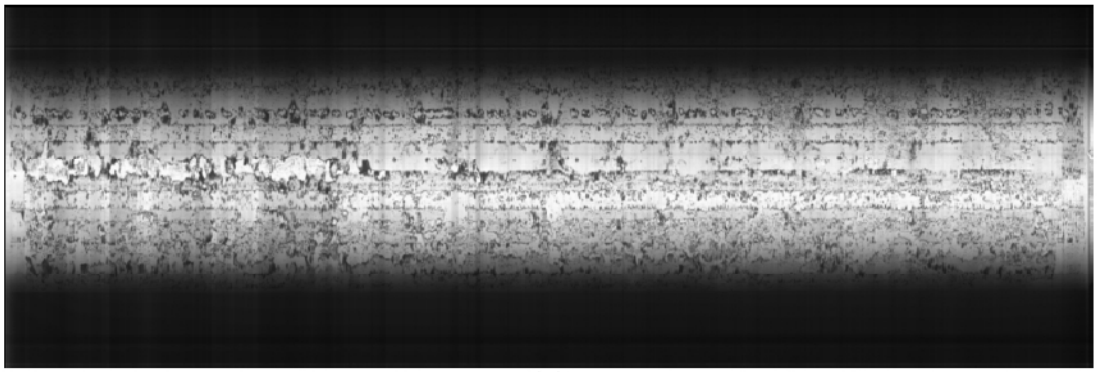

(c)

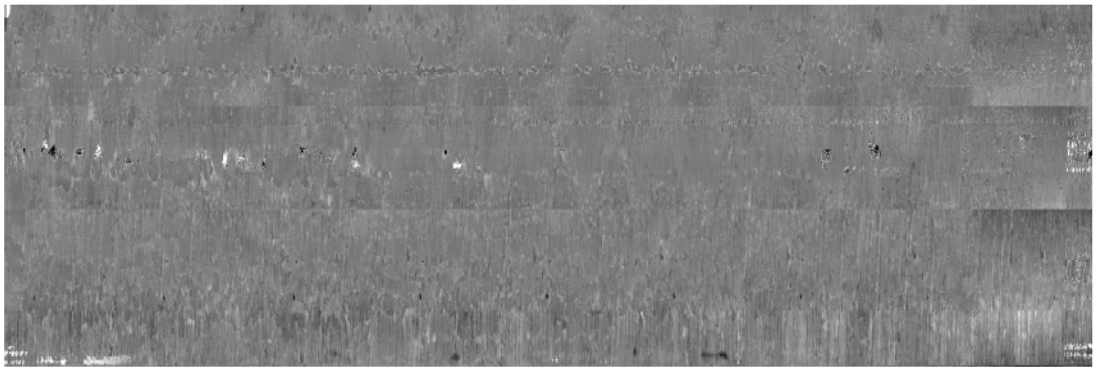

(d)

Fig. A2.13: Surface inspection of a slab with the final system:
(a) grey-scale top, (b) distance map top, (c) grey-scale bottom, (d) distance map bottom

APPENDIX 3

DEFECT DETECTION FOR THE SCARFING AREA (WORK PACKAGES 1, 3-5)

In order to verify the quality of scarfing and to reduce costs and the levels of manual scarfing, it is necessary to minimise the amount of human intervention between casting and the subsequent processing of semis. This can be achieved by using an automatic inspection system to verify that slabs are of sufficient quality to bypass human intervention. This system could also be used to validate and replace mandatory human inspection of certain steel grades which were always historically checked for quality after scarfing. The following areas of automated inspection have been researched with the target of reducing the amount of scarfing:

i. Burr detection
ii. Subsurface inspection before scarfing
iii. Surface inspection after scarfing

A3.1 MACHINE VISION SYSTEM FOR BURR DETECTION

At Arcelor, it has been noted that burr, a result of the torch cutting process, can be found at the start and the end of slabs and this may lead to intermediate inspection and rectification. (Burr can lead to later problems in the rolling mills.) Despite the best efforts of the manufacturers of torch cutters, burr can be 20 mm to 30 mm wide[A3.1]. Burr can be removed by scarfing or with a machine deburrer. Although the deburrer has an inbuilt system to detect its own functionality, it cannot notify operators if slabs still have burr after they have been supposedly de-burred.

Therefore, an automated system to inspect slabs after they have been de-burred has been built and tested. This system uses a machine vision system to examine closely the start and end of a slab as it moves past a fixed inspection point over a roll. This system detects whether burr is still present, by seeing if the slab is lifted off the roll as the burr lifts the slab up. The system is capable of monitoring and alerting if the slab goes beyond a certain angle of tilt because of this lift. When no burr is present, the slab should be flat and not be tilted as it passes over the roll. A photograph of this system, mounted above a roll can be seen in Fig. A3.1.

This system is based on monochrome CMOS (Complimentary Metal Oxide Semiconductor) cameras that view a 180 mm x 50 mm region. The software is capable of logging data when a slab is present and acquires images at a constant rate. The software then compares regions 1 and 2, as highlighted in Fig. A3.2. The system is designed to seek horizontal edges inside these two regions and via a series of algorithms calculate the slab angle. By averaging and comparing results before and after the slab passes the roll, an output can be calculated and plotted. Figure A3.3 shows sensor output when the slab is at an angle (i.e. burr is present) compared with the usual shape, when no burr is present.

It is hoped to leave the camera system installed to monitor the performance of the deburrer on-line and feed back to the process operators. All the slabs with burr have been correctly identified and the evolution of deburrer performance can be monitored. A 5% level of false detection was given by the system on the slabs, but these can be attributed to the last part of the slab passing over the roll. The algorithm is being refined such that this will no longer pose a problem.

Figure A3.4 shows the results of continuous burr detection for several days worth of data logging.

A3.2 AUTOMATED SUB-SURFACE INSPECTION BEFORE SCARFING

The sub-surface inspection of hot moving slabs at Arcelor is performed using an off-line automated plane tool, which removes a small surface strip on the slab surface allowing inclusions and pinholes to be detected using automated visual inspection. This off-line tool is shown operating in Fig. A3.5. This system is an enhancement to a prototype (constructed in ECSC Project No. 7215 (Surfin'CC)[A2.1]) that has been fully automated and improved in several ways. The condition of the slabs passing through the

sub-surface inspection system is the same as for the case of the surface CH inspection system. To achieve automatic visual inspection, a CCD camera has been motorised and is controlled by the same computer as the planing tool. This allows changing the position of the planed strip at will. For example, samples can be taken from the middle or the edge of the slab. The software has also been improved and it is possible to mesh together partial images to obtain one unique image for each inspected strip, which is shown in Fig. A3.6. The automatic recognition for the edge of planed strips has also been made in order to avoid false defect detection outside the strip. Another important improvement is the calibration of images for not only detecting, but also classifying inclusions and pinholes by their size and relative position, i.e. cluster formations.

Different sensors (such as stress sensors, accelerometers and thermocouples) have been mounted with the planing tool. Software for data acquisition and signal processing has also been developed. This provides information on the features of the cleaning system and has been used to obtain the optimum operating parameters (such as the velocity of the slab, width, depth, etc).

An ancillary mechanical device for sampling has been designed and constructed. The device is illustrated in Fig. A3.5 and is used to remove the steel strip that has been planed so that it can be sampled and analysed for inclusions.

A3.3 AUTOMATED SURFACE INSPECTION AFTER SCARFING

At Arcelor, it is hoped to link the quality of coils, found by downstream inspection systems such as Parsytec, back to the slab yard and the scarfing process. It is hoped to establish a link between the difference in product quality when the slabs are scarfed and not scarfed. Currently 100% of the scarfed slabs are operator inspected after scarfing. A reliable, automated inspection system would therefore be very useful as it would avoid operator intervention and associated costs.

A3.3.1 Defects in Slabs and Automated Inspection of Slabs After Scarfing

Currently surface defects are still found after scarfing and can be categorised into one of the following main areas:

(i) Inclusion/Pinholes. This is not a result of poor scarfing, but rather can be linked to problems arising in the casting mould.
(ii) Black skin areas (areas missed by the scarfer). These defects are caused when flame torches from the machine scarfer are not working efficiently (or do not work at all).
(iii) Narrow and deep grooves generated by poor quality scarfing. Again, this is an issue with regard to the flame torches not working correctly in the scarfer.

Should any of these defects be present after scarfing, the slabs are often re-scarfed either using the machine scarfer or by hand. At each point after scarfing, the slabs are always manually inspected. Inclusions and pinholes cause the majority of problems in downstream processes, so these defects were tackled as a priority.

An automated system for inspecting slabs after scarfing would minimise manual inspection and lead to the possibility for hot scarfing straight after torch cut-off in the caster which would mean that hot charging could be possible, therefore saving significant costs on reheating furnaces and reducing detrimental quality and metallurgical issues which result from using these reheat furnaces.

Therefore, to inspect slabs automatically, the following approaches have been investigated:

1. Slab shape inspection using triangulation techniques
2. Feasibility testing for inclusions and pinhole detection using different inspection techniques.

A3.3.2 Shape Inspection of Scarfed Slabs using Triangulation Techniques

A new line scan optical system has been developed to examine the surface of slabs after scarfing. This new system makes it possible to relate the features of the slab surface to the quality of the rolled product, thereby identifying the effect of scarfing on the final product and removing the need for manual visual inspection.

In the laboratory, a system for mapping the surface of the scarfed slab was developed. A solution based on conoscopic holography was rejected due to the high cost of the required sensors. In this case, since the semi is colder and its surface is cleaner, it is possible to construct a profilometer at a lower cost, based on a triangulation technique as shown in Fig. A3.7. Here, two laser line sources illuminate the slab surface at an angle and two CMOS cameras record the change in the illuminated line as the slab passes underneath. An interferential filter in front of the camera permits only the arrival of light equivalent to the laser wavelength to pass through. The obtained images are then processed to obtain a surface map of the slab. Using this technique, it is possible to map the surface with a resolution of 1 mm in the transversal direction, 5 mm in the longitudinal and 0.5 mm in depth. A laboratory prototype, later modified an installed on plant is shown in Fig. A3.8 and was constructed in order to check the feasibility of the system. The characterisation of a rough surface with this prototype is shown in Fig. A3.9.

Software for reliably detecting the laser line in acquired images has been developed. This system works very well provided that the slab surface is sufficiently clean. When scale is present, the laser light is diffused and results in a low light level being detected by the camera, therefore giving poor results. (The scale can be removed, which gives far better results.)

After the results obtained in the laboratory and the feasibility tests in the plant, a prototype system for on-line inspection of scarfed slabs has been installed on-line, as can be seen in Fig. A3.10. The system is based on a machine vision triangulation system, using 2 280x1024 Complementary Metal-Oxide Semiconductor (CMOS) monochrome cameras and a 665 nm 10 mW laser for triangulation. This system has been installed to inspect slabs after the machine and manual scarfing, covering 1000 mm slab width.

The aim of this system was to obtain the size of the grooves in the scarfed surface and to relate these dimensions to possible problems with defects after rolling. As automatic tracking of slabs is not available in this part of the line, the newly developed system uses a web camera for automatic capturing of the slab number. The system worked well for a long period of time. However, due to poor background light, and motion blurring, the camera does not always capture the slab number, despite the triangulation system detecting the presence of a slab. A screen capture from the camera is provided in Fig. A3.11. Improvements are being made to overcome this problem and correlate the information from the inspection system with downstream quality results.

Figure A3.12 shows several examples of results obtained with this inspection system. Here it can be seen how surface quality can change depending on the scarfer condition. This type of information provides a fast tool for evaluating scarfing quality.

A3.3.3 Feasibility Testing and Comparison of Different Technologies for Inclusion and Pinhole Detection After Scarfing

Different techniques have been investigated for potential on-line inspection use. The objective is to detect the inclusions and pinholes that may remain in the slab after scarfing. Both inclusions and pores are detectable as they leave a small crater in the slab surface after scarfing. The techniques that have been investigated and trialled are:

i. Grey level CCD camera
ii. Infrared thermography
iii. Laser triangulation

iv. Conoscopic holography
v. IVP-Ranger camera
vi. Grey level CCD camera with infrared lighting
vii. Spectral camera

Tests have been conducted in the scarfing yard with scarfed slabs (for techniques i and ii) and in the laboratory (for techniques iii to vii), which were all conducted on the same sample of scarfed slab.

The results of each technique are discussed below and can be summarised in Table A3.1.

(i) CCD Camera Inspection

A monochrome CCD camera was placed above a scarfed slab and different illumination techniques were tried. For example, brightfield and darkfield configurations were tested at both narrow and wide angles.

None of these tests were satisfactory. The inhomogeneous slab surface, different angles of the scarfed paths and small particles of scale made it too difficult to correctly configure the camera system. There were also problems with obtaining suitable illumination.

(ii) Infrared Thermography Inspection

Most of the problems with the CCD camera system were overcome through the use of an infrared thermography camera. Here, the illumination comes from infrared emission from the scarfed slab itself and therefore problems due to reflections and the angle at which the slab passes the camera were not present[(A3.2)].

Here, the inclusions can be detected as they leave a small crater in the slab surface after scarfing. Results of this system can be seen in Fig. A3.13 and a simple algorithm for comparing these hot spots to a reference value background has been built and used.

The main drawback to this technique is the difference in emissivity between the scarfed surface and particles such as dust, black skin and scale. All of these elements are also seen as hot spots, due to their higher emissivity which cannot be discriminated from inclusions. Most of these particles can, however, be removed with a brush. Figure A3.13 also shows the effect before and after brushing.

This technique can therefore be used for finding inclusions on-line provided the surface is cleaned beforehand.

(iii) Laser Triangulation Inspection

This system uses a CMOS sensor and laser line generator. The laser line has 10 mW power, 670 nm wavelength and a 15° aperture. The CMOS sensor is a 1280*1024 monochrome array with a 35 mm lens. An interference filter has been used to allow only the laser wavelength to be detected.

A 60° angle was used between the laser and the camera, allowing a resolution of 0.25 mm per pixel laterally, with 0.5 mm depth. Software, used to interpret the data has been created.

The reference sample has different pore sizes and presents a 'black skin' region and other scarfing marks and can be seen in Fig. A3.14. All the different laboratory tests for each of the inspection systems were performed on this reference sample. Pore 1 had a diameter and a depth of 3 mm*0.7 mm. Pore 2 measured 5 mm*2.3 mm, Pore 3

measured 4 mm*0.7 mm and Pore 4 measured 1.5 mm*0.4 mm. A photograph of the sample showing the pinholes can be seen in Fig. A3.15.

The sample was moved underneath the sensors and the data acquired at a variety of speeds. Forty-five frames per second (fps) were recorded. If a higher-powered laser was used, the system could be operated at much faster speeds. This is because the greater the laser power, the more light is detected and therefore sensitivity is increased.

The results can be seen in Fig. A3.16. The smallest pore, Pore 4, was not detectable. In order to find this size of pore, a 150 mW laser would have to be used. Here, the sample was moved at 5 mm/s at 90 fps.

Because scarfing can lead to steel being more reflective (particularly on the fins which are peaks on the top of the scarfed grooves), false defect detection can arise.

(iv) Conoscopic Holography Inspection

Since significant expertise has already been gained using CH for this project, it was decided to conduct a feasibility study to determine whether CH could be applied. The main drawback to using this system for finding small defects such as inclusions and pinholes is that faster CH scanning rates (and therefore faster CH systems) would have to be purchased. Currently, the system operates at 60 lines/sec. This means that slabs can be divided into 5.5 mm divisions at line speeds of 20 m/min. To have a resolution of 0.3 mm, then the speed of the slab passing through would have to be reduced to 1 m/min, which would be too slow. A method of improving this would be to purchase the latest CH cameras, which operate at 250 lines/sec and could process slabs at 20 m/min. The cost of these sensors would need to be taken into consideration for any installation.

The same sample, tested with the laser triangulation system has also been tested using the CH equipment. These results can be seen in Fig. A3.17.

The main drawback to implementing this system is the cost and the acquisition speed, along with the computer processing that is required. The cameras used are similar to the ones used to find defects on-line in the caster. However, new cameras are now available. These are Firewire cameras that can provide 10-bit resolution as compared with the slower transfer rates of the RS-232 8 bit acquisition cameras. The use of the Firewire camera would significantly improve the amount of data that could be stored. Preliminary results from this system can be seen in Fig. A3.18.

Algorithms for fast recovery of the phase signal have been adapted such that more adequate 2D filtering and manipulation of the phase signal could be implemented. The signal-to-noise ratio was reduced via a series of laboratory developments. The speckle pattern generated by the laser caused the bulk of the interference as these reflected rays did not have the anticipated spatial or temporal coherence. Work has shown that the signal-to-noise ratio can be improved by up to ten times. Significant increases in the acquisition speed and subsequent processing are expected to be achieved using this technique.

(v) Multiscan Camera Inspection

Some of the problems encountered with conventional triangulation can be overcome by the use of the novel camera sensor IVP-Ranger that has recently been launched on the market. This ‘multiscan camera’, has the ability of individually addressing rows with individual integration time, has fast acquisition rates (up to 10 kHz), and individual on-chip processors with specialist algorithms for triangulation. This represents an important advance in the application of triangulation techniques for potential on-line inspection systems.

In order to assess the suitability of the IVP-Ranger for surface inspection of scarfed slabs, a sensor was hired from the supplier and tested in the laboratory on the reference sample.

Figure A3.19 shows a typical result obtained with this camera. The results obtained are slightly better than those for the triangulation configuration. This can be attributed to the higher frame rate and better resolution of the new device. However, from these results, this solution does not seem to improve the measurement situation for detecting inclusions. Moreover, due to the hardware processing that requires constant threshold values for laser detection, the reflections caused by the surface finish are not properly recovered and appear as zones with 0 values, therefore reducing the quality of the measurements. This problem is solved in conventional triangulation by means of dynamic thresholding, but this is not possible in this situation.

(vi) Machine Vision with Infrared Lighting

Infrared lighting is expected to give fewer reflection problems from the scarfed surface than conventional lighting. Infrared lighting is commonly used in machine vision when problems regarding surface finish or colour must be reduced.

Tests have been performed on the reference sample in order to check the feasibility of this solution. Figure A3.20 shows the results from these trials. These results were obtained by using an infrared light source, a monochrome CMOS sensor and a filter in front of the camera. However, although pinholes can be detected in this image, false defect detections, attributed to other formations in the surface make this approach unusable.

(vii) Spectral Camera

Another alternative has been tested, looking for different responses to various wavelengths of light. For this purpose, a machine vision system with spectrometer sensitivity between 0.4 and 1.0 μm has been tested on the sample. Although scale has a different emissivity and wavelength variation from that of scarfed steel, (which was a problem for the infrared thermography approach) these different wavelength distributions can be seen differently in the spectrometric sensor when a highlighted region of interest is either a defect, scale or a pore. As this effect is more intense when the wavelength increases, a test with infrared lighting and a 1.0 μm sensor was performed. Although higher wavelengths would be more interesting, no available light source and sensor could be obtained for the tests. Figure A3.21 shows the wavelength distribution of light reflected back from a line along the sample surface.

Each row in the wavelength distribution shows the light distribution depending on its wavelength for the point in the same row as the line marked in the photograph in Fig. A3.21.

The two maximum bands in the figure indicate the response to ambient light (pixels between 200-600) and to the additional infrared lighting used (pixels between 750-1050).

Several processing alternatives were considered: main peak values, main peak wavelength positions, etc., both for the visible and the infrared regions. Special care was taken not to use the absolute quantity of light information, as these values can be easily obtained from conventional imaging without needing a spectrometer. From these measurements, the relation between the amount of light in the infrared side and for the visible side showed an interesting value for enhancing the pores. Figure A3.22 shows the image of the sample which is obtained when using this technique for processing.

A3.4 SUMMARY

Table A3.1 summaries the results found in these trials. Installing a conoscopic holography system has the greatest potential to give excellent results for finding defects, but the drawback to this technology is the cost. On the other hand, laser triangulation is relatively inexpensive and was proven to find some of the defects. A higher powered laser for triangulation should therefore be tested on-line as this may overcome issues regarding image sensitivity and prove a more cost effective option than the CH system.

A3.5 REFERENCES

A3.1 Boogen, J: 'Informacion sobre equipos de oxicorte y escarpado' (Catalogo) Jose Boogen Maquinaria y Materiales para industrias, 1987

A3.2 Plotnikov, Y A, Winfree, W P: 'Visualization of subsurface defects in composites using a focal plane array infrared camera', Proceedings of SPIE, Vol. 3700, 1999, pp26-31

Table A3.1: Comparison of techniques for surface inspection of scarfed slab

	Grey level CCD	IR Thermog.	Laser Triang.	Conosc. Holog.	IVP Ranger	Grey CCD + IR light	Spectral Camera
Ability to detect pores	--	--	+	++	+	+	-
Simplicity and robustness of the set-up	++	++	+	++	+	+	+
Sensitivity and reliability	--	--	+	++	+	-	-
Adaptability for on-line conditions (speed, dust, etc.)	n.a.	n.a.	+	-	+	-	--
Cost for full width coverage	n.a	n.a	+	--	-	+	++
Development needed	n.a.	n.a.	+	-	++	+	--

++ very good → -- very poor;
n.a. = not applicable because it is not a valid solution

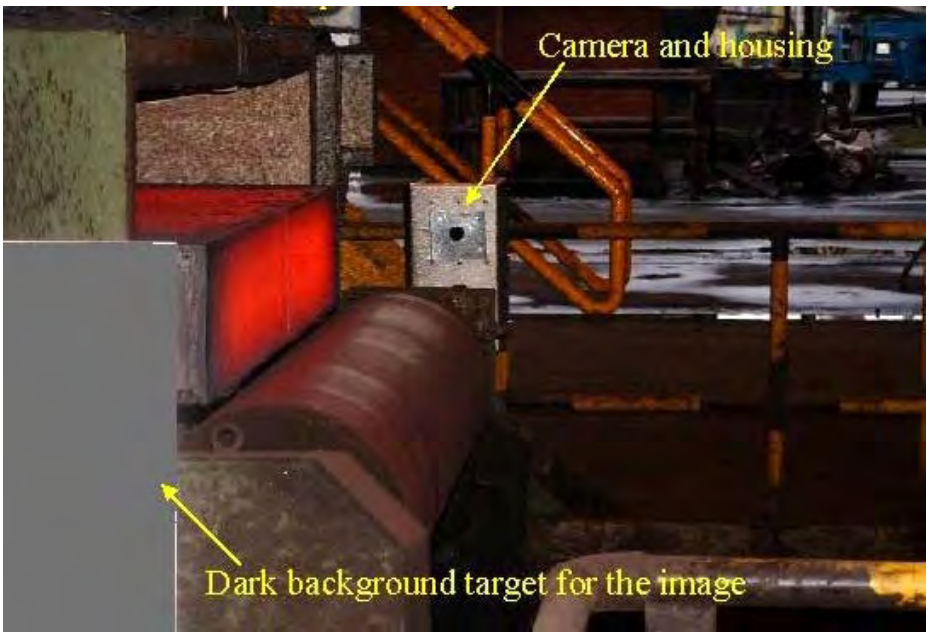

Fig. A3.1: Installation of the burr detection system on the production line at Arcelor

Fig. A3.2: The image of the roll area selected by the CMOS camera.
The rectangle areas represent the two parts the camera examines and compares

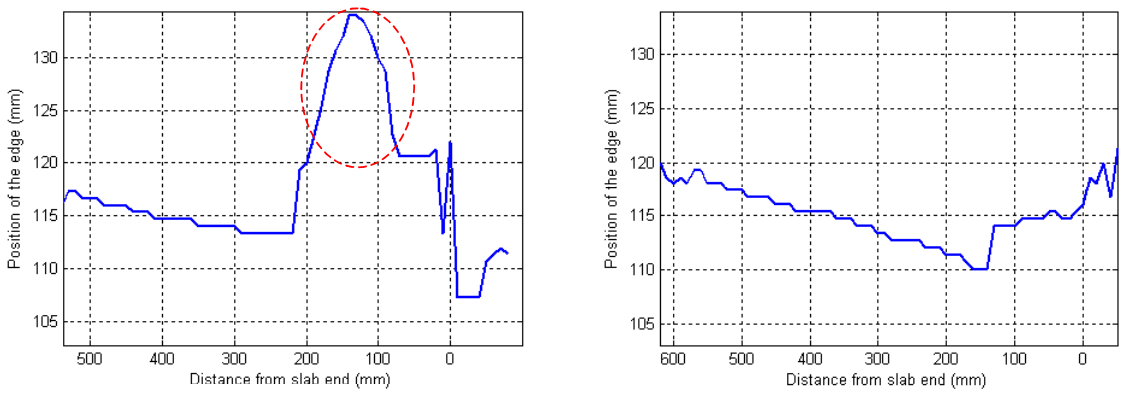

Fig. A3.3: Results for slabs with burr (left) and without burr (right)

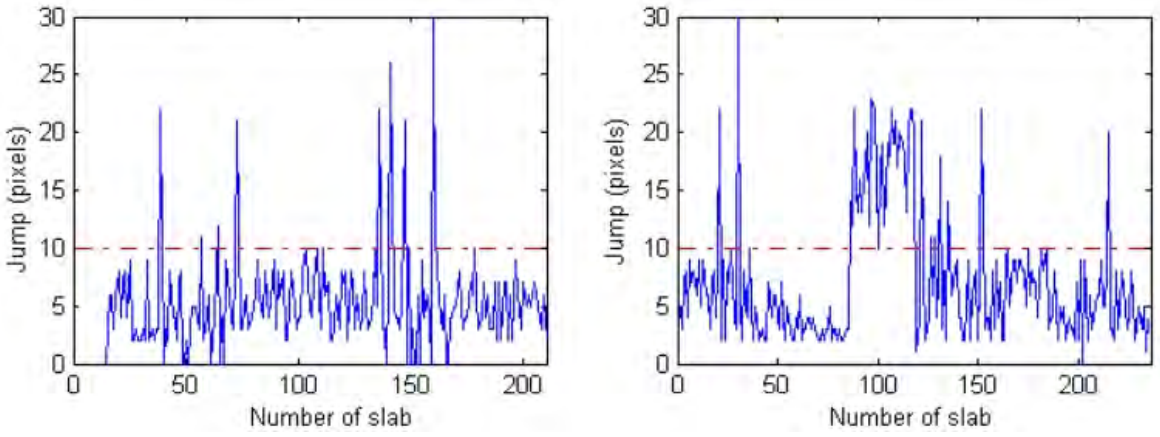

Fig. A3.4: Evolution of burr detection along two different days.
Slab jump above 10 pixels indicates the existence of burr not properly removed.

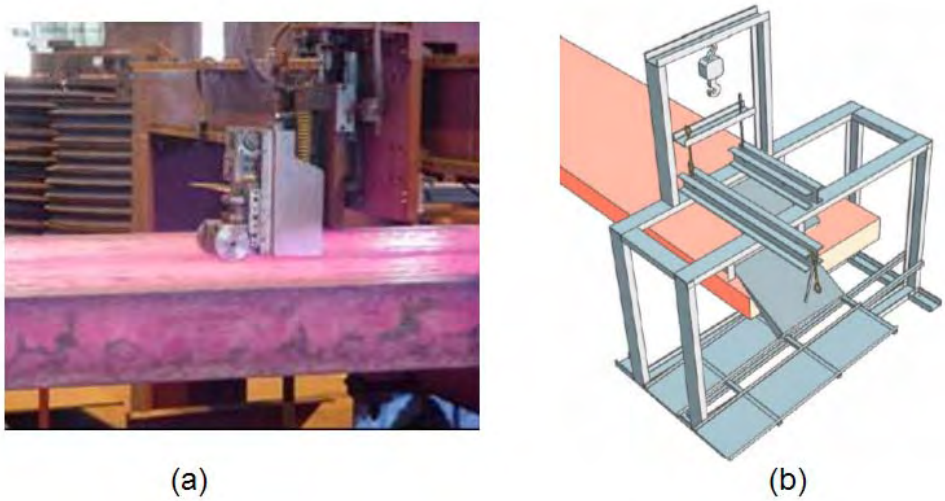

Fig. A3.5: (a) Photograph of the plane tool operating on a hot slab at Arcelor
(b) Drawing of the ancillary mechanical device for sampling of the planed steel strip

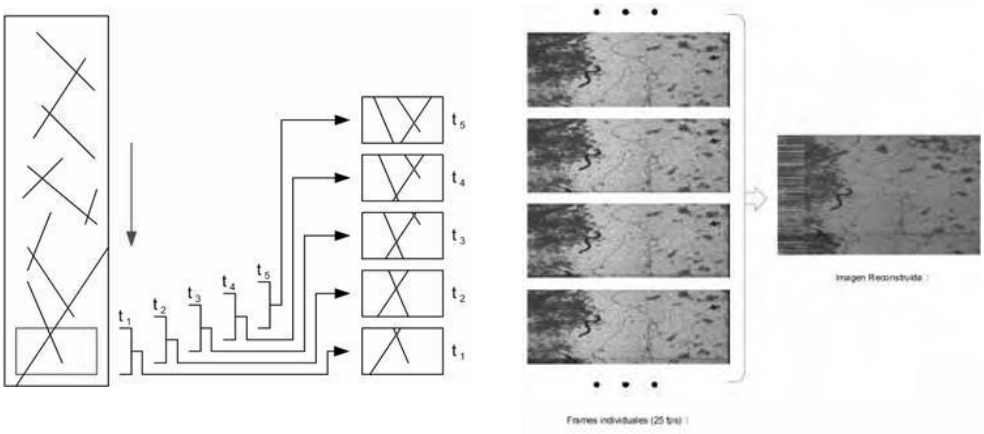

Fig. A3.6: Partial images of the inspected strip meshed together

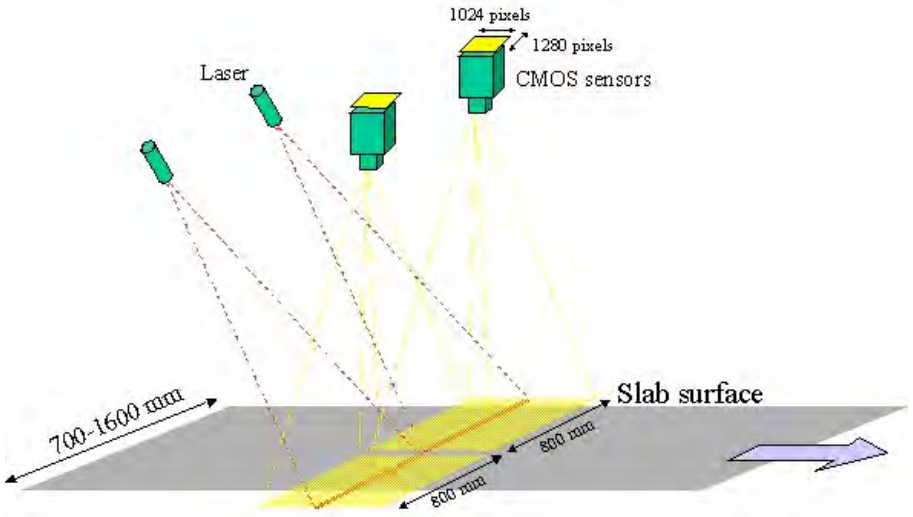

Fig. A3.7: Scheme of the new automated line scan optical system for inspection of slab surface after scarfing

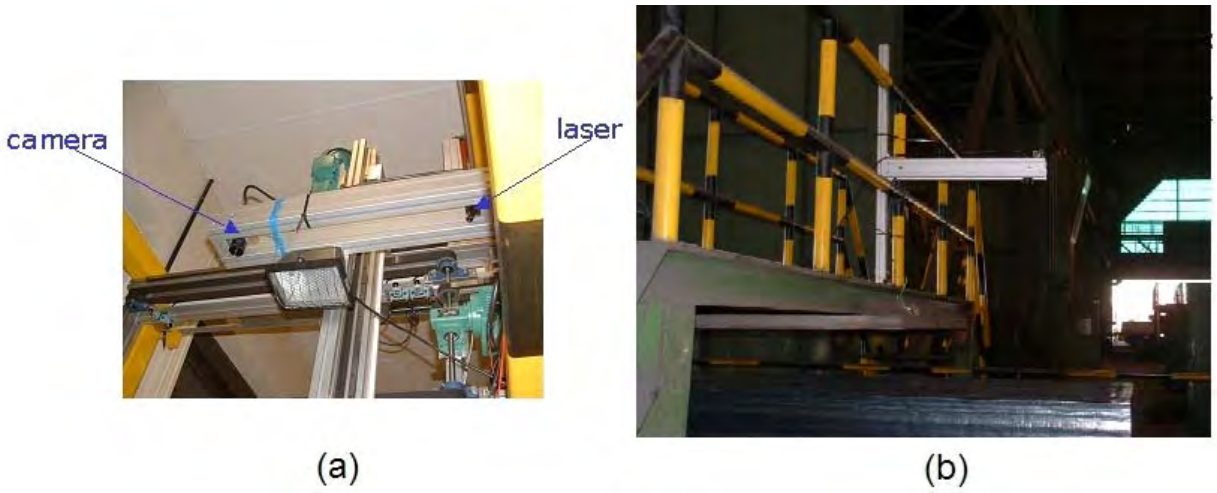

Fig. A3.8: Feasibility tests of the new line scan optical system:
(a) in the lab with moving samples and (b) in the plant with scarfed slabs

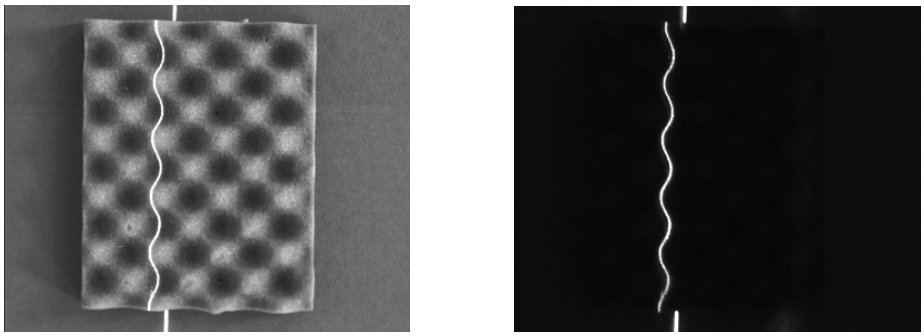

Fig. A3.9: Example of the acquisition of a surface profile using the lab prototype

Fig. A3.10: The new line scan optical system inspecting scarfed slabs in the Arcelor plant

Fig. A3.11: Blurred image of the slab number obtained with the webcam

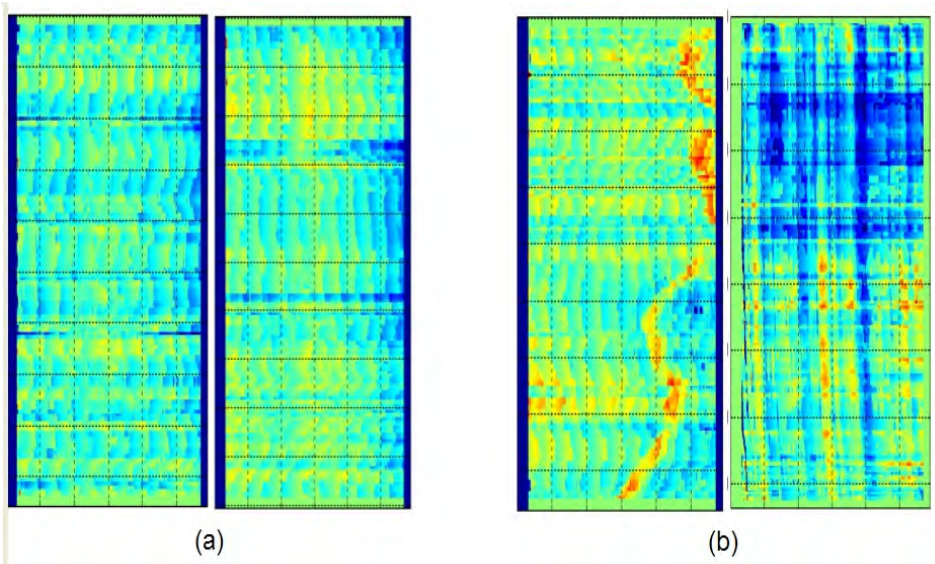

Fig. A3.12: Examples of acquired surface maps with the new line scan optical system:
(a) two scarfed slabs with good surface quality (Nov 2006) and (b) two slabs with poorer quality (Oct 06)

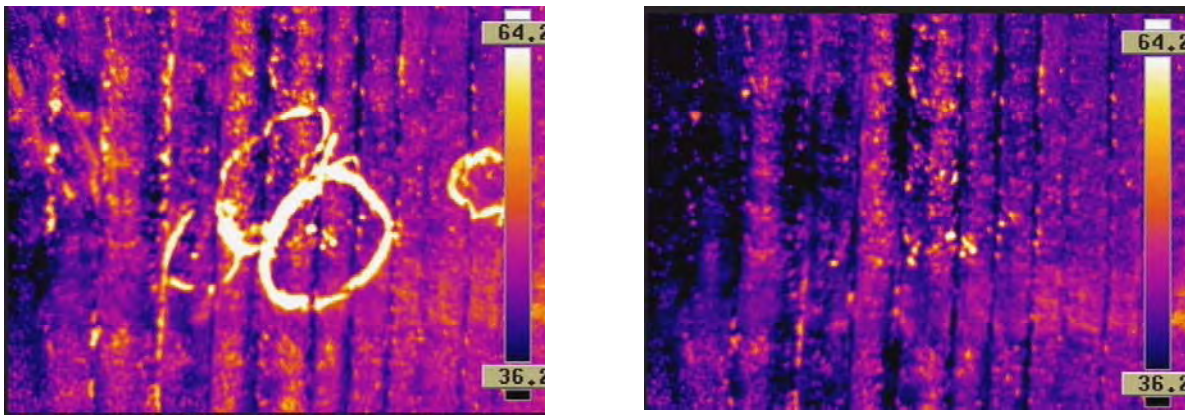

Fig. A3.13: Results of the thermographic inspection of the inclusions, before cleaning the surface (left) and after cleaning the surface (right); the real inclusions appear in both images

Fig. A3.14: Dimensions and photograph of the slab sample used to test different inspection devices

Fig. A3.15: Part of the slab sample used to test different devices for inclusion detection.
Pore 1 had a diameter and a depth of 3 mm*0.7 mm. Pore 2 measured 5 mm*2.3 mm, Pore 3 measured 4 mm*0.7 mm and Pore 4 measured 1.5 mm*0.4 mm.

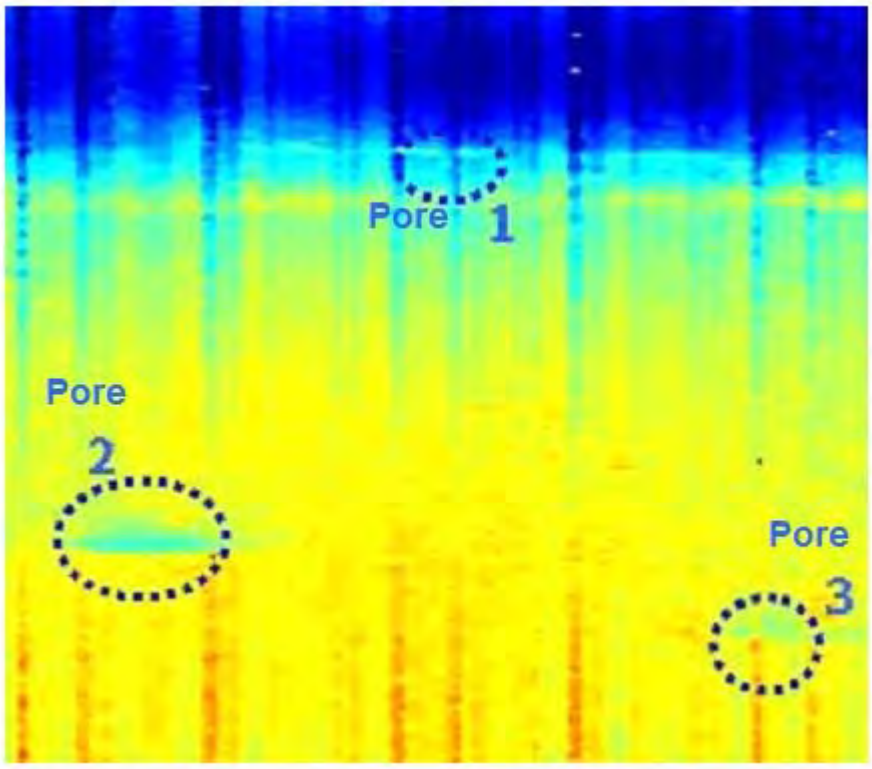

Fig. A3.16: Results from the laser triangulation technique at 90 fps, when the slab sample was moving at 5 mm/s

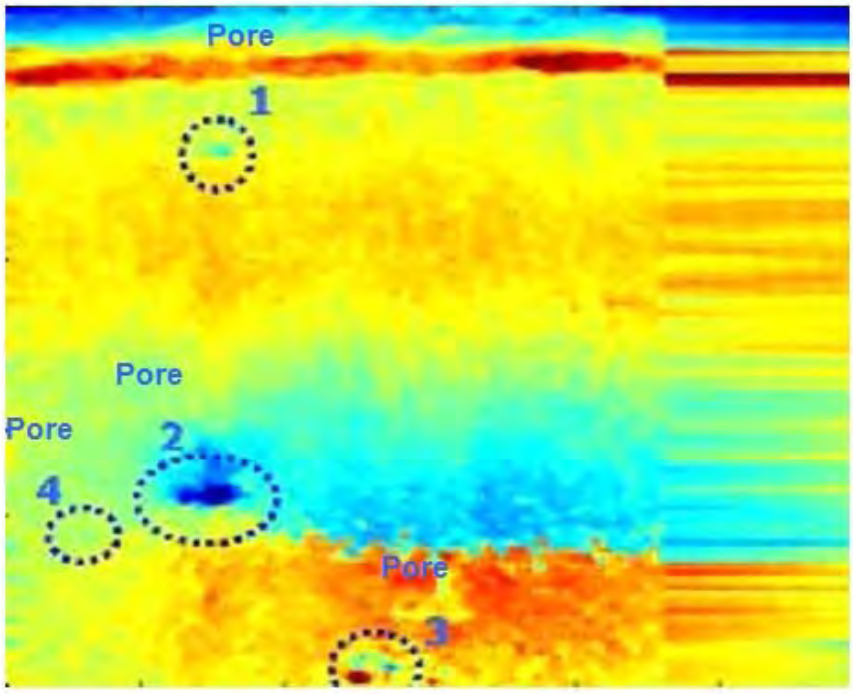

Fig. A3.17: Image of sample taken using the CH system at 30 fps when the slab sample was moving at 5 mm/s. All four pores are detected.

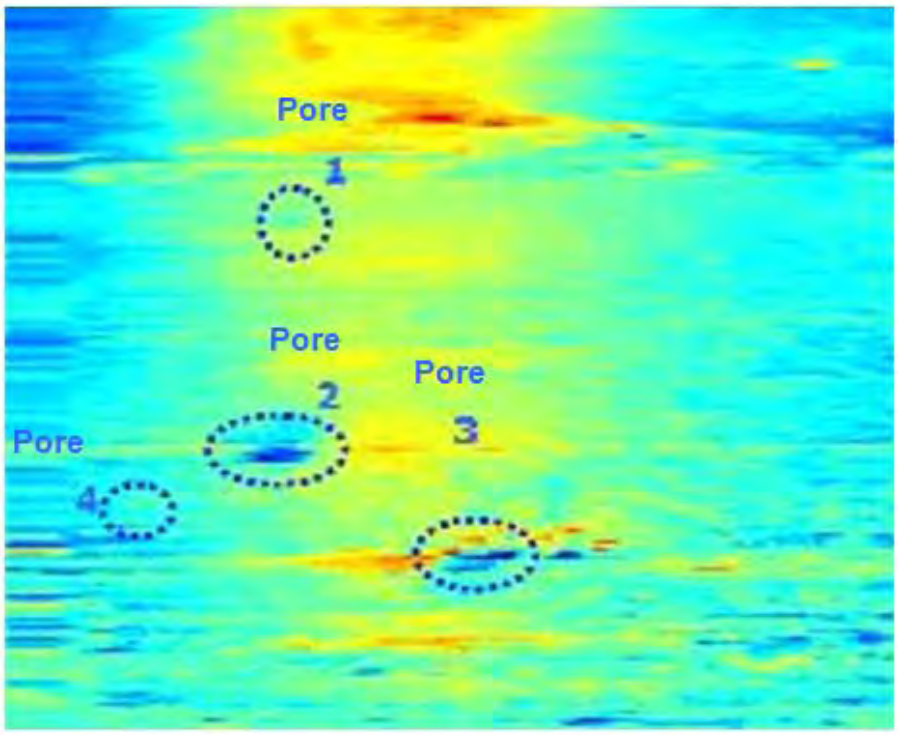

Fig. A3.18: Image of sample taken using the IEEE CH system
5 mm/s speed, 30 fps second

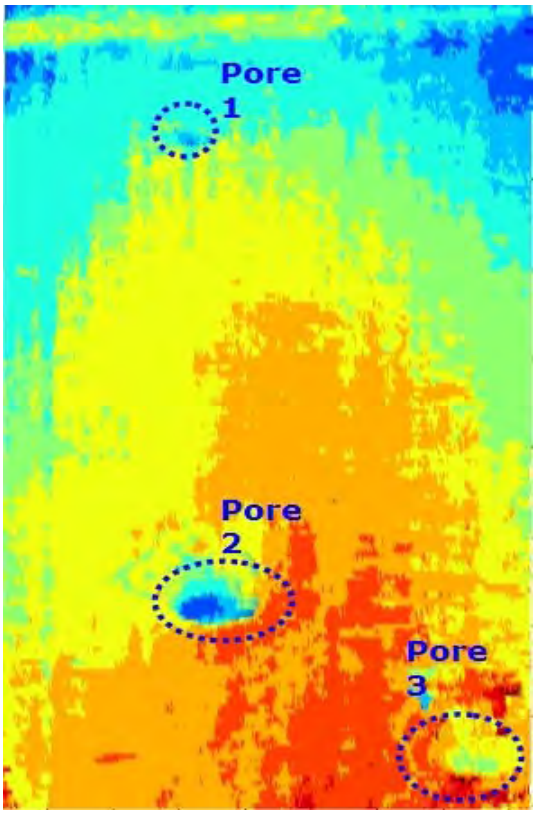

Fig. A3.19: Tests of inclusion detection on a steel sample using the novel IVP-Ranger sensor

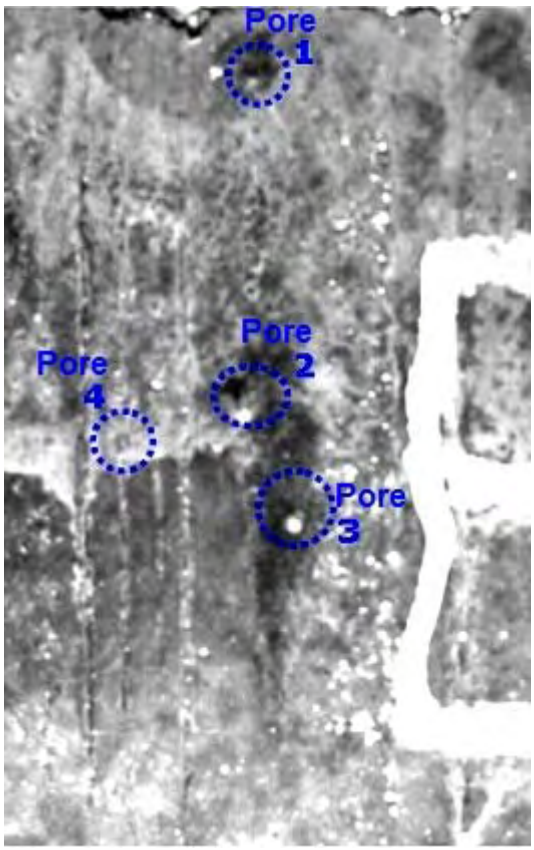

Fig. A3.20: Inclusion/pinhole detection using machine vision and infrared lighting

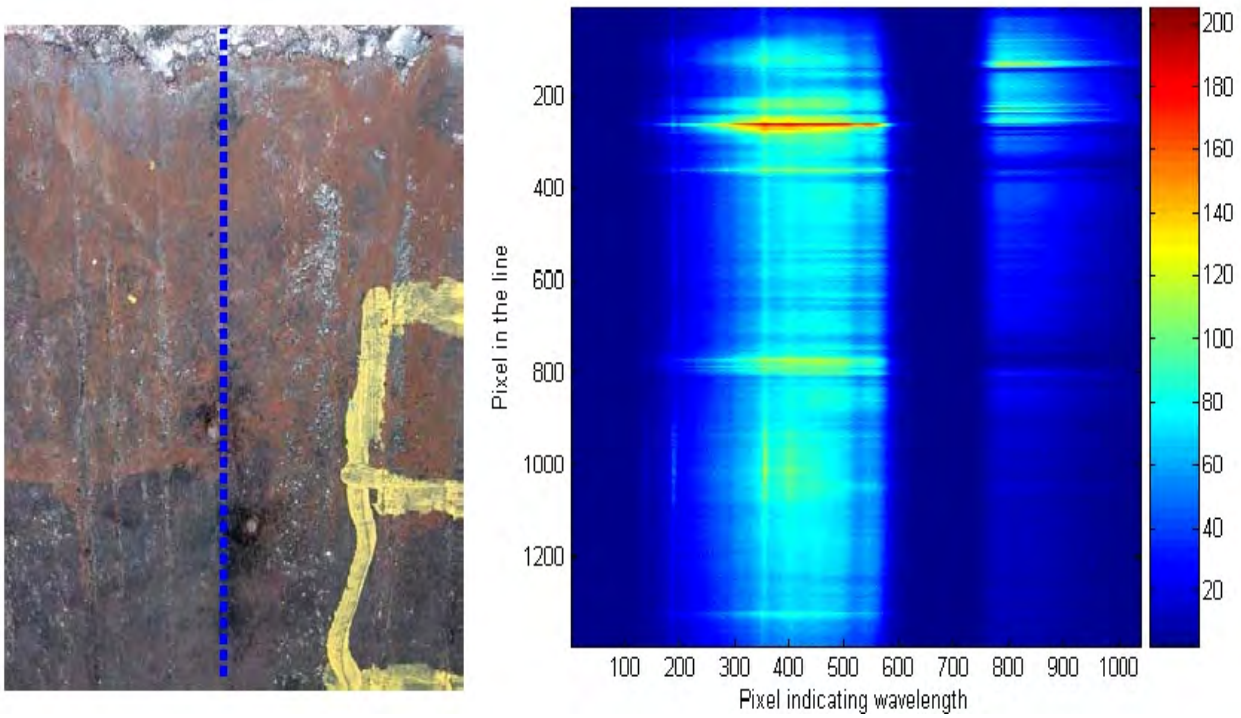

Fig. A3.21: Wavelength distribution obtained with spectral camera on the indicated line on the sample

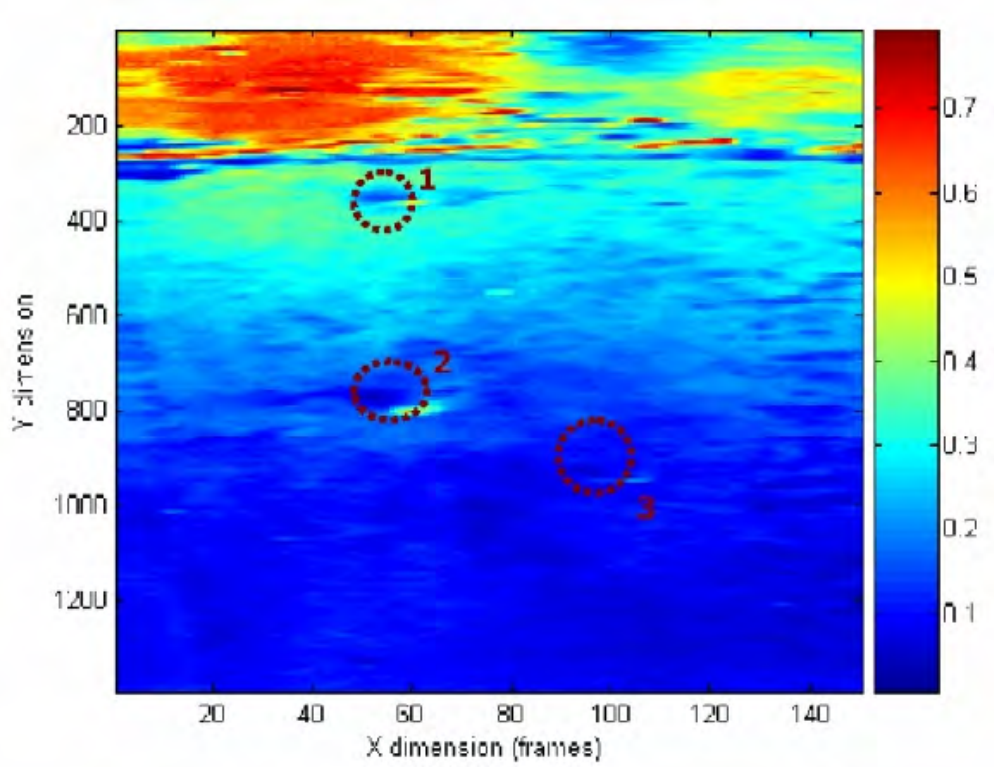

Fig. A3.22 Tests of inclusion detection on a steel sample using spectral camera

APPENDIX 4

SCARFING AND TRACKING DEFECTS THROUGH THE MILL (WORK PACKAGES 3-5)

A4.1 SCARFER COMPARISON BETWEEN CORUS AND ARCELOR

A trial was planned to compare the effectiveness of different scarfing machines at removing defects from as-cast slabs. This comparison would have been conducted by Corus R, D & T, using the scarfer at Casting Plant A and the scarfer at Casting Plant B. Due to significant delays in commencing this trial work, caused by logistical and workload issues at Plant B, this work was cancelled. However, it is justifiable to discuss the work that would have been undertaken, as several meetings were held with plant personnel.

The trial would have taken a number of defective slabs from Plant A and split them into two groups. One group would be scarfed at Plant B, the other at Plant A. Both machines would perform similar surface rectification treatments before the scarfed slabs were sent to Plate Mill A, where they would have been rolled to plate and later surface quality inspected. A comparison could then have been made as to the effectiveness of the two scarfers. Plant A and Plant B operate very different scarfing machines, which would have made this trial particularly interesting.

Plant A operates a scarfer similar in design to that shown in Fig. A4.1. The scarfer is built around a large lowering frame with a metal skid supporting the scarfing torches. The scarfer is stationary and material to be scarfed is transported on a carriage by a pulley-wire-drive system. Iron powder equipment is used as an aid to start scarfing the slab surface. When in operation, the machine provides a controlled method for scarfing of the slab surface. Scarfing depth ranges from approximately 1.5 mm to 6 mm at a speed of 5 m/min to 50 m/min. Slabs can be scarfed up to a temperature of 1000 °C. This design of machine allows only one side of the slab to be scarfed at any one time. To scarf both sides the slab must be turned with the aid of a crane. There is no opportunity for the narrow edges of the slab to be scarfed. All operations are controlled using computer communication and the operator controls the scarfing process with the use of VDU screens.

Plant B uses an Androfer scarfing system designed and operated by a sub-contractor. Figure A4.2 shows an example of an Androfer scarfer in operation. The design details of the machine are as follows:

- Adjustable hand-held lever system.
- Advanced hydraulic system for manipulation including a torch-feedback system to the control lever.
- Scarfing torch with nozzles.
- Sound-insulated and air-conditioned cabin with an excellent view of the scarfing process.
- Spot-and selective scarfing of slabs.
- Scarfing passes between 50 mm to 80 mm for spot-scarfing.
- Scarfing path width of 80 mm to 300 mm for high operating performance.
- 6 to 10 times more efficient compared to hand-scarfing.
- Economic efficiency. Operating costs more favourable than hand scarfing.
- Same advantages as hand scarfing by touch-feedback system.

At Arcelor, the treatment of the slabs inspected via surface and sub-surface systems can currently be performed by either manual or automatic scarfing. This design is similar to that used by Corus, as shown in Fig. A4.1. The main characteristics of the scarfing station are:

Range of slab widths:	548 mm – 1.634 mm
Range of slab thickness:	152 mm – 280 mm
Scarfing depth:	0 mm – 3 mm

Range of scarfing speed:	13 m/min – 46 m/min @ 760 °C
	8 m/min– 25 m/min @ 21 °C
Number of units:	(6 wide face and 2 narrow face) x 2
Gases:	Oxygen and propane
Purge water pressure:	15 bar

During one of the project meetings, held at Arcelor, the scarfing product quality of all the three sites was compared. Arcelor had the most even scarfing pattern and the troughs along the slab surface were even.

A4.2 TRACKING SCARFED SLABS THROUGH PLATE MILL B

A4.2.1 Work Conducted

Two slabs with surface defects (Cast Nos. 79532 and 79556) were tracked from Plant A Concast to Plate Mill B. Both slabs were the first slabs cast, from two different sequences. Each slab underwent standard scarfing processing, which involved two top surface scarfer passes and proof dressing on the bottom surface. No edge scarfing was performed because the scarfer was not capable of doing this. Typically, Plant A had applied a third pass to the top surface of both the first and last slabs from a sequence; however, this was not done for this trial. After each scarfing pass, the top surface of the slab was inspected using magnetic particle inspection. Figures A4.3 and A4.4 schematically show the results of this inspection for the front-end slabs of cast 79532 and 79556 respectively.

A4.2.2 Results

For cast 79532 (Fig. A4.3), only three cracks were found after the first pass and only remnants of one of these remained after the second pass. None of these fine cracks would have been detected under normal inspection. The remnant crack was not dressed out, as the trial was adapted to determine whether this crack could lead to a defect in the final plate.

For cast 79556 (Fig. A4.4), eight areas of cracking were found after the first pass, one of which was particularly extensive. After the second pass, only the remnants of two cracks remained in this poor area, which again would not have been detected under normal inspection procedures. These remnant cracks were not dressed out because they were to be used to see if these defects would be detected in the rolled plate.

At Plate Mill B, both slabs were inspected prior to rolling. Without the use of magnetic particle inspection, both slabs were reported to be crack-free. However, both these slabs did have other quality issues. Scarfer overlap (“fin”) was found running the length of both slabs. This “fin” is known to form shell type defects in the plate and was therefore removed prior to rolling. The trailing end of both slabs was reported to be heavily “scalloped”. This defect is caused by the scarfer burners digging into the surface of the slab at start-up. Both slabs had to be cropped back 50 mm in order to remove the defect, leading to a shorter sized plate which resulted in yield losses. Large quantities of “wash” were found hanging from the top surface at the ends of both slabs. This was unacceptable for rolling to plate as it caused sliver type defects in the rolled plate. All the “wash” was removed from both slabs before they were sectioned and charged in the equalising furnace.

Before rolling, both slabs were sectioned into three sub-slabs. These six samples were then rolled to six plates of gauges between 70 mm and 100 mm. Upon inspection, the top surfaces of the plates were found to be defect-free. However, the bottom surfaces were found to cracked. These cracks were found to be scattered over the body of the plates within the middle two thirds of the plate width. The cracks were generally short (10 mm to 50 mm) and running in a longitudinal direction. The cracks were not normal longitudinal cracks but believed to be transverse, which in turn became elongated due to the rolling process. All six plates were unacceptable to the customer and were therefore rejected and scrapped at a total loss of 60 tonnes.

A4.2.3 Summary

This trial demonstrated that although scarfing could remove some of the surface defects, more than one scarfing pass was required. Manual inspection could not find any defects in the slabs before they were sent to the rolling mill. The hypothesis that more severe cracks can be rectified during rolling and that they could be "closed up" and would therefore not be detectable on the plate surface was found to be false. The reason for the cracking on the bottom surface of the plates is unknown. One suggestion concerned the procedure of heating up the slab to suitable scarfing temperatures. At Plant A, slabs to be scarfed are placed on top of another hot slab to raise the temperature to suitable levels for scarfing. Therefore, the bottom surface of the slabs may have been subjected to severe thermal shock (temperature gradients) that may have caused thermal cracking of the surface to take place. With only a proof dressing pass being practiced on the bottom surface, the cracks were too small to be detected in the scarfing area.

A4.3 TRIAL WORK TO TRACK SLABS THROUGH THE PROCESS ROUTE, FROM CASTER TO ROLLED PLATE

Problems have been experienced with cracking for thick plate rolled at Plate Mill B from 12" (300 mm) slabs made at Casting Plant A. This is despite the fact that the slabs are checked for surface quality issues before they leave Plant A and the slabs are scarfed accordingly. An investigation to see whether cracks were present but undetectable to the naked eye was conducted. This was via metallurgical examination of sulphur print samples from three casts. Dye penetrative tests were also conducted in the slab yard on slab grades that were not normally dye tested. It was also interesting to see whether the current procedures concerning scarfing and dye-penetrative testing were suitable.

The majority of rejections at Plant A appear to be related to low casting speeds as this can effectively result in overcooling of the strand surface. This is shown in Fig. A4.5, which shows the correlation between the proportion of rejections and casting speed for different steel grades for speeds ≤0.47 m/min. Figure A4.6 shows the position of rejected slabs in the casting sequence. It can be seen here that problems arise mainly with the first two slabs of the sequence (when the caster is cold and thermal stresses are induced) and the last slab of the sequence, when the casting speed is reduced. Figure A4.7 shows the quality code of the steel against proportion rejected. The surface quality problems are associated primarily with microalloyed grades, particularly M1. The large rejection proportion from grades M2 and M3 come from a small sample distribution, making these grades less statistically significant.

A4.3.1 Trial Work Undertaken

A4.3.1.1 Dye-Penetrative Testing

Dye penetrative testing was performed on the first, second and last slabs of casts 60933 and 60935 of M1 quality. Dye penetrative tests were also conducted on cast 60954 of M4 quality (the first time this grade had been cast). Tests on cast 60969 of M5 quality (which had been cast slower than the usual practice because of an unusually high superheat) were also carried out. M1 and M4 are both microalloyed grades and M5 is a non-microalloyed steel grade. Table A4.1 shows the metallurgical composition of the casts investigated and the standard processing requirements for these grades.

A4.3.1.2 Metallurgical Investigation of Sulphur Print Samples

Sulphur print samples for cast 60933, slab 5B and 6B and cast 60942, slab 5B were transported to the laboratory for surface examination. Figure A4.8 shows where the sulphur print samples were taken off the as-cast slab, which is at the end of slab B. Figure A4.9 shows how the narrow and broad face surfaces were removed from the sulphur print samples for further work. Firstly the samples were immersed in acid to remove any oxide scale and to reveal any cracking. The locations of major cracks were then sectioned further, polished and etched to reveal their grain structure and to allow a measurement of crack depth to be taken.

A4.3.2 Results and Discussion

A4.3.2.1 Dye-Penetrative Testing

Some of the slabs were fully dye-penetrative tested in the scarfing yard as shown in Table A4.2; with comments made if any extra scarfing passes were required. In addition, cast 60933, slab C had additional testing performed as cracks were seen upon visual inspection. Figure A4.10 shows a photograph of this series of cracks, which were present for a small length of the slab, in the off-corner region of the slab on the broad face.

Figure A4.11 shows transverse cracks present on cast 60933, slab E, again in the off-corner region of the slab on the broad face. These were of the order of 3 cm in length and were present for most of the length of the slab.

Small longitudinal cracks were present on cast 60933, slab 6B. These were of the order of 1 cm in length and present for around 80 cm from the number end of the slab in the off-corner region on the broad face.

A4.3.2.2 Metallurgical Investigation of Sulphur Print Samples

(I) General Observations

Non-metallic deposits, thought to be mould flux were found in small quantities on the narrow faces of all the samples. The samples were as-cast and had not been scarfed.

Figures A4.12 to A4.14 schematically show the sulphur print samples, with the edges 'opened up' to show the surfaces and associated defects. This net diagram is based on the cuboid shape cut from the slab, as shown schematically in Fig. A4.9. This shows that the cracking appears to be worst in the 'off-corner' region of the samples, around 250 mm to 300 mm in from the edge, with the narrow faces themselves not exhibiting many fine or large cracks. They also show that the most cracking occurs on the top surface. This could be due to the fact that during casting the sprays on the upper surface caused water to flow down the strand, whereas on the bottom surface, the water falls away from the bottom face due to gravity. There was also a slight depression in this region, which may have caused the water to run down the slab preferentially in this area. This could have been caused by different cooling rates in the spray chamber on the surface and may therefore have induced thermal stresses.

(II) Cast 60933, Slab 5B

Figure A4.15 shows the network of small cracks, numbered 1 in Fig. A4.12. Figure A4.16 shows the microstructure of the same crack. These small crack networks only extended to a maximum size of around 2 mm into the sample and although they are wide, they would be expected to be removed by scarfing.

Figure A4.17 shows a close-up of the crack marked as number 2 in Fig. A4.12. It was found that these cracks were very shallow, measuring approximately 1 mm in depth. It is thought these were representative of most of the fine cracks observed.

(III) Cast 60933, Slab 6B

Figure A4.18 shows heavier cracking, corresponding to samples numbered 3 and 4 in Fig. A4.13. These cracks were in the form of crack networks and covered areas with a width of approximately 3 cm. Figure A4.19 shows that the cracks extended up to 7.5 mm in depth. Figure A4.20a shows the deepest crack found in these two samples, at 8.5 mm deep. Figure A4.20b shows an enlargement of the lower region of this crack, where the weaker ferrite band has cracked along the grain boundaries. It is thought that towards the surface, the cracks result from a combination of interdendritic and grain boundary cracking, whereas within the body of the material they result from grain boundary cracking.

Assuming that the standard scarfing procedure of two top passes removes 7 mm of the surface, these cracks will still be present afterwards.

(IV) Cast 60942, Slab 5B

Figure A4.21 shows the cracks corresponding to sample number 5 in Fig. A4.14. Figure A4.22 shows the microstructure of the crack just below the surface. The crack appears to line up with the dendrites, which suggests interdendritic cracking. This crack did not run deep enough to view any grain boundary cracking. Interdendritic cracking is usually initiated high up in the caster.

A4.3.3 Summary of Findings and Recommendations

The majority of the cracking found can be classified as 'light' and should normally be removed by scarfing. The only exception to this was the cracks viewed during the dye penetrative testing work on cast 60933, slab 6B, of M1 quality. The sulphur print sample exhibited cracking to 8.5 mm in depth. This is significant, as it would not be removed by the standard scarfing practice. This crack appeared to follow grain boundaries at its deeper end, where the crack had run down the weaker ferrite band. Close to the surface, the crack may have been interdendritic, which was also shown in the other, more shallow cracks.

Most of the heavy cracks on the sulphur print samples occurred between 250 mm and 300 mm in from the edges of the slab, in the off-corner region, which also exhibited a slight depression. It is thought that spray water may have run down these depressions and caused additional, excessive cooling, therefore inducing cracks.

The dye penetration tests were not particularly effective. Simple visual inspection managed to find surface defects successfully, whilst dye penetrative testing did not yield many additional defects. However, tests did aid in highlighting existing cracks clearly.

A4.3.4 Future Work

As a result of this work, it was suggested that excessive secondary cooling was taking place. The plant changed from a hard to a soft cooling practice. Further work was conducted on slab samples which were assessed for surface defects. None were found and no critical reports have been made back to the casting plants by customers.

What is interesting is that the slabs that were dye penetrative tested were passed as 'all clear' by operators before they were dye penetrative tested by research staff. The defects found with the dye were too small for normal visual inspection. Two slabs out of twenty-one contained these defects. If dye penetrative testing was quicker and easier to conduct, then it would be recommended to conduct further trials to determine whether the steel grades involved would require mandatory machine scarfing.

A4.4 FURTHER TRIAL WORK TO TRACK SLABS THROUGH THE PROCESS ROUTE

A4.4.1 Introduction

A series of 12" (300 mm) slab samples were analysed and various characteristics were mapped and reviewed in terms of the surface quality. This work continued from that discussed in Section A4.3. Here, two full cross-section transverse samples were received from one slab. One of the cross-sections was from the as-cast semi. The second cross-section came from the same slab after it had been scarfed. The steel samples were taken from a semi intended for rolling to thick plate.

The casting superheat was 41 °C and the casting speed was 0.44 m/min. This was slightly lower than the planned 0.49 m/min, which is the preferred speed to minimise crack formation.

The two samples were full cross-section, transverse slices. The as-cast sample was taken from the back end of the second slab produced from strand 6. The slab was then slow cooled until it reached the scarfing temperature. After scarfing, the second sample was cut from the back end of the second slab. In this case three scarfing passes were done to the top surface and two passes to the bottom surface. The narrow face sides of the slab were not scarfed. The samples were assessed for the locations of any surface cracking. This involved immersing surface sections in hot hydrochloric acid in order to remove oxide scale *(i.e. the pickling process)*. A flow diagram of the work undertaken can be seen in Fig. A4.23.

Figure A4.10 illustrates how the as-cast sample was cut from the parent slab. The initial sample had a longitudinal length of 300 mm. The sample was cut in half to produce two samples with longitudinal lengths of 150 mm. The sampling was performed such that for any cracks that were found the corresponding unpickled sample could later have any cracks analysed by SEM (Scanning Electron Microscope).

The samples for pickling were sectioned to produce a series of pieces of the slab surface with a minimal sample thickness. These were immersed in an acid bath until the majority of the surface scale had been removed. The surfaces were then assessed to identify locations of any cracks and photographs were then taken.

A4.4.2 Results and Discussion

Cracking was found only on the top face and at the mid-face of one of the sides of the slab. The cracks were generally present as small networks of branched cracks and were not very severe. The crack networks were very localised and generally the cracks appeared to be transverse in nature with some longitudinal branching. In some of the samples the main cracking was found to be at the base of the oscillation marks. This would tend to indicate the cracks are transverse spongy cracks indicating the strand surface has been slightly cold when going through the straightener.

The scarfed sample was examined in a similar way but without the initial sectioning to preserve a sample suitable for SEM. All the surface sections were pickled to remove oxide scale. No surface cracking was found. However, the pickling operation did reveal a feature that was not apparent prior to pickling. On one sample, a feature that looked like a sliver of metal, somewhat separate from, but embedded into, the scarfed surface was apparent. It was about the size of a 1 Euro piece and is shown in Fig. A4.24. A section was taken through this feature and polished to a 1 micron finish. Etching with picric acid solution to show the dendritic structure showed that the surface feature was separate from the parent slab but that the parent slab dendritic structure was slightly deformed immediately below the sliver of metal. The dendritic structure in the sliver was composed of globular dendrites. It would appear as though the sliver was impressed into the surface of the slab while the steel was still hot. It is possible that this sliver has been scarfer wash but it should be noted that it was not visible until pickling had been carried out. It is possible that this fragment would become rolled into the surface during plate production and result in a surface defect.

In conclusion, these types of defects can be attributed to either excessive cooling in the top zone, below the mould, or the strand being too cold before entering the straightener which would lead to cracks forming in the oscillation marks. However, the problem disappeared before the investigation could continue (e.g. use thermal imaging cameras/thermocouples to check the surface temperature was correct in the caster).

A4.5 CHARACTERISATION OF SCARFED SLABS TO INVESTIGATE THE OCCURRENCE AND SOURCE OF DEFECTS

A4.5.1 Database Design at Plant C

Following an initial period of knowledge gathering that involved meetings with technical, production, scheduling and process control personnel at Plant C, several data sources were identified as being of potential value in this exercise. These data sources are listed in Table A4.3. Data were routinely collected from several of these data sources associated with different operations in the process route from steelmaking and hot rolling at Plant C through to pickling at Plant D. This process route included the Parsytec surface inspection systems at the hot rolling and pickling stages. The infrastructure associated with the data collection is illustrated in Fig. A4.25.

The retrieval of data is carried out daily using various techniques (Fig. A4.25a) and a data mart is populated daily (Fig. A4.25b) with new data for coils processed at Plant D. Clementine is an enterprise data-mining workbench that enables the user to quickly develop predictive models using business expertise and deploys them into manufacturing operations to improve decision-making. Clementine has an open architecture utilising existing IT infrastructures to enable rapid predictive modelling and deployment. Therefore, a suite of Clementine models (Fig. A4.25c), shown in Fig. A4.26, are applied to update a downloadable Microsoft Access database (Fig. A4.25d) containing through-process records for the manufactured coils. This information is uploaded to a web site that contains graphs, surface defect maps and tables with information for the coils processed up to that point in time.

A4.5.2 Tracking Lamination Defects (First Trial)

After discussion with Plant C it was agreed that a study of steel grades G1 (non-scarfed) and G2 (scarfed) would be informative. These are automotive steel grades. Apart from different scarfing practices, the grades are manufactured in a similar way and the hypothesis was that by comparing Parsytec results, the final product quality would be much better for the mandatory scarfed G2 grades than the non-scarfed G1 grades.

Overall, 681 slabs of G1 grade and 882 slabs of G2 grade were identified. From this data set, the next step in the analysis was to separate all examples of slabs for which Parsytec information was available. From this revised data set, detailed casting information was extracted from the PI database. In total data from 574 slabs of G2 grade and 490 slabs of G1 grade were obtained.

Figure A4.27 graphically shows the results of some statistical analysis undertaken on the grade G1 and G2 data set. The analysis focused on lamination defects of which there were three classifications, Lam 1, Lam 3, and Lam 4. It is clear from the graphs that the expected differentiation between the two steel grades was not evident. Thus, it was decided that the G2 grade could be sent to the hot mill unscarfed. Since this decision was made no quality issues have arisen. The success of this analysis has meant that two further grades (G4 and G5) were similarly investigated using the same method as described above.

A4.5.3 Tracking Lamination Defects (Second Trial)

The objective of this work was to obtain through-process data from steelmaking to hot rolling, including information about coil surface quality and to analyse this with a view to assessing the effectiveness of the current scarfing strategy for two grades of steel, G4 and G5, cast at Plant C. This work was undertaken after the successful completion of the first trial.

A4.5.3.1 Data Collection

Grade G4 is an IF steel containing niobium and requires mandatory machine scarfing. Grade G5 is also an IF steel grade and is only for general-purpose applications and is therefore not scarfed. In all other respects the grades are very similar. The hypothesis was that by comparing the results from the Parsytec system results would indicate whether or not grade G4 really needed to be scarfed.

Clementine data mining models were used to query the database for slabs that were cast as grades G4 and G5. The data were for a 16-month period and provided a large dataset for analysis. From this dataset the next step in the analysis was to separate all examples of slabs for which hot mill Parsytec information was available. In total 1690 slabs had Parsytec information, 946 slabs of G4 grade and 744 slabs of grade G5.

Lamination type defects were queried using the hot mill Parsytec information, on the top and bottom surface of the rolled strip. These laminations were classified as being "Big_Lam" (big laminations), "Med_Lam" (medium laminations), and "Small_Lam" (small laminations). The hot mill Parsytec system counted the number of lamination defects it identified for both the top and bottom surfaces of the strip and then calculated a total count for that coil (e.g. "Big_Lam_Coil_Count").

In addition to the hot mill Parsytec information, the Clementine models were used to extract the "remark codes" generated for each slab cast. A remark code is a number that corresponds to a casting or steelmaking condition and is used for the downgrading or upgrading of slabs to particular grades. The Clementine model generated a data file, which had a record for every slab and every remark code. 1690 slabs were analysed. These remark codes and Parsytec data were manipulated using Microsoft Access and Excel so that for every slab/coil number there was only one row of data concerning coil surface quality (i.e. laminations) and casting remark codes. By sorting the data in this manner, subsequent data analysis was much easier.

A4.5.4 G4 and G5 Grade Comparison

The analysis of the data focused on comparing the total coil counts of big, medium and small laminations for the slabs cast as G4 and G5 grade. It was hoped that, on the whole, the slabs that were scarfed, i.e. G4 grade, would have lower total lamination counts than that of slabs that were not scarfed, i.e. G5 grade. The analysis was built around a series of hypotheses in which the data were sorted using the remark codes so that the comparison was made on a like-for-like basis between the two grades.

The first hypothesis was as follows:

Hypothesis 1:
"The steel grade which is scarfed (G4) will have lower lamination defects than that of the steel grade that is not scarfed (G5) regardless of caster, strand or casting conditions."

The theory behind this hypothesis was that, as Grade G4 is scarfed, all the surface and sub-surface defects that cause laminations would be removed. This would mean that those defects would not be carried through to the mill where they would cause lamination defects in the strip. However, as Grade G5 does not undergo scarfing and is sent direct to the mill for rolling and defects exist, then these would cause lamination defects in the rolled strip.

To test this hypothesis the total counts for big, medium and small laminations were compared for Grades G4 and G5. Data came from two of the casters and strands at Plant C. In total, there were 946 coils of G4 grade and 744 coils of G5 grade. Figures A4.28 to A4.30 show the percent frequency populations of total coil counts for big, medium and small laminations respectively.

Due to the small differences in percent frequency between grades G4 and G5, the number of defects from each coil were grouped into ranges. Table A4.4 shows the format in which the data were analysed and presented in Figs. A4.28 to A4.30.

By grouping the counts and adding the percent frequencies together the effects of scarfing could be better analysed. A comparison between the two grades was made by subtracting the total frequency percentage in each range for grade G5 from that of Grade G4. A figure that was positive indicated that there had been an increase in the percentage frequency for Grade G4 for that lamination count range. A figure that was negative indicated a decrease in the percent frequency. It was hoped that for high lamination counts the results would be negative, i.e. the percent frequency had fallen for the scarfed

Grade G4. This would mean the occurrence of coils with many laminations had fallen indicating scarfing had effectively removed many of the lamination causing defects. If this were the case it would therefore be expected that for low lamination counts the results would be positive, i.e. the percent frequency had increased for Grade G4.

By referring to Fig. A4.28 it can be seen that for big laminations the count ranges above 0 to 5 per coil have predominantly negative values. This indicates a reduction in high counts for Grade G4 compared to G5. This results in a positive value for the range 0 to 5 counts per coil of 4.43. Thus, there was an overall improvement in the surface quality of the rolled coil due to scarfing. However, it must be noted that the overall improvement is very small as the differences in percentage frequency are well below 5. It was hoped that the effects of scarfing would have exhibited a more pronounced effect for bigger lamination defects.

For medium lamination defects (Fig. A4.29), a slightly better improvement is seen. The count ranges above 0 to 5 per coil showing negative values when comparing Grade G4 with Grade G5. This indicates an improvement in coil surface quality on Grade G4 due to scarfing. However, it was hoped for a more pronounced effect due to scarfing.

For small lamination defects (Fig. A4.30) the effect of scarfing is more noticeable. This proves that scarfing Grade G4 removed a greater number of defects that led to lower numbers of small lamination counts in the rolled strip.

By taking all three lamination sizes into account it can be concluded that regardless of casting conditions (i.e. remark codes), caster or strand, coils made of Grade G4 exhibit somewhat better surface quality than that of coils made of G5 grade. However, the improvement is not significant and laminations still occur on scarfed coils made of G4 grade. In fact there are still occurrences of G4 grade coils exhibiting large numbers of laminations of all three sizes. The impact of scarfing is not as great as would be expected. This could suggest that the scarfing process is not as effective at removing lamination causing defects or that there are processes after scarfing that could contribute to creating lamination defects in the rolled strip.

A4.5.5 Additional Grade Comparisons

Additional analysis was conducted on two further hypotheses, which are detailed below:

Hypothesis 2 involves comparing G4 to G5 on the same strand. It is expected that G4 will have lower lamination defects than G5 coils because G4 is scarfed. The analysis concluded that, generally, slabs of grade G4 produced coils with lower lamination defect counts than the G5 grade. However, this improvement was found to be strand dependent. The strands are more or less the same width. One strand exhibited a far bigger improvement than the other. It was suggested that the slabs from the strand producing lower quality could not be easily rectified by scarfing alone. It was also stressed that the improvements through scarfing were not significant and laminations still occurred on coils made of G4. In fact there were occurrences of G4 grade coils exhibiting large numbers of laminations of all three size ranges. As found in Hypothesis 1, the scarfing process appeared to be much less effective at removing lamination causing defects than was first thought. However, there could have been a number of processes after or during scarfing that could also have contributed to the lamination defects in the rolled strip.

In Hypothesis 3, it was assumed that the coils of steel grade G4 will have fewer lamination defects than those of grade G5, and would not contribute to mould powder entrapment. The analysis offered a general trend that G4 slabs cast on the same strand with the same casting conditions eliminated the possibility of mould powder entrapment. It also suggested coils with lower lamination defect counts than those of non-scarfed slabs of G5 grade. As found in Hypothesis 2, this improvement was strand dependent. One strand exhibited a far bigger improvement than the other. It was suggested again that scarfing the lower quality slabs from the weaker strand did not eradicate all the surface defects. It was expected that bigger improvements would have been found for coils rolled from scarfed slabs, in particular for the big laminations. Similar percentage improvements across the whole analysis for big

laminations suggest that there could be other processes downstream of the caster that could be contributing to these defects. High laminations counts were also still seen to occur on coils made of G4 grade. In fact there were still occurrences of G4 grade coils exhibiting large numbers of laminations on all three size ranges.

All three of the hypotheses are summarised in Table A4.5.

A4.5.5.1 Discussion

A significant amount of data manipulation has taken place during this investigation. The initial dataset included 946 coils of Grade G4 and 744 coils of G5. These data were then filtered, which reduced significantly the number of coils for analysis. It was extremely difficult to filter the data so that similar casting conditions were obtained. This was due to the large variance in remark codes given to the slabs reflecting differing process conditions. If this analysis were to be undertaken again it would be necessary to obtain a far greater number of coils so that the statistical analysis could be improved. The coil surface quality data extracted from the original dataset using the Clementine models for through process tracking were not filtered to eliminate defects that could have been caused by rolling (or other unrelated non-caster issues). For this reason there may have been instances where defective coils caused by rolling problems were included in the dataset. Therefore, in future investigations, only lamination defects that were definitely of caster origin will be included. This could be an arduous task but would increase confidence in the results.

A4.5.6 Crack Prediction

A data mining exercise was conducted, concerning the surface quality of two steel grades, G9 and G10, at Plant C. Grade G9 is a medium carbon DWI steel that requires mandatory 100% machine scarfing. Grade G10 is a standard tinplate grade, which also undergoes 100% mandatory machine scarfing.

A large amount of slab surface quality data from the manufacturing process of these grades between January 2004 and April 2005, including scarfing and inspection data for longitudinal, star and transverse cracking were obtained. The intention of the work was to identify reasons for going from periods of incidences of defects (even after scarfing) to periods of problem-free slab manufacture. The trial considered the differences in casting parameters for the two scenarios. It was hoped to develop a method to predict the likelihood of severe cracking from the measured levels of such parameters.

By predicting the probability of cracking, the scarfing schedule can be tailored to scarf only the slabs that will have the highest probability of poor surface quality. The other slabs can then be sent direct to the hot mill, without scarfing. This will reduce the scarfing load, thereby reducing costs in both time and yield whilst improving delivery times and enabling some of these slabs to be hot-connected to the equalising furnace, reducing energy requirements.

The work has required access to Plant C's continuous casting mainframe data stores “PI” and “PSMET”. This network connection has now been established and the data analysis is underway.

Preliminary results for "Crack" and "No Crack" slabs for both strands of Caster 1, grades G9 and G10 have not yet highlighted any significant results due to the small population size. This work is continuing with a revised data extraction technique to generate enough data to be of statistical significance. Only when enough data have been extracted can they be analysed satisfactorily using data mining techniques.

A4.6 TRACKING COMPLEX OXIDE DEFECTS AND Fe_xO_y SLIVER DEFECTS

An investigation was also commenced into complex oxide defects and Fe_xO_y "sliver" defects on cold rolled and galvannealed strip grades. While the chemical composition of material within a line defect on strip can be used to indicate process origin, this information can be misleading. It is therefore also necessary to consider the size and geometry of defects as they evolve at each processing stage. Actual defects are difficult to identify and track through the process for a number of reasons. These include poor defect visibility, inspection shortfalls and the physical difficulty of inspection in high-speed rolling processes. However calculations of defect sites are made where possible for each stage.

The causes of Fe_xO_y sliver defects have not been proven, but argon bubbles in the cast slab may well be the origin. This is being examined as a potential root cause by Fe_xO_y defect characterisation together with plant data and examination of internal defect oxidation features associated with defects at different stages. Actual pinholes and artificially produced defects were tracked through the process route through to final rolled strip.

At Plant C, project work was undertaken on through-process tracking of artificial slab defects. This involved using a magnetic pillar drill to make a series of holes with different depths and diameters in a pre-scarfed slab. These holes were intended to represent a range of defects, including pinholes and cracks. The slab was then reheated and processed to strip according to Plant C guidelines, with defects mapped and measured at each stage via combinations of detailed human and camera system inspections. It was found that the depth and length, as taken from the slab, correlated to the final depth and length on the strip. As expected, the greater the depth and length of the initial slab defects, the greater the length of defects on the final strip product.

This work, conducted by Plant C, demonstrated that it was possible to track a slab from casting through to final product. Therefore, should any defective coils be manufactured, the slabs used can be identified and casting parameters during the manufacturing phase can be checked to troubleshoot and avoid any issues in the future.

A4.7 TRACKING DEFECTS USING THE CH SYSTEM AND PARSYTEC

A study concerning the effect of defects in slabs through the downstream processes, was initiated to track defects from slabs to hot rolled coil. Different tools were applied to develop an analysis technique for this purpose. For this project, it was necessary to link two sources of defect information:

- Slab surface defects, from the on-line CH crack detection system (Surfin), as shown in Fig. A4.31.
- Coil surface defects, from the Parsytec hot strip mill inspection system, as shown in Fig. A4.32.

It was possible a conduct rapid assessment and traceability of the products with Mityca software (shown in Fig. A4.33), a tool developed by Arcelor which provides detailed information about the product history.

A4.7.1 Slab Defect Classification

The first prototype of the on-line CH longitudinal crack inspection system has been working on-line from 2004 to 2006. Slabs with cracks that were detected by the CH system presented downstream defects if they were not properly rectified. As the work progressed further, it was possible to determine how these defects impacted downstream processes in terms of generating other surface defect anomalies.

Based on the inspection results of more than 2000 slabs, a classification of possible surface defects has been made in order to extend the study to other surface defects besides cracks. The categories shown in Table A4.6 have been defined. Some examples of these types of defects are illustrated in Figs. A4.34

to A4.36. It should be noted that this classification has been made with the results of the first prototype and thus is limited to only the top face of the slab. The new on-line inspection system makes it possible to analyse defects on the bottom face of the slab. During the first two weeks of operation, it has been possible to detect new defect configurations and examples of defects that passed unnoticed on those steel grades which were not systematically or mandatory inspected by the operator.

An example of a new defect detected is illustrated in Fig. A4.37. This has been found in the head and tail ends of certain slabs and can be attributed to fluid streams in the oxygen-cutting machines. This steel grade is always scarfed. Without automatic inspection it had not been possible to detect this problem prior to scarfing as the human operator in the scarfing yard only inspected the slabs after scarfing, when the defect had been removed. The CH system found the defect in the casting plant.

A4.7.2 Tracking of Defects – Results and Discussion

Until almost the end of the project, surface inspection of the slab at Arcelor was limited to a slab width of 900 mm. This partial information made it difficult to search for correlations between slab defects and the defects found with Parsytec after the hot strip mill. In addition, the automatic reports generated by the Parsytec system cannot be directly analysed, as different types of defects are taken into account simultaneously. Instead, a detailed coil-by-coil analysis is required. As a result of this situation, only infrequent studies could be performed, but the results were very promising.

A comparison of surface defects, using plant data and downstream quality inspections has been performed for some heats. Figure A4.38 shows the results obtained for a cast that contained longitudinal cracks. It can be seen that the identification of the occurrence of this problem by thermocouples in the mould is not always possible. By contrast, the existence of the defects is clearly revealed by the on-line CH crack detection system. Because the CH system could detect the presence of these defects after the casting process, it was possible to send slabs with no defects in them immediately downstream, thereby bypassing the scarfing process. The slabs/coils that were not scarfed were then carefully analysed by the Parsytec system. No defects were found in the coils. This successfully demonstrated the automatic inspection system saving costs by not having to scarf and manually inspect slabs. Now, the new CH system with top and bottom face inspection makes it possible for a more systematic study correlating slab quality with coil quality.

Table. A4.1: Contents of steel and standard processing requirements for casts investigated

Cast number	Date cast	Quality code	Contents of steel at tapping / %																
			C	Si	Mn	P	S	Al	N	Nb	Cr	Ti	Mo	Ni	H	SolAl	As	B	CO
60933	13/07/05	M1	0.17	0.36	1.41	0.014	0.005	0.043	0.0052	0.029	0.017	-	0.002	0.02	2.9	0.041	0.002	0.0001	-
60935	13/07/05	M1	0.16	0.36	1.4	0.012	0.005	0.04	0.0063	0.028	0.029	-	0.007	0.023	2.1	0.038	0.002	0.0001	-
60942	13/07/05	M1	0.16	0.36	1.41	0.014	0.004	0.035	0.0077	0.026	0.021	-	0.002	0.02	2.5	0.034	0.002	0.0001	-
60954	13/07/05	M4	0.083	0.33	1.47	0.006	0.004	0.036	0.0043	0.02	0.017	0.0075	0.002	0.41	2.6	0.038	0.002	-	-
60969	14/07/05	M5	0.2	0.23	1.09	0.014	0.005	0.042	-	-	0.019	-	0.002	0.021	2.4	0.04	0.002	0.0001	0.003

Quality code	Proof Dress	Normal Scarf, x top, x btm	Dye pen
M1	Bottom	Yes, 2T	-
M5	-	-	-
M4	N/A	N/A	N/A

Table A4.2: Observations of dye-penetrative tested slabs

Cast Number	Skelp		Top or bottom	Comments from cast and scarfer sheets	Observations after dye-pen
60933	5A		Btm	Standard processing, 1 extra pass on bottom	Clear
60933	5B		Btm	Standard processing	Clear
60933	5E		Tp	Standard processing	Cracks of order 2-3cm, transverse, between 290 and 330cm from number end in gutter, on left hand side viewed from number
60933	6A		Tp	Standard processing top, 1 extra pass on bottom	Clear
60933	6B		Btm	Standard processing	Cracks of order 1cm, longitudinal, between 60 and 140cm from number end in gutter on right hand side viewed from number
60933	6E		Tp	Standard processing	Clear
60935	5B		Tp	3 extra scarfer passes on top due to transverse cracks, proofed ok on bottom	Clear
60935	5D		Tp	3 extra scarfer passes on top due to transverse cracks, proofed ok on bottom	Clear
60935	6B		Btm	5 extra scarfer passes on top due to transverse cracks, proofed ok on bottom	Clear
60954	5A		Btm	Standard processing	Clear
60954	5B		Btm	Standard processing	Clear
60954	5E		Btm	Standard processing	Clear
60954	6A		Btm	Standard processing	Clear
60954	6B		Btm	Standard processing	Clear
60954	6E		Btm	Standard processing	Clear
60969	5A		Btm	Very high superheat, cast slowly, standard processing	Clear
60969	5B		Btm	Standard processing	Clear
60969	5E		Btm	Standard processing	Clear
60969	6A		Btm	Standard processing	Blowholes opposite to number end
60969	6A		Tp	Standard processing	Clear
60969	6B		Btm	Standard processing	Clear
NB. By the time a lot of these were dye-penned, scale was significant, obscuring the majority of the skelp surfaces					

Table A4.3: Data sources at Plant C

Data Source	Description
PSMET (Steelmaking Relational Database)	Relational data such as steel chemistry for given casts. Also aggregated information for slabs including time created.
PI (Steel Plant Dynamic Data, e.g. Casting Speed)	Data recorded at appropriate resolution to describe process. This is stored on a time base however, and slab boundaries/cast lengths are not incorporated.
Scarfing Database	Technical Department database detailing scarfing treatments for specific slabs.
Through Process Data Warehouse (TPDW)	Product tracking data giving key product identities through each process. Very large database with multiple entries added as new information is gained about products.
Hot Mill Database	This is a SQL Server database established in conjunction with 'Roll Management' ECSC project. This integrates data from hot mill systems including the Parsytec camera inspection system.

Table A4.4: Analysis table for coil lamination counts (Corus)

Big/Medium/Small Lam			
Range	% of Population		+/-
	G4	G5	
0 to 5			
6 to 10			
11 to 15			
16 to 20			
21 to 25			
26 to 30			
31 to 35			
36 to 40			
41 to 45			
46 to 50			
Total			

Table A4.5: Summary of each of the hypotheses

Hypothesis 1 Any strand, any caster	Hypothesis 2 Same caster & strand	Hypothesis 3 Same caster & strand Conditions the same, which should not contribute to mould powder entrapment
G4 slightly better than G5. Laminations still occurring on G4, on big, medium and small laminations. Scarfing does not significantly improve quality. Defects could arise from elsewhere.	One strand exhibited a bigger improvement for G4 than the other One strand was much better than the other. G4 grades again suffered from defects on big, medium and small laminations. Defects could arise from elsewhere.	One strand exhibited a bigger improvement for G4 than the other. Big laminations still found. Defects could arise from elsewhere.

G4 – Scarfed
G5 – Not Scarfed

Table A4.6: Categories for surface defects (D)
and inspection errors (E) for on-line surface inspection of slabs

D10. CRACK
D11. Center
D12. Border
D20. DEPRESSION
D21. Center
D22. Border
D23. Associated to scale
D30. MARK
D31. Longitudinal and continuous
D32. Longitudinal intermittent
D33. Periodic
D34. Deburrer mark
D40. OTHER
D41. Deformed
D42. Type B configuration
D43. Object
D44. Cast stopped
E10. ACQUISITION
E11. Sensor failed
E12. Partial
E13. Repeated frame
E14. False longitudinal mark
E20. PROCCESING
E21. Border detection
E30. CLASSIFICATION
E40. PROCCES CONDITIONS
E41. Stopped slab
E42. Twisted slab

http://www.gega.de

http://www.gega.de/

Fig. A4.1: Scarfer similar in design to that used at Plant A

http://www.multiserv.co

http://www.gega.

Fig. A4.2: Androfer^{TM} scarfer in operation

Cast 79556 Skelp 5A Top Face (305x1970mm)
Magnetic Particle Inspection Results After Scarfing Passes

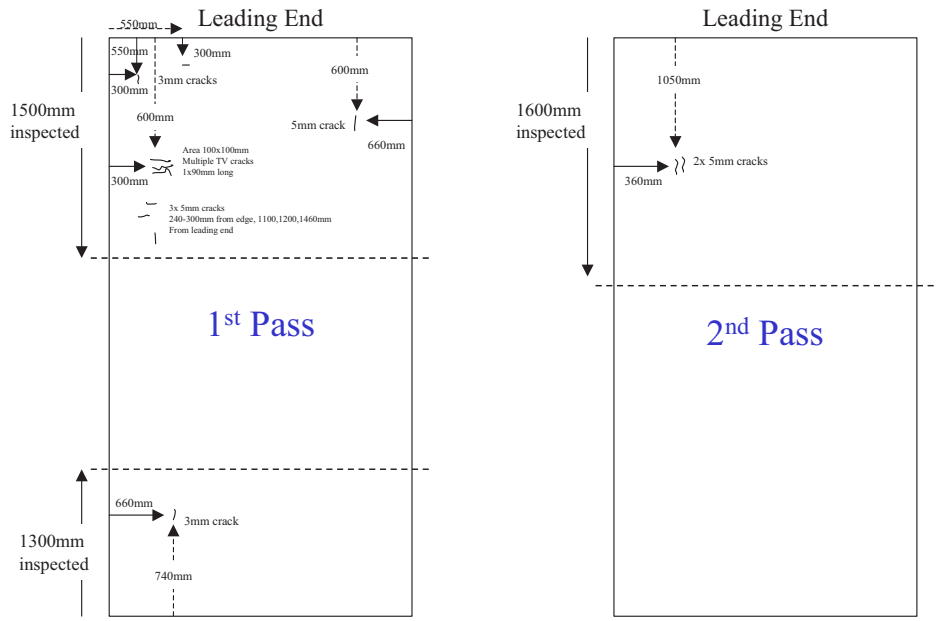

Fig. A4.3: Magnetic particle inspection for cast 79532

Cast 79532 Skelp 5A Top Face (305x1970mm)
Magnetic Particle Inspection Results After Scarfing Passes

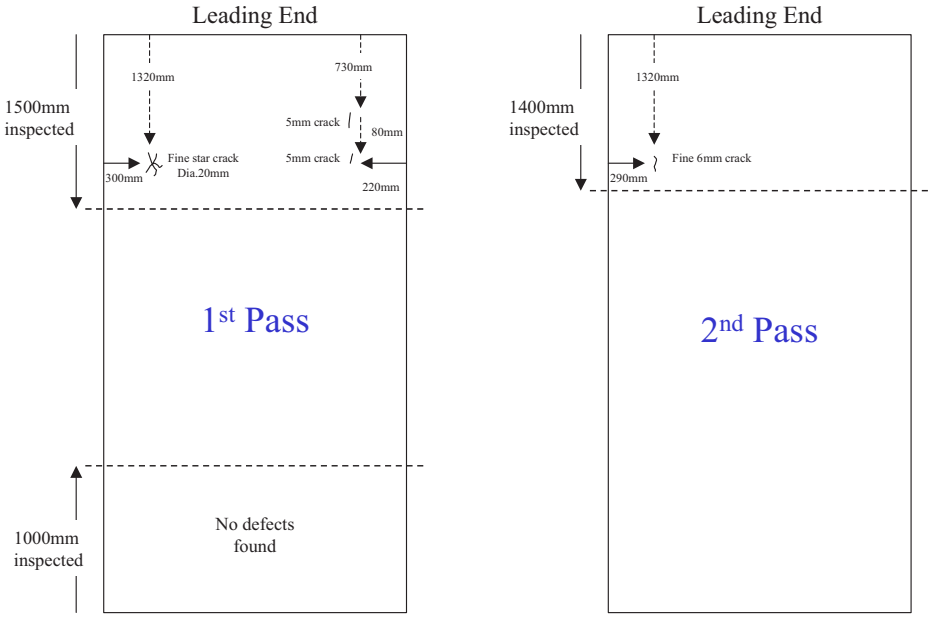

Fig. A4.4: Magnetic particle inspection for cast 79556

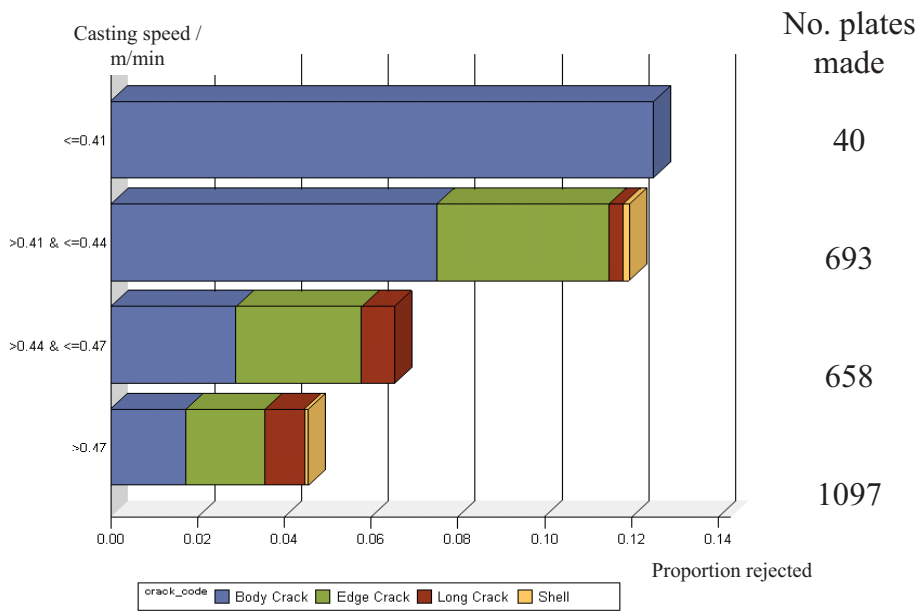

Fig. A4.5: Proportion of plates rejected against casting speed of associated slab (Courtesy Corus Plant A)

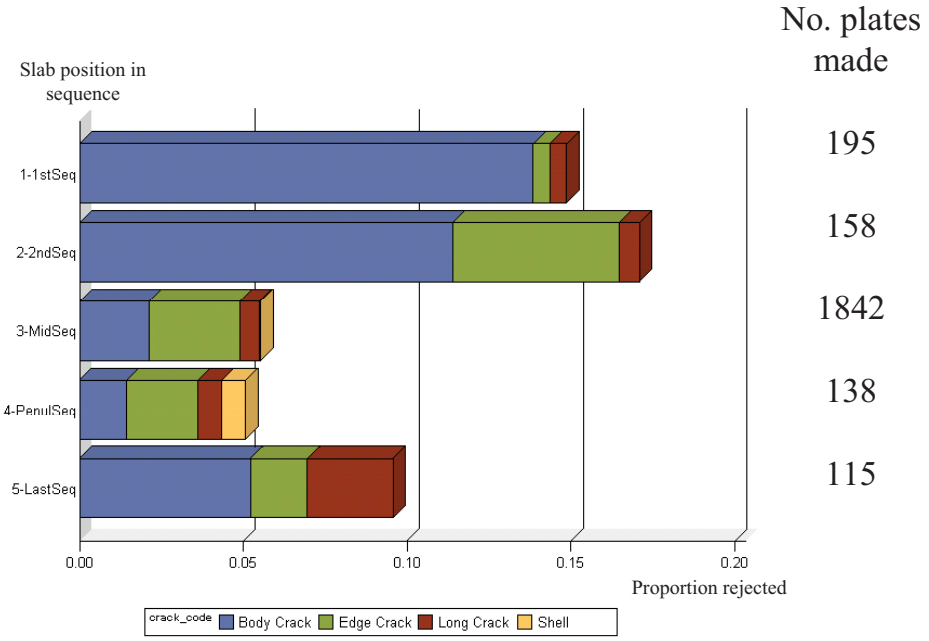

Fig. A4.6: Proportion of plates rejected against position in sequence of associated slab (Courtesy Corus Plant A)

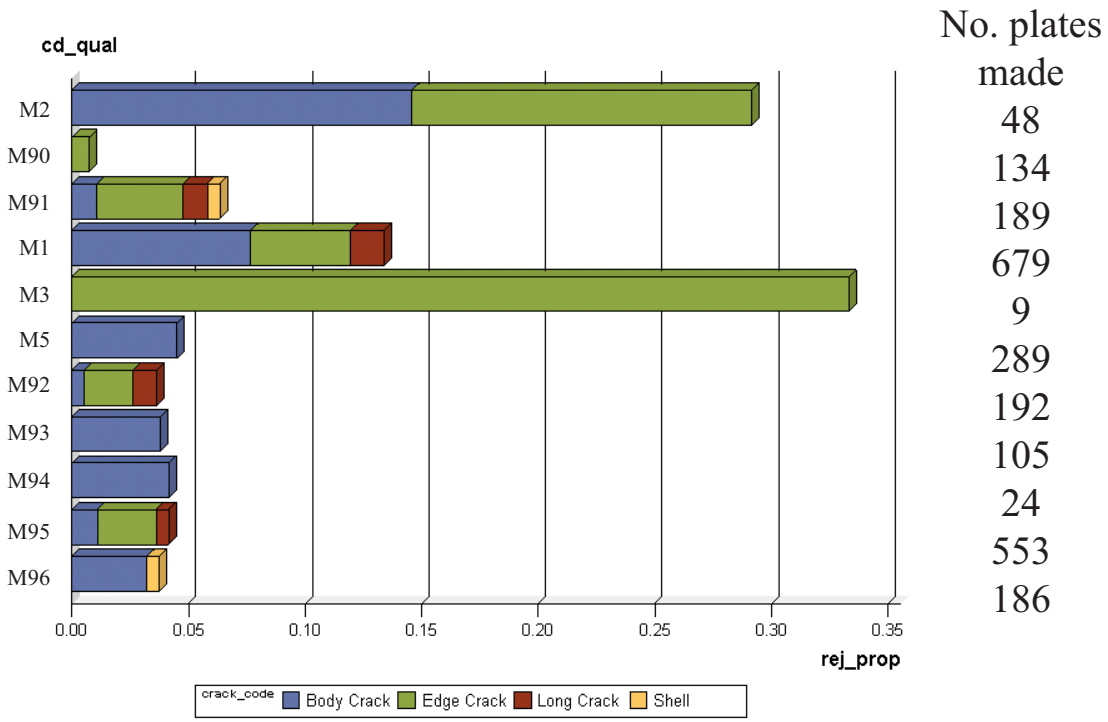

Fig. A4.7: Proportion of plates rejected against quality code of steel
(Courtesy Corus Plant A)

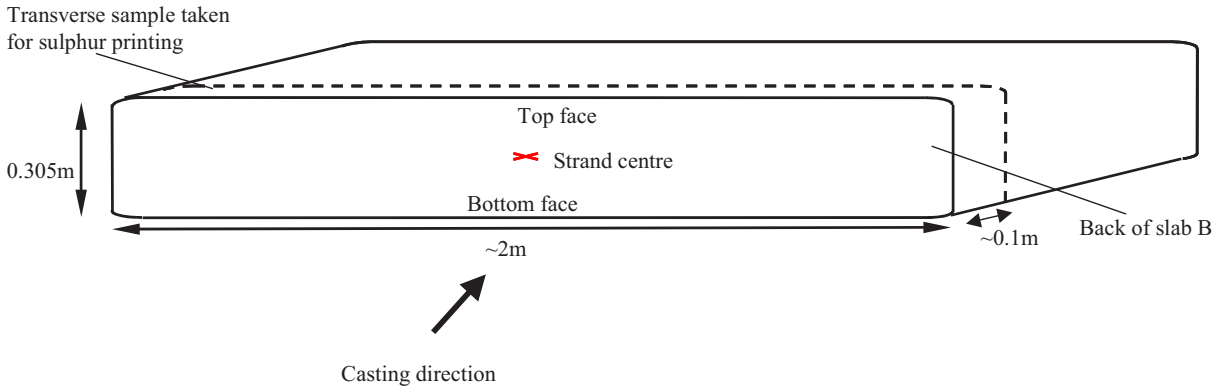

Fig. A4.8: Sulphur print sampling diagram

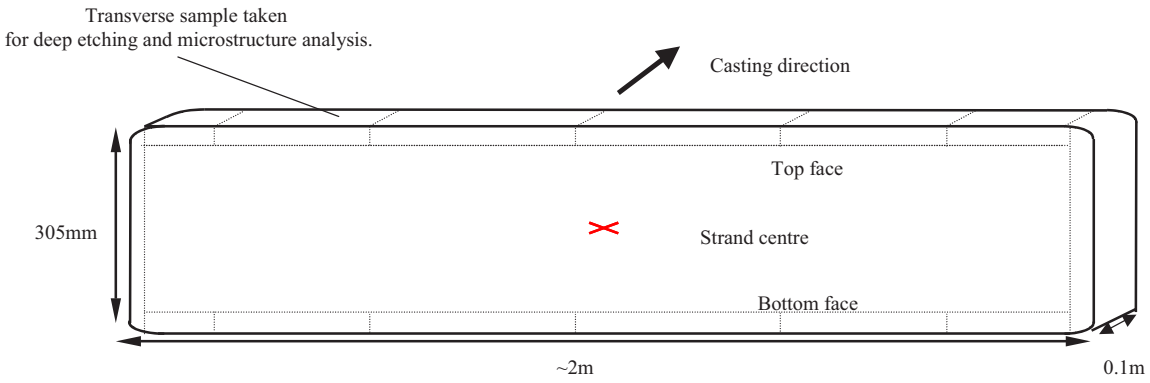

Fig. A4.9: Sampling diagram for de-scaling with acid bath and microstructural work

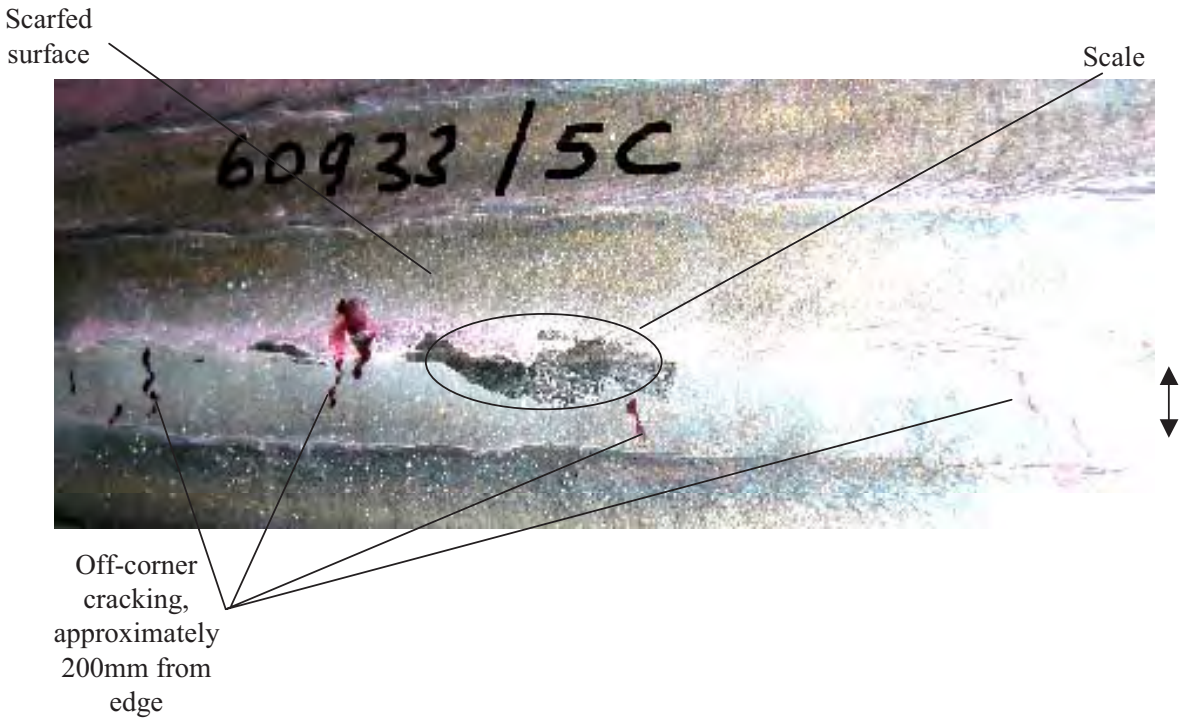

Fig. A4.10: Photograph of cracks found on broad face of cast 60933, slab 5C

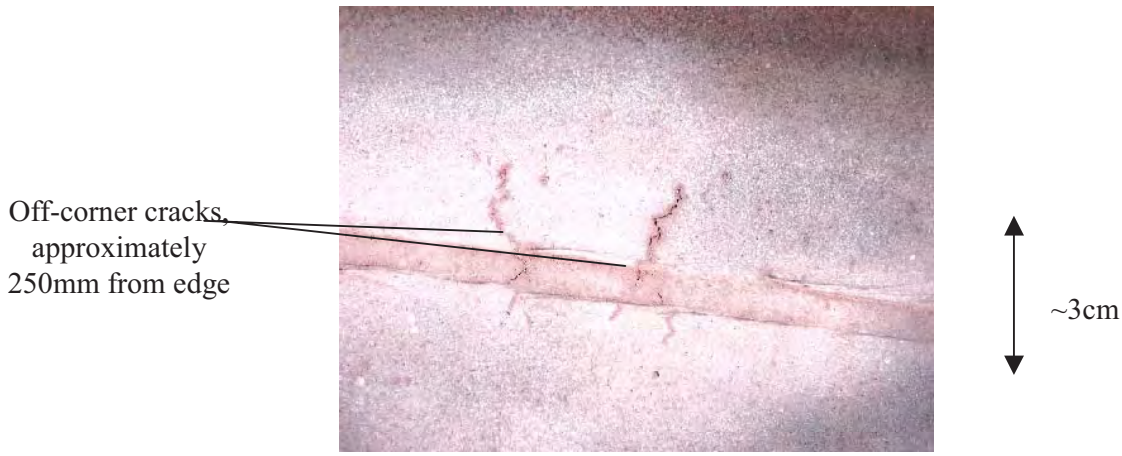

Fig. A4.11: Photograph of cracks found on broad face of cast 60933, slab 5E

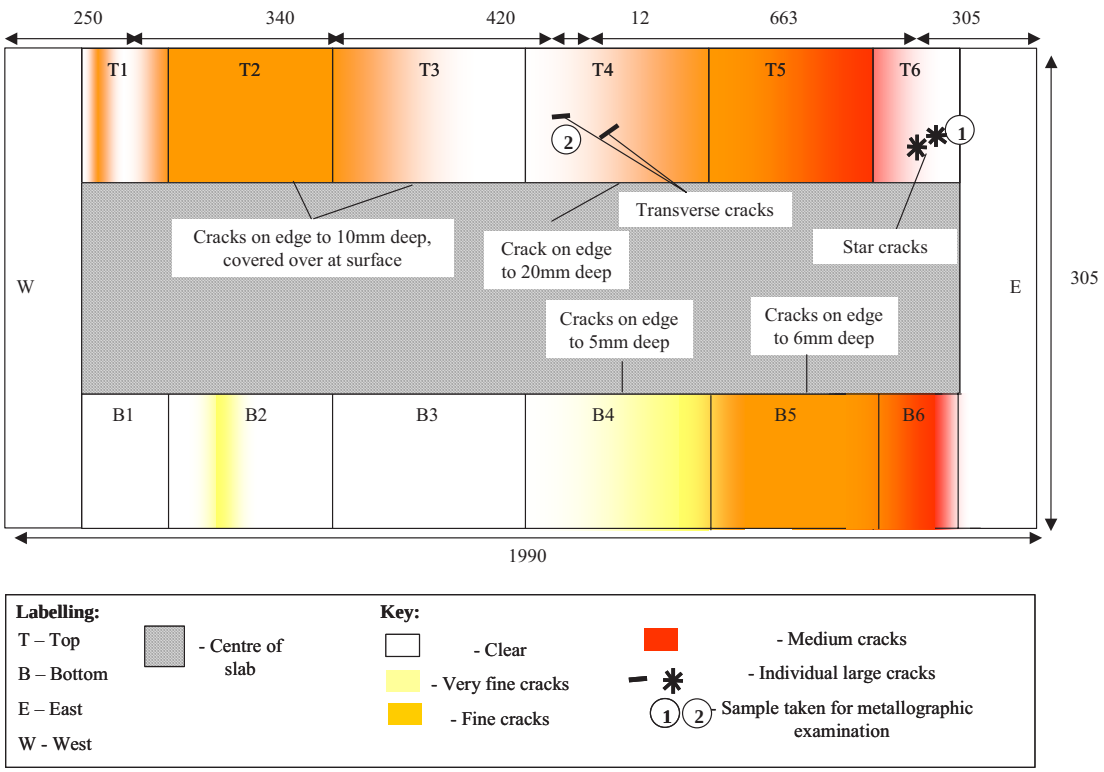

NB. All dimensions in mm

Fig. A4.12: Section of cast 60933, slab 5B showing surface defects on folded out edge and broad face

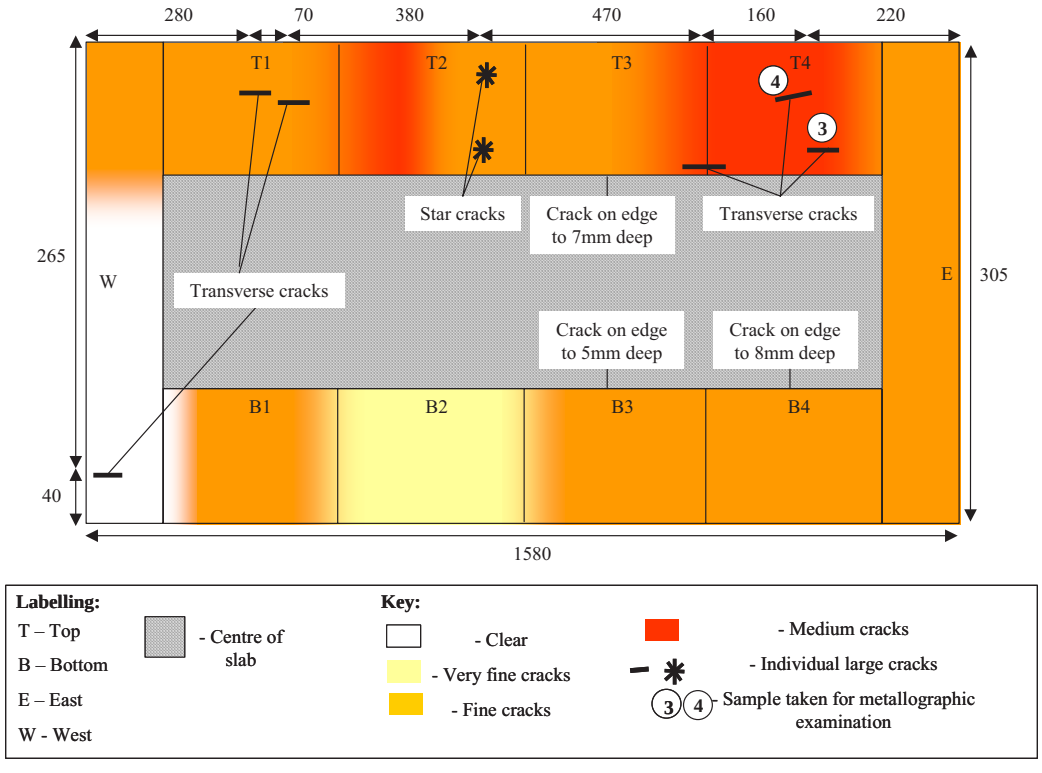

NB. All dimensions in mm

Fig. A4.13: Section of cast 60933, slab 6B showing surface defects on folded out edge and broad face

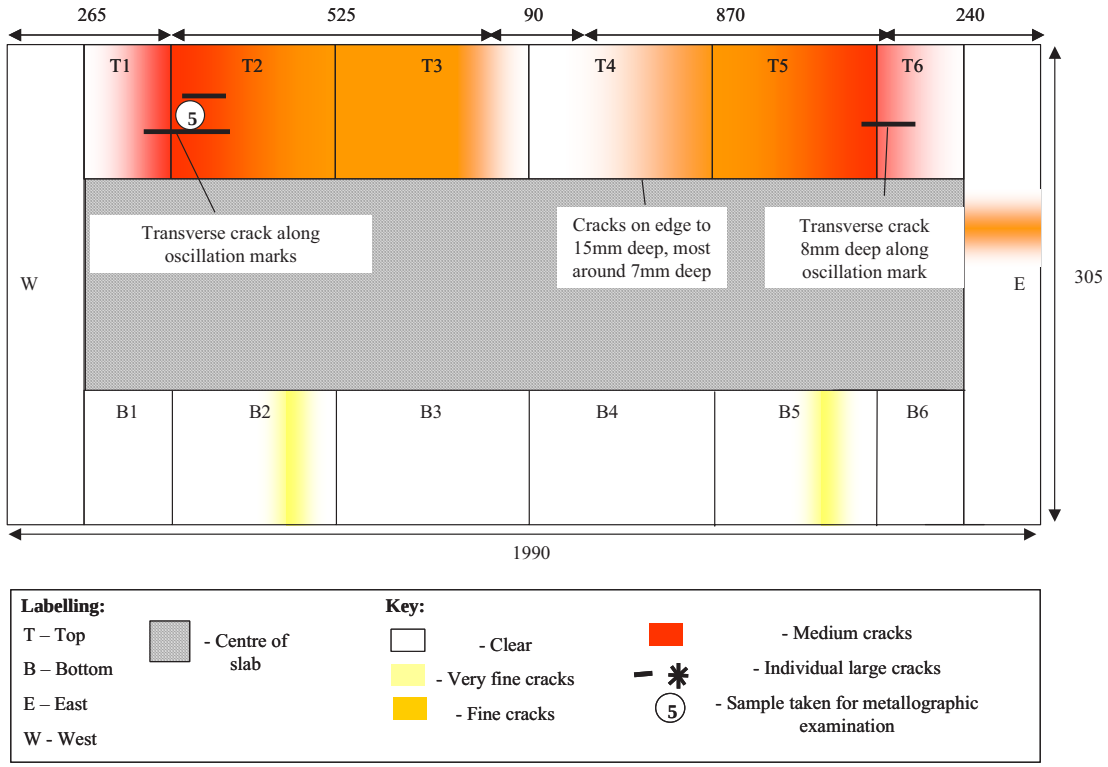

Fig. A4.14: Section of cast 60942, slab 5B showing surface defects on folded out edge and broad face

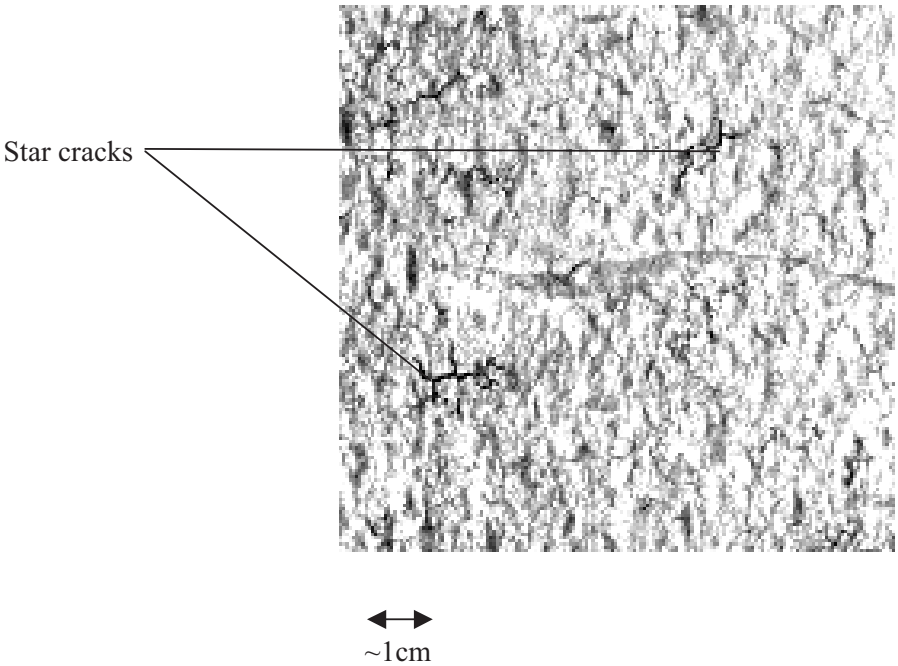

Fig. A4.15: Photograph of crack networks from Fig. A4.12, cast 60933, slab 5B, sample 1 after deep etching to remove scale

Fig. A4.16: Cross-section and microstructure of crack networks, cast 60933, slab 5B, sample 1, after etching, x50

Fig. A4.17: Cross-section of small crack, cast 60933, slab 5B, sample 2, after etching, x50

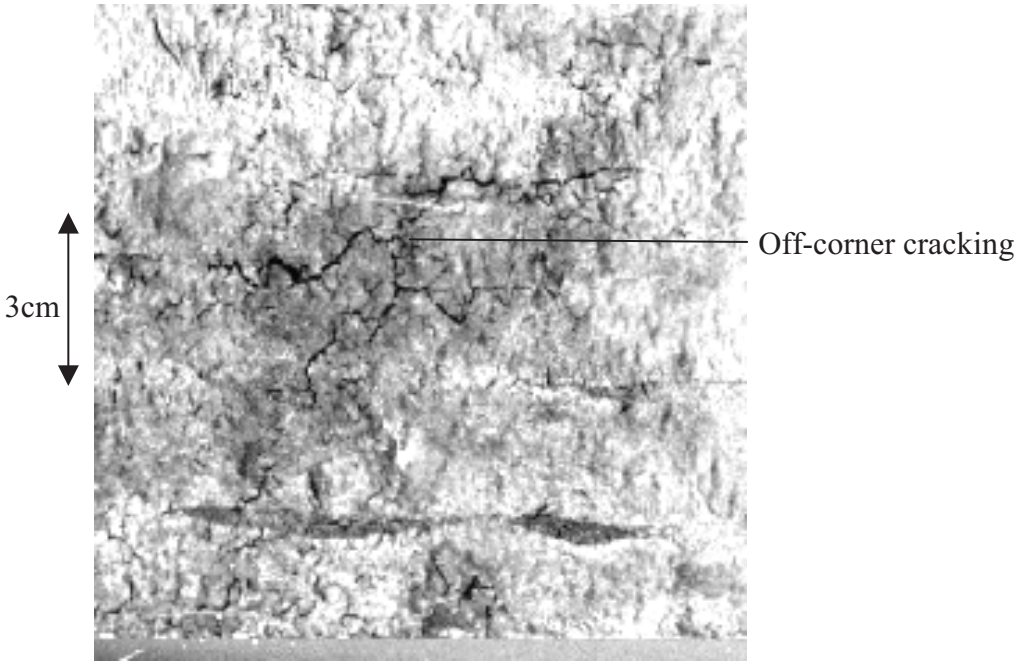

Fig. A4.18: Photograph of cracking from Fig. A4.13, cast 60933, slab 6B, samples 3 and 4, after deep etching to remove scale

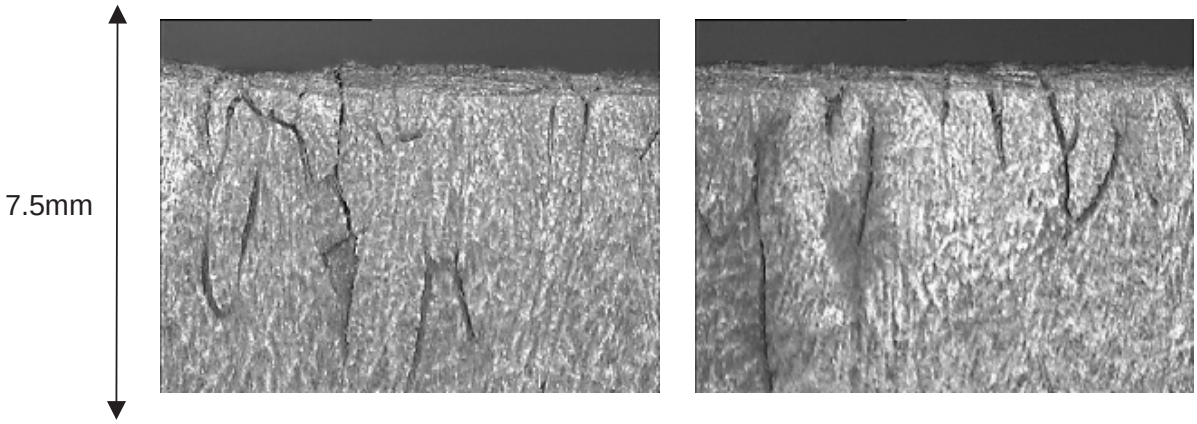

Fig. A4.19: Cross-section of crack, cast 60933, slab 6B, samples 3 and 4

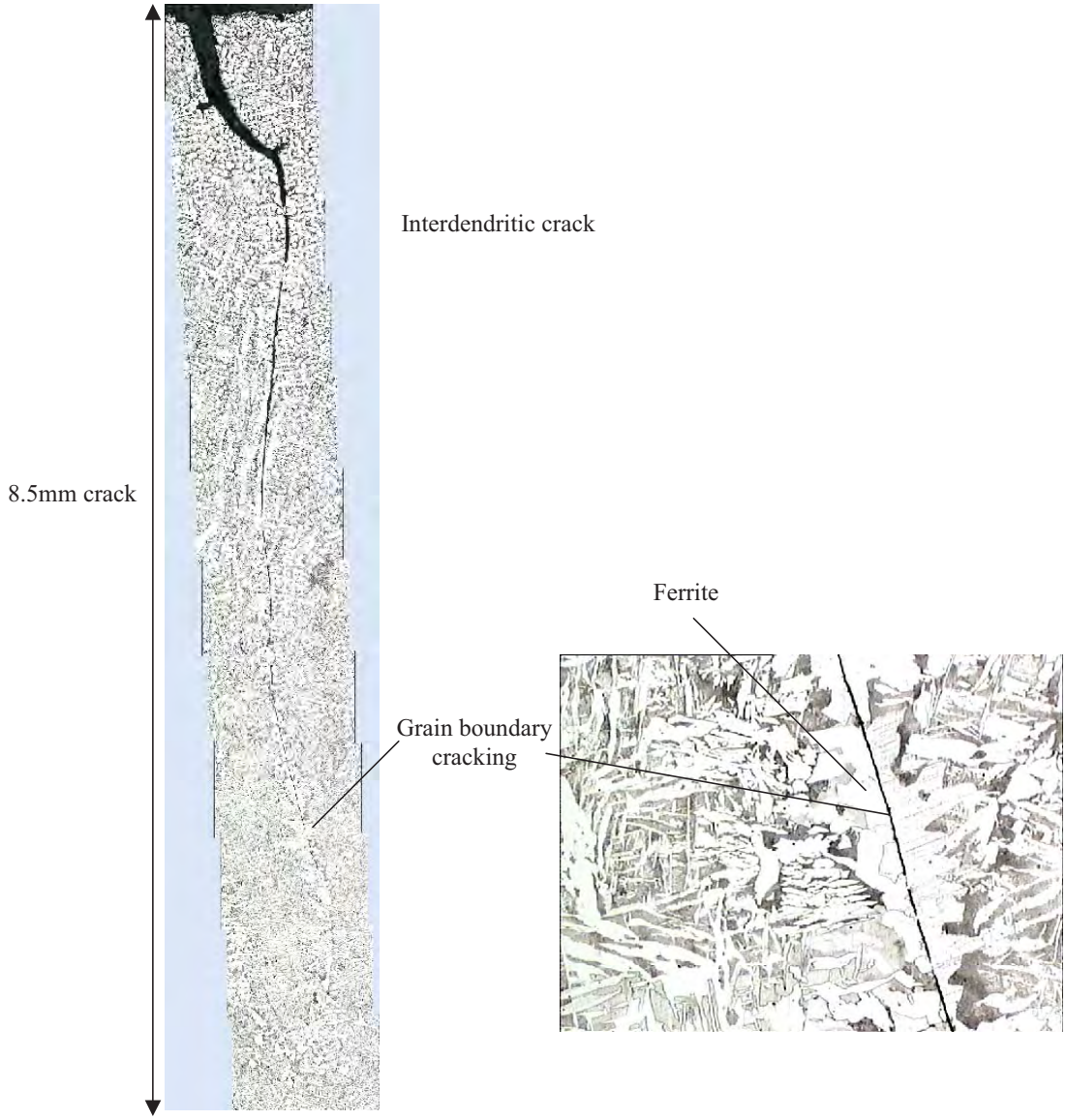

(a) 8.5 mm crack, after etching x50

(b) 8.5 mm crack, after etching x100

Fig. A4.20: Microstructures of cracks, cast 60933, slab 6B, sample 4

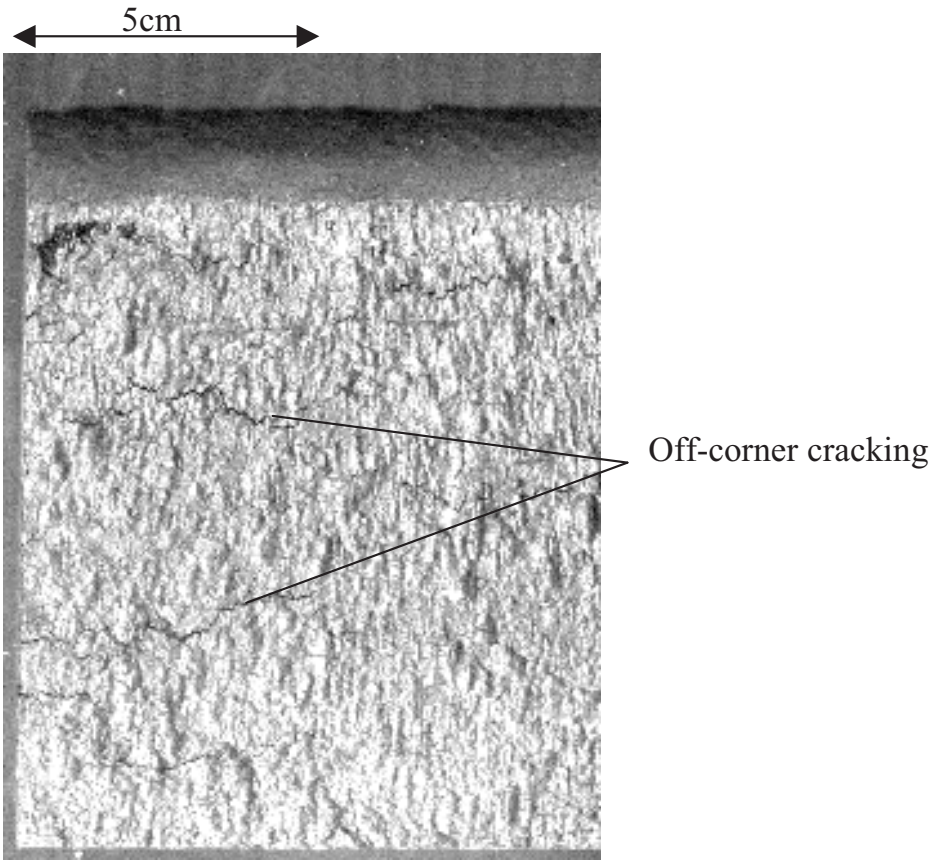

Fig. A4.21: Photograph of cracking from Fig. A4.14, cast 60942, slab 5B, sample 5 after deep etching to remove scale

Fig. A4.22: Cross-section and microstructure of crack, cast 60942, slab 5B, sample 5, after etching, x100

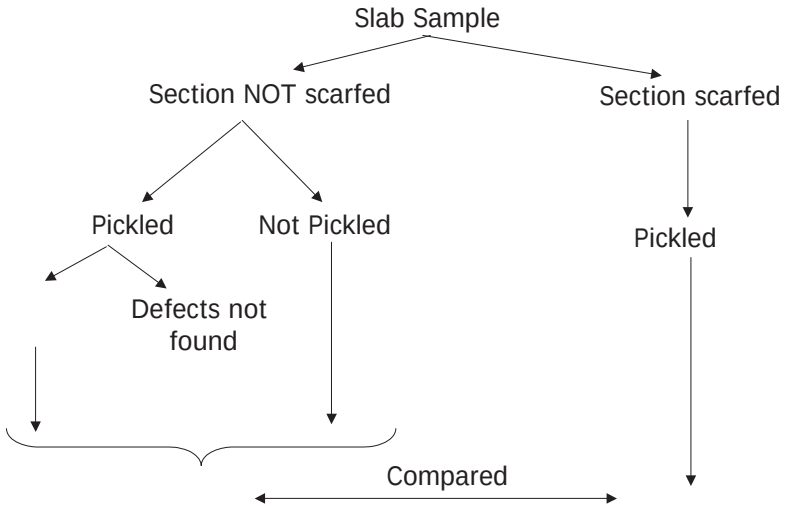

Fig. A4.23: Schematic summarising the sampling technique

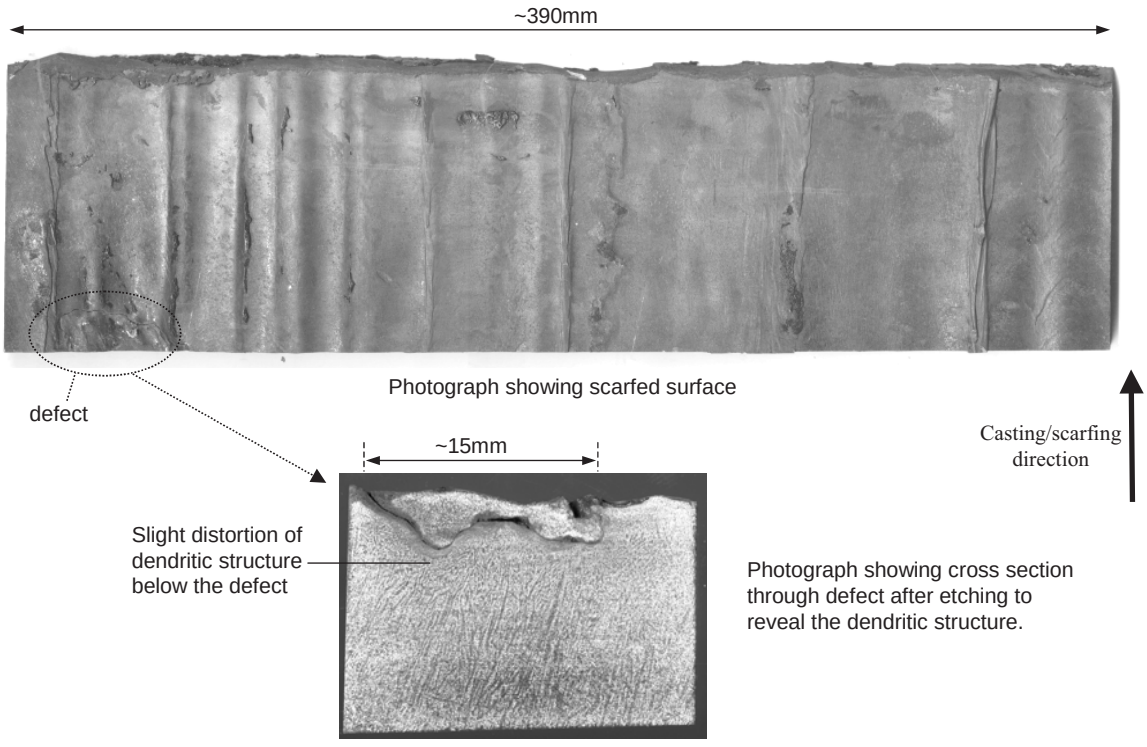

Fig. A4.24: Photograph of the sliver found in the scarfed sample

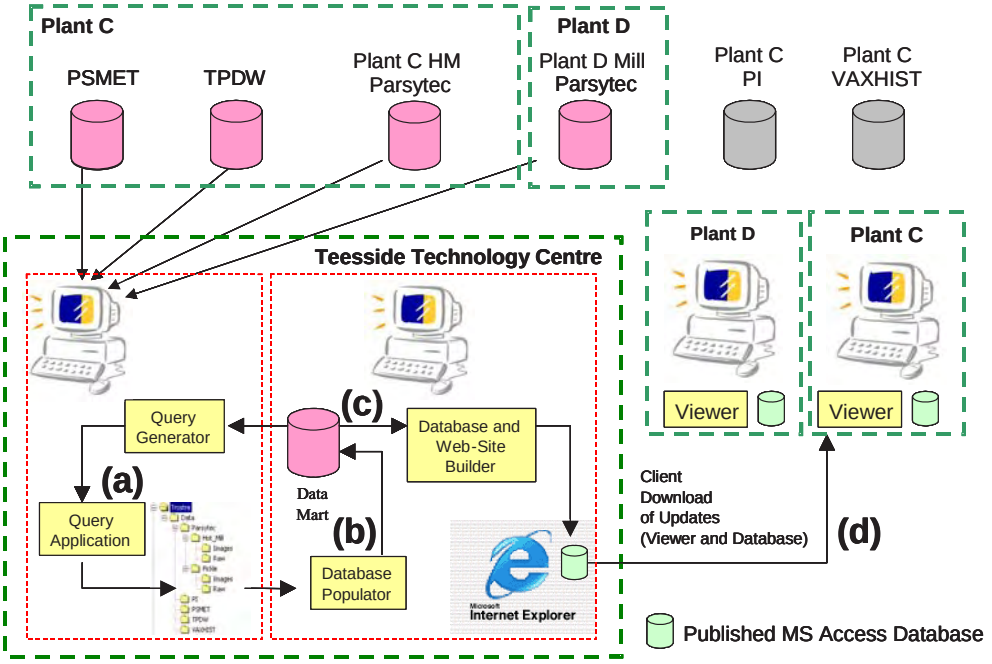

Fig. A4.25: Data collection infrastructure for the slab tracking and inspection project

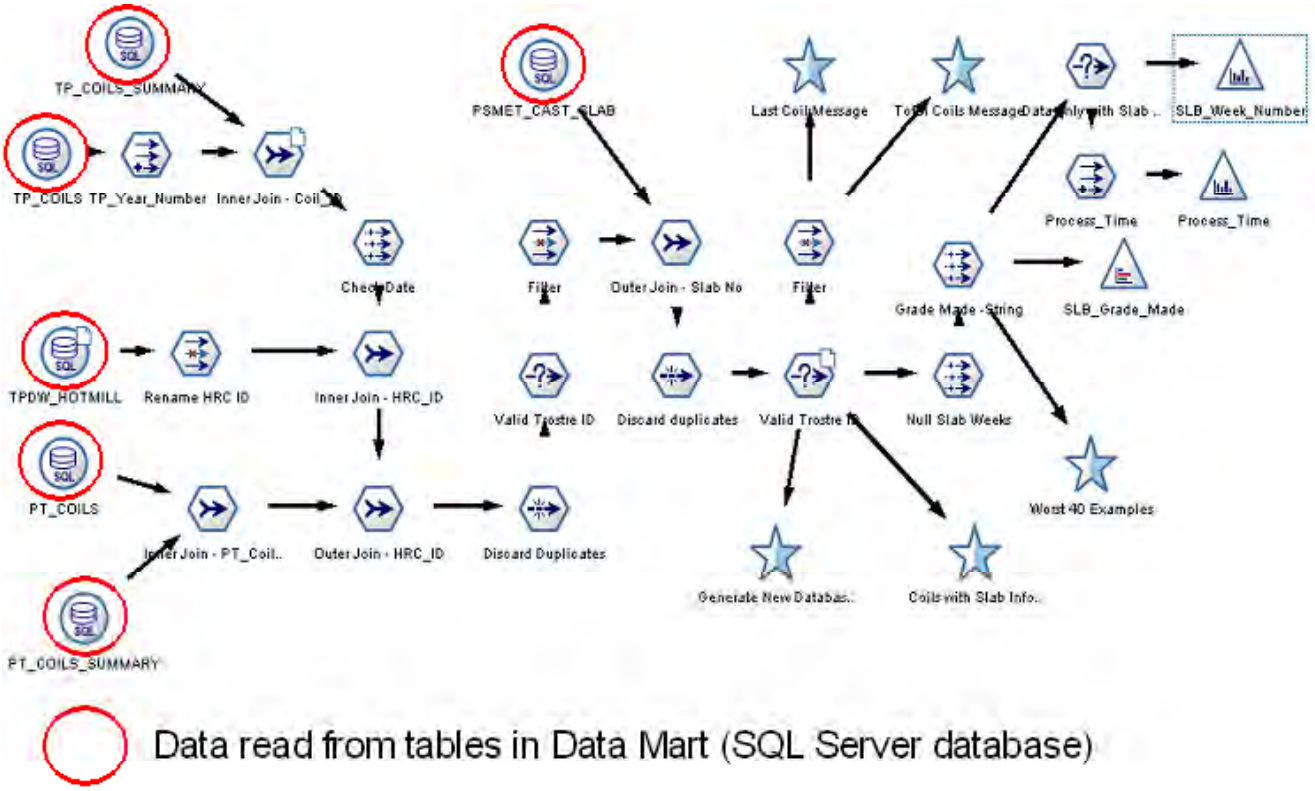

Fig. A4.26: The use of Clementine for data analysis

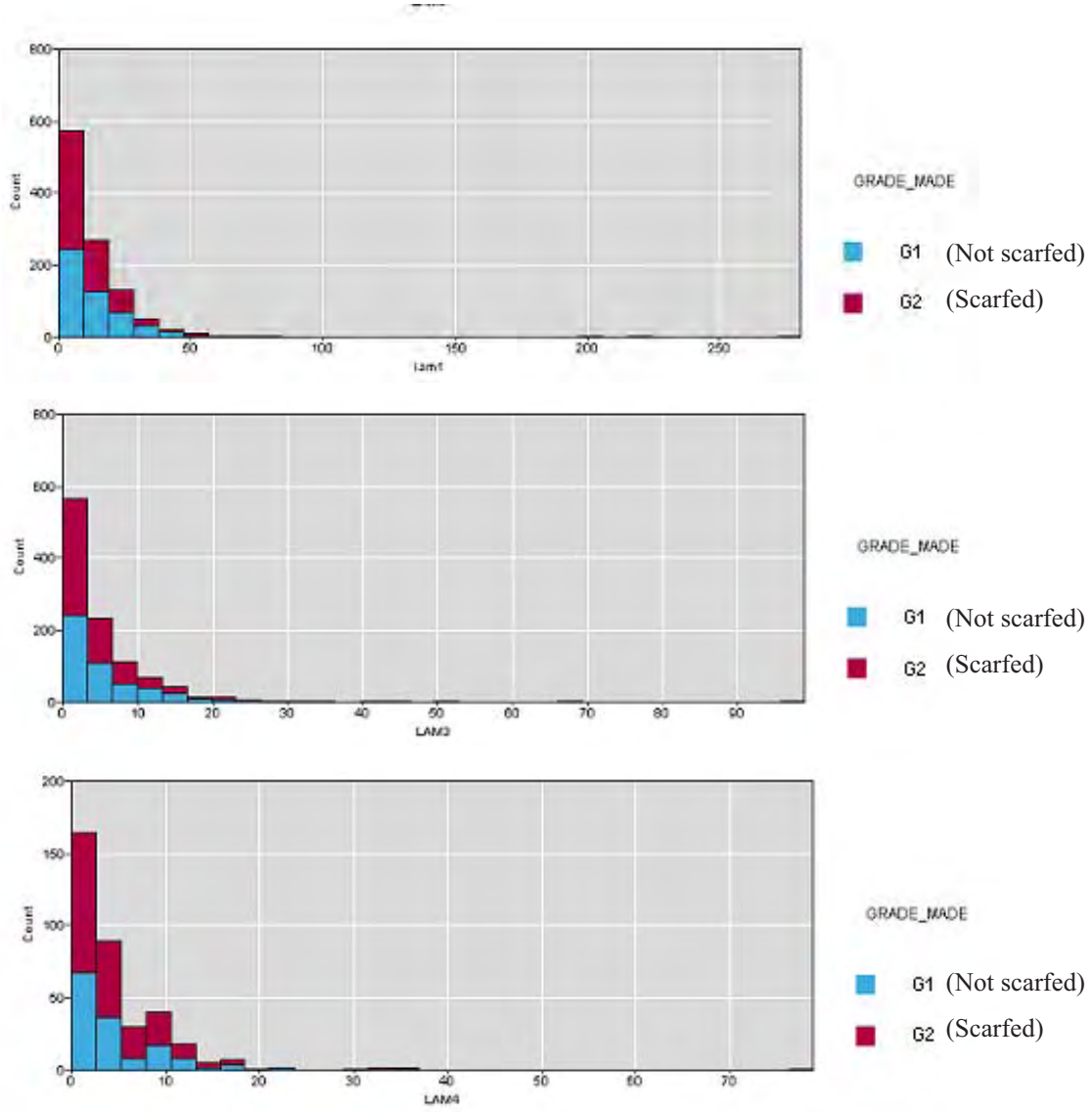

Fig. A4.27: Lamination results for steel grades G1 and G2

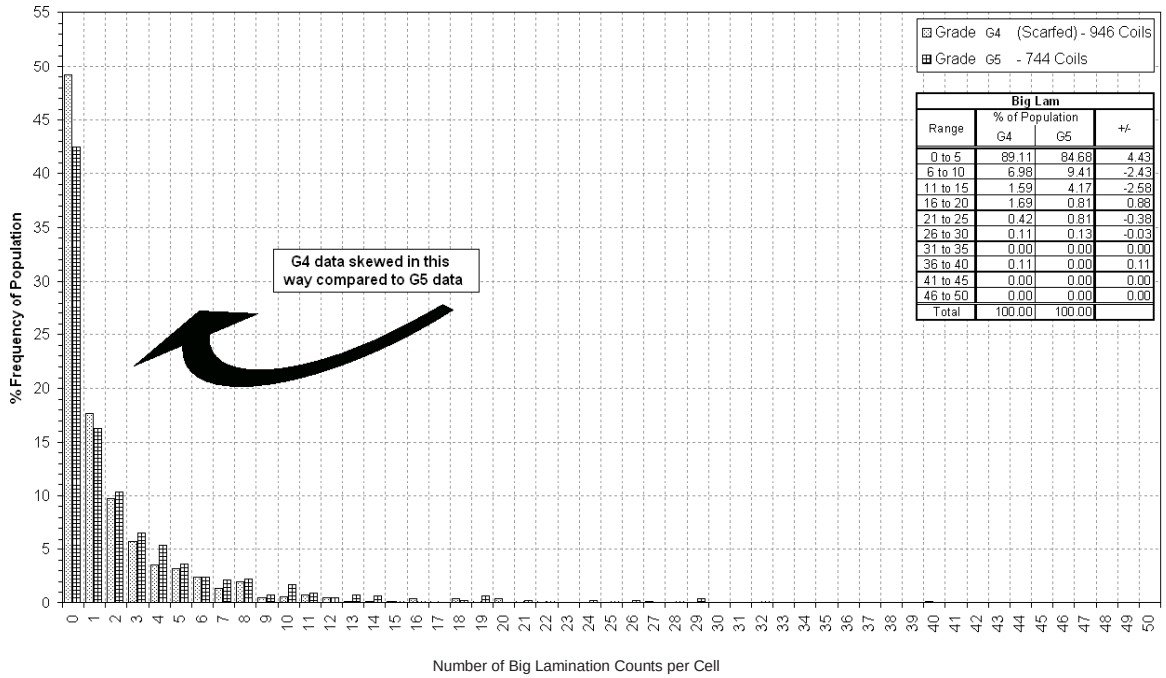

Big Lam			
Range	% of Population		+/-
	G4	G5	
0 to 5	89.11	84.68	4.43
6 to 10	6.98	9.41	-2.43
11 to 15	1.59	4.17	-2.58
16 to 20	1.69	0.81	0.88
21 to 25	0.42	0.81	-0.38
26 to 30	0.11	0.13	-0.03
31 to 35	0.00	0.00	0.00
36 to 40	0.11	0.00	0.11
41 to 45	0.00	0.00	0.00
46 to 50	0.00	0.00	0.00
Total	100.00	100.00	

Fig. A4.28: The effect of scarfing on big laminations

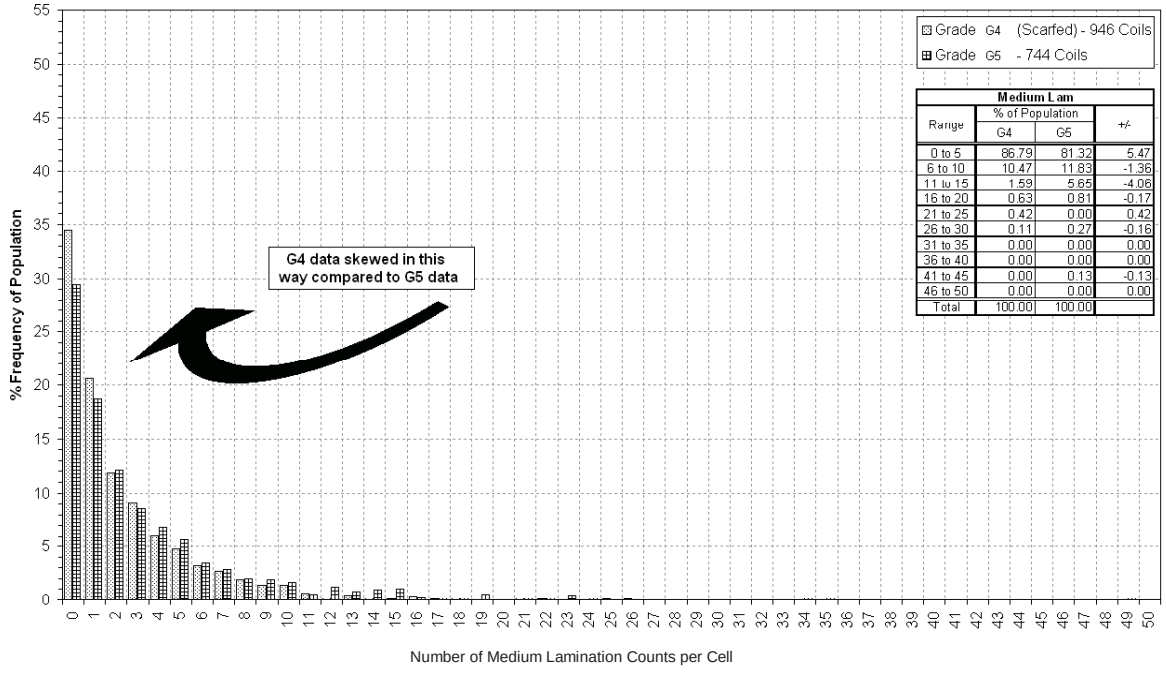

Medium Lam			
Range	% of Population		+/-
	G4	G5	
0 to 5	86.79	81.32	5.47
6 to 10	10.47	11.83	-1.36
11 to 15	1.59	5.65	-4.06
16 to 20	0.63	0.81	-0.17
21 to 25	0.42	0.00	0.42
26 to 30	0.11	0.27	-0.16
31 to 35	0.00	0.00	0.00
36 to 40	0.00	0.00	0.00
41 to 45	0.00	0.13	-0.13
46 to 50	0.00	0.00	0.00
Total	100.00	100.00	

Fig. A4.29: The effect of scarfing on medium laminations

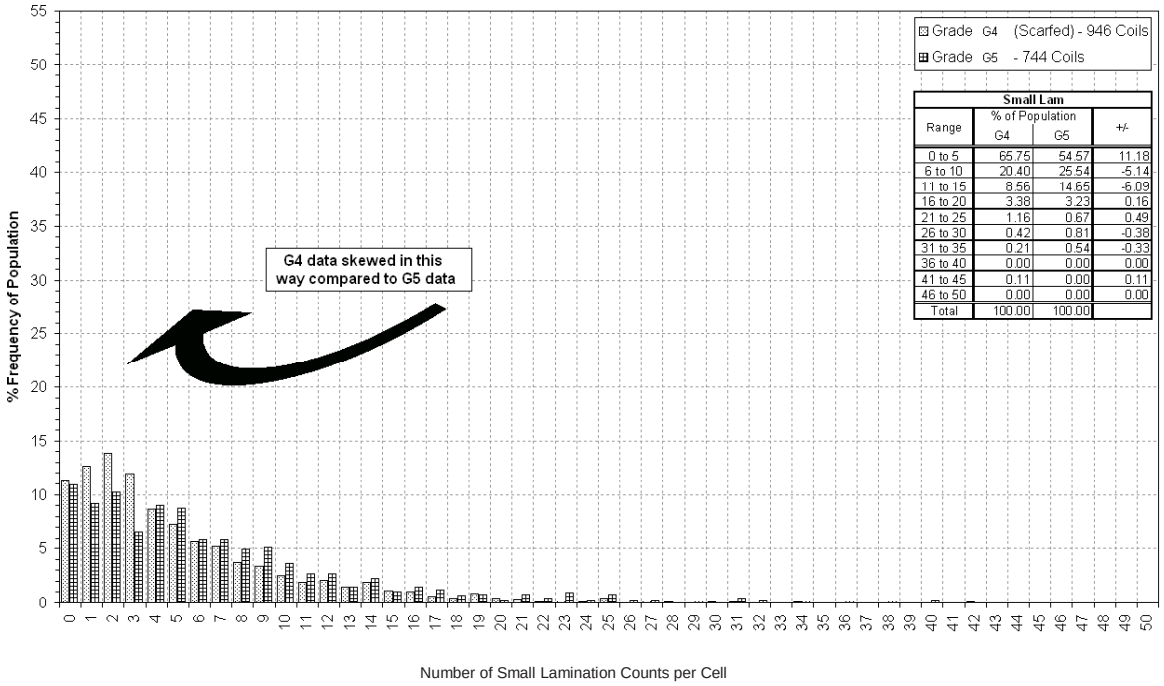

Small Lam

Range	% of Population G4	% of Population G5	+/-
0 to 5	65.75	54.57	11.18
6 to 10	20.40	25.54	-5.14
11 to 15	8.56	14.65	-6.09
16 to 20	3.38	3.23	0.16
21 to 25	1.16	0.67	0.49
26 to 30	0.42	0.81	-0.38
31 to 35	0.21	0.54	-0.33
36 to 40	0.00	0.00	0.00
41 to 45	0.11	0.00	0.11
46 to 50	0.00	0.00	0.00
Total	100.00	100.00	

Fig. A4.30: The effect of scarfing on small laminations

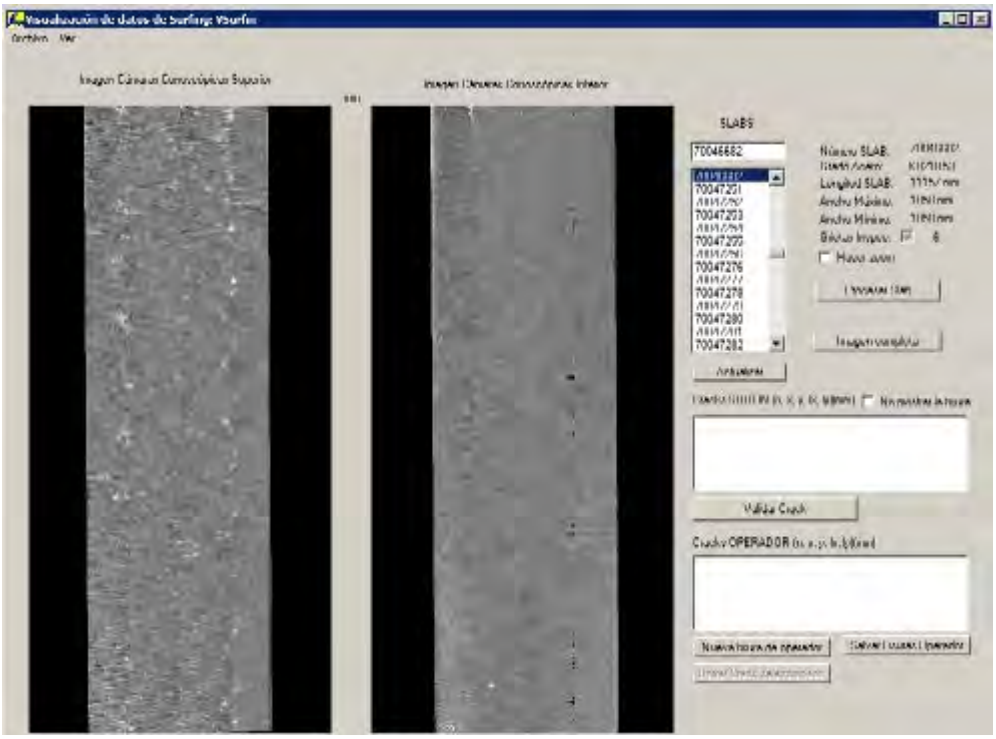

Fig. A4.31: User interface for the slab surface CH inspection system (Surfin)

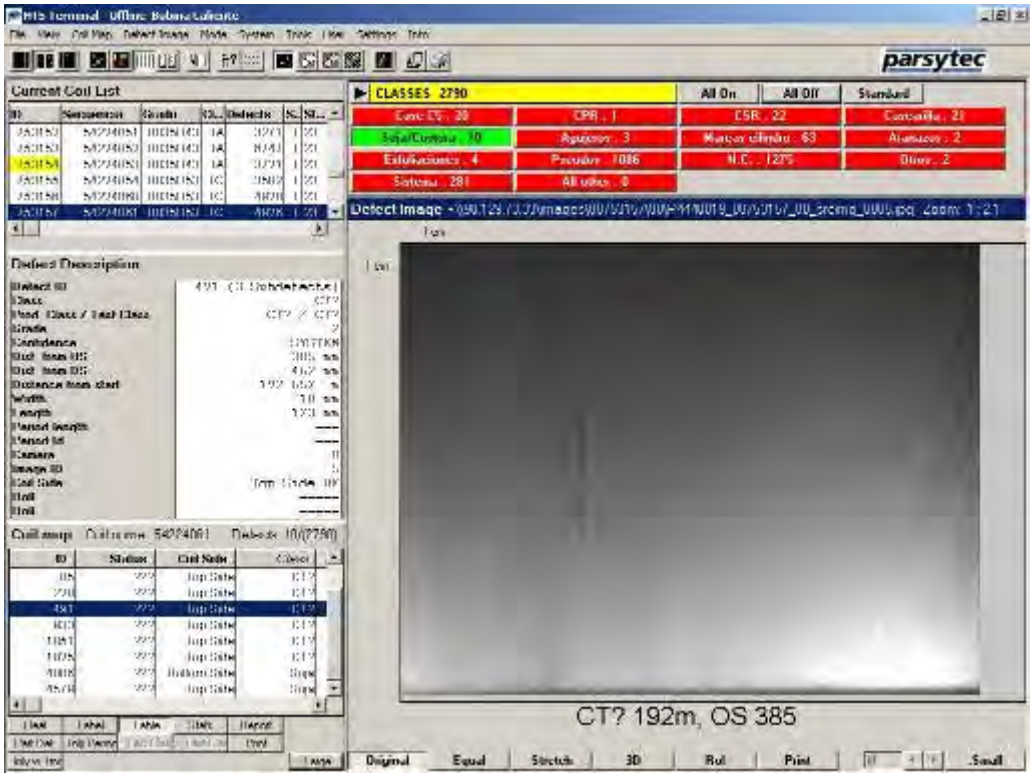

Fig. A4.32: User interface for hot coil surface inspection system (Parsytec)

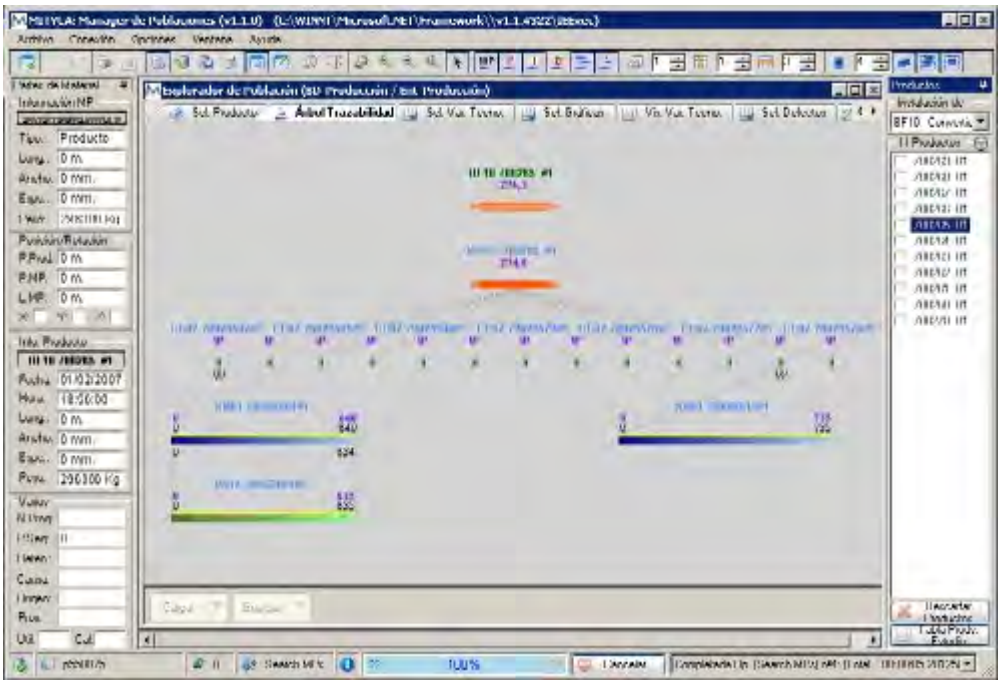

Fig. A4.33: User interface for product traceability system (Mityca)

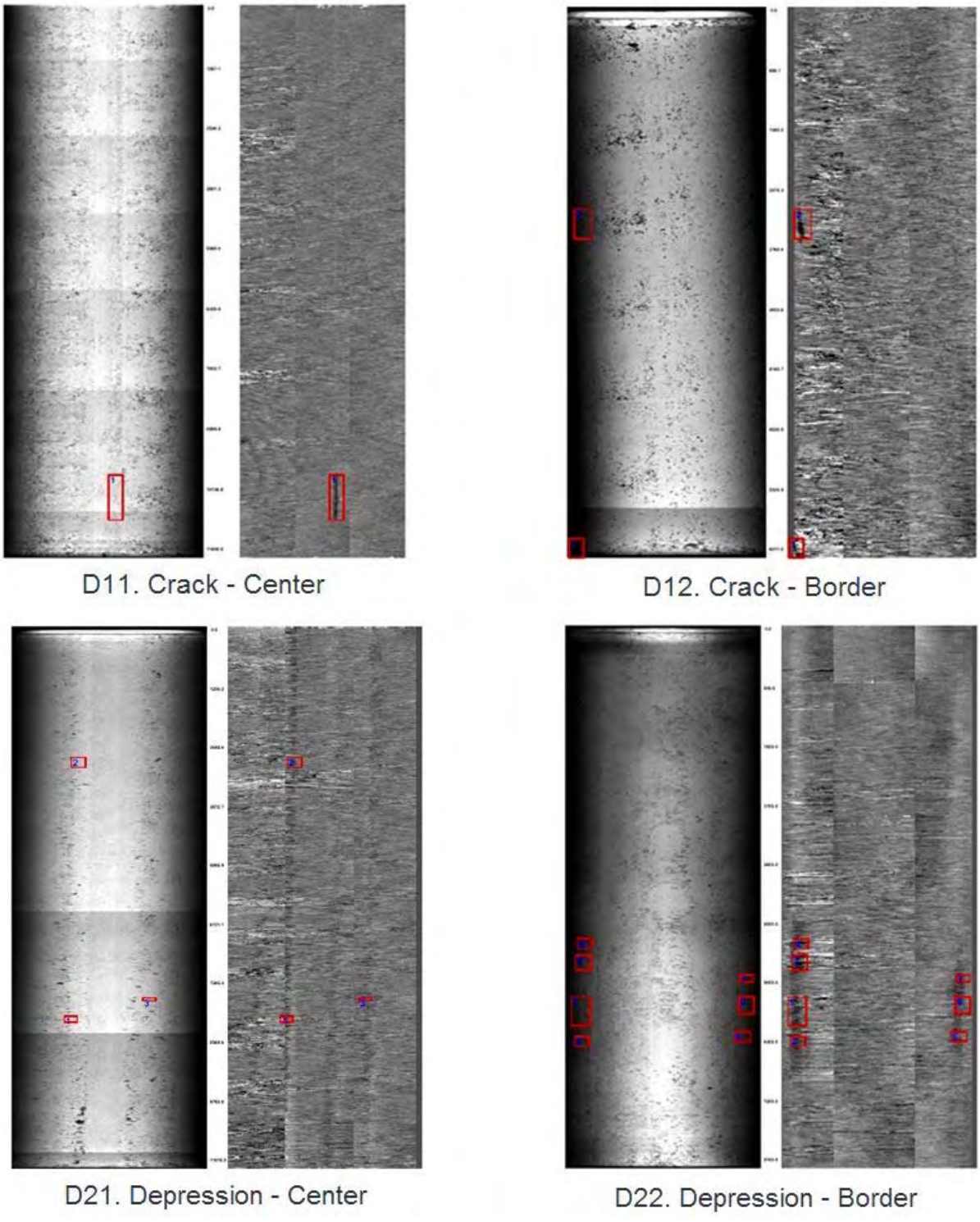

Fig. A4.34: Examples of surface defects detected from CH
with on-line surface inspection of slabs

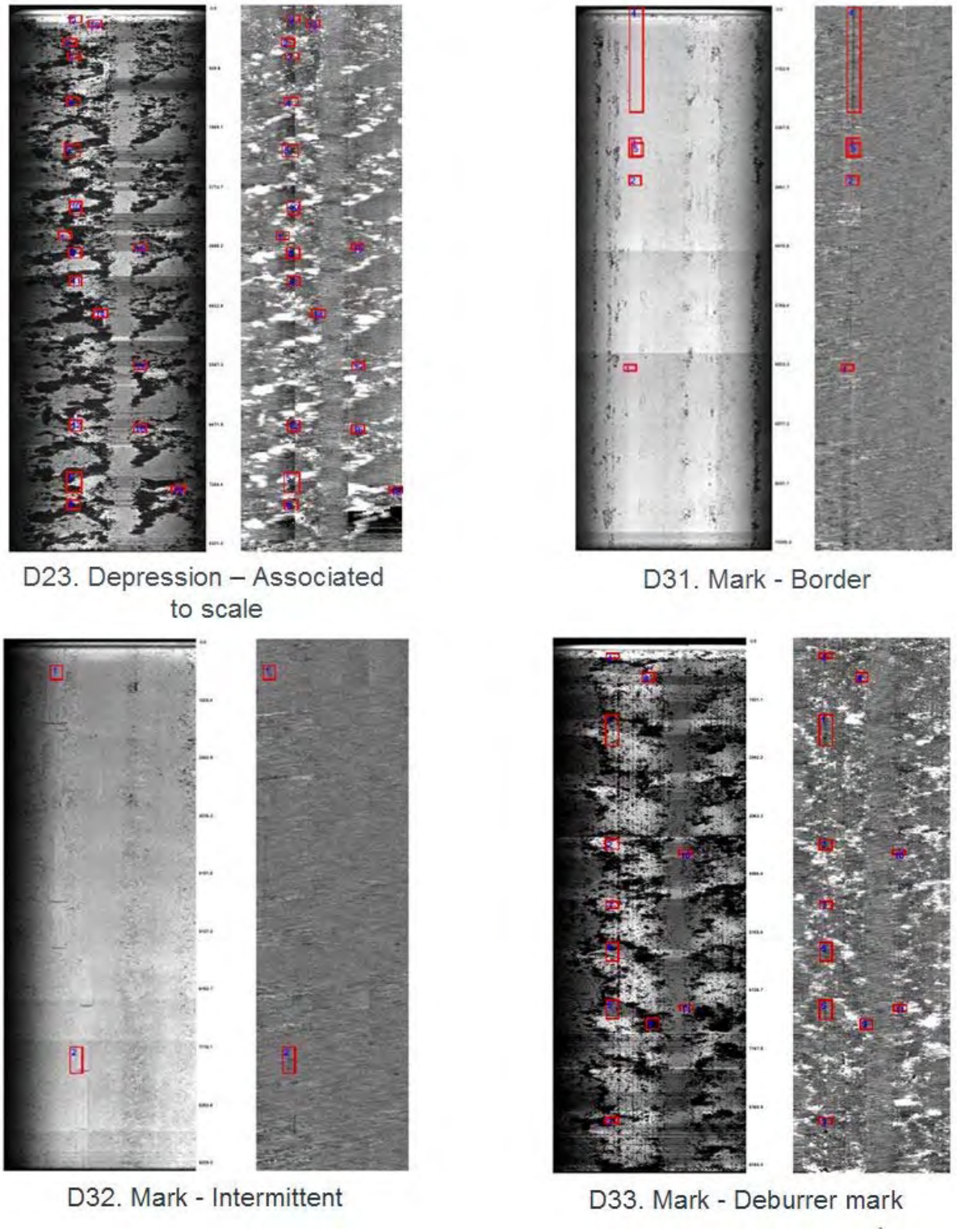

Fig. A4.35: Examples of surface defects detected with CH on-line surface inspection of slabs

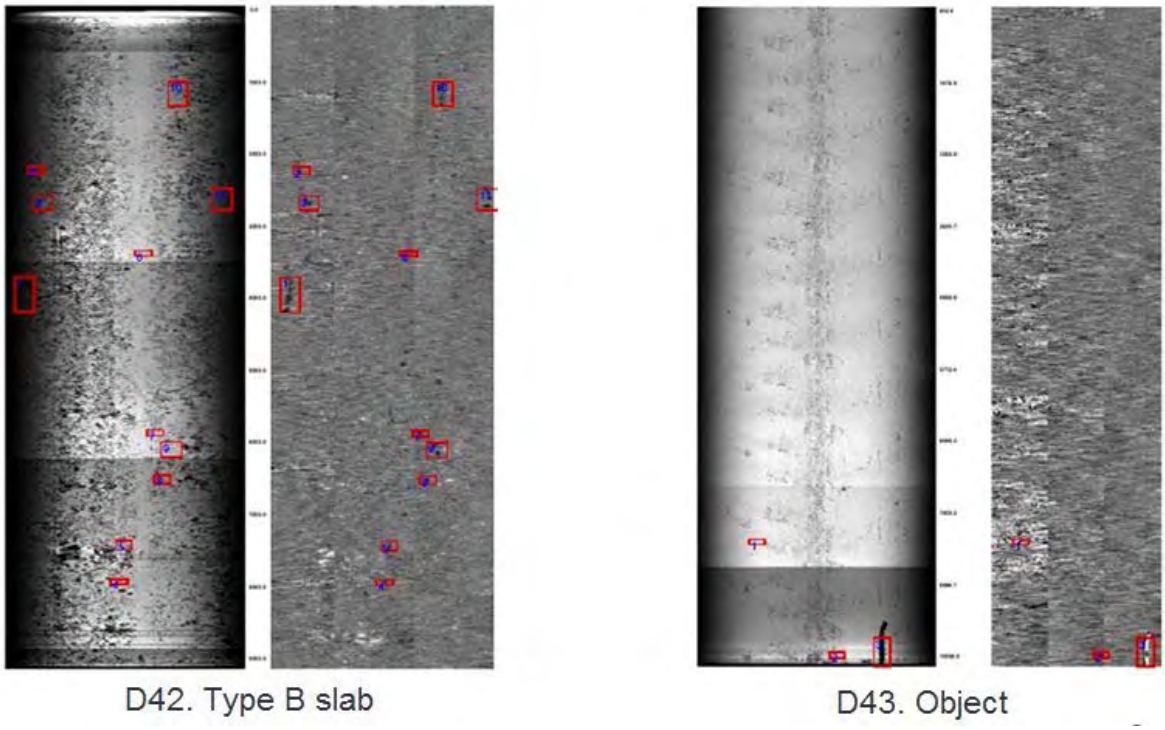

Fig. A4.36: Examples of surface defects detected
with CH on-line surface inspection of slabs

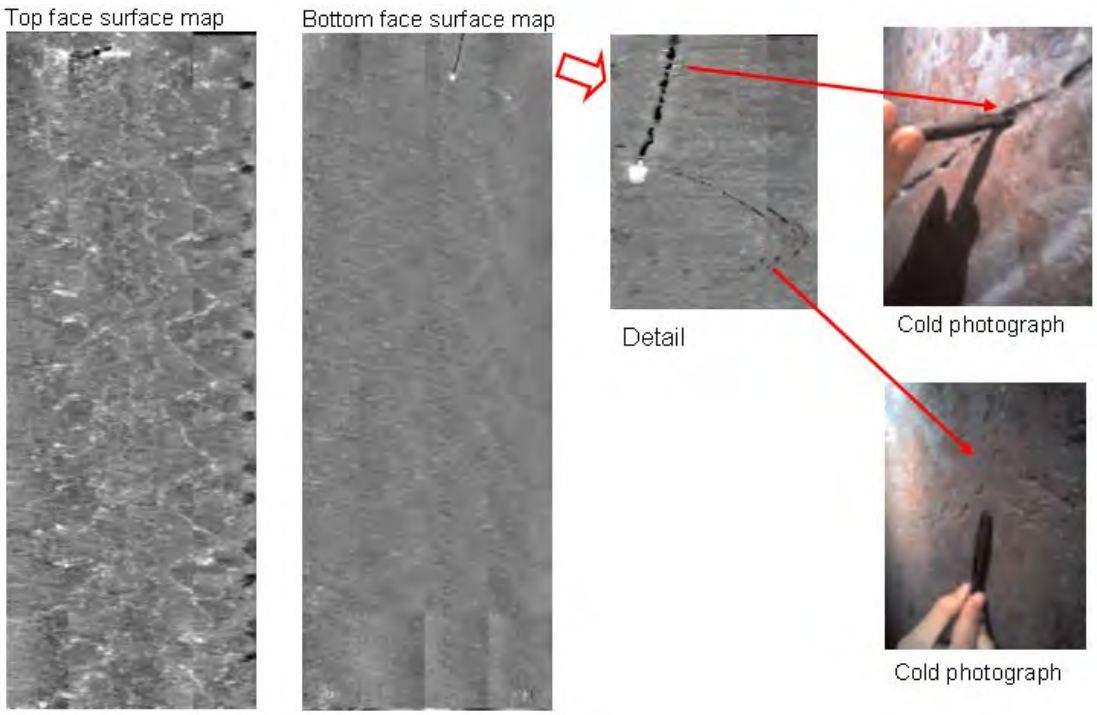

Fig. A4.37: Example of a new type of defect detected in the bottom face of some slabs

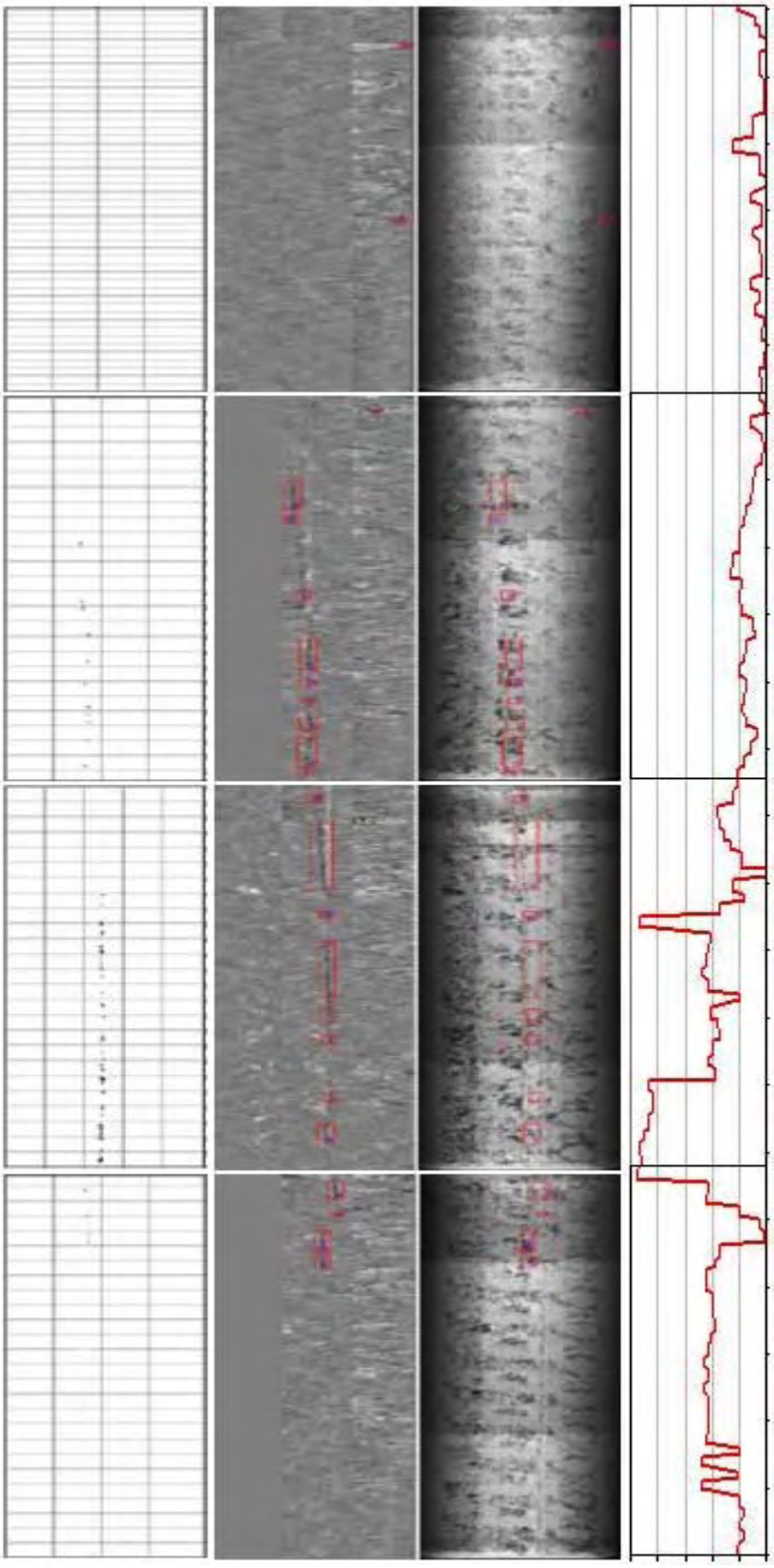

Fig. A4.38: Results for consecutive slabs with longitudinal cracks. From right to left: temperature asymmetry in mould wall, grey scale image of the slab, Conoscopic Holography distance maps and Parsytec defect detection results on hot rolled coil

CONTENTS

European Commission

EUR 23176 — The measurement and prediction of surface quality by new developments in EMATS and scarfing and the effect of scarfing on surface defects through the mills

I. Baillie, P. Griffith, A. W. Smith, M. McDonald, L. Sancho, J. Diaz, V. Colla, M. Sgarbi

Luxembourg: Office for Official Publications of the European Communities

2008 — 143 pp. — 21 × 29.7 cm

Research Fund for Coal and Steel series

ISBN 978-92-79-07647-3

ISSN 1018-5593

Price (excluding VAT) in Luxembourg: EUR 20